A Study of Impinging Gas Jets on Liquid Surfaces

By
Ho Yong Hwang, M.S., B.S. POSTECH, South Korea

A Thesis
Submitted to the School of Graduate Studies
in Partial Fulfilment of the Requirements
for the Degree
Doctor of Philosophy

McMaster University

DOCTOR OF PHILOSOPHY (2008) McMaster University

(Department of Materials Science and Engineering) Hamilton, Ontario

TITLE: A Study of Impinging Gas Jets on Liquid Surfaces

AUTHOR: Ho Yong Hwang, M.S., B.S. POSTECH, South Korea

SUPERVISOR: Professor Gordon A. Irons

NUMBER OF PAGES: xix, 213

Abstract

Impinging oxygen jets are widely used in steelmaking industries. The momentum transfer from the gas to liquid and resulting instability affect the overall productivity and operational stability. The purpose of this research is to understand the surface deformation, its stability and momentum transfer from the gas to the liquid.

Video imaging and Particle Image Velocimetry were used along with water modelling techniques. Surface deformations mainly followed the dimensionless relationship of previous researchers. The surface instability was interpreted with Blowing number and Kelvin-Helmholtz instability. Spatial and time oscillation behaviour were analyzed with Power Spectral Density analysis.

A new mathematical model with the full stress boundary condition at the surface was developed. The technique combines the Cartesian Cut Cell and Volume of Fluid method and the surface boundary was modelled as a pressure boundary. The numerical code was tested with the Broken Dam and wave instability problems. Both showed good agreement with the reported physical phenomena. Numerical tests of impinging jets showed similar surface depression depth with the water model experiments. The model was compared with other models. The liquid momentum level was higher as the gas flowrate increased and the effects of physical property changes on surface instability and momentum transfer efficiency were investigated with the mathematical model. With observations from the numerical test, momentum transfer mechanisms were proposed. Simulations of momentum transfer at industrial flow rates were also carried out.

Acknowledgements

"And if by chance they find themselves unable to accept any of the existing creeds, all they can do is to begin afresh from the beginning."— K. Popper

Thinking about the quote, I regret whether I could have done better or been strict to myself. And this reminds me the people helped me physically, mentally and academically to finish this work.

First of all, I want to thank to my supervisor Dr. Irons for his excellent supervising with his deep knowledge in process metallurgy and many kind advice. My supervising committee, Dr. Hrymak and Dr. Provatas gave me a lot of good advice, suggestions for the computational aspects and usage of SHARCNET account saved a lot of time for the computational work.

There were a lot of help from the professors and doctors other than supervising committee, I thank to Dr. Coley and Dr. Ji for steelmaking aspects, Dr. Brooks and Dr. Subagyo for surface instability parts and Dr. Guo and Dr. Lightstone for Computational Fluid Dynamics.

For the experimental parts, I appreciate Dr. Guo and Mr. Owen Kelly's help for the preparation of setup, materials and their valuable advice to shorten the work.

I also thanks to my colleagues for their useful advice, ideas and sharing good time with them. Specially I thank to Fernando Guevara and Judy Li—long time residents at JHE348, Kumar Krishnashapirody, Yi Chen, Jianhwa Li, Kamalesh Mandal, Mohammad Rhamdani and Kevin Graham.

And most importantly, I have to express a deep thanks for mental support from my family to keep up my study—Ji Jung and my children Joanne and Peter and my parents in South Korea.

To Ji Jung

Table of Contents

List of Figures

List of Tables

[1]Since the actual height of PIV picture was around 25 cm, and a 64×64 interrogation area was used, the measurable velocity range was calculated with its frame straddling time steps. This table was used as a reference in the measurement procedure.

List of Symbols

Abbreviations

Bo	Bond Number, $\frac{\rho_l g n_0^2}{\sigma}$
$\mathrm{Fr_{lm}}$	Local modified Froude number, $\frac{\rho_g u_g^2}{\rho_l g n_0}$
Mo	Morton Number, $\frac{g\mu_l^4}{\rho_l \sigma^3}$
Re	Reynolds number, $\frac{\rho u l}{\mu}$
$\mathrm{We_n}$	nominal Weber number, $\frac{\rho_g u_s^2}{\sqrt{\rho_l g \sigma}}$
CCD	Charge Coupled Device
Nd-YAG	Neodium- Yittrium Aluminium Garnet
PIV	Particle Image Velocimetry
PSD	Power Spectral Density function
VOF	Volume of Fluid

Subscript

cv	Control Volume
E	East computation node
e	East face of the computational cell
fs	Free Surface
g	Gas Phase
int	Interrogation window
l	Liquid Phase
N	North computation node
n	North face of the computational cell
nn	$\boldsymbol{n} \cdot () \cdot \boldsymbol{n}$ component of tensor
nt	$\boldsymbol{n} \cdot () \cdot \boldsymbol{t}$ component of tensor
P	Current computation node
S	South computation node
s	South face of the computational cell
sa	Surface Area
sv	Surface Volume
W	West computation node

w Wall

w West face of the computational cell

1 Phase 1

2 Phase 2

Greek

η Deflection constant for impinging gas velocity

κ Surface Curvature

μ Viscosity

ϕ Level Set function at Equation (2.17) or arbitrary function

ρ Density

σ Surface Tension

τ_{nn} Normal direction Stress Tensor component

τ_{nt} Tangential direction Stress Tensor component

θ_{eq} Equilibrium Contact Angle

$\boldsymbol{\tau}$ Stress Tensor

Superscript

$'$ Correction of variable

i i-th Phase

n Current time step

$n+1$ Next time step

T Transpose of tensor

x Extra face generated from merged cell

Roman

$\dot{M}$ Momentum rate at the nozzle exit

$\dot{m}$ Mass Flux through the cell face

$\boldsymbol{n}$ Surface Normal Vector

$\boldsymbol{t}$ Surface Tangential Vector

$\boldsymbol{u}$ Velocity Vector

A Surface Area

D Strain tensor

d Diameter of Nozzle

d_0 nozzle diameter

d_c Cavity diameter

d_k Distance from a point (x, y) to (x_k, y_k)

$d_{1/2}$ Width of a jet at the half maximum velocity

F Volume Fraction Function

$F(x, y)$ Interpolation value

F_B Body force
F_q Qian et al. (1996)'s parameter
g Gravity constant
h Distance from the surface to nozzle exit
h Surface height at Equation (2.15)
K Turbulent Jet constant
L Length of Nozzle
M Mass in a computational cell
n_0 Cavity depression
P Position of partner cell at Equation (4.32)
p Pressure
p_d Dynamic pressure
Q Position of geometric correction at Equation (4.32)
$Q(x, y)$ Least square estimation at position (x, y)
$Q_k(x, y)$ Least square estimation at position (x_k, y_k)
R_w Distance limit of interpolation neighbor selection
t Time
u Velocity
u_0 Nozzle exit velocity of a jet
u_m Centerline velocity of a jet
u_n Surface normal velocity
u_s Deflected surface gas velocity
u_t Surface tangential velocity
u_{tfs} Surface tangential velocity at the surface computation point
V Cell Volume
v Velocity
w Veritical velocity at Equation (2.15)
$W(x, y)$ Interpolation weight function
x Distance from the nozzle exit

Chapter 1

Introduction

Impinging gas jets are widely used in steelmaking practices. The Basic Oxygen Furnace (BOF) process uses a supersonic oxygen jet of around Mach 2.0 (Fruehan 1998) to impinge on the metal bath surface and this jet contributes to the reactions and slag formation. During jetting, oxygen removes carbon and other impurities such as phosphorus, silicon and manganese. The main reason for adopting the BOF is its extremely high refining rate; however, the high reaction rates have never been completely explained or understood from a mechanistic point of view because of the complex nature of multiphase and multicomponent reactions inside the BOF. One reason for the high reaction rate is a large amount of interfacial area among the metal droplets produced by the high jet momentum, so that the metal and gas phases are emulsified in the slag layer (Meyer et al. 1968). The contribution of this extra area to the overall reaction rate is estimated to be less than 50% by Price (1974). Another site for the high reaction rate is the hot spot at the jet impact point. As indicated by Price (1974) the temperature measured by optical pyrometry around that impact point is 2000$\sim$2400°C which is 500$\sim$800°C higher than bulk bath temperature, and 75$\sim$80 % of the carbon is removed in the jet impact zone.

Electric Arc Furnace (EAF) practice also uses oxygen jets to melt scrap, to remove carbon, to refine impurities and more importantly to sustain a foamy slag (Peaslee and Robertson 1994). Even though oxygen blowing in the EAF benefits its productivity and energy consumption, it can also lead to several operational problems such as excessive splashing onto water-cooled panels, slag/steel build-up on the lance, and large waves in the furnace (Fruehan 1998; Peaslee and Robertson 1994).

Thus, the supersonic oxygen jet and the interaction of it with the liquid surface cause the breaking of droplets, interface area change between the phases and the momentum transfer from the gas to liquid. These physical changes contribute to the

high reaction rate in a steelmaking vessel. So the important geometrical variations are the wave formation and the jet cavity shapes.

The objective of this study is to contribute to understand the impinging gas jet on liquid surface phenomena comprehensively. The geometrical shape, surface instability, wave and momentum transfer were investigated with water and mathematical modelling techniques.

1.1 Water Modelling

Water was chosen because of the similarity of kinematic viscosity between liquid steel and water and the difficulty of direct investigation in high temperature experiments. The dynamic similarity can be achieved with the impinging gas jet (Chatterjee et al. 1976).

The cavity shapes and the area are a result of the combined forces of the dynamic pressure and buoyancy (Banks and Chandrasekhara 1963), the vertical force balances are well reproduced in theory and experiments, but the horizontal shapes, spatial and temporal oscillations and the momentum response of liquid due to top blown gas were not understood well.

The water model investigation is to clarify the above ambiguity; the modelling is composed of two parts, video imaging and velocity measurement with Particle Image Velocimetry (PIV). For the spatial and temporal oscillation, Power Spectral Density (PSD) analysis was applied to quantify the wavelength and frequency behaviour and the kinetic energy transfer was quantified and compared with different blowing conditions to understand the liquid side response.

1.2 Mathematical Modelling

Mathematical modelling of these phenomena is helpful to understand the fluid dynamics inside of the furnaces and the free surface computation is required for this physical system.

Among the many free surface computation techniques, the Volume of Fluid (VOF) method is widely used for the prediction of free surface shape and the fluid dynamics characteristics in multi-phase flow. There are several metallurgical applications, as discussed in the next chapter.

For free surface computation, generally the flow of denser fluid is more important and the momentum comes from the denser fluid in most cases. Thus, neglecting shear stress on gas side is a good approximation. However, the impinging gas jet case has a gas-side momentum source, so it is necessary to apply the full stress boundary condition to represent the physical situation.

For this purpose, a mathematical model combining Cartesian Cut Cell and Volume of Fluid method is proposed. The proposed method is validated with existing physical evidence, such as broken dam problem and wave generation by wind. Air/Water cases are mainly simulated varying flow conditions and physical properties of water. Preliminary tests with steelmaking physical properties and flow rates in a simplified geometry were simulated.

Chapter 2

Literature Review

2.1 Turbulent Gas Jets

A free jet is a fluid stream ejected from a nozzle into an open ambient fluid environment. The ejected flow may be turbulent or become turbulent over a short distance and time if the jet velocity is high enough (Schlichting 1979). As a result of this turbulence, the stationary ambient fluid and jet fluid intermix, so that momentum, mass and other transport properties are exchanged between the free jet and ambient medium; this process is known as *entrainment*.

Flow visualization with shadow graph techniques (Anderson and Johns 1955) and mean and turbulent velocity measurements (Wygnanski and Fiedler 1969; Sforza et al. 1966; Trentacoste and Sforza 1967; Rajaratnam 1976) show three geometrically distict regions of a free turbulent jet: *Potential core*, *Transition region*, *Fully developed region*. Different authors use different names to describe the same regions, so these are noted in parentheses below. These regions are illustrated in Figure 2.1.

Potential Core (Initial flow region): The axial velocity is constant and close to the jet exit velocity. The turbulent core width is eroded by the entrainment and the core length is proportional to the initial inlet pressure or velocity (Tago and Higuchi 2003; Szekely and Themelis 1971).

Transition region (Characteristic Decay): The axis velocity decay is dependent on the initial nozzle geometry and the flow gradually emerges to the Fully developed regime.

Fully Developed Region (Axisymmetric decay, Self-Similarity region): The flow becomes independent of the initial geometry and the velocity decay has an axisymmetric 3D nature. The outer envelope of the jet acquires the form of a regular cone. The flow follows similarity relationships in this region.

In the Fully Developed region, the mean velocity and turbulent velocity similarity regions do not usually match each other. According to Wygnanski and Fiedler (1969), the mean jet flow becomes self-similar some 20 nozzle diameters downstream, while 40 nozzle diameters are required for axial turbulence, and 70 diameters for radial turbulence intensities.

Assuming this self-similar behaviour, along with momentum and energy conservation, the turbulent jet flow can be solved with the boundary layer approximation (Schlichting 1979; Szekely and Themelis 1971; Rajaratnam 1976). The similarity solutions show the following simple jet centerline velocity and expansion relationships

$$\frac{u_m}{u_0} \propto x^{-1/2} \qquad \text{plane jet} \tag{2.1}$$

$$\frac{u_m}{u_0} \propto x^{-1} \qquad \text{circular jet} \tag{2.2}$$

$$d_{1/2} \propto x \qquad \text{plane and circular jet} \tag{2.3}$$

These relationships have been confirmed by many experimental measurements (Wygnanski and Fiedler 1969; Sforza et al. 1966; Rajaratnam 1976).

Combining the boundary layer and Prandtl's mixing length theory, the free turbulent jet can be solved analytically; Tollmien and Görtler type solutions are introduced by Rajaratnam (1976). Görtler's solution is known to be superior around the jet center and Tollmien's for jet boundaries; they are compared graphically in Figure 2.2

2.2 Impinging Gas Jets on Liquid Surfaces

When a gas jet impinges on a liquid surface, the surface is deformed to balance the applied pressure from the jet and the lifting force from the surrounding liquid. The shape is the result of the balance of the dynamic, gravity and the capillary forces. Figure 2.3 shows a simple impinging jet with the corresponding geometric variables. Molloy (1970) classified liquid surface depression patterns into three stages; the typical shapes are illustrated in Figure 2.4.

Dimpling: With a low jet velocity or large nozzle height, a shallow and stable cavity forms. For air jet/water system, impact velocity at a stagnation point is less than 15 m/s (Figure 2.4a).

Splashing: With increased jet velocity or reduced nozzle height a shallow depression forms in the liquid surface and dense phase is entrained in the gas and splashed from the cavity craters. For air jet/water system the impact velocities are in the range of 15-75 m/s (Figure 2.4b).

Penetrating: For higher velocities or more reduced nozzle height, much deeper penetration of the liquid take place with reduced splashing (Figure 2.4c).

2.2.1 Computational Approaches

For the stable dimpling stage, Olmstead and Raynor (1964) solved the liquid depression profile with conformal mapping and numerical calculation, but the range of velocity was very limited.

Rosler and Stewart (1968) calculated the interface shape by matching the force balance along the surface assuming the pressure distribution as on a flat plate which is impinged by turbulent gas jet. Their equation resulted in the same form of the steady state Bernoulli's equation at the surface, which is used in the analysis of the surface waves (Lamb 1993). Evestedt and Medvedev (2004) reproduced Rosler's calculations and compared it with their experimental results.

Numerically solving Bernoulli's equation assuming an external pressure distribution is another approach to study impinging jet, and there are several publications concerning the surface wave with external pressure distribution (Vanden-Broeck 2002; Spivak et al. 2002; Maleewong et al. 2004). However, they are describing moving waves rather than stationary waves. With this approach, surface shapes had been extensively studied, but the momentum transfer from one to another phase was not taken into account.

Qian and coworkers (Qian et al. 1995; Qian et al. 1999) carried out experiments and computation on impinging gas jets on a liquid surface. They solved the gas phase first and applied the calculated static gas pressure to move the interface, and then they solved the liquid momentum equation with updated and fixed surface profiles. However, they did not give details of this interface movement algorithm.

2.2.2 Experimental Studies and Dimensionless Relationships

The extensive dimensional study of Banks and Chandrasekhara (1963) agrees well with theories and other researchers' experimental results.

The maximum depth of depression is determined through the balance between dynamic pressure and buoyancy force at the stagnation point.

$$\frac{1}{2}\rho_g u_g^2 = \rho_l g n_0 \tag{2.4}$$

This equation can be combined with turbulent jet theory, applying the centerline velocity $\frac{u_m}{u_0} = K\frac{d_0}{x}$ to produce

$$\frac{\dot{M}}{\rho_l g h} = \frac{\pi}{2K^2}\frac{n_0}{h} \tag{2.5}$$

for shallow depression and

$$\frac{\dot{M}}{\rho_l g h} = \frac{\pi}{2K^2}\frac{n_0}{h}\left(1+\frac{n_0}{h}\right)^2 \tag{2.6}$$

for a deep depression.

These relations can be found in the other sources (Davenport et al. 1967; Szekely and Themelis 1971). Turkdogan (1966) developed an almost identical analysis to Banks and Chandrasekhara (1963) and also showed good agreement with experimental observations.

Koria and Lange (1987) applied Equation (2.5) to multiple-hole nozzles with different angles. The experimental results showed good agreement in dimensionless relationships.

Qian et al. (1996) expressed Equation (2.6) differently and their experiments extended the depression relationship to the jet core and transition regions [1]. According to Qian et al.'s formulation, Equation (2.6) can be converted to

$$F_q = \frac{\dot{M}}{\rho_l g n_0 d_0^2} = \frac{\pi}{2K^2}\left(\frac{n_0+h}{d_0}\right)^2 \tag{2.7}$$

For small distances from the nozzle, Banks and Chandrasekhara expected $F = \pi/2$; this value is slightly higher than the measured value of 1.04. In the intermediate

[1] Bank and Chandrasekhara's dimensionless relationship assumes the similarity region of turbulent jet

region, F_q values increases quadratically with $\frac{h+n_0}{d_0}$ and finally matches with Equation (2.7).

Recently, Nordquist et al. (2006) compared depression depth results from many papers. They indicated the previous relationship does not match with nozzle diameters less than 2 mm. So they considered a macroscopic energy balance with some assumptions and derived a new relationship; the results match better for smaller nozzle diameters.

Contrary to the depth of the cavity that has a close relationship with jet momentum, jet cavity diameter is not sensitive to jet momentum above some high value (Turkdogan 1966; Cheslak et al. 1969). The diameter is more dependent on the distance from the nozzle and inclination angle. Bank and Chandrasekhara expected $d_c/h = 0.46$ for shallow depression and Cheslak et al. derived a paraboloid-shaped cavity shape equation. Banks and Chandrasekhara (1963) derived a dimensionless relationship between the ratio of cavity width and depression depth and dimensionless momentum with the assumption that the displaced liquid weight is equal to the vertical momentum change. The relationship has the following form

$$\frac{d_c}{n_0} = A\sqrt{\frac{\dot{M}}{\rho_l g n_0^3}} \tag{2.8}$$

A is the proportionality coefficient and it changes value according to the assumed cavity shape; $\sqrt{16/\pi}$ for parabola, $\sqrt{12/\pi}$ for elliptical and 2.9 for a deep cavity.

2.3 Splashing Phenomena

Ejection of liquid phases by splashing due to shear stress or pressure fluctuations of gas jet occurs throughout the oxygen steelmaking procedures. This splashing generates Metal/Slag/Gas emulsion, spitting of metal, skulling on the lance and can be used to spread slag coating layer to protect refractory linings. Thus, splashing has both beneficial and detrimental aspects on steelmaking practices (Fruehan 1998).

2.3.1 Droplet Generation Mechanisms

The detailed observations and physical situations at the onset of splashing have been reported and some mechanisms of droplet generation have been proposed in the

literature (Urquhart and Davenport 1973; Peaslee and Robertson 1995; Standish and He 1989).

Urquhart and Davenport (1973) proposed two different physical mechanisms. Periodic pressure variation at the stagnation point,which is due to uneven entrainment of surrounding gas during propagation, causes the jet cavity depth to oscillate vertically, and this oscillation is accompanied by droplet ejection. Horizontal displacement also contributes to generate droplet, but this mechanism is less frequent and more random.

Peaslee and coworkers (Peaslee and Robertson 1994; Peaslee 1993; Peaslee and Robertson 1995) described the large and long extension of the crater part as a *finger* in inclined jetting (Figure 2.5). Three sources of droplet generation are "tearing drops by the gas stream on both the crater side and finger, breakup of large droplets in flight by the jet stream and entrainment of liquid to the jet main stream."

Standish and He (1989) classified drop generation as two regimes from *dropping* to *swarming* and described this finger formation as the *swarming* regime. They explained this mechanism change as the reason for the sudden increase of droplet generation rate. The growth of ripples is an important reason for the droplet formation and they also indicated that the ripple growth can be aided by bottom blown bubbles, which travel along the cavity line and burst around the crater area.

2.3.2 Similarity Relationships

Droplet generation by an impinging jet on a liquid surface is dominated by the momentum intensity of the gas jet and the liquid properties, such as, density, viscosity and the surface tension. There are some important dimensionless relationships in this physical system.

He and Standish (1990) defined the *nominal Weber number*[2] as

$$\mathrm{We_n} = \frac{\rho_g u_s^2}{\sqrt{\rho_l g \sigma}}. \tag{2.9}$$

[2]The Weber number is defined as $\frac{\rho L u^2}{\sigma}$, so the nominal Weber number is not really a Weber number.

and they used this number as a criterion to determine the change of droplet generation mechanism. The sudden drop generation rate from *dropping* to *swarming* regime [3] changes when $\mathrm{We_n} \approx 10$.

Chatterjee and Bradshaw (1972) observed the critical depth of cavity depression and proposed a set of dimensionless relationships. Their experiments with many different kind of fluids show a logarithmic relationship between the *Bond* number, $\frac{\rho_l g n_c^2}{\sigma}$ and *Morton* number, $\frac{g\mu_l^4}{\rho_l \sigma^3}$,

$$\sqrt{\mathrm{Bo}} = 0.53 \log \mathrm{Mo} + 11.33 \tag{2.10}$$

Their experiments also show linear relationships between the logarithm of two different dimensionless numbers[4] with the logarithm of the *Morton* number. However, manipulation of these linear relationships show that there is a contradiction with Equation (2.10). According to them the critical depth for the onset of splashing is 1.54 cm for water, and 2.52 cm for liquid iron melts.

2.3.3 Kelvin-Helmholtz Instability

Kelvin-Helmholtz instability arises when two stratified phases are in relative motion. When unstable, a small perturbation on the interface can grow into large waves. General theories are well summarized by Chandrasekhar (1961).

In the case of the fluids in relative horizontal motion in the same direction, as illustrated in Figure 2.6, the stability condition can be simplified to

$$(u_g - u_l)^2 = \frac{2(\rho_g + \rho_l)}{\rho_g \rho_l} \sqrt{\sigma g (\rho_g - \rho_l)} \tag{2.11}$$

For (gas jet/liquid) system $\rho_g \ll \rho_l$ and $u_l \ll u_g$, Equation (2.11) can be further simplified,

$$\frac{1}{2} \rho_g u_g^2 = \sqrt{\sigma g \rho_l} \tag{2.12}$$

From this equation, the critical velocity is 6.5 m/s for the (air/water) system.

[3] This naming scheme should not be confused with Molloy's classification—in dropping regime, it is already generating small amount of splashes.

[4] $\frac{g\mu_l^2}{\sigma^2} n_c$ for viscosity independent case and $\frac{g\rho_l^2}{\mu_l^2} n_c^3$ for surface tension independent case.

Li and Harris (1995) proposed a linear relationship between critical tangential gas velocity around the jet cavity and impact velocity at the stagnation point,

$$u_g = \eta u_s \tag{2.13}$$

and Subagyo et al. (2003) proposed the *Blowing* number by combining Equation (2.13) and Equation (2.12)

$$\text{Blowing} = \frac{\eta^2 \rho_g u_s^2}{2\sqrt{\sigma g \rho_l}} = 1.0 = \frac{\eta^2}{2}\text{We}_n \tag{2.14}$$

At the onset of the splashing, η value is 0.46 (Li and Harris 1995) and 0.44721 (Subagyo et al. 2003) when comparing to the nominal Weber number criterion.

The *Blowing* number and He and Standish's *nominal Weber* number are almost identical except for the coefficient, but the *Blowing* number gives more physical meaning by interpreting the number as a measure of how many times the critical Kelvin-Helmholtz instability is exceeded.

Funda and Joseph (2001) applied viscous potential flow analysis to extend Chandrasekhara's inviscid analysis. From their theory and computation, the critical velocity for (air/water) case is around 5.75 m/s, which is 8.8 % reduced from the inviscid case. The Figure 2.7 shows neutral curve—stable and unstable boundary of velocity and wavenumbers, and the growth rate vs. wavenumber plot. The wave growth is faster on the higher wave number side from the minimum of the neutral curve, so as the velocity increases, more unstable waves are expected at smaller wavelengths.

2.4 Free Surface Modeling

Despite the recent developments of computational fluid dynamics, the physical nature of free surface or multiphase fluid motions cannot be described fully. Tracking the molecular motions on large scales is well beyond current capabilities. So various models have been proposed by many researchers, and some of them are classified and reviewed in literature (Caboussat 2005; Smolianski 2001; Ferziger and Perić 2002a; Scadovelli and Zaleski 1999).

The modelling methods can be classified by how they handle specific obstacles appearing in free surface computations,

- Lagrangian or Eulerian for general formulation and mesh movement

- Interface Tracking or Capturing method for surface determination and advection method.
- Sharp interface or diffuse interface for surface variable treatment
- Interface fitted grid or fixed grid method for computational geometry

Conceptually, the Lagrangian methods are best for fitting multiphase computation, since the system of coordinates follows the exact interface location and the well-defined interface position enables relatively easy implementation of boundary conditions. But the fluid deformation makes the mesh tangle and eventually the mesh becomes over or less populated in some locations, so they need special care for rezoning and reconstructing of meshes (Zwart et al. 1999; Perot and Nallapati 2003). When the surface topology changes, such as a merging or detaching situations, the implementations are not easy, so these methods are mainly used for small deformation cases.

Therefore, Eulerian fixed grid approaches are more popular. However, the Lagrangian and Eulerian distinctions are now almost obsolete, since many of new methods take advantage of the two and are hybrid methods. For example, the front tracking method uses a fixed grid technique to compute velocities, but tracks surface locations (Tryggvason et al. 2001; Unverdi and Tryggvasson 1992), and some Volume of Fluid methods advection uses polygon movement or line segment movements to track exact location of the surfaces (Ashgriz et al. 2004; Guignard et al. 2001; Biausser et al. 2004).

The traditional classifications are not rigid now and they can be linked to each other. So one can select a method depending on the purpose, physical nature of the problem and the ease of implementation and computation efficiency. This section will review interface tracking and capturing methods and try to point out how the new or old concepts are merged in the framework of existing methods.

2.4.1 Interface Tracking Methods

2.4.1.1 Particle Methods

The particle method is the oldest, but still useful method for free surface modeling. The earliest example is The Marker and Cell method (MAC) (Harlow and Welch

1965). In this method, velocities are computed in a fixed grid and the interface is tracked with massless particles which follow the liquid motion. This removes some complexity arising with surface topology changes, but the particle movement requires extra computational effort and the actual surface locations must be separately determined. The implementation of boundary conditions are approximated in staggered grid locations. There are some improvements of the stress boundary conditions in this method (Nichols and Hirt 1971; Chen and Hwang 1995; Demirdžić and Perić 1988).

2.4.1.2 Height Function

The height function method is the easiest to understand since the surface representation is reduced by one dimension. The kinematic condition can be exactly coupled with mass conservation, the boundary fitted adjustable grid can be implemented easily, and exact location of the surface enables the exact computation of stress boundary conditions and surface tension forces. But as indicated by its name, the height function cannot have two values at one position, so multiple interfaces are not possible with this method. Two height function correction methods are commonly used, as indicated in Apsley and Hu (2003),

- Patching with mass balancing corrections
- Systematic solver using kinematic condition

$$w = \frac{\partial h}{\partial t} + \boldsymbol{u} \cdot \nabla h \tag{2.15}$$

where w is the vertical velocity, h is the height, so the substantial derivative of height must be matched using its velocity.

Muzaferija and Perić (1997) treated the height displacement change within a time step with the mass flux balance which is based on the space conservation law (Demirdžić and Perić 1988). The cell vertices are modified after correcting height function.

Thé et al. (1994) used a framework of collocated variables for the momentum calculation, but for the surface movements, staggered volume and partial cell mass fluxes were applied to the mass conservation equation.

Egelja et al. (1998) also used a mass balance equation to track the free surface height, but they used Tri-Diagonal Matrix Algorithm (TDMA) solver to obtain the surface elevation. The correlation equations are based on the linear interpolation and the mass conservation equation.

Another interesting approach is from Lu et al. (2004) and Chen (2003). They added the vertically averaged continuity equations to the pressure-velocity coupling equation or pressure Poisson equation solver to find the surface location. Lu et al.'s approach is similar to pressure-velocity-density coupling method described in Ferziger and Perić (2002b).

Height functions exactly track the movement of the surface and the formulations are relatively simple, so it is also popular for Direct Numerical Simulations (Shen et al. 1999; Fulgosi et al. 2003) or Large Eddy Simulations (Shi et al. 2000; Shen and Yue 2001) to determine the details of flow structures.

2.4.1.3 Front Tracking Methods

The Front Tracking method usually uses a Eulerian fixed grid for momentum calculation and tracks the surface movement with the calculated velocities. Physical properties are approximated with a smoothed δ-function through the phase boundaries for the stability of computation. The surface is tracked with connected points or surface elements (Tryggvason et al. 2001; Unverdi and Tryggvasson 1992; Levesque and Shyue 1996). The Level-Set similar method or Level-Set Method itself (Gloth et al. 2003) are usually used for the momentum calculation. Some implementations of the front tracking method are hybrid methods which solve momentum in Eulerian cells and track the surface with the Lagrangian concept, which means it has the same difficulty encountered in the Lagrangian method, such as point connectivity and mesh rezoning.

2.4.2 Level-Set Method

The Level-Set Method was first proposed by Osher and Sethian (1988) and developed by many researchers (Sussman et al. 1998; Chang et al. 1996; Sussman et al.

1994; Fedkiw and Liu 2002). The Level-Set function is defined with a signed distance function across the interface,

$$\phi = \begin{cases} -d & \text{for phase 1} \\ 0 & \text{for the boundary} \\ d & \text{for phase 2} \end{cases} \tag{2.16}$$

the sign depends on the definition of distance and the points where $\phi = 0$ is the actual interface position. So in contrast to the VOF method (Section 2.4.3) the Level-Set function is a continuous function and there is no mathematical difficulty to calculate local curvature and surface normals. The physical properties are usually averaged by a smoothed Heaviside function across the boundary

$$\rho(\phi) = \begin{cases} \rho_1 + (\rho_2 - \rho_1)H(\phi) & \text{for inner phase} \\ \frac{1}{2}(\rho_2 + \rho_1) & \text{for the boundary} \end{cases} \tag{2.17}$$

Momentum is solved with the conventional method and the Level-Set functions are advected with the following hyperbolic conservation equation

$$\frac{\partial \phi}{\partial t} + \boldsymbol{u} \cdot \nabla \phi = 0 \tag{2.18}$$

Since the advection of the signed distance function and the movement of the $\phi = 0$ level are not completely related with mass conservation, mass losses are reported in the literature (Sussman et al. 1994; Sussman et al. 1998). There are two approaches to solve this problem, one is using particle spread and tracking each particle simialr to the front tracking method or particle methods (Fedkiw and Liu 2002; Enright et al. 2002). The other method is to couple the Level-Set Method with VOF method, which is known to be better in mass conservation (Sussman and Puckett 2000; Son and Hur 2002; Son 2003).

Separate phase computations and application of exact boundary conditions are performed with Ghost Fluid Method (Fedkiw and Osher 2002) and Boundary Condition Capturing Method (Liu et al. 2000; Kang et al. 2000).

2.4.3 Volume of Fluid

The volume of Fluid Method was first devised by Hirt and Nichols (Nichols et al. 1980; Hirt and Nichols 1981). It is an Eulerian fixed grid method to capture the surface location with a liquid or main phase volume fraction function which is defined as

$$F = \begin{cases} 1 & \text{when cell is full} \\ 0 & \text{when cell is empty} \\ 0 \sim 1 & \text{otherwise} \end{cases} \tag{2.19}$$

Physical properties are averaged by volume fraction and this average is directly applied to the momentum equation regardless of its phase.

$$\rho = F\rho_2 + (1 - F)\rho_1 \tag{2.20}$$

The conventional VOF method solves one set of momentum, mass and other scalar functions, so it is efficient from its computer memory storage aspect.

After solving the mass and momentum equations the volume fraction function will be advected with the following equation, but there are many variations for this equation

$$\frac{\partial F}{\partial t} + \boldsymbol{u} \cdot \nabla F = 0 \tag{2.21}$$

Despite the fact that this equation has the same form as Equation (2.18), the advection term is for the volume fraction of an existing phase, so mass conservation is preserved in the VOF Method.

2.4.3.1 Surface reconstruction and Volume Tracking Methods

There are many papers are available on the VOF advection techniques and those have been well compared in the literature (Benson 2002; Rudman 1997; Rider and Kothe 1998). Figure 2.8 compares several methods graphically.

The original SOLA-VOF(SOLution Algorithm-Volume of Fluid) (Hirt and Nichols 1981) constructs parallel surfaces depending on whether it is horizontal or vertical, and used a Donor and Accepter scheme to move the volume fraction (Figure 2.8b). When the volume is advected, the void fraction is also checked and the advection equation limits the volume and void fraction change so that F does not go below

zero or above unity. Ubbink and Isa (Ubbink and Issa 1999) extended the donor and acceptor method for use in unstructured grid systems.

Young's Method (Young 1982) is a piece-wise linear construction (PLIC) method; it represents the interface with line segment corresponding to its orientation and volume fraction, so it is accurate and most popular (Figure 2.8c). However, the original Young's Method has some numerical diffusion, so nowadays explicit geometrical schemes are used more often (Son 2003; Son and Hur 2002; Gueyffier et al. 1999).

Ashgriz and Poo (Ashgriz and Poo 1991) developed the FLAIR (Flux Line segment model for Advection and Interface Reconstruction) Method. In this method, the interface line construction is placed in the cell face between two neighbor cells instead of the cell center, so the surface construction is staggered (Figure 2.8d). This method generates better reconstruction of the surface than SOLA-VOF, but superiority to Young's Method is not clear.

Since better estimation of surface orientation gives better momentum computation, and volume advection quality, and since the surface representation becomes very important when the surface tension contribution is larger, there are many improvements in surface representation techniques. Benson (2002) introduced piecewise parabolic construction and Ginzburg and Wittum (2001) used spline interpolants to construct the interface.

For the volume advection, Lagrangian concepts were introduced by Puckett et al. (1997). They consider velocity direction of the cell corner vertices and count the contribution of actual diagonal donor cells. (Harvie and Fletcher 2001) used similar concepts and showed better results. SL-VOF(Semi Lagrangian-Volume of Fluid) (Biausser et al. 2004; Guignard et al. 2001) tracks line segment movement instead of the volume conservation equation. Ashgriz et al. (2004) tracked each partial polygon movement in unstructured grids and called it CLEAR-VOF(Computational Lagrangian Eulerian Advection Remap-Volume of Fluid).

2.4.3.2 Surface normal and Curvature

The surface orientation and geometric information are important to obtain an accurate representation of the surface, and consequently leads to the computation being closer to the real situation. Specifically, when surface tension is included or has

an important role in momentum transfer, the computation can produce a completely different pattern compared to neglecting surface tension.

The surface normal vector and curvature estimation methods are usually introduced together, since the curvature estimations usually depend on the surface normal. The surface normal vector is mathematically defined as

$$\boldsymbol{n} = \frac{\nabla F}{|\nabla F|} \tag{2.22}$$

Because of the discrete nature of volume fraction function, the estimation of Equation (2.22) requires special care and several methods are reviewed in the literature (Benson 2002; Cummins et al. 2005).

Based on the normal vector estimation, curvatures are calculated with the following formula

$$\kappa = -\nabla \cdot \boldsymbol{n} \tag{2.23}$$

the sign depends on the definition of the phase and the direction of the normal.

The local height function is the same as used in SOLA-VOF (Hirt and Nichols 1981). It determines the direction first depending on its orientation and constructs local height functions by summing up 3 cells in the 9-cell stencil as illustrated in Figure 2.9a.

The convolved volume fraction function is most popular and the construction is well described in (Rudman 1997) for uniformly sized cells. This method can be interpreted as an average of discrete gradients which are generated with nearest neighbor cells (see Figure 2.9b). This construction is mathematically identical with the method used in the Continuum Surface Force Model (Blackbill et al. 1992).

The reconstructed distance function is a similar to Level-Set method. It construct distance function from volume fraction, then the curvature estimation is straightforward because of the continuity of the distance function (Figure 2.9c). The example can be found in coupled Level-Set and VOF method (Son 2003).

The performance of those methods are compared by Cummins et al. (2005), and they recommended not to use the height function method when $\kappa\Delta x$ value is higher than 1/5, which means that the radius of curvature is less than five cells.

Some newer methods have been introduced in the literature. In the spline construction method (Ginzburg and Wittum 2001) the curvature is directly obtained

from the arc length gradient. Meier et al. (2002) used a least-squares fit the of curvature value with a known curvature reference and three geometrical parameters which are the relative amount of liquid volume compared to a flat interface, volume fraction and tilt angle. Least squares improvements are mentioned in the literature (Benson 2002; Puckett et al. 1997); the details of implementations are described in Martorano et al. (2006) and in Appendix B.

Increasing the number of cells may be another choice to improve the quality of the surface representation and flow behavior. The adaptive Mesh Refinement technique has been recently applied to VOF formulations (Greaves 2004; Theodorakakos and Bergeles 2004; Wang et al. 2004). They used a quad-tree data structure to find neighbor cells. A special geometrical treatment is required for refining or coarsening cells.

2.4.3.3 Surface Boundary Conditions

The standard boundary condition in vector form at the two-phase boundary is shown in Blackbill et al. (1992)[5]

$$(p_1 - p_2 + \sigma\kappa)\boldsymbol{n} = (\boldsymbol{\tau_1} - \boldsymbol{\tau_2}) \cdot \boldsymbol{n} + \nabla\sigma \tag{2.24}$$

and the normal and tangential direction components are separately expressed as

$$p_1 - p_2 + \sigma\kappa = \tau_{nn1} - \tau_{nn2} + \nabla_n\sigma \tag{2.25}$$

$$0 = \tau_{nt1} - \tau_{nt2} + \nabla_t\sigma \tag{2.26}$$

This boundary condition is usually approximated depending on the physical situation. In most cases, the spatial gradient of surface tension ($\nabla\sigma$) is neglected except in the case where Marangoni flow is important. If the momentum is not from gas-side shear in Air(1)/Water(2) system, air side tangential shear stress (τ_{nt1}) can be neglected and the pressure (p_1) can have a fixed value. When the body force is greater than viscous forces, normal shear stresses (τ_{nn}) can be neglected also. So the

[5]The paper cites Landau and Lifshitz (1987).

boundary condition for Air/Water free surface system generally were reduced to the following formula,

$$p_1 - p_2 + \sigma\kappa = 0 \tag{2.27}$$

$$0 = \tau_{nt2} \tag{2.28}$$

The normal component has a jump condition because of the surface tension term; treatment of surface tension was an issue in the early development stage of the VOF method.

The SOLA-VOF scheme (Hirt and Nichols 1981) added surface tension terms directly to the velocity computation as a surface force. Blackbill et al. (1992) invented the Continuum Surface Force (CSF) method to treat the surface force as a body force around the free surface based on Equation (2.27). The volume integral converges to a surface integral when the thickness becomes small.

$$\lim_{h\to 0} \int_{\Delta V} F_{sv}(\boldsymbol{x})\, dV = \int_{\Delta A} F_{sa}(\boldsymbol{x}_f s)\, dA \tag{2.29}$$

The volume forces are approximated with the following equation. They used a smoothed volume fraction function when calculating the gradient for stability

$$F_{sv}(x) = \sigma\kappa(x)\frac{\nabla F(x)}{[F]} \tag{2.30}$$

$[F]$ is the jump in volume fraction, so it is 1.0. Using the CSF method makes the discretization of the flow equation simpler, since it removes all the difficulty arising from surface geometry information and orientation, but this method is based on the simplified boundary condition Equation (2.27); the extension to the general case is not straightforward.

For the tangential component of boundary conditions, the gas side shear stress is usually neglected and normal part of stress terms (τ_{nn}) are completely neglected in many VOF computations.

There have been some efforts to apply more exact boundary conditions by including more of the stress terms in Equation (2.25) and (2.26). Chen et al. (1995) applied the stress term in the normal stress boundary condition in one phase with improved surface orientation information, but in the actual implementation, they separated the

pressure part and stress part and set them to be zero; also the gas side shear stress was neglected. The Finite Element implementation (Jeong and Yang 1998) gives more flexibility in application of surface boundary condition, but the tangential shear stress was not fully implemented.

In the VOF framework, the surface boundary conditions are applied in very limited conditions. However, with the Height Function (Fulgosi et al. 2003) or fixed boundary situations (Lombardi et al. 1996), the tangential shear stress conditions are well implemented.

For the solid boundary, the wall adhesion effect must be included. The application is straightforward to change surface normal vectors at the wall using the known contact angle, if one assumes only the equilibrium contact angle

$$\boldsymbol{n}_w = \boldsymbol{n}_{wall} \cos\theta_{eq} + \boldsymbol{n}_{tangent} \sin\theta_{eq} \tag{2.31}$$

2.5 Cartesian Cut Cell Method

The Cartesian Cut Cell method is an alternative to the body fitted grid method to compute complex geometrical boundary situations. Recent moving grid extensions to this method enable the computation of flow around a moving non-regular shaped solid object, solidification or melting (Udaykumar et al. 1999; Shyy et al. 1996; Udaykumar et al. 1996).

In the Cartesian Cut Cell method, the phase boundary cuts the regular cartesian grid cell faces, and based on this cut the cell will be separated as illustrated in Figure 2.10. When the cells are cut, relatively small or thin new cells are generated and if one proceeds with a computation with those cells, the computation may be too unstable and may take a long time for convergence. To remove this situation, cell merging techniques are usually used; the details of procedures are explained in the literature (Shyy et al. 1996; Clarke et al. 1986; Yang et al. 1997) and Chapter 4.

Coirier and Powell (1995) compared body-fitted grid and Cartesian grid methods with adaptive mesh and uniform mesh cases. The absolute error level was higher in the Cartesian grid method, but kept the same second-order accuracy as with the body-fitted system. They indicated that the cell merging technique significantly improves

in computation efficiency. Lower error level in structured body fitted grid case was attributed to a fortunate flow stream line alignment with the grid.

For the merged cell faces, flow properties are interpolated; a second order directional interpolation scheme was devised by Ye et al. (1999b, 1999a). They also applied a preconditioned Bi-Conjugate stabilized (Bi-CGSTAB) solver and obtained approximately 6 times faster computation time. Udaykumar et al. (2001) extended the second order interpolation scheme to moving boundary problems and devised a unique multigrid technique which fits the Cartesian grid situation. There is another implementation of multigrid solver for Cartesian grid method (Tai and Shyy 2005). Udaykumar et al.'s multigrid defines a volume fraction parameter and neglected multigrid cells with less than a critical volume fraction (0.5); Tai and Shyy's method subtracts unmerged cell's coefficients and applies multigrid coarsening directly across the boundary, so a smearing error across the boundary is expected.

Some hybrid methods are also applied to the Cartesian Cut Cell method. In these hybrid methods, solid boundaries are treated with the Cartesian Cut Cell method and some conventional fluid-fluid boundary method, such as VOF or immersed boundary method are used for the fluid interfaces. Qian et al. (2003) computed surface wave behavior along a sloping beach with VOF. Udaykumar et al. (1997) computed droplet movement through a constricted tube.

2.6 Metallurgical Applications

Liovic and cowokers (2001, 2002) applied the VOF method with CSF surface boundary modeling to several metallurgical multiphase flow cases such as rising bubbles, flow over a weir and submerged gas injection. The bubble rising velocity agreed well for small bubbles (~ 3 mm) and their computation was useful for the development of a new vessel design.

Guo and Irons (2002) combined a two-fluid model with VOF to simulate the bubble plume and spout height variation. The measured height were considerably larger than the computed values; they indicated bubble plume momentum was modelled properly, but the discrepancy was likely due to neglect of the phenomena associated with bubbles breaking the free surface.

Olivares et al. (2002) used the VOF with RNG (ReNormalization Group) k-ϵ turbulence and investigated top, bottom and combined blowing cases in a BOF converter to the experiments and numerical computation. The penetration depth was related with modified Froude number and the mixing time in numerical modeling and experimental results agreed well with each other.

Forrester and Evans (1996) used CFX-FLOW3D^{TM} sowftware package for an impinging gas jet in confined and unconfined liquid containers. Nguyen and Evans (2003) used VOF in FLUENT^{TM} to simulate a similar situation. Forrester and Evans showed faster liquid movement than experimentally reported values, and Nguyen and Evans showed some discrepancy in surface geometrical shapes. Odenthal et al. (2007) used FLUENT^{TM} with some modification to compute 3-Dimensional behavior of top and bottom blowing situations in the BOF and AOD; the computation results gave good insight of the flow behavior inside of the converter, but the computation cost was very high[6].

Ersson et al. (2006) coupled Thermo-Calc^{TM} and FLUENT^{TM} to compute the carbon content in the droplet and hot spot position. The carbon content was assumed to be the same for the bulk and hot spot positions. So they expected very thin hot spot ranges. This is an example of more advanced extension of free surface application to reacting metallugical systems.

As reviewed above, the VOF method is popular for metallurgical processing system with free surface and many commercial software now provide VOF or other free surface computation. Iron and Steelmaking systems are essentially multiphase reacting systems. The increase of computation power enables the computation of some complex situation which was impossible before. Free surface computation is expected to contribute more to the design and the control of the metallurgical process in the future.

[6]A typical computation time indicated by the author was two weeks for five second simulation with 5 parallel processors

2.7 Experimental Techniques

A general review of the flow measurement techniques was done by Szekely (1979). The Particle Image Velocimetry(PIV) technique is well reviewed by Gharib and Daribi (2000) and Prasad (2000).

General PIV procedures are described briefly. Tracer particles, with similar density to the fluid, are spread in the fluid of interest. The moving particles in the fluid are illuminated with a laser light sheet in a short time period. The image is taken by a digital camera. The sequential image is subdivided into smaller rectangular areas—interrogation areas. One interrogation area can move over the other and maximum cross-correlation of illuminated particle intensity is calculated.

$$C(\boldsymbol{s}) = \int_A I(\boldsymbol{x}) I(\boldsymbol{x} + \boldsymbol{s})\, d\boldsymbol{x} \tag{2.32}$$

This procedure is schematically illustrated in Figure 2.11, the shift of interrogation area determines the displacement of the group of particles in that area. The time step between the two images permits determination of the velocity.

The PIV technique has some advantages and disadvantages over the other techniques. If the tracer particle is carefully chosen, PIV can be classified as a nonintrusive method; the fluid is not disturbed around the measurement probe. Contrary to point based methods such as Pitot tube, Hot Wire technique, and LDA (Laser Doppler Anemometry), PIV technique can measure many velocities at once since it is processing 2-dimensional cross-sectional images. Recent development of digital image processing also enables an extension to 3D with stereo PIV and high speed PIV.[7]

The PIV technique has some drawbacks over other techniques. As indicated in the previous paragraph, the tracer must be carefully selected. Unfortunately, no tracer can have exactly the same density as the fluid, so the particle motion does not follow the fluid exactly. Cross-correlation method gives spatially averaged information over the interrogation area. Escaping particles from the interrogation area cause some error on the computation of velocity gradients. Therefore, particle and interrogation area and time step must be chosen carefully for the accuracy of the measurement.

[7] http://www.lavision.de

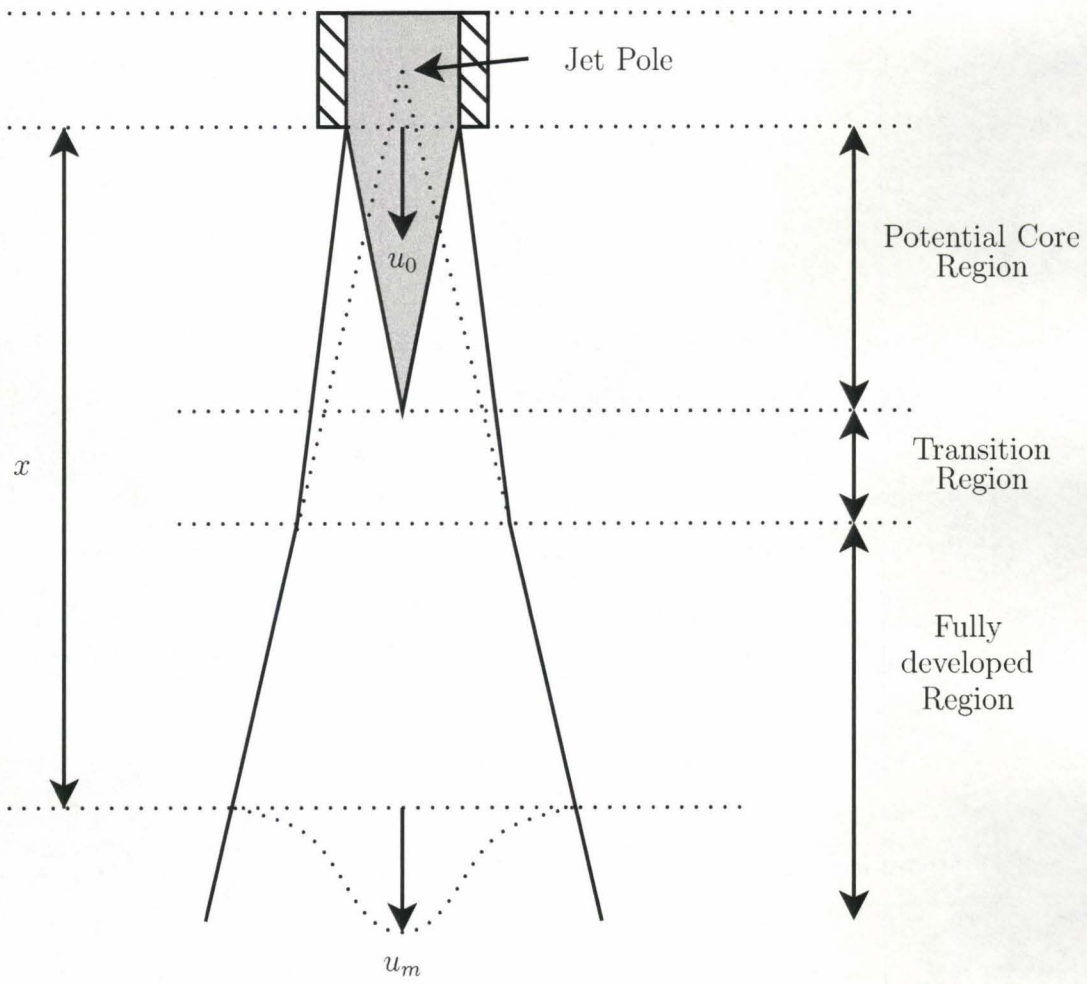

Figure 2.1: Three regions of a turbulent gas jet (Szekely and Themelis 1971)

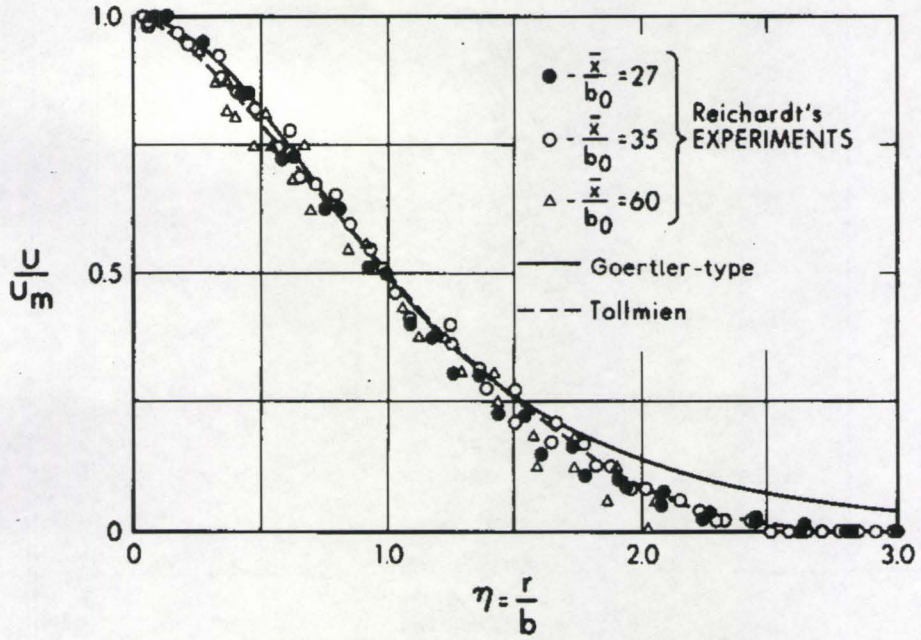

Figure 2.2: A comparison of Görtler and Tollmien type solution of turbulent free jet, The figure is from Rajaratnam (1976)

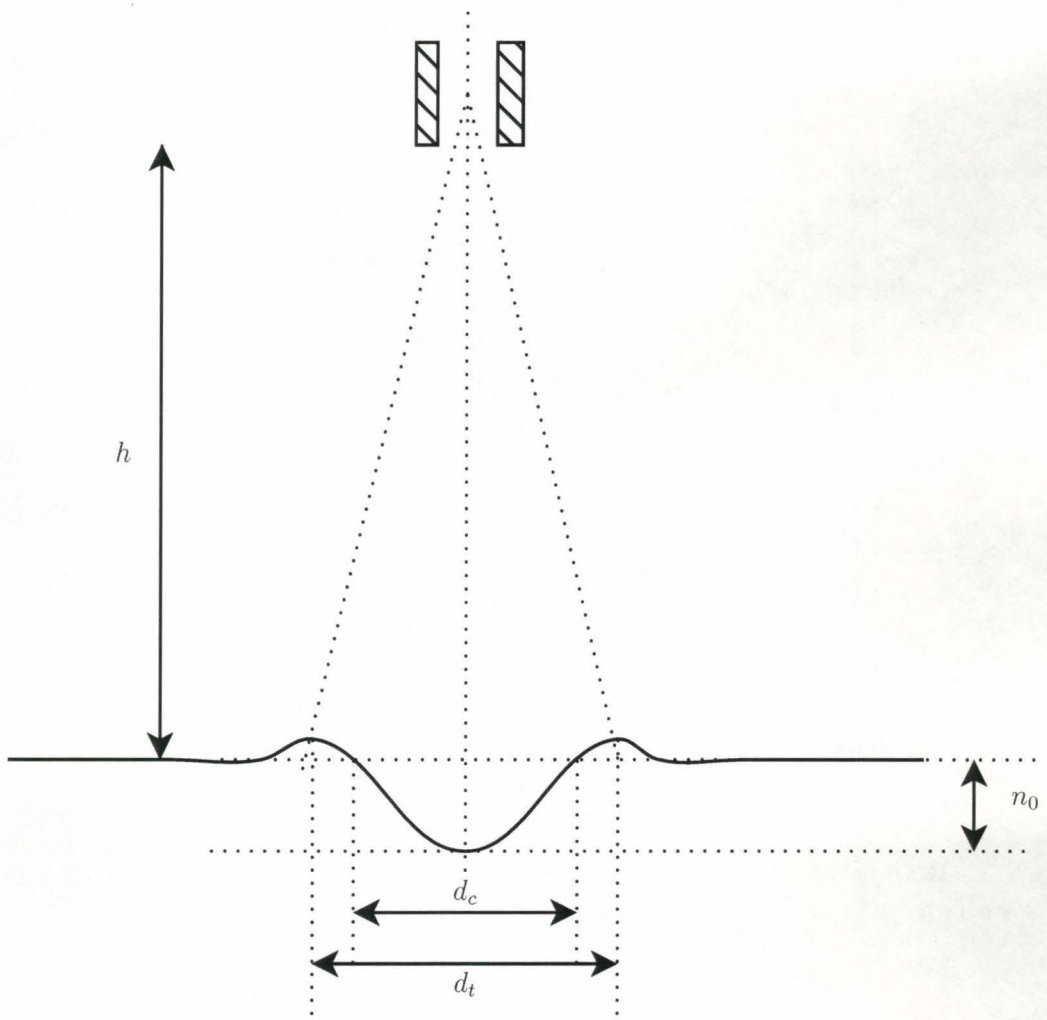

Figure 2.3: A typical shape of liquid surface depression caused by an impinging top jet. The variable naming scheme is based on Banks and Chandrasekhara (1963).

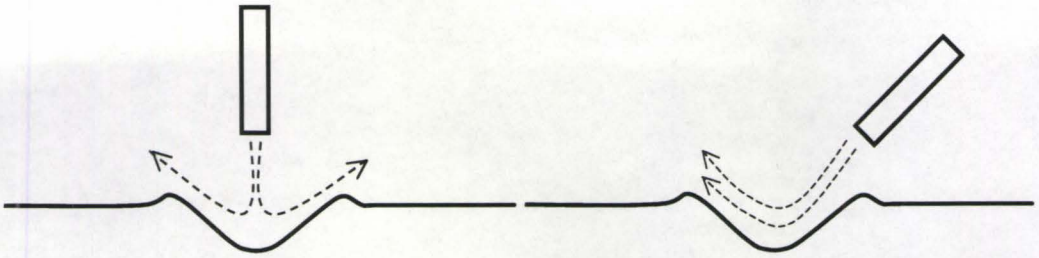

(a) Dimpling

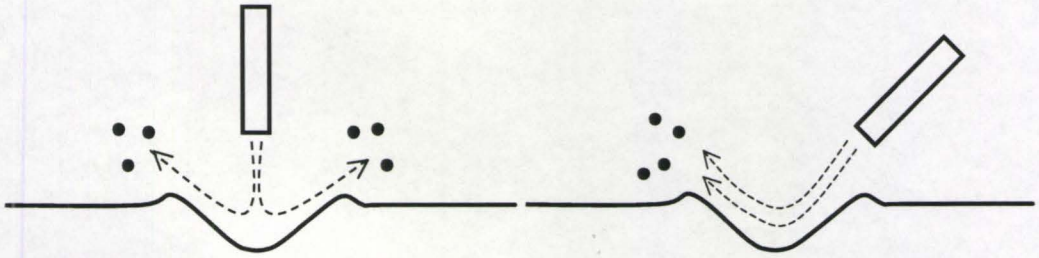

(b) Splashing

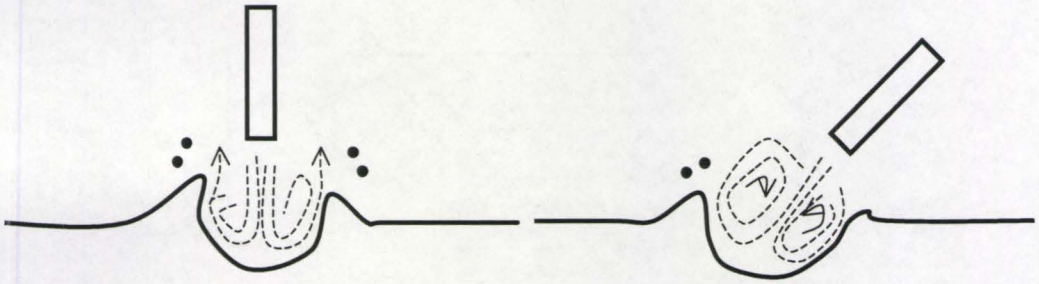

(c) Penetrating

Figure 2.4: Three depression patterns of vertical and declined jets (a) Dimpling stage: Shallow and stable depression (b) Splashing: droplet generation (c) Penetrating: reduced splashing and deeper cavity (Molloy 1970).

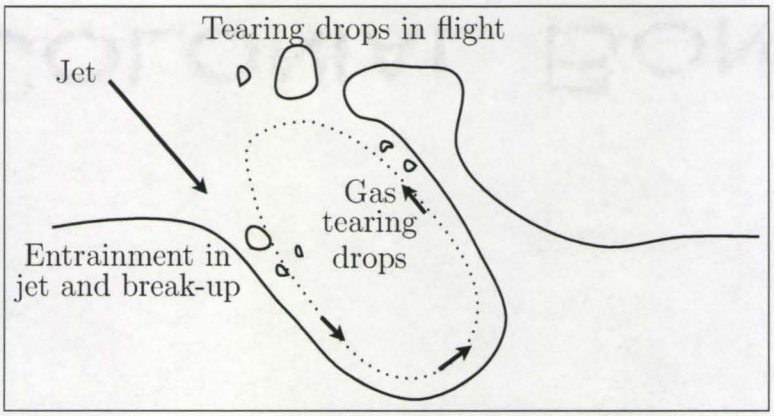

Figure 2.5: Droplet generation mechanism proposed by Peaslee and Robertson for inclined jetting (Peaslee and Robertson 1994).

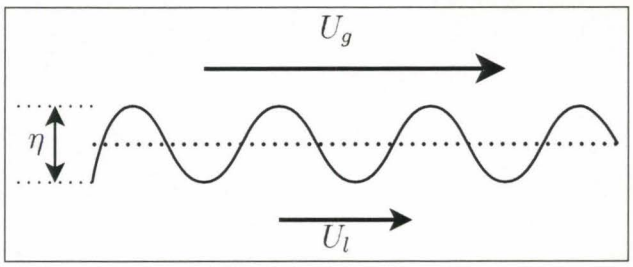

Figure 2.6: Kelvin-Helmholtz Instability occurs when two stratified fluids flow with different velocities

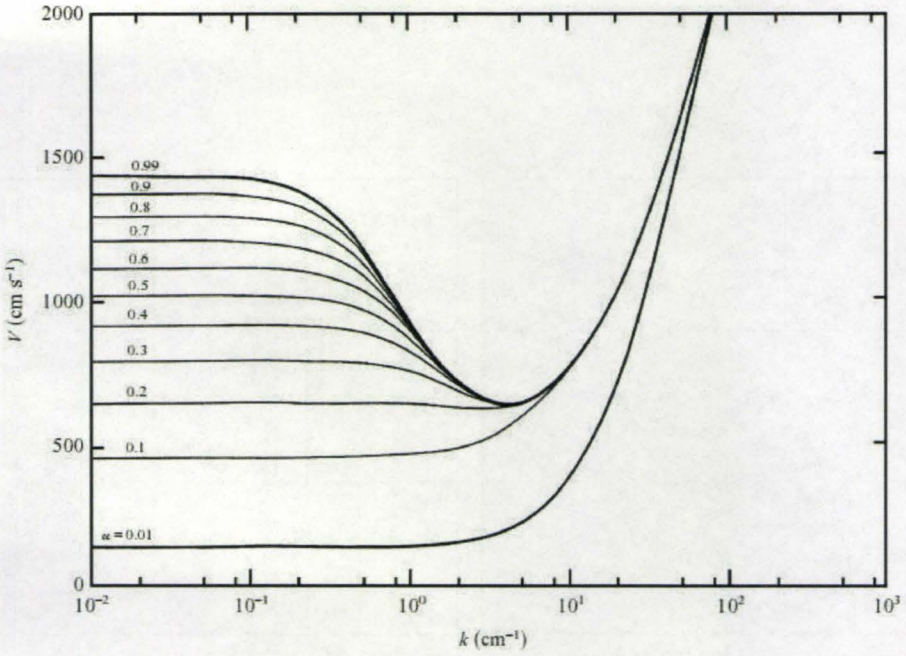

(a) Neutral Curve

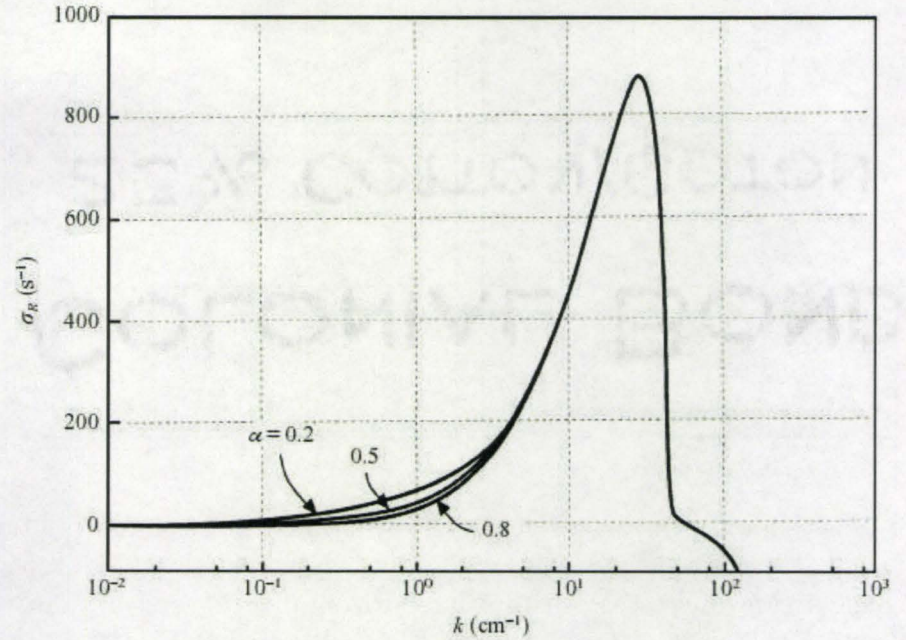

(b) Growth Rate

Figure 2.7: (a) A Neutral curve, which indicate the stable and unstable velocity and wavenumber regions, (b) Real part of growth rate(σ_R) vs. wavenumber plot. This shows the most growing wavenumeber is located right side of critical wavenumber. All figures are from Funda and Joseph (2001).

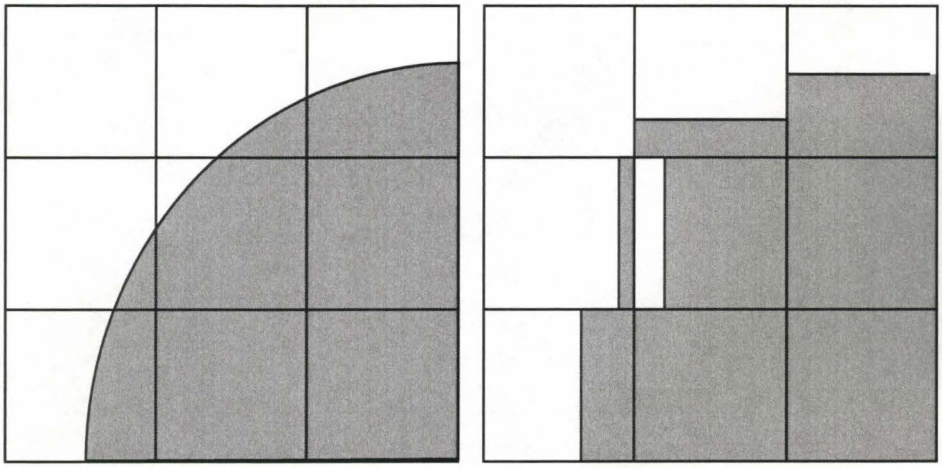

(a) Original

(b) Donor Accepter

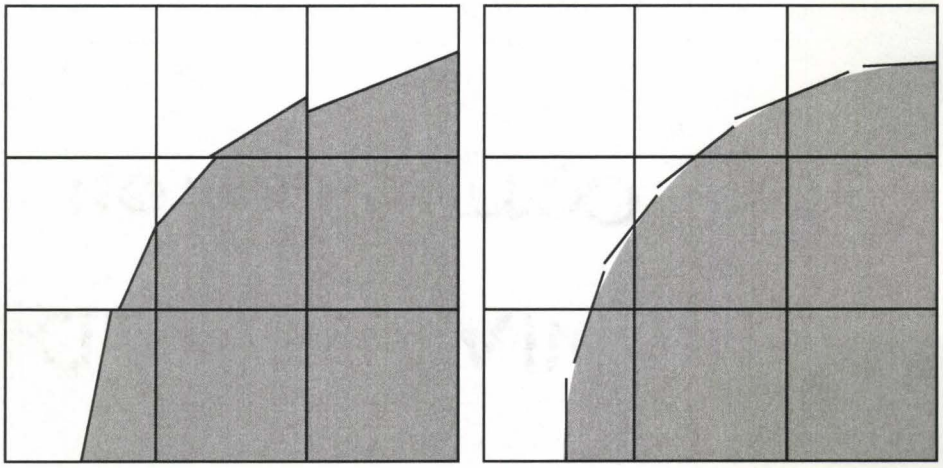

(c) Youngs

(d) Flair

Figure 2.8: The comparison of surface reconstruction from volume fraction function, (a) Original surface, (b) SOLA-VOF (Hirt and Nichols 1981) type Donor-Acceptor construction make the surface flat horizontally or vertically, (c) Young's Method (Young 1982) draw a line inside of each cell and (d) FLAIR (Ashgriz and Poo 1991) constructs line across the each cell faces.

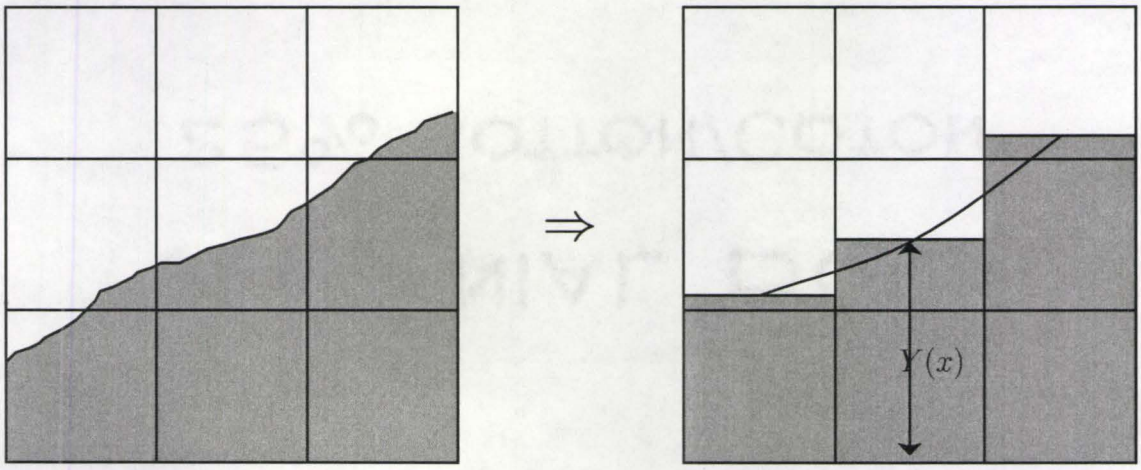

(a) Height Function Method

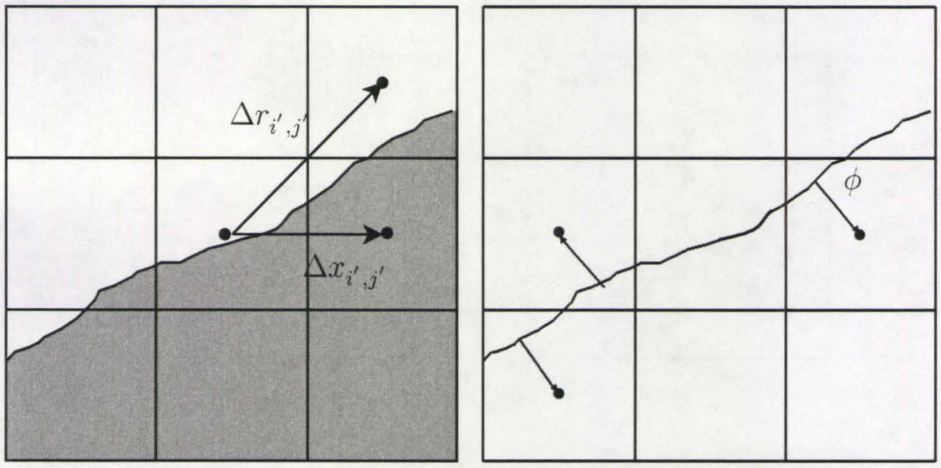

(b) Convolved Volume (c) Distance Function

Figure 2.9: A comparison of surface geometry determination methods, (a) Local Height Function Method determines Height function with the sum of 3 cells and obtain the gradient with $\frac{dY}{dx}$ and curvature with $\frac{Y''}{(1+Y'^2)^{3/2}}$, (b) Convolved Volume method is an average of discrete gradients, $n_x = \sum_{i',j' \neq i,j} \left(\frac{1}{2} - F_{i,j}\right) \frac{\Delta x_{i',j'}}{|\Delta r_{i',j'}|^2}$ and (c) The distance function method use the same formula with Level-Set formalism, $\kappa = \nabla \cdot \frac{\nabla \phi}{|\nabla \phi|}$

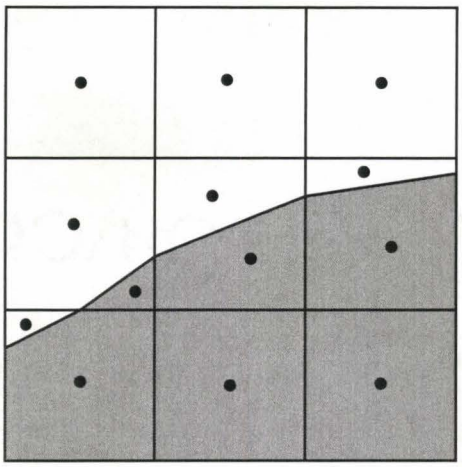

Figure 2.10: Cell cut example of solid object(gray). Small cells are seen in the bottom left and thin cell is in the right side.

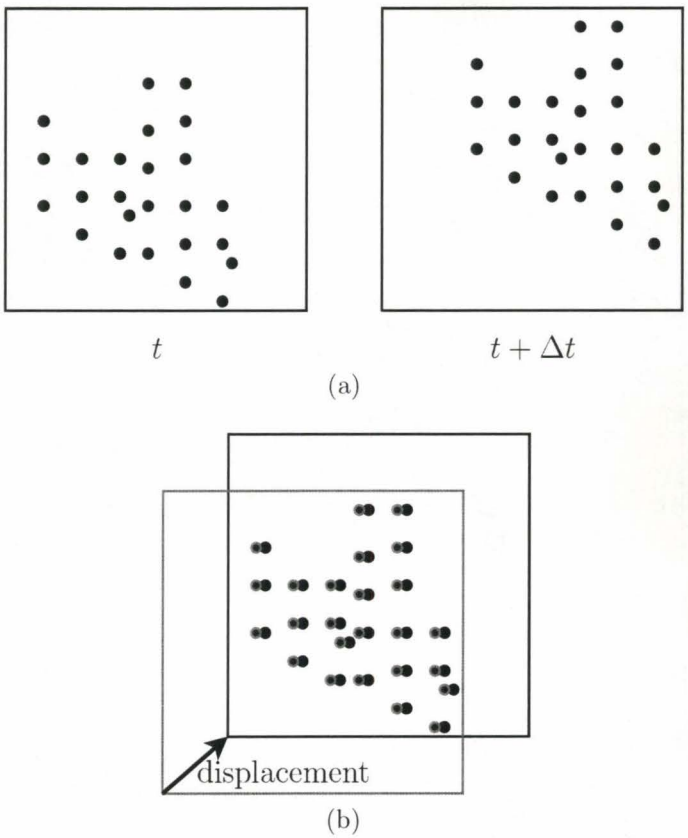

Figure 2.11: Finding displacement between the sequential PIV images in (a). The displacement is shown in (b).

Chapter 3

Experiments

3.1 Apparatus

3.1.1 Surface Geometry

To measure the liquid surface response when a gas jet impinges it, a top gas jetting system was constructed. The jetting system consisted of cylindrical straight lance, flowmeter and gas supply unit (gas cylinder and pressure regulator).

The lance diameter was 2.85 mm inner diameter and 4.76 mm outer diameter. To ensure fully-developed turbulent flow inside of the lance, the lance length was kept much longer than the required length. The maximum inlet velocity was approximately 300 m/s and the Reynolds number was $\mathrm{Re} = 2.0 \times 10^8$. According to White (2006), the minimum pipe length to diameter ratio for fully developed turbulent flow was determined with Equation (3.1). Therefore the required length was around 30 cm, but for convenience for clamping, a 50 cm length was used.

$$\frac{L}{d} = 4.4\mathrm{Re}^{1/6} \tag{3.1}$$

DataMetrics^{TM} 810LM-PAX hotwire type flowmeter was used to measure the gas flowrate; the maximum capacity of this flowmeter was 500 SLPM and minimum reliable flowrate was 10 SLPM . The flowmeter was calibrated with Wet Test meters; the procedure is described in Section 3.2.

Gas cylinder pressure was kept at 345 kPa (50 psi) throughout the experiments.

Preliminary tests were performed with a cylindrical tank of 45 cm diameter and 50 cm height filled with tap water to 20 cm. However, the jet cavity geometries were disrupted by the wave itself because of the vigorous splashing. The jet cavity shapes mainly depended on the impinging jet pressure; the liquid tank dimensions did

not have much effect when the tank size is much greater than the cavity dimension. Therefore, in the main experiment, a tank of $50 \times 50 \times 50$ cm filled with distilled water to 20 cm height was used with a wall jet configuration to extract better geometrical information. Note that the wall jet configuration uses a cylindrical lance in contact with the vertical wall. The tank and gas systems are illustrated in Figures 3.1 and 3.2.

The jet cavity image was taken with Sony DCR-TRV 80 HandyCam^{TM}; the frame rate was 30 frames/sec. To emphasize the free surface line, the camera aperture was maintained with low values and a 200 W lamp was used on the back and lower side of the tank to illuminate the surface. The moving picture frames were stored in JPEG image files and used for later analysis.

3.1.2 Particle Image Velocimetry

The liquid flow induced by the impinging jet was measured with Particle Image Velocimetry (PIV) which was the Lavision^{TM}integrated system (Göttingen, Germany). The PIV system consist of a Nd-YAG green (532 nm) pulsing laser unit, 1.4 megapixel digital camera and PIV control and analysis software. The pulsing laser has 100 mJ maximum power and minimum time interval was 0.5 μs . The laser was classified as CLASS IV; proper eye protection was required throughout the measurement. The double pulsed laser was synchronized with the digital camera shutter with a special time control—frame straddling, which is well described by LaVision (2004) and Gharib and Daribi (2000). The camera had progressive scan interline transfer CCD (Charge Coupled Device) type and it was double-shuttered for the frame straddling mode.

Dantec^{TM}'s hollow glass beads of 9∼13 μm were used as the seeding particles. The seeding particle should be small, but it should have a certain size to maximize the illumination signal to noise ratio (Melling 1997). The current particle size range is adequate to obtain enough scattering cross section diameter.

The laser beam was converted to a sheet using a cylindrical lens and the distance was adjusted in a way that the light sheet covered the whole area of interest. The cylindrical tank with 45 cm and 50 cm height filled with distilled water in 20 cm was contained inside of larger square tank to minimize the distortion of the image and excessive expansion of laser light sheet. The laser sheet was aligned vertically and the

particle images were taken at right angles from this illuminated plane; a schematic of the equipment is illustrated in Figure 3.3.

3.2 Calibration

Before the main experiments, the flow meter and the jet nozzle was calibrated. The DataMetric^{TM}flowmeter, which has 500 SLPM maximum flowrate, was calibrated using Precision Scientific^{TM} wet test meters. The wet test meters' capacities were too small compared to the designed flowrate for this study, so three wet test meter were combined and their maximum reliable capacity of flowrate was 51 SLPM. Figure 3.4 shows the result of calibration up to 50 SLPM and extrapolated values of this calibration were used for higher flowrates.

Gas jet behaviour depends to some extent on the nozzle tip geometry, so for an accurate estimation of impact velocities at the jet cavity, the centerline jet velocity was measured with Pitot Tube (Szekely 1979).

A custom made Pitot Tube was used, which consisted of the pressure measuring unit, the tube and mercury and ethyl alcohol column manometers. For high velocity, the mercury column was used and for low velocity, the alcohol column was used. The measured dynamic pressure was converted to velocity with Equation 3.2

$$\frac{1}{2}\rho_g v^2 = p_d \tag{3.2}$$

The measured data was compared with those of Wygnanski and Fiedler (1969) in Figure 3.5. The data was fitted to linear regressions for the free jet and wall jet case, and these relationships were used for the jet centerline velocity calculation throughout this study.

$$\text{Free Jet} \quad \frac{u_0}{u_m} = 0.185\frac{x}{d_0} - 1.141 \tag{3.3}$$

$$\text{Wall Jet} \quad \frac{u_0}{u_m} = 0.180\frac{x}{d_0} - 1.727 \tag{3.4}$$

3.3 Experimental Procedure

3.3.1 Surface Geometry

The experimental setup was prepared as described in Section 3.1. The flowrate was controlled from 10 SLPM to 100 SLPM and the lance distance from the liquid surface varied from 6 cm to 24 cm The gas flowrate and distance conditions are summarized in Table 3.1.

The video images taken by the camera were chopped to each frame and the frame image was stored and image filtering was applied to emphasize the free surface interface line. The filters were contrast adjustment, gamma saturation and negative. An edge detection filter was also available, but it produced spurious edges because of the noise level.

From the filtered images, the free surface line was digitally extracted using digitization software (Grafula 3) which works semi-automatically or manually. An example of filtering and digitizing procedure is shown in Figure 3.6.

A series of 60 sequential images over 2 s were digitized for each experimental condition and each digitized surface profile was analysed to extract the geometrical data. The time series of depth of cavity, width of cavity at the average surface level, width of cavity at the top elevation position and horizontal position of deepest cavity position were stored and analysed with a Fast Fourier Transform for the frequency behavior. Fast Fourier Transform was applied to the surface profile to obtain the spatial frequency (wavelength) information. The details of analysis procedure are contained in Appendix C.

3.3.2 PIV Measurement

The general cross-correlation analysis is well described by Gharib and Daribi (2000) and Prasad (2000). The selection of interrogation window size must consider the actual flow velocity range; a recommended criteria (Kean and Adriantems 1990) is

$$0.1\text{px} < \text{displacement} < \frac{1}{4} d_{\text{int}} \tag{3.5}$$

where px is pixel size and d_{int} is interrogation window size. The picture has 1360×1024 resolution and the actual height of the picture was around 25 cm, so the measurable velocity ranges are calculated and listed in the Table 3.2.

For each measurement, the gas jet was impinged to the liquid surface and the PIV measurement was done after waiting 3∼5 min to establish steady state velocity in an average sense[1]. A test measurement was done for each PIV measurement with the approximate Δt. With the measured minimum and maximum velocity from this test measurement, a proper Δt was determined and the measurement was repeated with this time step.

To obtain best picture the camera aperture and laser power were adjusted for each flowrate and lance height conditions. Table 3.3 lists the Δt, camera aperture and laser power conditions for the measurements.

The measured velocity with PIV system was analysed with DaVis$^{\text{TM}}$ 6.2 software of LaVision^{TM}. A 64×64 pixel interrogation window was selected and only single path algorithm was used. A median filter was applied to each velocity analysis and statistically spurious vectors are eliminated and added with interpolation. The 20 vector measurements were averaged and the cavity side and non liquid part was masked out. Appendix F shows the measured vectors with a sample background images for each flowrate.

3.4 Surface Geometry Results

3.4.1 Cavity dimensions

The jet cavity dimensions were obtained as described in Section 3.3.1. Figure 3.7 shows the mean depth of the jet cavity, the cavity becomes deeper when the gas flow rate is increased.

The mean cavity width was also plotted in Figure 3.8. The two variables, surface level width and top lip width follow each other closely for every flowrate. Contrary to Cheslak et al. (1969), the rate of width change was a function of the flowrate. The

[1]The system never reaches to steady state because of the oscillation of cavity and the surface wave, but the internal flow develops an average velocity after some time depending on the flowrate

decrease of the rate in the higher flowrate is considered to be the regime change in splashing mode as reviewed in Section 2.2.

Equation (2.6) was used to determine the similarity relationship of the cavity depth. The equation was slightly modified to represent the linear functional behavior of the length group with momentum group dimensionless parameters and the square root of the slope represents the turbulent gas jet constant(K)

$$\frac{n_0}{h}\left(1+\frac{n_0}{h}\right)^2 = K^2\frac{2\dot{M}}{\pi\rho_l g h} \tag{3.6}$$

The linear regression (Figure 3.9) shows that the slope is 60.941 and corresponding K value is 7.81. This value is slightly higher than other reported values (5.5~7.5), but those values do not consider virtual origin information, which is obtained from the jet velocity measurement or calibration procedure in this study.

The onset of splashing is hard to determine since the size of splash droplets must be determined prior to splashing criteria. Very small size of drops were generated around the waves even in very low flowrate; this was checked by holding a tissue close to the waves. Therefore, the onset of splashing was determined when the surface starts to eject some visible drops (3~5 mm) around the perimeter of the cavity. The flowrate for the onset of splashing was summarized in Table 3.4. At higher flowrate the jet penetrates into the liquid surface and bubbles form. This penetration was only observed in 6 cm lance height case above 60 SLPM flowrate.

3.4.2 Fast Fourier Transform

The Fast Fourier Transform was applied to the time series of geometrical variables and the surface profiles to pick out the characteristic frequencies and wavelengths. In low lance height case (6 cm), the Fourier transform shows almost all ranges of frequencies[2](Figure 3.10~3.11). In the case of the horizontal position of cavity depth (Figure 3.12), 2 Hz was pronounced in 6cm height case, but this speciality was not extended to other lance heights (12cm, 18cm, 24cm). As the lance height was increased, lower frequencies, 4~8 Hz, became relatively dominant in depth and width case and this is lower than in previous work 5~12 Hz (Peaslee and Robertson 1994). The other FFT results (12cm, 18cm, 24cm height) are plotted in Appendix F.

[2]The time interval was 1/30 sec, so the frequencies over 15 Hz were not measurable here.

3.5 Particle Image Velocimetry Results

At relatively low flowrate, 50 SLPM (Figure 3.13), the gas momentum is well transfered at lower lance height (Figure 3.13 for 6cm), so the velocity vectors are larger. However, in the case of higher flowrate, 100 SLPM (Figure 3.14), the momentum transfer from the gas to liquid is better at higer lance position. This part will be discussed in the Chapter 5 with some momentum transfer indicators.

Table 3.1: The Flowrate and distance conditions selected for the surface geometry measurements

Flow rate(SLPM)	**6** cm	**12** cm	**18** cm	**24** cm
10	○			
15	○	○		
20	○	○		
25		○		
30	○	○	○	
40	○	○	○	
50	○	○	○	○
60	○	○	○	○
70	○			○
80	○	○	○	○
90	○			
100	○	○	○	○

Table 3.2: Minimum and maximum velociites that can be measured for frame straddling times[a] .

Δt (μs)	**Min** (mm/s)	**Max** (mm/s)
500	48.83	7812.50
1000	24.41	3906.25
2000	12.21	1953.13
3000	8.14	1302.08
4000	6.10	976.56
5000	4.88	781.25
6000	4.07	651.04
7000	3.49	558.04
8000	3.05	488.28
9000	2.71	434.03
10000	2.44	390.63
15000	1.63	260.42
20000	1.22	195.31

[a]Since the actual height of PIV picture was around 25 cm, and a 64×64 interrogation area was used, the measurable velocity range was calculated with its frame straddling time steps. This table was used as a reference in the measurement procedure.

Table 3.3: The PIV measurement conditions for each flow rate and lance height.

Lance Height	Flowrate (SLPM)	Laser Power(%)	Aperture	Δt (μs)
6cm	**10**	10	4	30,000
	15	10	4	30,000
	20	30	8	10,000
	30	65	11	8,000
	40	65	11	8,000
	50	60	11	7,000
	60	30	8	5,000
	70	30	8	5,000
	80	25	8	5,000
	90	25	8	3,000
	100	25	8	3,000
12cm	**15**	30	5.6	30,000
	20	30	5.6	30,000
	25	30	5.6	20,000
	30	30	5.6	10,000
	40	30	5.6	8,000
	50	30	5.6	8,000
	60	25	5.6	8,000
	80	25	5.6	7,000
	100	20	5.6	4,000
18cm	**30**	25	5.6	20,000
	40	25	5.6	15,000
	50	25	5.6	15,000
	60	25	5.6	10,000
	80	20	5.6	8,000
	100	20	5.6	8,000
24cm	**50**	20	5.6	20,000
	60	20	5.6	15,000
	70	20	5.6	10,000
	80	20	5.6	8,000
	100	20	5.6	8,000

Table 3.4: The flowrate at the onset of splash for each lance height.

Lance Height (cm)	Onset Flowrate (SLPM)
6	15
12	30
18	45
24	60

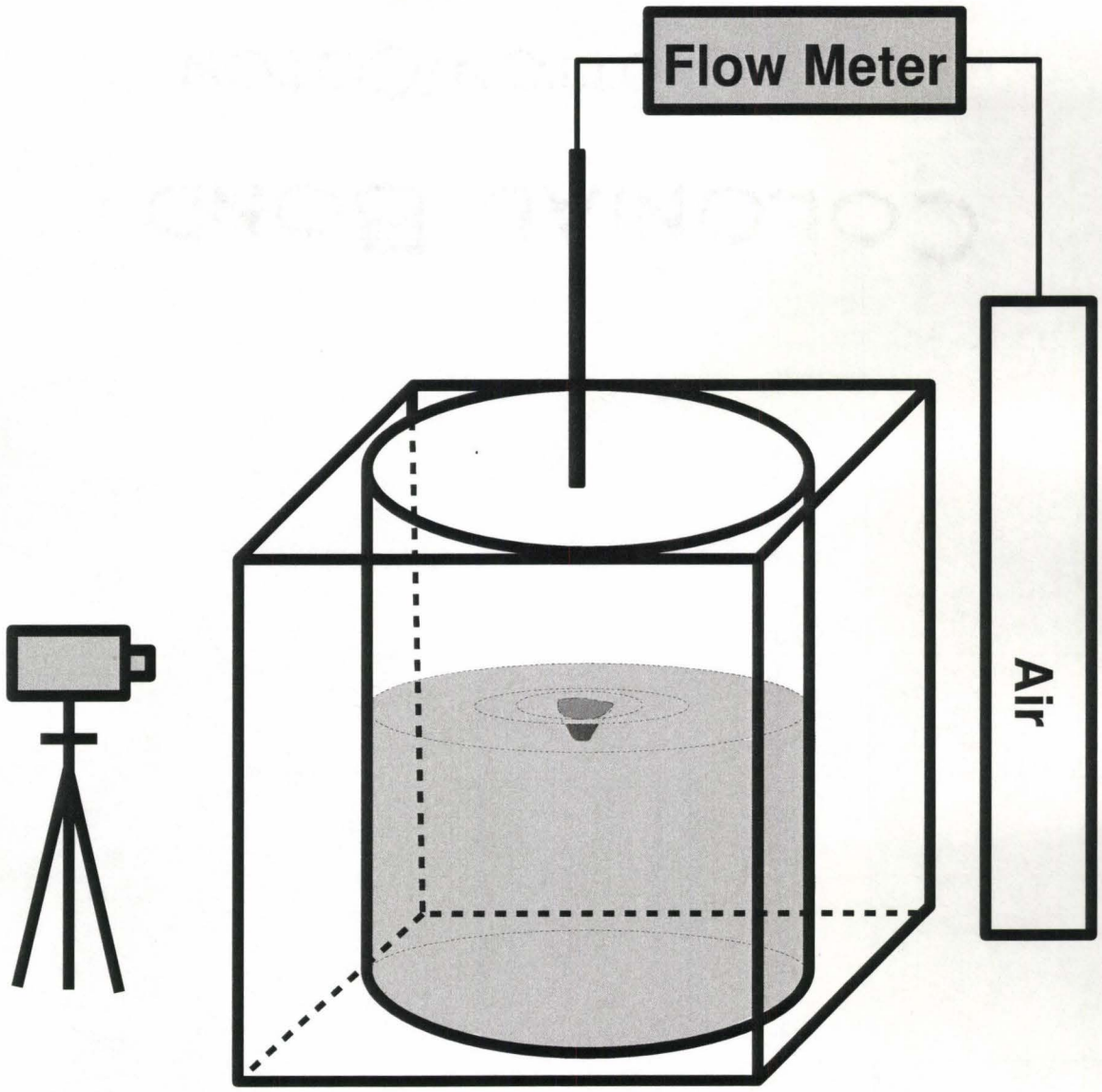

Figure 3.1: A cylindrical tank experimental setup which is used in preliminary tests.

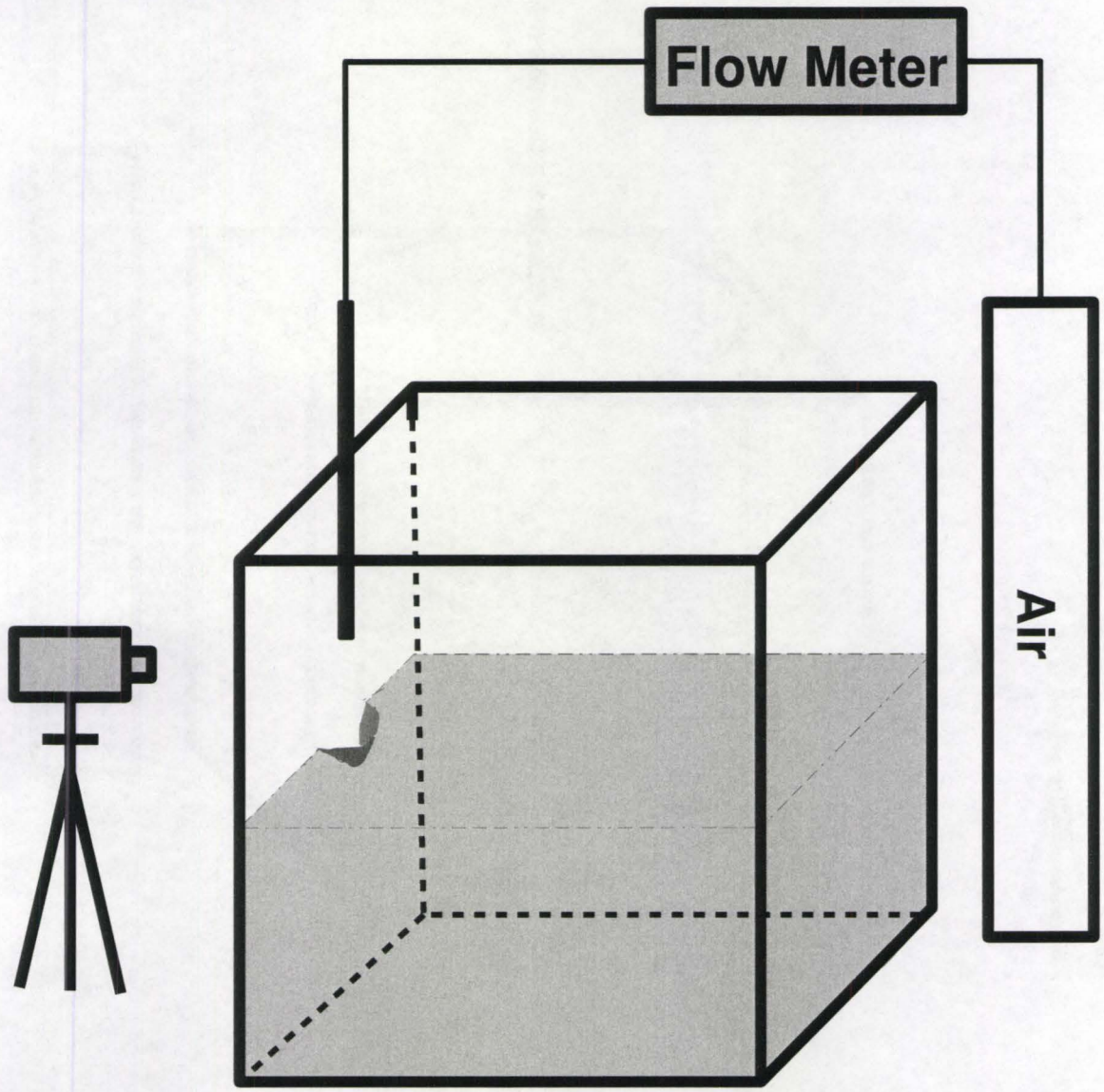

Figure 3.2: A wall jet the cubic tank experimental setup which is used in the main experiment work for surface geometry

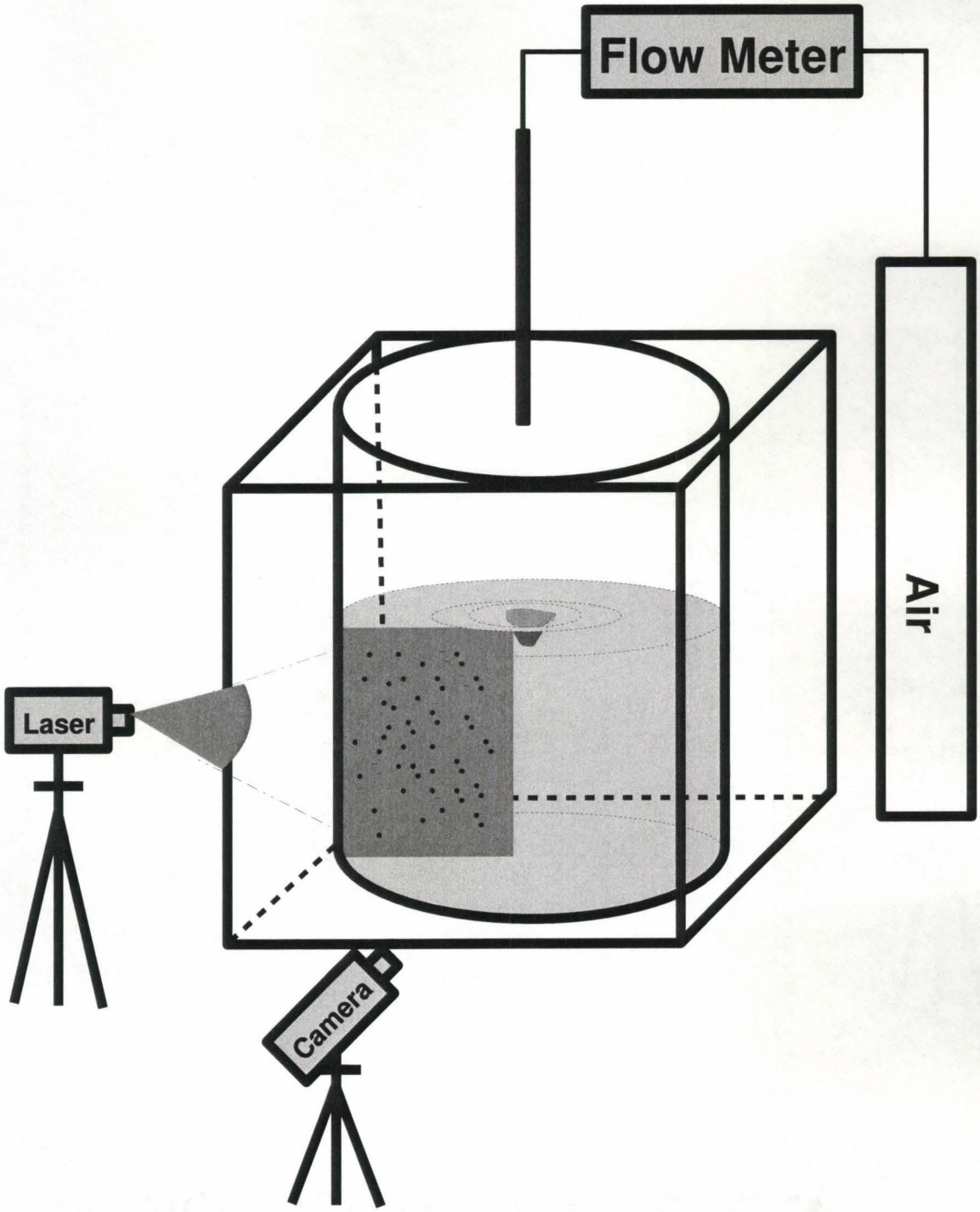

Figure 3.3: A typical Particle Image Velocimetry setup. the laser sheet was aligned vertically and the illuminated particles were photographed with the digital camera which was at right angle to the light sheet.

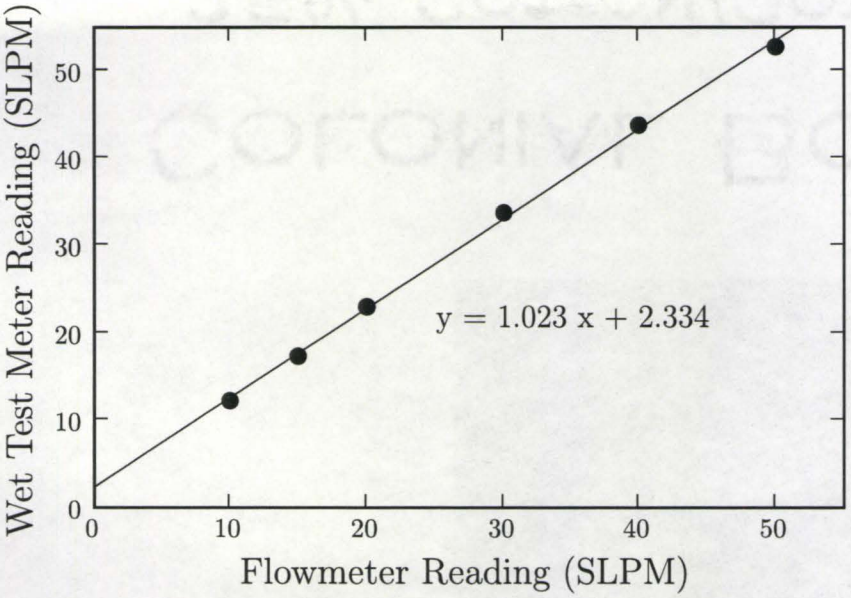

Figure 3.4: Calibration of the Flow Meter with the Wet Test Meter

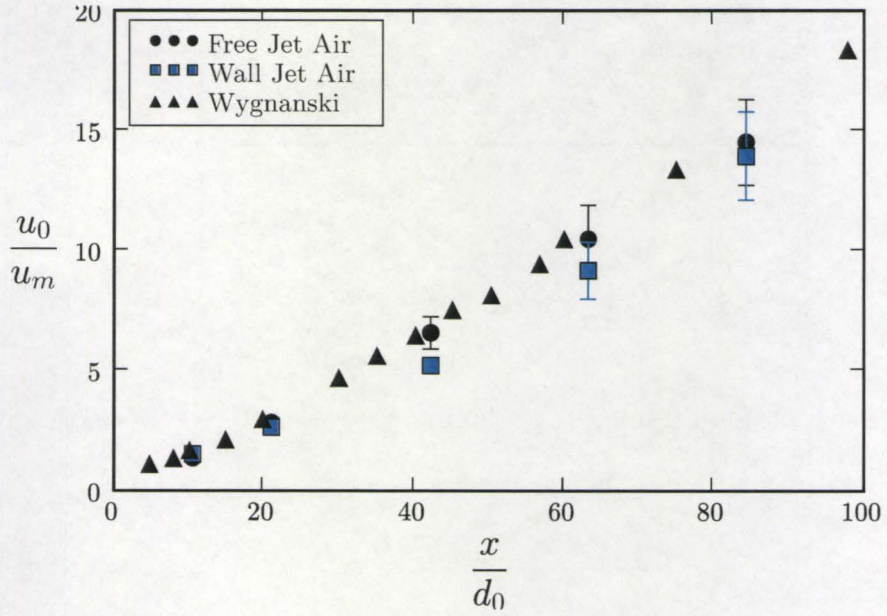

Figure 3.5: Calibration result of the jet using the Pitot tube, compared to Wygnanski and Fiedler (1969).

(a) Original Image

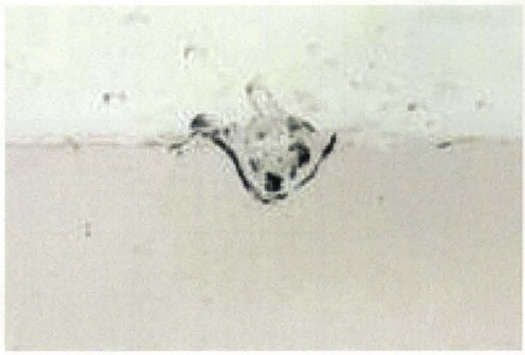

(b) Filtered Image

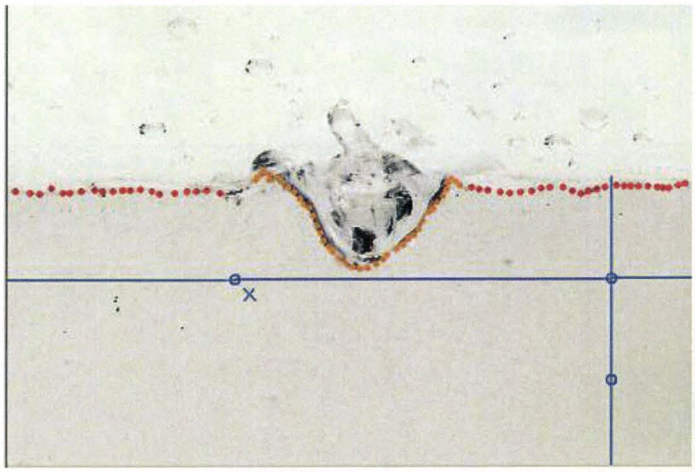

(c) Digitizing Procedure

Figure 3.6: Each original frame (a) of the images were filtered (b) and digitized (c) as described in the text.

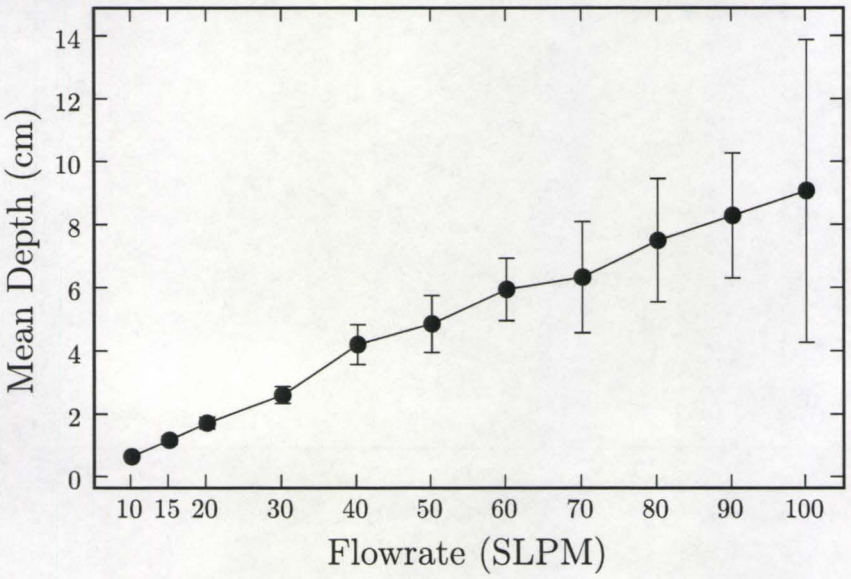
Mean Depth (cm)
0
2
4
6
8
10
12
14
10 15 20 30 40 50 60 70 80 90 100
Flowrate (SLPM)

(a) 6 cm

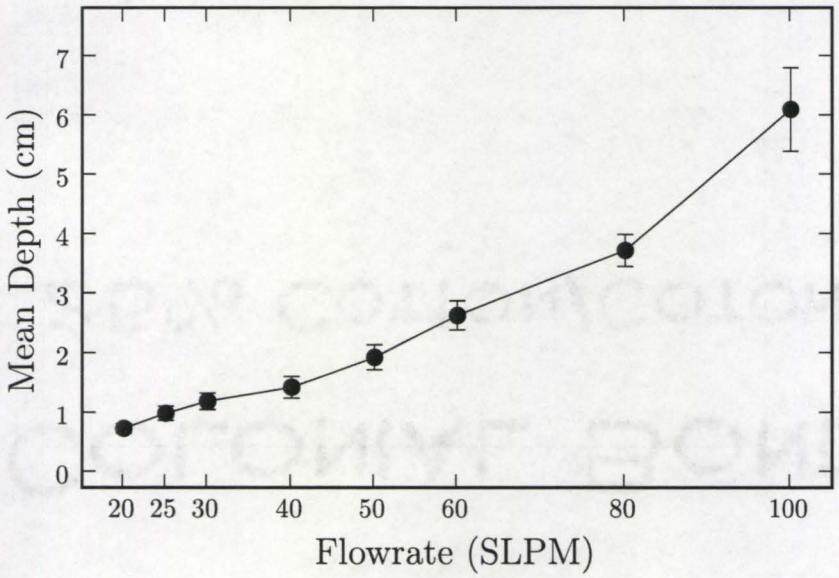
Mean Depth (cm)
0
1
2
3
4
5
6
7
20 25 30 40 50 60 80 100
Flowrate (SLPM)

(b) 12 cm

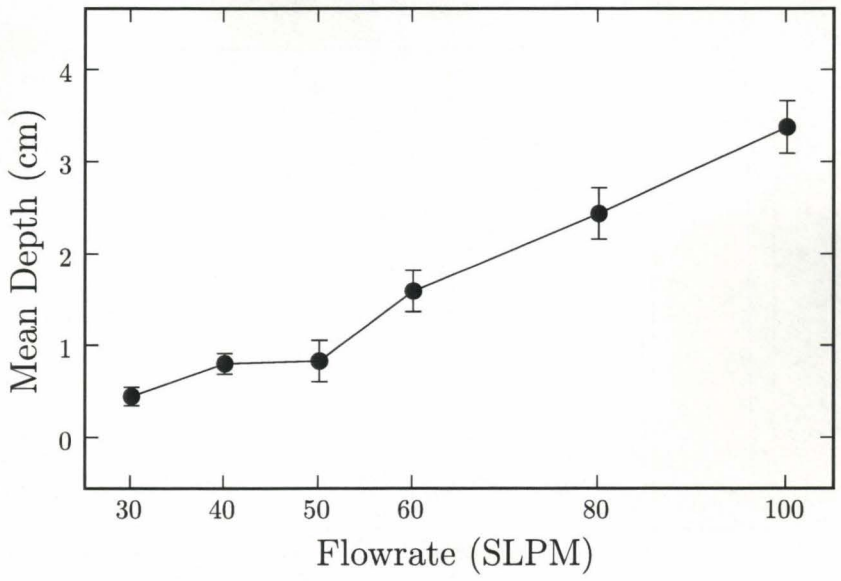

(c) 18 cm

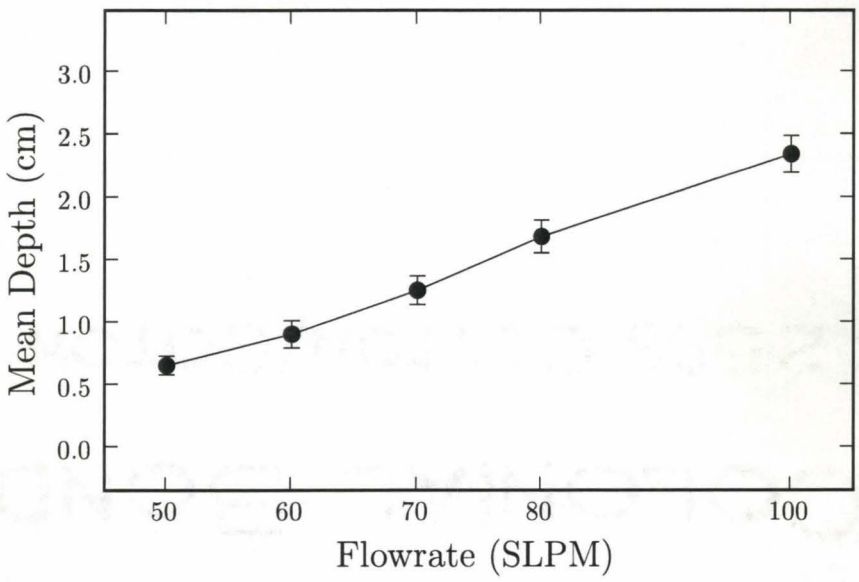

(d) 24 cm

Figure 3.7: The mean jet cavity depth change vs. gas flowrate at the nozzle, the error bar is ± standard deviations. The lines through the data just connect the points.

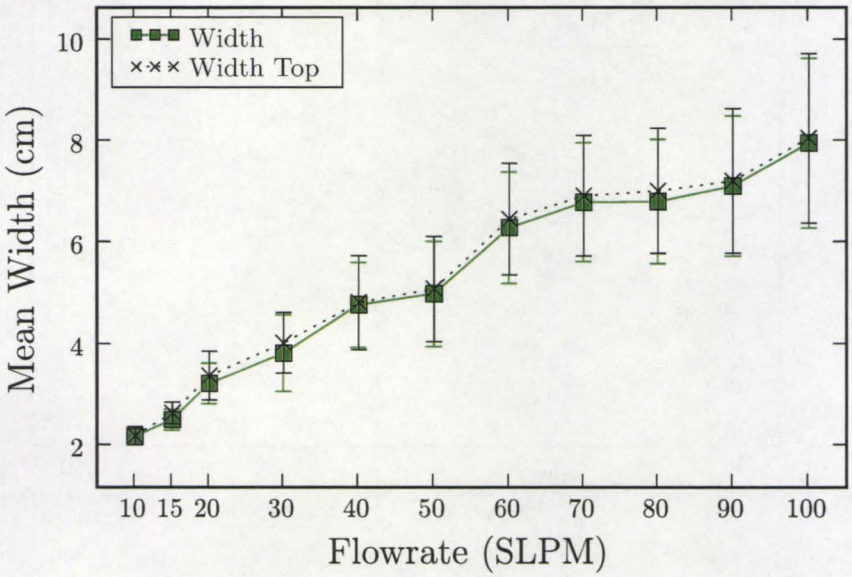
Width
Width Top
Mean Width (cm)
Flowrate (SLPM)
2
4
6
8
10
10 15 20 30 40 50 60 70 80 90 100

(a) 6 cm

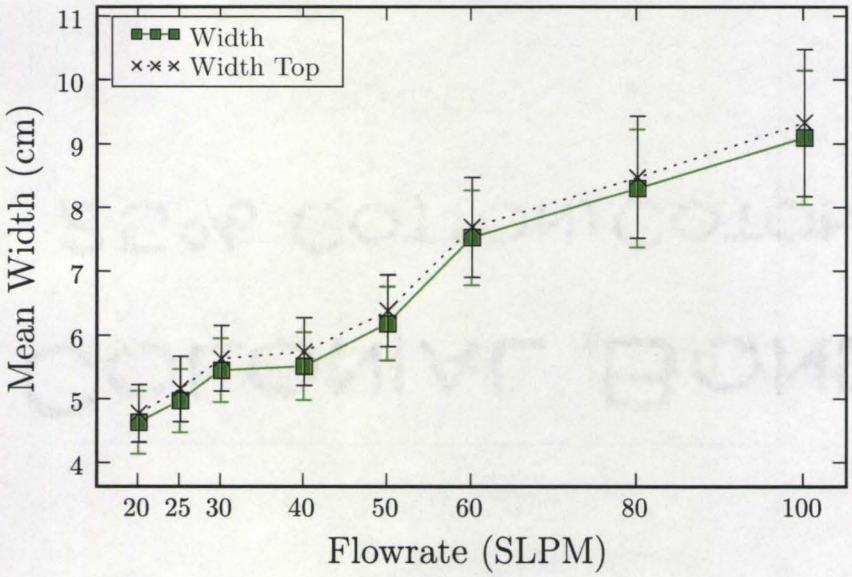
Width
Width Top
Mean Width (cm)
Flowrate (SLPM)
4
5
6
7
8
9
10
11
20 25 30 40 50 60 80 100

(b) 12 cm

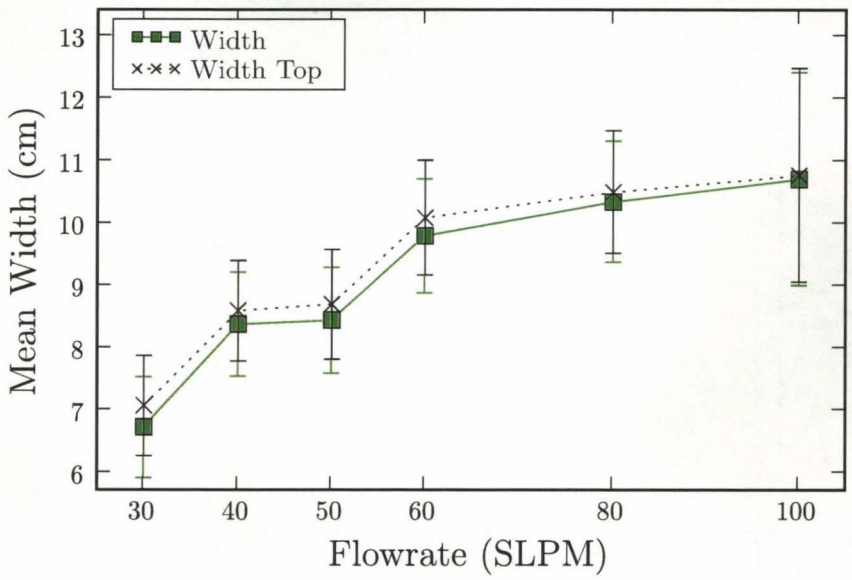

(c) 18 cm

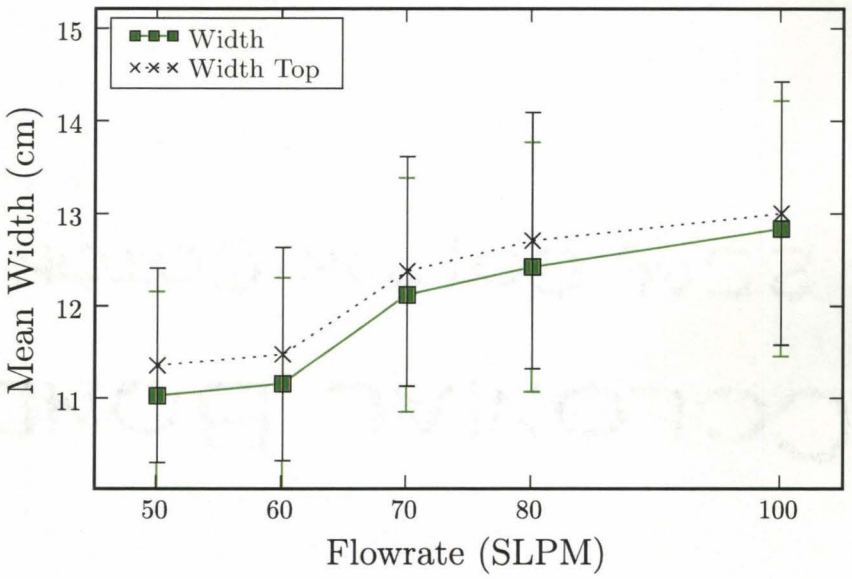

(d) 24 cm

Figure 3.8: The mean jet cavity width change vs. gas flowrate at the nozzle, the error bar is ± standard deviations. The lines through the data just connect the points.

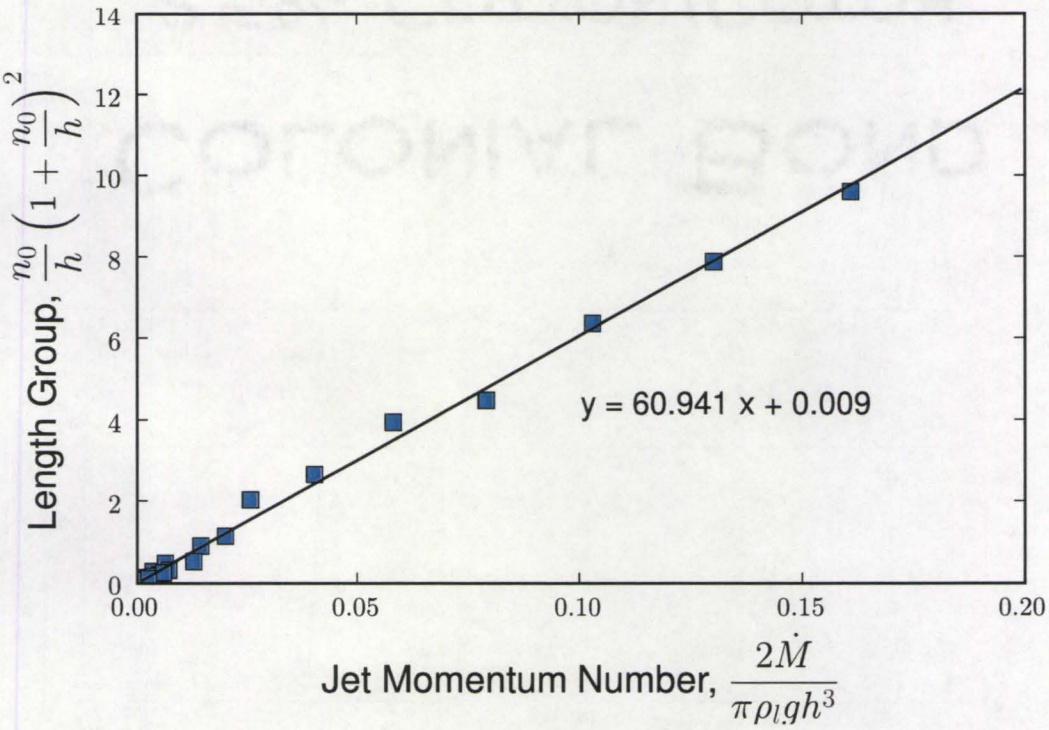

Figure 3.9: The deep cavity relationship from (Banks and Chandrasekhara 1963) was modified and used to determine the similarity behavior, horizontal axis is Momentum group and vertical axis is Length Group. The slope is the square of the turbulent gas jet constant.

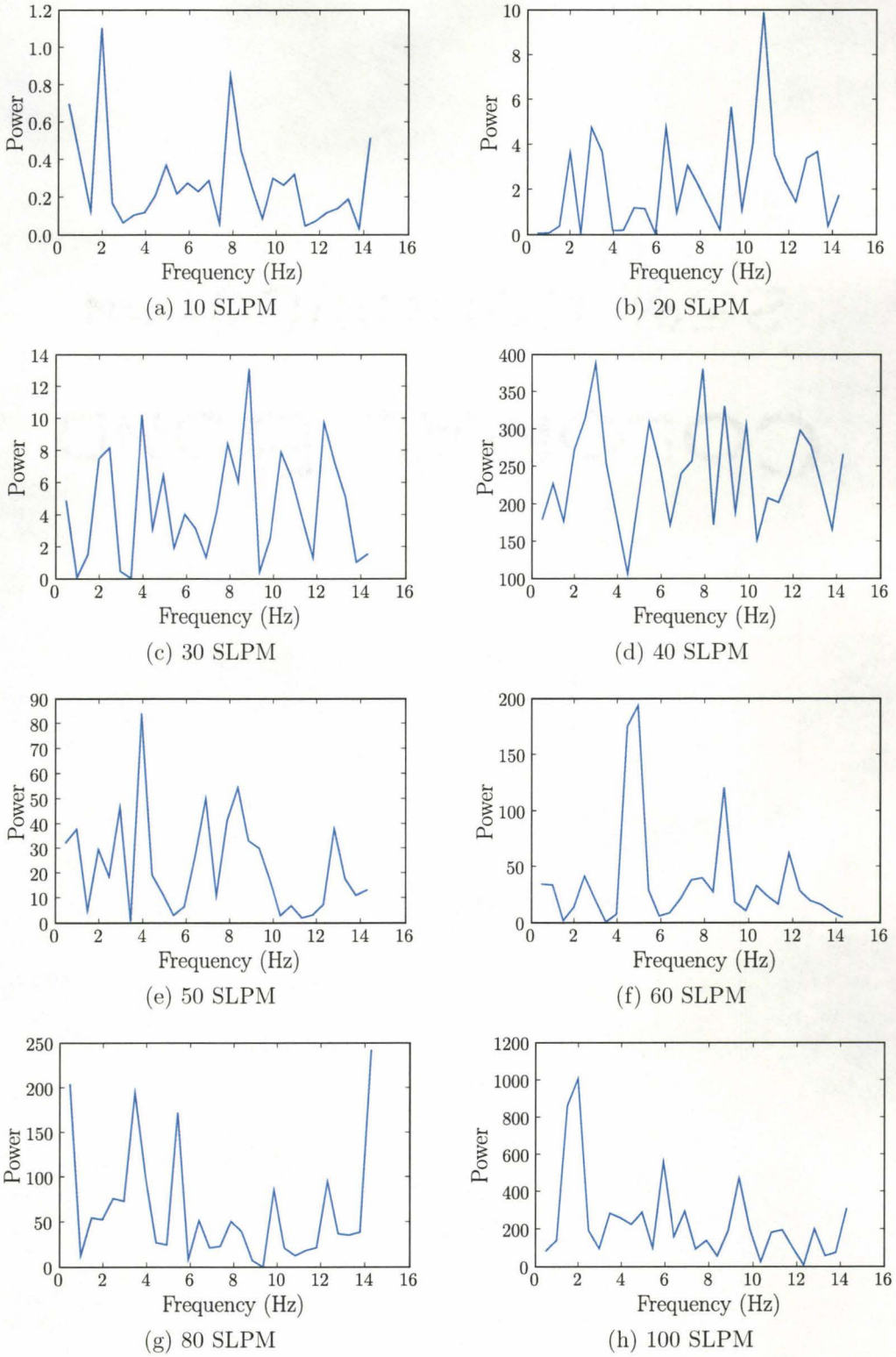

(a) 10 SLPM (b) 20 SLPM

(c) 30 SLPM (d) 40 SLPM

(e) 50 SLPM (f) 60 SLPM

(g) 80 SLPM (h) 100 SLPM

Figure 3.10: Fast Fourier transform of time series of cavity depth change when the lance height is 6cm.

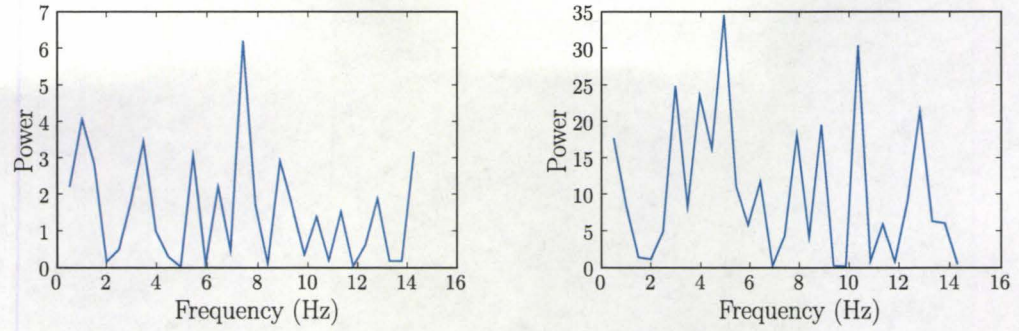

(a) 10 SLPM

(b) 20 SLPM

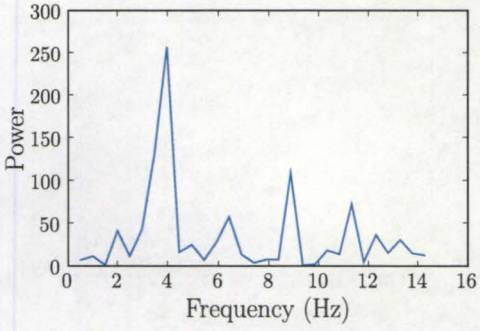

(c) 30 SLPM

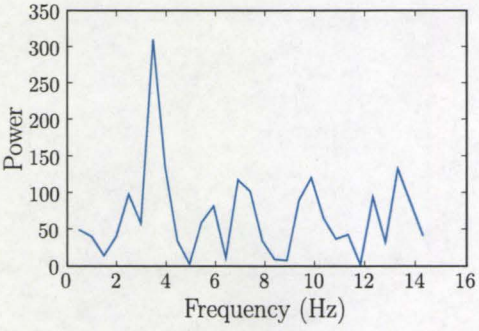

(d) 40 SLPM

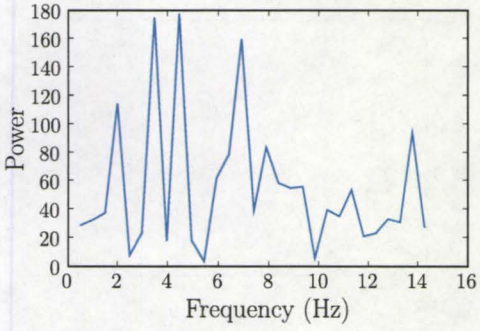

(e) 50 SLPM

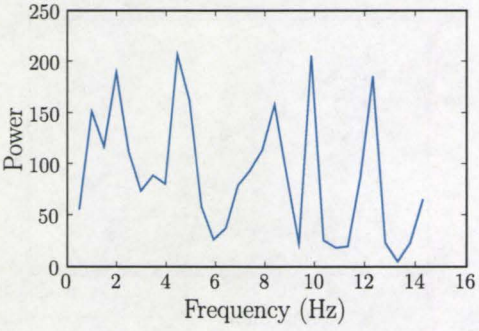

(f) 60 SLPM

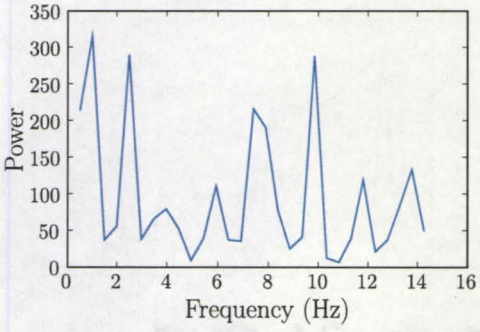

(g) 80 SLPM

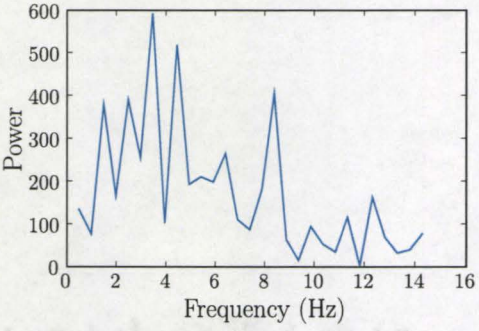

(h) 100 SLPM

Figure 3.11: Fast Fourier transform of time series of cavity width change when the lance height is 6cm.

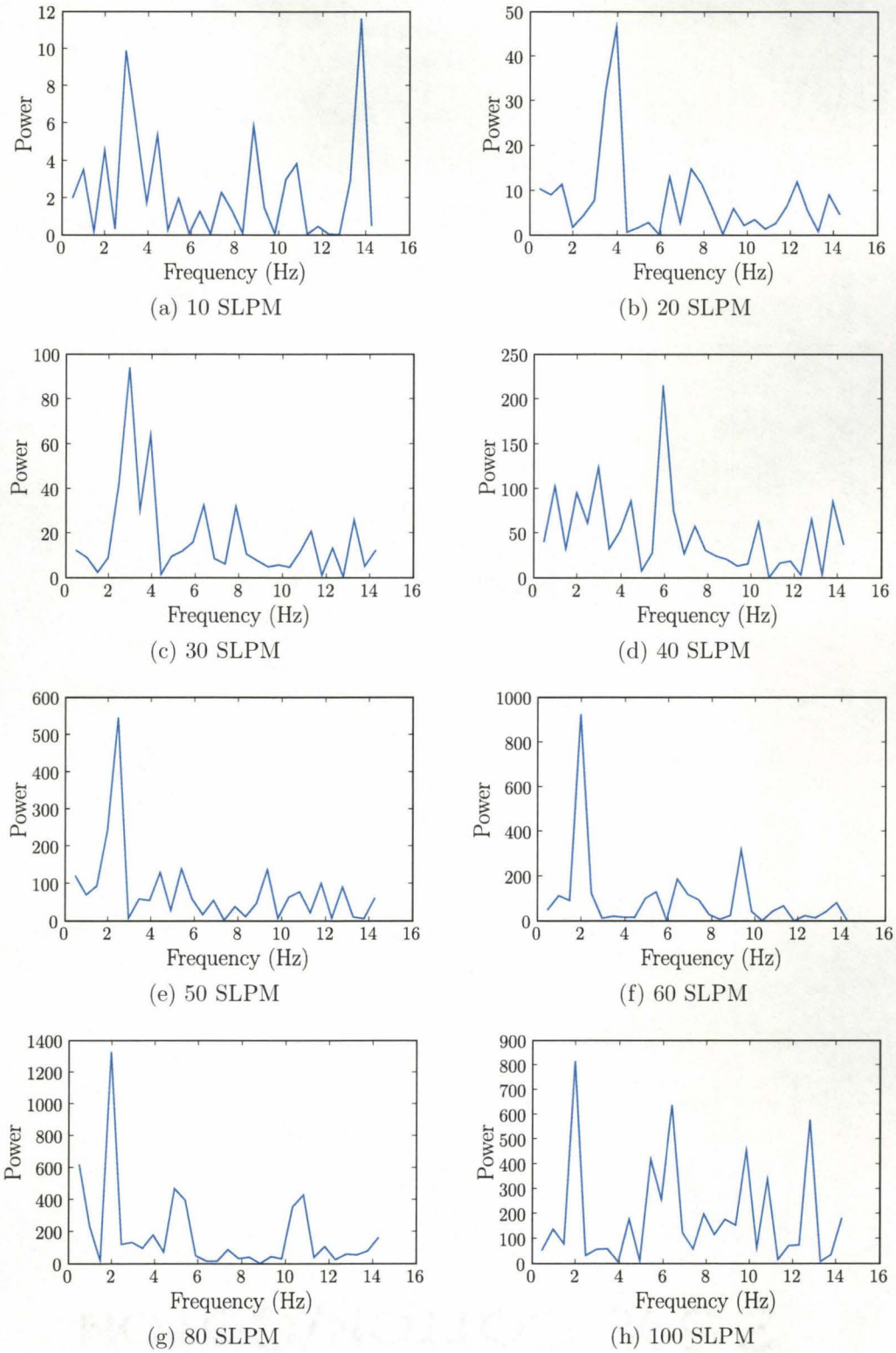

(a) 10 SLPM (b) 20 SLPM

(c) 30 SLPM (d) 40 SLPM

(e) 50 SLPM (f) 60 SLPM

(g) 80 SLPM (h) 100 SLPM

Figure 3.12: Fast Fourier transform of time series of the horizontal position of the cavity depth change when the lance height is 6cm.

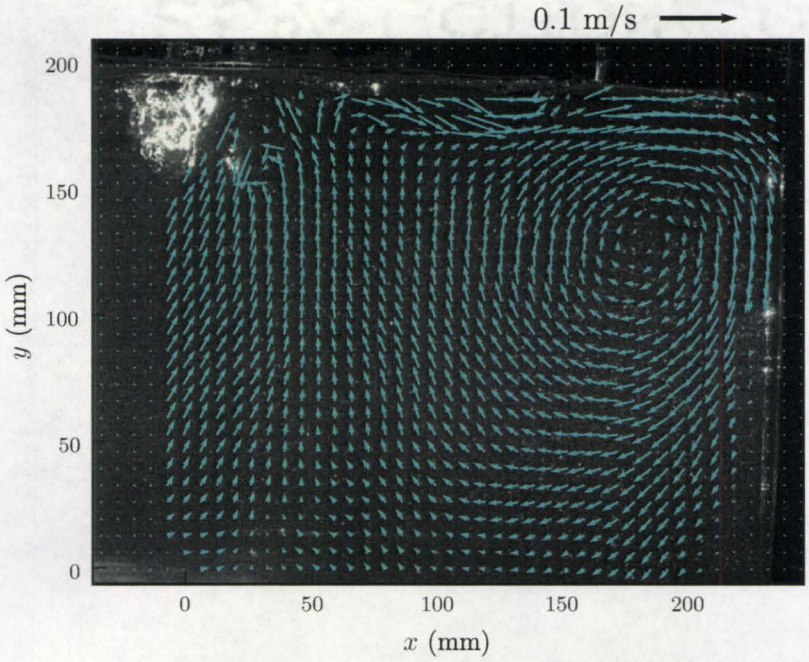
0.1 m/s
200
150
100
50
0
y (mm)
0
50
100
150
200
x (mm)

(a) 6 cm

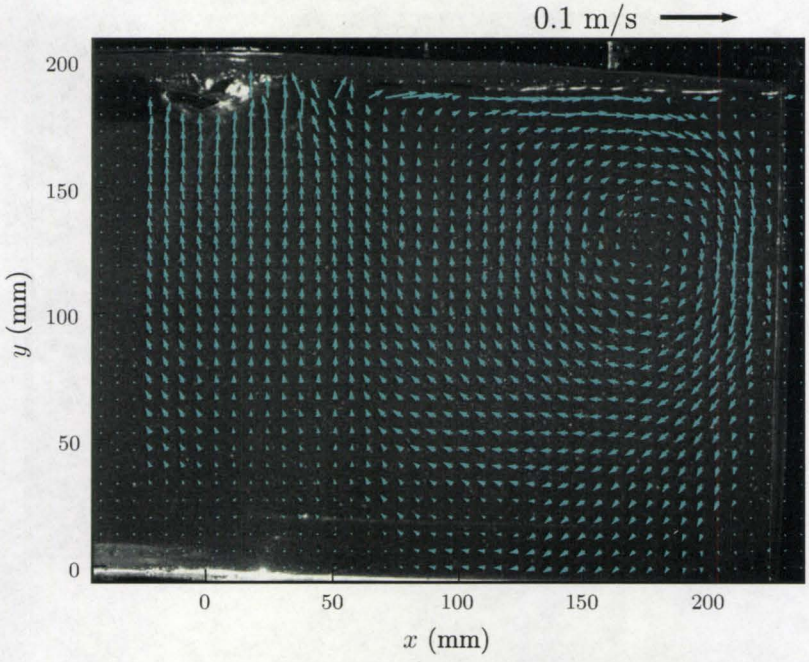
0.1 m/s
200
150
100
50
0
y (mm)
0
50
100
150
200
x (mm)

(b) 12 cm

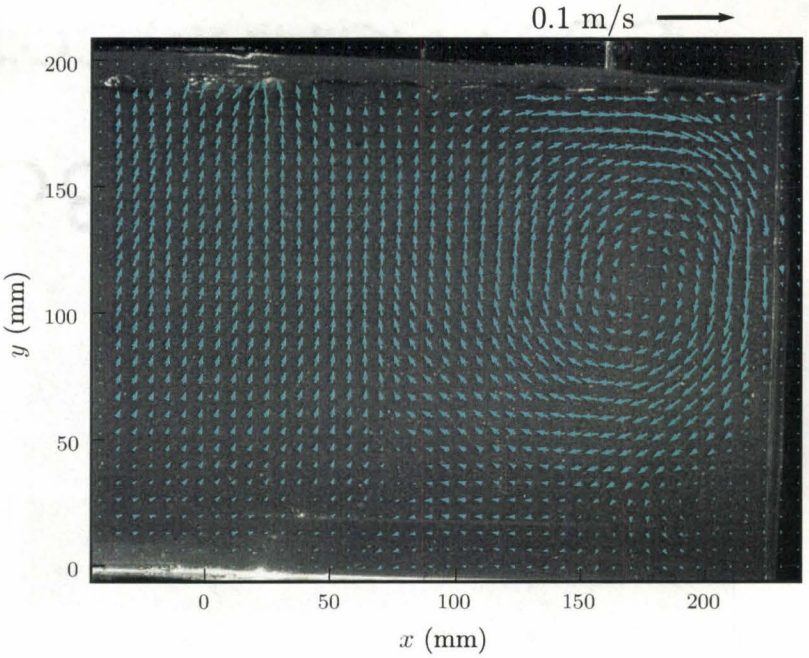

(c) 18 cm

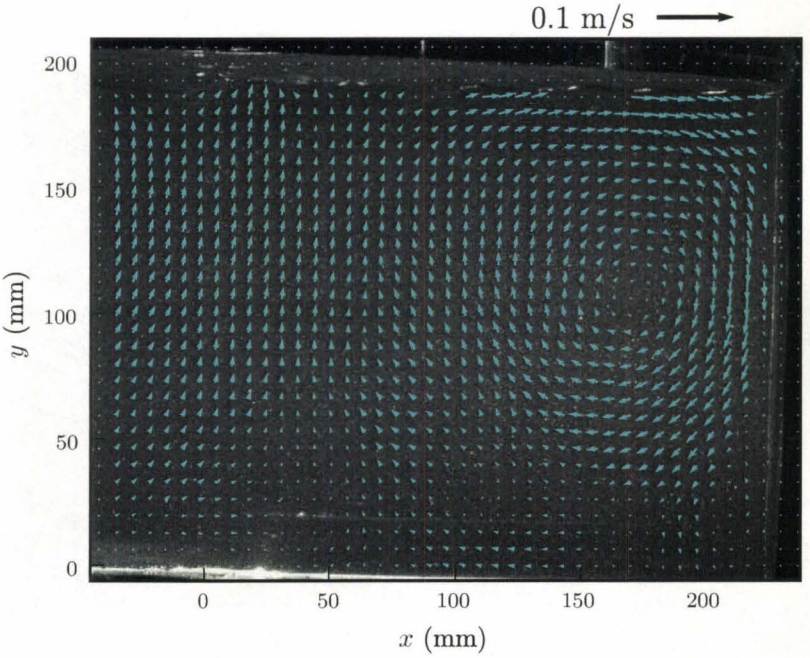

(d) 24 cm

Figure 3.13: The comparison of PIV velocities in 50 SLPM flowrate.

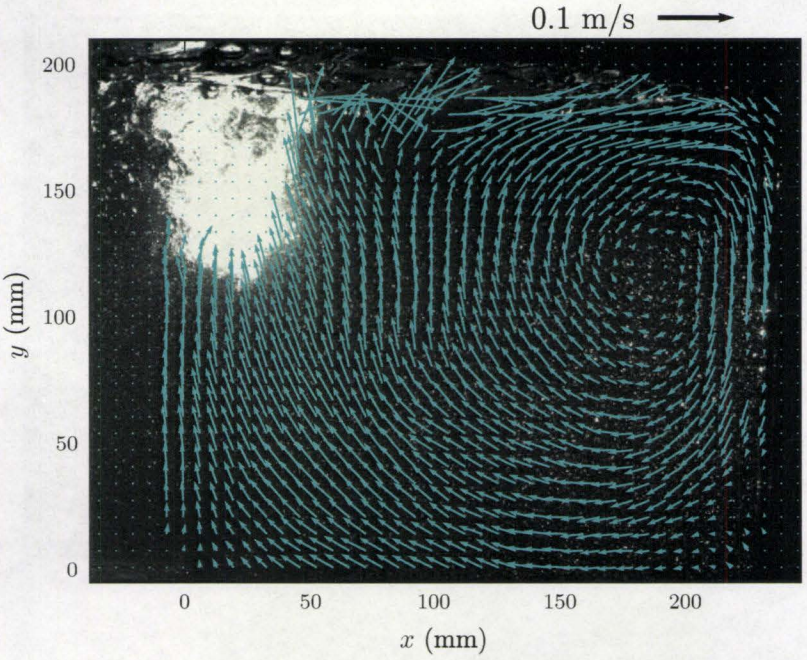
0.1 m/s
200
150
100
50
0
y (mm)
0
50
100
150
200
x (mm)

(a) 6 cm

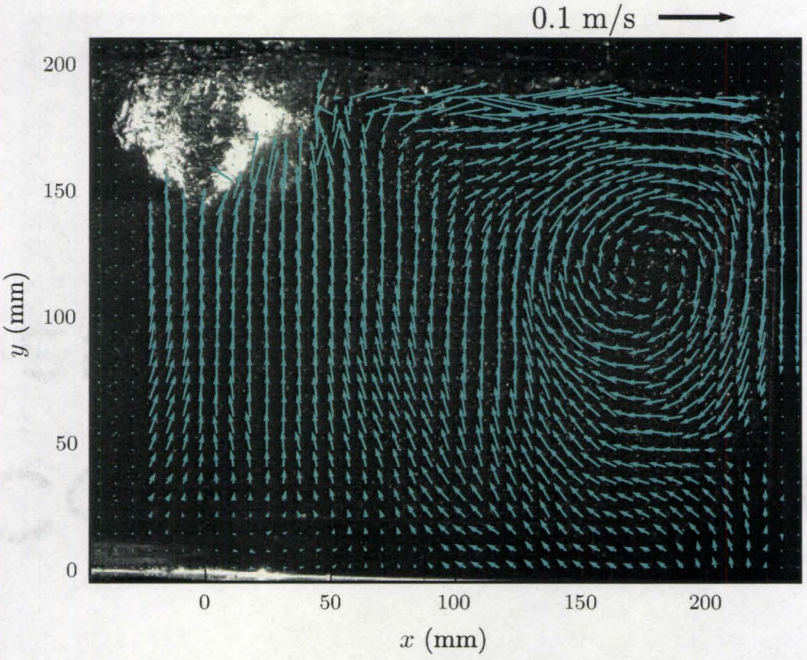
0.1 m/s
200
150
100
50
0
y (mm)
0
50
100
150
200
x (mm)

(b) 12 cm

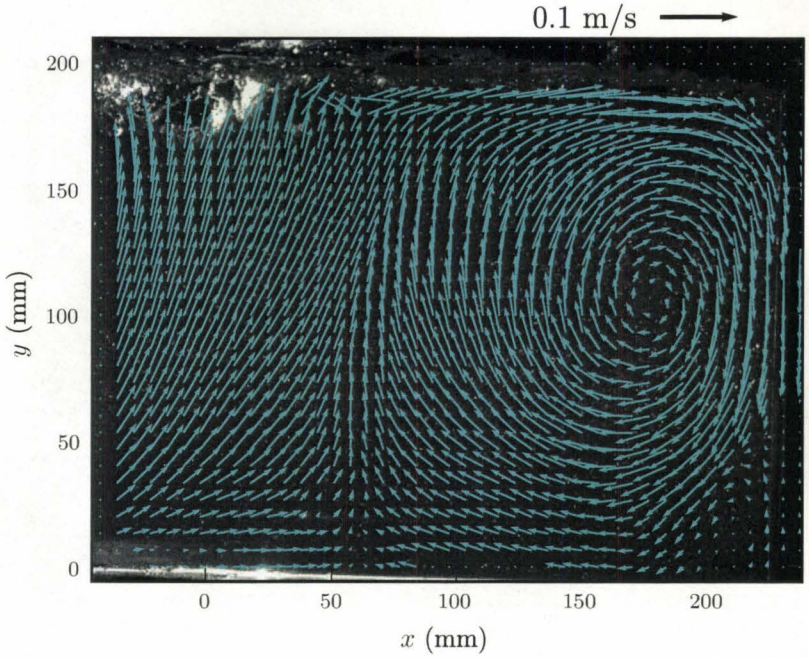

(c) 18 cm

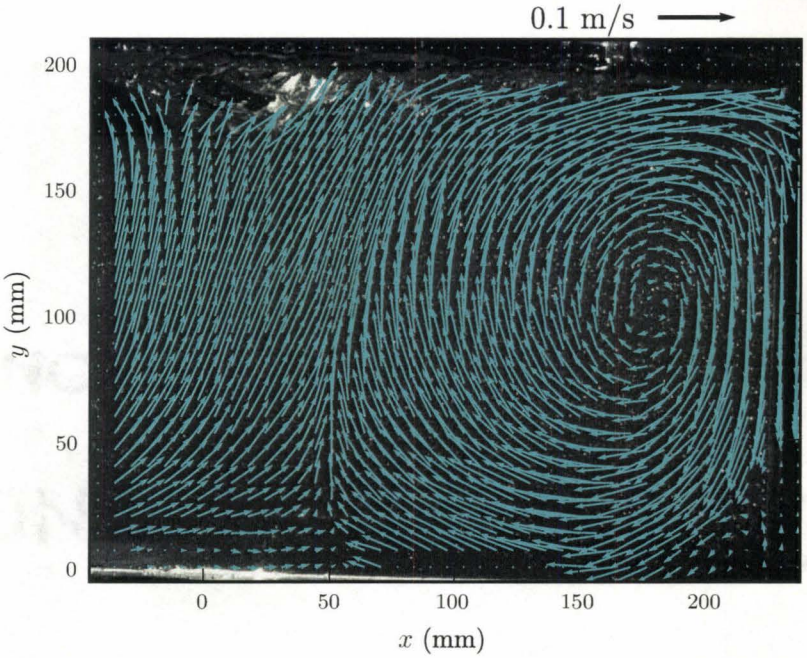

(d) 24 cm

Figure 3.14: The comparison of PIV velocities in 100 SLPM flowrate.

Chapter 4

Mathematical Modelling

Many free surface modelling codes neglect the gas side shear stress equation. However, this approximation is not proper for an impinging gas jet, so the full stress boundary condition is required. Other issues that are important are the discontinuous shear stress for the surface boundary conditions, surface tension forces and the capability to represent multiple interfaces. To fulfill all these requirements, a volume fraction function was used to separate the computational domains for each phase. The computation of momentum was done with a Cartesian-Cut-Cell framework and the liquid volume was advected with the conventional Volume of Fluid method.

4.1 The Governing Equation

The flow system is limited to the incompressible, immiscible, isothermal and non-reacting two-phase flow. The governing equations to solve this system are mass conservation, the Navier-Stokes equation and the volume advection equation from the Volume of Fluid Method.

$$\nabla \cdot \boldsymbol{u}^i = 0 \tag{4.1}$$

$$\rho^i \left(\frac{\partial \boldsymbol{u}^i}{\partial t} + \nabla \cdot \boldsymbol{u}^i \boldsymbol{u}^i \right) = -\nabla p^i + \nabla \cdot \boldsymbol{\tau}^i + \boldsymbol{F}_B^i \tag{4.2}$$

$$\frac{\partial F}{\partial t} + \boldsymbol{u} \cdot \nabla F = 0 \tag{4.3}$$

here i means i-th phase of the system and $\boldsymbol{F}_B$ is the sum of the body forces. The velocity of the denser phase was used for VOF advection. Since a Newtonian fluid was assumed, the stress tensor is represented as

$$\boldsymbol{\tau} = 2\mu \boldsymbol{D} = \mu \left[\nabla \boldsymbol{u} + (\nabla \boldsymbol{u})^T \right] \tag{4.4}$$

where $\boldsymbol{D}$ is the strain rate tensor.

4.2 Separation of Domains and Cell Merging

For the computation of a separate shear stress tensor for each phase, the calculation domain was separated with volume fraction information. The surface was represented with PLIC (Piecewise Linear Interface Construction) scheme and a least squares improvement was applied; as described in Appendix B.

With this line construction of the interface, the calculation cells are cut and each cut of the cell produces fragments of computational cells; each neighbor cells and coefficients are assigned as illustrated in Figure 4.1. However, if one proceeds with this geometrical condition, some small or thin cells (W^2 and E^1 in Figure 4.1b) induce instability to the computation, so that very low relaxation factors are required for stability. In the worst case, the computation may not proceed.

Therefore, the cell merging technique was used to stabilize the computation. For efficiency of the computation, the cell merging criteria was set to be 0.5 volume fraction. With this setting each computational cell requires only one phase representation, so no modification of memory storage structure for each variable is required. The cut cell will contain the major ($F \geqq 0.5$) and minor ($F < 0.5$) cells and the minor cells are merged to its neighbor cell. The node is moved to the centre of mass of the merged cells, as illustrated in Figure 4.1d.

The merging partner cell was determined from the surface orientation. The general merging procedures are listed in Algorithm 1 and illustrated in Figure 4.2. There are some special cases; cells will not be merged with boundary node even its orientation is facing the boundary, as in Figure 4.2f, and the partial cells are allowed to be extended up to two cells at the boundary, as in Figure 4.2g. When a cell is merged to a differently orientated cell, sometimes the orientation mismatches are too severe and the surface normal projection of the distance vector from the surface to centre of mass is located outside of the cell. In this case, the pressure correction becomes unstable, so the cell is merged to the diagonal neighbour (Figure 4.2h).

The computer storage requirement increases quadratically in the 2D case, but the surface line only changes linearly, so the surface information need not be stored for the whole computation cell. The surface description requires merging partner cell information and local geometrical information also. The size of the array to store surface variables is determined from the number of partially filled cells and its

Algorithm 1 General cell merging procedure

```
if cell orientation is horizontal then
  if vertical neighbor's phase is same with this cell then
    Set vertical neighbor as partner
  else if horizontal neighbor is this phase then
    Set horizontal neighbor as partner
  else
    Set the diagonal neighbor as partner
  end if
else
  if horizontal neighbor's phase is same with this cell then
    Set horizontal neighbor as partner
  else if vertical neighbor is this phase then
    Set vertical neighbor as partner
  else
    Set the diagonal neighbor as partner
  end if
end if
```

neighbours. Neighbors were counted up to second nearest neighbours; in that case, all the information required is stored. Base cell positions are indexed and the variables are just referenced from the surface part, so unnecessary referencing or assignments was avoided which helps the computational efficiency.

4.3 Discretization

The procedures of discretization follow general Finite Volume Methods (Ferziger and Perić 2002b; Patankar 1980; Versteeg and Malalasekera 1995). A Collocated arrangement of variables was used for simplicity in geometry of the cut-cell. In this case, cell face velocities need to be interpolated based on the momentum equation and an example configuration of the cell variable arrangement is shown in Figure 4.3.

The governing equations of this two phase system are the mass (4.1), momentum (4.2) and the space conservation. The space conservation relationship is required for the moving boundary formulation and the surface movement is considered as a boundary movement. To do this, the space and mass conservation equations are combined into an equation for pressure correction; the details of this part are explained in Section 4.3.3.

The discretization for the Cartesian cut cell configuration is straightforward, except for the extra shear stress terms and the extra cell faces coming from the cell cut and cell merging process. The extra cell faces are illustrated in Figure 4.1d with thick gray lines. So the mass and diffusion fluxes at these extra faces must be added in the discretization process.

In the stress tensor of a Newtonian fluid in Equation (4.4), the $(\nabla \boldsymbol{u})^T$ term usually vanishes in the Cartesian grid. But when cell cuts breaks the rectangular shape, this term does not vanish and must be included in the discretization process.

4.3.1 Momentum Equation

The Navier-Stokes equation in vector form, Equation (4.2), was integrated over a Cartesian cut cell control volume as a typical procedure of Finite Volume discretization,

$$\int_V \rho \frac{\partial \boldsymbol{u}}{\partial t}\, dV + \int_A (\rho \boldsymbol{u})\, \boldsymbol{n} \cdot \boldsymbol{u}\, dA = -\int_A p\boldsymbol{n}\, dA + \int_A \boldsymbol{n} \cdot \left[\mu \nabla \boldsymbol{u} + \mu (\nabla \boldsymbol{u})^T\right]\, dA + \int_V \boldsymbol{F}_B\, dV \quad (4.5)$$

Discretization of one direction can be applied to the other direction without losing any generality, so the discretization of each integral in Equation (4.5) is shown only for the x-direction. An Implicit Eulerian approach (Ferziger and Perić 2002b) was generally applied throughout the discretization procedure.

The transient integral was approximated with the first order time difference of mass and velocity products.

$$\int_V \rho \frac{\partial \boldsymbol{u}}{\partial t}\, dV \Rightarrow \frac{M^{n+1} u_P^{n+1} - M^n u_P^n}{\Delta t} \quad (4.6)$$

Here M is the integrated mass of the cell, and the superscript n is the current time step and $n+1$ is the next time step.

In the convection integral, $\rho \boldsymbol{n} \cdot \boldsymbol{u}$ is approximated by the mass flux through the cell faces, which is computed as $\dot{m} = \rho A \hat{u}$, and the merged cell face contributions must be considered here. The hat velocities, momentum interpolated face velocity

$(\hat{u})$, are described in Section 4.3.3. Figure 4.4 shows a schematic diagram of mass flux through each cell face including the merged cell.

$$\begin{aligned}\int_A (\rho \boldsymbol{u})\, \boldsymbol{n}\cdot\boldsymbol{u}\, dA \Rightarrow & \dot{m}_e u_e + \dot{m}_e^x u_e^x - \dot{m}_w u_w - \dot{m}_w^x u_w^x \\ & + \dot{m}_n u_n + \dot{m}_n^x u_n^x - \dot{m}_s u_s - \dot{m}_s^x u_s^x\end{aligned} \tag{4.7}$$

Here the subscripts e, w, n, s are each direction and superscript x is the term for the merged cells. Since the interface was assumed to be impermeable, there is no mass flux through the surface. The mass fluxes were calculated with hat velocities ($\hat{u}_e$, $\hat{u}_w$, $\hat{v}_n$, $\hat{v}_s$) which were determined by the momentum interpolation method described in Section 4.3.3. The face velocities (u_e, u_w, u_n, u_s), were approximated with a first order upwind scheme.

Similar to the convection integral, the pressure volume integral was converted to a surface integral with the Gauss theorem. The surface pressure must be considered here

$$-\int_V \frac{\partial p}{\partial x}\, dV \Rightarrow -\int_A p\boldsymbol{n}\, dA \Rightarrow -\left(A_e p_e - A_w p_w \pm n_x A_{fs} p_{fs}\right) \tag{4.8}$$

In the last term in Equation (4.8), the $\pm$ sign is determined by the phase calculated. Since the surface normal is calculated pointing to phase 2 (liquid), it is negative for phase 2 and positive for phase 1.

The viscous stress integral is divided into non-transposed and transposed terms. The non-transposed term is expressed in the following way for the x-momentum equation.

$$\begin{aligned}\int_A \boldsymbol{n}\cdot\mu\nabla\boldsymbol{u} dA \Rightarrow & + \mu_e A_e \left.\frac{\partial u}{\partial x}\right|_e + \mu_e^x A_e^x \left.\frac{\partial u}{\partial x}\right|_e^x \\ & - \mu_w A_w \left.\frac{\partial u}{\partial x}\right|_w - \mu_w^x A_w^x \left.\frac{\partial u}{\partial x}\right|_w^x \\ & + \mu_n A_n \left.\frac{\partial u}{\partial y}\right|_n + \mu_n^x A_n^x \left.\frac{\partial u}{\partial y}\right|_n^x \\ & - \mu_s A_s \left.\frac{\partial u}{\partial y}\right|_s - \mu_s^x A_s^x \left.\frac{\partial u}{\partial y}\right|_s^x\end{aligned} \tag{4.9}$$

The transpose term is discretized in a similar way, but with special care to compute the velocity gradient terms.

$$\begin{aligned}\int_A \boldsymbol{n}\cdot\mu\left(\nabla\boldsymbol{u}\right)^T dA \Rightarrow &+\mu_e A_e \left.\frac{\partial u}{\partial x}\right|_e + \mu_e^x A_e^x \left.\frac{\partial u}{\partial x}\right|_e^x \\ &-\mu_w A_w \left.\frac{\partial u}{\partial x}\right|_w - \mu_w^x A_w^x \left.\frac{\partial u}{\partial x}\right|_w^x \\ &+\mu_n A_n \left.\frac{\partial v}{\partial x}\right|_n + \mu_n^x A_n^x \left.\frac{\partial v}{\partial x}\right|_n^x \\ &-\mu_s A_s \left.\frac{\partial v}{\partial x}\right|_s - \mu_s^x A_s^x \left.\frac{\partial v}{\partial x}\right|_s^x\end{aligned} \tag{4.10}$$

The y-momentum discretization is listed in Appendix A. When the surface cells are included, the shear stress terms from the surface must be counted. The surface shear stress is obtained during the surface velocity calculation, which is outlined in Section 4.4. Surface stress is calculated in the normal and tangential directions, so each directional contribution is added to each directional momentum equation.

$$\text{x-direction} \Rightarrow \pm\left(\tau_{nn}n_x + \tau_{nt}t_x\right) \tag{4.11}$$

$$\text{y-direction} \Rightarrow \pm\left(\tau_{nn}n_y + \tau_{nt}t_y\right) \tag{4.12}$$

The sign depends on the phase calculated due to the surface normal direction convection. $\tau_{nn} = \boldsymbol{n}\cdot\boldsymbol{\tau}\cdot\boldsymbol{n}$ and $\tau_{nt} = \boldsymbol{n}\cdot\boldsymbol{\tau}\cdot\boldsymbol{t}$. Finally, the body force terms are discretized directly. In this study, only gravity is included.

$$\int_V \boldsymbol{F}_B\, dV \Rightarrow g_x M_P^n \tag{4.13}$$

Since the volume fraction in the next time step is not known yet, the momentum equation is modified with the mass equation. The time dependent mass equation,

$$\frac{\partial\rho}{\partial t} + \boldsymbol{\nabla}\cdot\left(\rho\boldsymbol{u}\right) = 0 \tag{4.14}$$

is integrated and discretized similarly to the momentum equation.

$$\frac{M^{n+1}-M^n}{\Delta t} + \dot{m}_e + \dot{m}_e^x - \dot{m}_w - \dot{m}_w^x + \dot{m}_n + \dot{m}_n^x - \dot{m}_s - \dot{m}_s^x = 0 \tag{4.15}$$

If we multiply Equation (4.15) by u_P^{n+1}

$$\begin{aligned}&\frac{M^{n+1}u_P^{n+1} - M^n u_P^{n+1}}{\Delta t} + +\dot{m}_e u_P^{n+1} + \dot{m}_e^x u_P^{n+1} - \dot{m}_w u_P^{n+1} - \dot{m}_w^x u_P^{n+1} \\ &+\dot{m}_n u_P^{n+1} + \dot{m}_n^x u_P^{n+1} - \dot{m}_s u_P^{n+1} - \dot{m}_s^x u_P^{n+1} = 0\end{aligned} \tag{4.16}$$

This equation is subtracted from the discretized momentum equation and finally one can solve the following momentum equation.

$$\begin{aligned}&\frac{M^{n+1}u_P^{n+1} - M^n u_P^{n+1}}{\Delta t} + \dot{m}_e\left(u_e - u_P^{n+1}\right) + \dot{m}_e^x\left(u_e^x - u_P^{n+1}\right)\\ &- \dot{m}_w\left(u_w - u_P^{n+1}\right) - \dot{m}_w^x\left(u_w^x - u_P^{n+1}\right) + \dot{m}_n\left(u_n - u_P^{n+1}\right) + \dot{m}_n^x\left(u_n^x - u_P^{n+1}\right)\\ &- \dot{m}_s\left(u_s - u_P^{n+1}\right) - \dot{m}_s^x\left(u_s^x - u_P^{n+1}\right) = \text{Pressure} + \text{Viscous} + \text{Body Force}\end{aligned} \tag{4.17}$$

Equation (4.17) can be arranged to the general linear system of equation,

$$A_P\phi_P = A_E\phi_E + A_W\phi_W + A_S\phi_S + A_N\phi_N + B \tag{4.18}$$

where ϕ can be any variable. This equation can be solved with the general solver (Patankar 1980; Ferziger and Perić 2002b).

4.3.2 Mass and Space Conservation

The mass conservation equation defined in Equation (4.1) will be used for the internal fluid, since incompressibility is assumed. However, the surface is a moving boundary and the effect of moving surface is not small in this study. Some correction is required for this effect.

The Space conservation law (Demirdžić and Perić 1988) must be considered in a moving boundary Finite Volume method and the mass conservation equation will be modified accordingly around the surface.

Starting from the Reynolds transport theorem, which is well explained by White (2006),

$$\frac{D}{Dt}\int_{V(t)}\phi\,dV = \int_{V(t)}\frac{\partial}{\partial t}\phi\,dV + \int_{A(t)}\boldsymbol{n}\cdot(\boldsymbol{v}_{cv} - \boldsymbol{u})\phi\,dA \tag{4.19}$$

$\boldsymbol{v}_{cv}$ is the velocity of control volume movement and $\boldsymbol{u}$ is fluid movement and ϕ can be any fluid variable. The space conservation law can be written as

$$\frac{D}{Dt}\int_{V(t)} dV = \int_{A(t)}\boldsymbol{v}_{cv}\cdot\boldsymbol{n}\,dA \tag{4.20}$$

for an incompressible fluid and using density(ρ) as a ϕ in Equation (4.19)

$$\frac{D}{Dt}\int_{V(t)}\rho\,dV = \cancel{\int_{V(t)}\frac{\partial}{\partial t}\rho\,dV} + \int_{A(t)}\boldsymbol{n}\cdot(\boldsymbol{v}_{cv} - \boldsymbol{u})\rho\,dA \tag{4.21}$$

and multiplying the space conservation equation by ρ yields

$$\frac{D}{Dt}\int_{V(t)} \rho \, dV = \rho \int_{A(t)} \boldsymbol{v}_{cv} \cdot (n) \, dA \tag{4.22}$$

Since the cell wire-frames are not changed with time and the surface line is moving, the space conservation approximates the surface movement only. The effect of a time changes of the wetted fractions of the cell walls are smaller than the surface contribution, so they are neglected. With this assumption, Equation (4.21) and (4.22) generate the following equation

$$\rho \int_{A_{fs}} \boldsymbol{n} \cdot \boldsymbol{v}_{cv} \, dA = \rho \int_{A(t)} \boldsymbol{n} \cdot (\boldsymbol{v}_{cv} - \boldsymbol{u}) \, dA \tag{4.23}$$

At the free surface, the boundary movement follows the fluid movement and the cell wire-frames are assumed not to move. The left hand side is the surface movement contribution only and the right hand side is non-surface contribution, as illustrated in Figure 4.5. So new mass conservation equation at the surface is derived and the final form can be written as

$$\rho \int_{fs} \boldsymbol{n} \cdot \boldsymbol{v}_{cv} \, dA = \rho \int_{A(t)} -\boldsymbol{n} \cdot \boldsymbol{u} \, dA \tag{4.24}$$

where fs means free surface. If it is rewritten in the form of a mass flux with the merging cell configuration, the following equation is produced and this equation is used as the pressure correction equation.

$$\pm \rho A_{fs} v_{fsn} + \dot{m}_e + \dot{m}_e^x - \dot{m}_w - \dot{m}_w^x + \dot{m}_n + \dot{m}_n^x - \dot{m}_s - \dot{m}_s^x = 0 \tag{4.25}$$

where the v_{fsn} is surface normal velocity and the liquid side is defined to be positive. The surface term is $+$ for gas side and $-$ for the liquid in Equation (4.25).

4.3.3 Pressure Correction

In the collocated grid system, all the flow variables are defined at the center of the computation cell, so the velocity to calculate the mass flux through the cell face needs to be interpolated. The simple choice of the Central Difference scheme results in a converged pressure field that resembles a *checker board.*

To remove this pressure *checker board* anomaly, momentum interpolation must be used and the general procedures are well-documented in literature (Rhie and Chow

1983; Ferziger and Perić 2002b; Demirdžić et al. 1993) for the structured and unstructured grid cases. The basic idea is to separate the interpolation procedures for the terms with pressure and without pressure in the momentum equation. Some advanced methods separate more terms (Choi 1999; Date 2003).

From Equation (4.18) for the u velocity as an example, pressure terms are written separately from the source term (B) and the equation is rewritten in the case of P cell

$$u_P^* = \frac{\sum_{nb} A_{nb} u_{nb}^* + b_P}{A_P} - \frac{\Delta V_P}{A_P} \left.\frac{dp}{dx}\right|_P \tag{4.26}$$

where b_P is the source term without the pressure part.

When the e face is of interest, P cell and E cell information are used for interpolation. The following two representations are logically equivalent, but a mathematical error exists in Equation (4.27).

$$\hat{u}_e^* = \overline{\frac{\sum_{nb} A_{nb} u_{nb}^* + b_P}{A_P}} - \overline{\left(\frac{\Delta V}{A_P}\right)_e} \left.\frac{dp}{dx}\right|_e \tag{4.27}$$

$$\hat{u}_e^* = \overline{(u^*)_e} - \overline{\left(\frac{\Delta V}{A_P}\right)_e} \left[\left.\frac{dp}{dx}\right|_e - \overline{\left.\frac{dp}{dx}\right|_e} \right] \tag{4.28}$$

where overbar means an interpolation. The second equation is used for the discretization of pressure correction.

The SIMPLE velocity-pressure coupling scheme is used for the correction equation

$$\hat{u}_e' = -\overline{\left(\frac{\Delta V}{A_P}\right)_e} \left.\frac{dp'}{dx}\right|_e = -\overline{\left(\frac{\Delta V}{A_P}\right)_e} \frac{1}{\Delta x}(p_E' - p_P') \tag{4.29}$$

From Equation (4.25) $\dot{m}_e$ terms are easily computed and discretized with Equation (4.29). The contribution from the extra face of the merged cell, $\dot{m}_e^x$, has no node for discretization of pressure correction, so an interpolation is used to obtain the velocity at this face; the interpolation scheme is explained in Section 4.3.4.

The surface contribution, v_{fsn}, is approximated with the same method as in Equations (4.28) and (4.29).

$$v_{fsn}^* = \overline{(v_n^*)} - \overline{\left(\frac{\Delta V}{A_P}\right)_{fs}} \left[\left.\frac{dp}{dn}\right|_{fs} - \overline{\left.\frac{dp}{dn}\right|_{fs}} \right] \tag{4.30}$$

$$v_{fsn}' = -\overline{\left(\frac{\Delta V}{A_P}\right)_{fs}} (p_{fs}' - p_P') \tag{4.31}$$

where v_n is the surface normal direction projection of the velocity of each cell. The surface is assumed to be a pressure boundary with fixed pressure which is obtained from the normal direction stress balance. p'_{fs} is set as 0 and this simplifies the discretization procedure. This scheme is inspired by Muzaferija and Perić (1997) and more generalized by applying full normal and tangential stress terms. The details of the boundary conditions are explained in the Section 4.4.

Majumdar (1988) indicated that the momentum interpolation scheme may not produce a consistent result without relaxation; relaxation is applied relative to the previous iteration stage.

Around the surface cells, the computation points are located at the centre of mass, so the surface point and the computation point are not aligned well. The second order correction of pressure is applied, as described in Ferziger and Perić (2002b). The correction equation is written as follows and illustrated in Figure 4.6.

$$\left.\frac{dp'}{dn}\right|_{fs} = \frac{p'_P - p'_{fs}}{\Delta n} + \frac{(\nabla p')_P \cdot \boldsymbol{r}_{Q-P}}{\Delta n} \tag{4.32}$$

This second correction affects the mass balance and the quality of the VOF advection.

4.3.4 Interpolation

As shown in Section 4.3.1, there are many variables to be computed in non-regular computation nodes such as cell faces, and extra faces from the merged cells. Therefore, a proper interpolation and extrapolation scheme is required. The centre of mass of the cells is not located in a regular position and cell cutting eliminates regularly aligned neighbours. An interpolation scheme that can deal with non-regularly distributed interpolants is required.

In the Cartesian cut cell methods, Udaykumar et al. (2001) proposed selecting 6 neighbours and solving directionally quadratic equations to obtain the extra cell face information. However, when the surface becomes close to a flat interface, the solution matrix becomes singular or near singular, so the selection of neighbours needs special care.

Several methods are appropricate for this case and they are reviewed and compared by Renka (1999). The Quadratic Shepard method (Renka 1988a; Renka 1988b)

was chosen, since it is the simplest among the reviewed methods, and the error level is similar to other methods. This method computes a least square fit of two-dimensional quadratic polynomial for each computation nodes, and neighbour coefficients are weighted with an inverse distance type function. So the final functional form of interpolation is

$$F(x,y) = \frac{\sum_{k}^{N} W_k(x,y) Q_k(x,y)}{\sum_{k}^{N} W_k(x,y)} \tag{4.33}$$

where $Q_k(x,y)$ is the local least square estimation of the function at (x_k, y_k). The weight function $W_k(x,y)$ is defined with the inverse distance function,

$$W_k(x,y) = \left[\frac{(R_w - d_k)_+}{R_w d_k}\right]^2 \tag{4.34}$$

$$(R_w - d_k)_+ = \begin{cases} R_w - d_k & , \text{if } d_k < R_w \\ 0 & , \text{if } d_k \geqq R_w \end{cases} \tag{4.35}$$

where R_w is the predefined limit of distance, and d_k is the distance from (x,y) to (x_k, y_k).

The original method requires computing the least square fit of the each computational node, so the computation is quite expensive. Therefore, the method is modified to compute the least square fits only around the affected surface cells and linear interpolation is used for the other regularly arranged cells.

4.3.5 Other geometrical irregularities

The line construction of the surface produces non-matching cell faces, as illustrated in Figure 4.7. This non-matching face is considered as a phase boundary and all the required variables are obtained with the interpolation method. The same surface treatment is applied, but the computed contribution from this part is added to the source term; no implicit formula is used for this part.

Surface cells and its neighbour's computation nodes are usually not well aligned, so a geometrical correction is applied to these cases. The procedure is almost the same as the second correction of the pressure part.

When the major phase of a cell changes in a time step, the value of velocity and pressure at the previous time step do not exist. Calculation at the next time step and source terms require these values, so interpolation is applied based on neighbour values. This interpolated value does not guarantee the mass balance for the newly generated cell, so sometimes the pressure correction becomes unstable. For stability, the solver is modified to accept different relaxation factors for each computational cell. Low under-relaxation factors are used for the cells changing their phase or for those severely distorted. The underrelaxation scheme is applied to the multigrid scheme too. When the multigrid cell is severely separated from the bulk domain, it has less facing area to its neighbor multigrid cells, so the multigrid correction is underrelaxed.

4.4 Surface Boundary Conditions

In the two dimensional case, one must solve 6 variables at the surface; the variables are u_1, v_1, u_2, v_2, p_1, p_2. When applying a kinematic condition

$$u_1 = u_2 \tag{4.36}$$

$$v_1 = v_2 \tag{4.37}$$

the number of variables becomes 4. However, the only available boundary conditions are the normal and tangential stress conditions. Therefore, a closure problem arises and proper modelling is required.

In Equation (2.24), the spatial gradient of surface tension is not important in this study, but the other terms must be included. The normal and tangential parts of the condition are

$$p_1 - p_2 + \sigma\kappa = \tau_{nn1} - \tau_{nn2} \tag{4.38}$$

$$0 = \tau_{nt1} - \tau_{nt2} \tag{4.39}$$

Direct solution of the above equations with extrapolated pressures from each phase is extremely unstable. Small fluctuations of pressure yield a failure in the velocity computation, so an iterative approach is applied.

A more stable option is to iterate the boundary condition. First the phase 1 (gas) pressure was extrapolated to the surface; τ_{nn} are obtained with previous time step, then a balance for p_2 is obtained, and this is used for the phase 2 momentum

computation. Surface normal velocities are extrapolated from the phase 2 (liquid) and corrected with a pressure correction in that phase. Every time the surface normal velocities and the internal velocities are updated, the tangential shear stress condition is applied to obtain the surface tangential velocities. In the case of phase 1, the obtained surface normal velocities are just accepted and the interface is regarded as a moving solid wall, but the tangential velocities are updated.

The tangential velocities are obtained with the known surface normal velocity and the shear stress condition. The shear stress condition can be written in detail

$$\mu_1 \left(\frac{\partial u_t}{\partial n} + \frac{\partial u_n}{\partial t} \right)_1 = \mu_2 \left(\frac{\partial u_t}{\partial n} + \frac{\partial u_n}{\partial t} \right)_2 \tag{4.40}$$

The tangential gradient of the normal velocity is obtained with the corrected and interpolated surface normal velocities at the centre of the surface and cell cut position. With the normal gradient of tangential velocity, a simple linear equation is constructed.

$$\mu_1 \frac{u_t(P_1) - u_{tfs}}{\Delta n_1} - \mu_2 \frac{u_t(P_2) - u_{tfs}}{\Delta n_1} = (\mu_2 - \mu_1) \frac{\partial u_n}{\partial t} \tag{4.41}$$

where P_1 and P_2 are corresponding phase computational nodes. The surface tangential velocity, u_{tfs}, can be easily solved.

4.5 Multigrid

The momentum and pressure discretization have the same form as Equation (4.18), so the same solution method is applied for the linear system of equations.

The general solution methods are well summarized from the direct matrix solver to the iterative solvers (Ferziger and Perić 2002b; Golub and Van Loan 1996). Udaykumar et al. (2001) indicated that the pre-conditioned Conjugate Gradient solver was adequate for the static boundary situation, but it is not adequate for the moving boundary case because of the more significant change in pressure fields.

As reviewed in Chapter 2, in the multigrid method of Udaykumar et al. (2001) a coarse grid volume fraction function was defined and this volume fraction function was used to determine whether the grid will be included in the coarse grid part of the multigrid computation or not. However, omitting part of the coarse grid cells from the computation can slow down the overall solution procedures in some surface geometries.

Tai and Shyy's (2005) method applies the multigrid across the phase boundary. Without special care to select finer grid mesh to be corrected in the restriction stage, the multigrid correction is transferred through the cell boundaries. The coarse grid residual information is mixed across the phases, so this scheme is not logically consistent for separate computation domains for each phase in this study.

Therefore, a more simple zeroth order algebraic multigrid scheme is applied with a Point Gauss-Seidel (PGS) internal solver. To account for the separation of the computation domain, a coarse grid computation storage is assigned to each individual phase. If only the coarse grid has the corresponding phase in their finer grid cells, that part of coarse grid is included in that level of multigrid computation. During the construction of coarse grid coefficients, other phase cells are excluded, so smearing error across the boundary is prevented. A schematic diagram is drawn in Figure 4.8 for the selection of coarse grid cells to include. A simple V-cycle multigrid sequence is used for calculation.

4.6 VOF Advection Method

In Young's method (Young 1982), the volume fraction was computed with Equation (4.3) and the Explicit Euler discretization scheme (see Ferziger and Perić 2002b). The face flux of the volume fraction is obtained by applying a first-order Taylor series approximation with higher order first derivative estimation at the upwind cell position. In the case of the east face, the face flux was approximated as

$$\overline{F}_e = F_P + \frac{1}{2}(1-\eta)\Delta x D_j \tag{4.42}$$

where η is defined as $u\Delta t/\Delta x$ and D_j is the first derivative of F. The author indicates that numerical diffusion can be minimized with a higher order approximation of D_j and removing unphysical behaviour. However, the face flux error with this method can be easily shown graphically. Figure 4.9a shows a geometrical representation of Equation (4.42) and Figure 4.9b shows its geometrical error. The left hatched region in Figure 4.9b should be advected to the right cell, but Young's method will under- or over-estimate the volume flux depending on the surface construction.

To remove this anomaly, geometrical volume fluxes (Son and Hur 2002; Gueyffier et al. 1999) are obtained based on the line surface construction. The volume fraction change was obtained by adding these volume fluxes from each base cell face.

$$(F^{n+1} - F^n)V = -(\delta F)_e + (\delta F)_w - (\delta F)_n + (\delta F)_s \tag{4.43}$$

where (δF) is the computed face flux for each cell face. A one-dimensional example is shown in Figure 4.10a.

The pressure corrected face velocities are used for face velocity and volume flux calculation, but when this velocity is not available (extra faces from merged cells and surface cells with changing phases), interpolated values are used.

For the merged cells, any velocity at the merging face will satisfy a mass balance in the whole merged cells, but this does not guarantee the right mass balance at the unmerged base cells. So the mass balancing velocity at the partial cell is computed and used for volume flux computation. This procedure is illustrated in Figure 4.10b.

4.7 Solution Procedure

Based on the above discussion and modelling considerations, the overall procedure for the computation is:

1. Set the base grid system for whole domain; this is used for the general geometrical variables.
2. Construct line representation of the surface based on the volume fraction function (F)
3. The line construction cuts the base cell, so determine the merging partner cells and their geometrical information.
4. Apply interpolation to obtain newly generated cell information.
5. Obtain the coefficients for the non-surface cells based on
   - collocated arrangement; Rhie-Chow type momentum interpolation
   - First order upwind
   - SIMPLE pressure correction
6. For the surface cells, apply the same scheme as 5, but the surface geometry must be considered and non-regular parts were included as an explicit source term.

7. Momentum computation
   (a) Apply the boundary condition Equation (4.38) and obtain p_2 along the surface.
   (b) Solve liquid velocity components.
   (c) Obtain surface normal velocity with momentum interpolation.
   (d) Update tangential surface velocity components.
   (e) Correct pressure, assuming the surface as a fixed pressure boundary.
   (f) Correct liquid velocity components.
   (g) Update tangential surface velocity components.
   (h) Solve gas velocity, assuming the surface normal velocity is fixed.
   (i) Update tangential surface velocity components.
   (j) Correct pressure.
   (k) Correct gas velocity components.
   (l) Update tangential surface velocity components.
   (m) Repeat until convergence is achieved.
8. Determine the velocity for VOF advection.
9. Advect the volume fraction with the modified Young's method.
10. Advance time.

4.8 Validation Test

4.8.1 Broken Dam test

The Broken Dam problem has been widely used as a test problem for free surface computation (Hirt and Nichols 1981; Jeong and Yang 1998; Greaves 2004; Qian et al. 2003; Guo and Irons 2002).

Martin and Moyce (1952) measured the bottom wetting distance and the remaining column height by high speed photography. Initially, the water column was constrained in a thin waxed paper diaphragm. The paper was released by passing a high electrical current to the metal frame and melting the beeswax connecting the paper to the frame. Several initial aspect ratios (width(b) to height(a)) of the water column were tested in their experiments. Among them, the ratio $b/a = 2$ is most popular for the free surface computation test.

For the present code, two different sizes of initial water column of $b/a = 2$ were tested. One had an initial width of 6 cm, which is similar to Martin and Moyce's (1952) experiment and the other was 1.25 m. The computation domain was restricted horizontally to the dimensionless distance ($z/a = 4$) as other test cases. A closed box of 80×60 uniform cells was used for the whole domain for both cases and the cell spacing was adjusted according to the initial width. Initially 20×40 cells were filled with water and the gas phase was air. A 10^{-3} second time step was used for both cases. Physical properties at 1 atm and 20 °C were used for the computation and those properties and physical constants are summarized in Table 4.1.

Figure 4.11 shows the surface profile change with time. The dimensionless time step between the each surface profile is indicated in the figure. The profiles are almost the same for the two cases. Figure 4.12 shows an example of velocity profiles in air and water side at the dimensionless time around 2.22. The overall shape of the velocity vectors are the same for both cases. As expected from the modeling condition of sharp cutting interface, quicker response was observed in air side; the other VOF method (Qian et al. 2003) shows smoother velocity change across the surface and the air side response was delayed by one or two cells away from the interface.

The dimensionless wetted distance (z/a) and the remaining height (h/a) was compared with Martin and Moyce's experimental results and other computational results. There is some discrepancy in the literature for the comparison of numerical result with the experimental data of Martin and Moyce. Hirt and Nichols (1981) and (Jeong and Yang 1998) claim their numerical results show good agreement with the experimental data, but it was impossible to find the matching experimental points in Martin and Moyce's data.

All the computational results show a faster movement of the leading edge than Martin and Moyce's experimental result. Greaves (2004) indicated "the discrepancy is due to the difficulty in determining the exact location of the leading edge in the experiment," and there could be some effect of remaining waxed paper for initial delay.

However, the overall slope of the wetted distance—the speed of the liquid front movement, matches well with experiments. The computational results are compared with others and the experimental result in Figure 4.13a. The overall behavior was

almost the same as other researchers, but a slight delay was observed for higher dimensionless time; it is still faster than experimental results. The remaining height changes more slowly than the leading edge movement and the computation and experimetal results match very well (Figure 4.13b).

4.8.2 Surface wave generation and instability

Observations of wind generated waves have been summarized by Munk (1947). For wind speeds between 1.1 and 6.6 m/s the surface is smooth, but not planar; in this stage small ripples are immediately smoothed. When the wind speed exceeds the critical value, Kelvin-Helmholtz instability criterion, 6.5 m/s, waves grow rapidly.

The wave initiation, which occurs at 1 m/s, far below the critical velocity of Kelvin-Helmholtz instability, is due to the turbulent gas pressure fluctuations and the resonance between the pressure fluctuations and the surface waves (Phillips 1957; Teixeira and Belcher 2006). The wave growth is related to its friction velocity and tangential stress (Mitsuyasu and Honda 1982). Kelvin-Helmholtz instability explains the sudden growth and the detachment of the droplets. However, pressure fluctuations and frictional forces initiate the disturbances. Other possible interactions of the gas turbulence and surface waves are well summarized by Teixeira and Belcher (2006), but the correlation between those two is beyond the scope of this validation test for the code.

To check the capability of the code to simulate wave generation and its instability, a simple wind induced wave test was designed. A 45 cm long and 3 cm deep dish, as illustrated in Figure 4.14 contains calm water initially. Wind from 2 m/s to 8 m/s was blown tangentially across the water surface from left to right. A 2.5 mm×2.5 mm uniform cell was used and the front 2.5 cm and rear 2.5 cm were covered by a thin solid lid for the stability of the computation. A 1 ms time step was used up to 6 m/s case; 250 μs time step was used for 7 and 8m/s cases.

Figure 4.15 shows the surface profiles at different wind speeds. For 2 m/s wind, the surface shows very slight undulation, but could not effectively generate waves. From 4 m/s to 5 m/s the surface shows small waves with a typical wavelength of 1.5 cm. From 6 m/s some wave amplitudes increase sharply and droplet detachment could be observed at the 8 m/s case.

Munk (1947) suggested a gas flow separation on the leeward side of the unstable wave—which is over the critical wind speed, 6.5 m/s. Lower pressure develops around the point and gas passing this separation impinges on the next windward side crest. Figure 4.16 shows Munk's illustration and an example of the velocity field of this test. Up to 5m/s no separation was observed and the gas velocity followed tangentially to the surface. From 6 m/s separation occurs on the leeward side of a crest. Pressure was lowered at the leeward side and windward side experienced higher pressure, so this accelerated the wave propagation. The directions of shear at this separation are opposing, so the wave crest experiences a shear stress from trough to crest on both windward and leeward sides. The shear from both sides pulls out the wave crest vertically and it results in the sudden wave amplitude increase. These phenomena are not incorporated in the Kelvin-Helmholtz instability analysis.

Generally, the wave behaviour in this test matches with physical observation from the intermediate to critical wind speed. No wave formation at low wind speed—2 m/s, is thought to be caused by the absence of a proper turbulence model in the gas and liquid, and consequently the absence of the turbulent pressure fluctuations.

To compare with conventional VOF method and current model, tests using FLUENT^{TM} were conducted. The grid setup was the same with current model. Test was done for 5 m/s, 7m/s and 8 m/s wind speeds, time steps used were same with the current model; 10^{-3} s for 5 m/s 2.5×10^{-4}s for 7m/s and 8 m/s cases. This FLUENT^{TM} calculation used the Volume of Fluid method with Courant Number restriction, 0.25 (Default) and Geometric-reconstruction (PLIC) method and PISO (Fluent Inc. 2006), PRESSTO!, First order Upwind and Full-cycle Multigrid schemes.

Figure 4.17 shows the wave shapes from this FLUENT simulation at the time of 1.4 s. The waves are less periodic and the amplitude was smaller comparing to the current model, Figure 4.15; current model's wave amplitude was more than 2 cm from trough to crest when it generates droplet, but this FLUENT simulation shows maximum around 1 cm size. The shape of wave breaking was similar to the current model, but there was no droplet generation for the FLUENT simulation up to 8 m/s wind speed.

The main differences of the current model and conventional VOF method are the phase separation and the full stress condition with wall function approximation of gas

side shear stress. The current model shows around 1 cm/s wind speed difference from the real situation for the critical phenomena and the conventional VOF test shows less wave amplitude and critical behaviour. It is thought to be the shear stress and pressure force transfer is relatively poorer for the conventional VOF cases.

4.9 Computational Results

4.9.1 Grid setup and conditions

4.9.1.1 General setup

For the impinging jet case, numerical test grids were prepared with the similar geometrical dimensions of the experiments in Cartesian coordinate form. A high gas jet speed requires very short time steps for numerical stability, but the behaviour of turbulent gas jet close to the nozzle exit is not a main interest of this study. Therfore, the starting point for the gas jet was set in the Fully-Developed Regime (See Section 2.1). The top inlet boundary was set to be close to the liquid interface and the Görtler type analytic solution (Schlichting 1979; Rajaratnam 1976) of a free jet velocity distribution with the parameters for the Prandtl's mixing length theory was used (see Appendix D). The parameter for Prandtl's mixing length theory is from Schlichting (1979),

$$\nu_\tau = \frac{1}{4\sigma^2} x u_m \tag{4.44}$$

where σ is 7.67 for the plane jet case and x is the distance from the nozzle exit.

A schematic diagram of this numerical setup is illustrated in Figure 4.18. A 45 cm×26 cm Cartesian box with 5 mm×5 mm uniform grid around the liquid interface and 5 mm×1 cm grid in the deep water part were used. Gas outlets were placed at the left and right side of the top boundary and the lengths were limited to be 1.5 cm to prevent a back flow of the gases in the pressure boundary. Water was placed up to 20 cm height initially and assuming the imaginary origin of the gas jet, which was located higher than the inlet boundary position and the gas inlet velocities were varied.

For high flowrates over 50 SLPM inlet gas velocity was increased up to over the first second, and then kept constant. The tested lance height and flowrate were summarized in Table 4.2.

4.9.1.2 Effect of top boundary

The top boundary location and the size of the gas domain had an effect on the trajectory of the gas deflected from the liquid surface. Figure 4.19b shows results of the gas deflections for a higher top boundary compared to Figure 4.19a for a lower boundary. When it had more space, impinging gas was deflected with higher angle and less gas contacted the liquid at the sides. So less momentum transfer was expected with more top space.

However, the momentum transfer primarily occurs close to the cavity area and the side contributions were not great. Figure 4.20 shows the overall momentum difference between two setups, 6 cm and 12 cm gas domain height. The larger gas area had 89 % of the momentum of the smaller domain, so doubling the height had a limited effect on the overall momentum transfer.

4.9.2 The Effect of Grid Size

Since the free surface was represented with piecewise linear scheme, a finer grid is expected to represent smoother details of wave shapes. The momentum transfer from the gas to liquid is directly related to the interfacial area, surface representation, so more momentum transfer in finer grid setup is expected.

The current setup of the grid was refined and coarsened to investigate the effect of the number of grid in the calculation domain. The coarsened grid had uniform cells and the finer grid was produced by dividing the current setup (Section 4.9.1) by half in x and y direction, 4 times greater in number.

Figure 4.21 shows the transferred momentum in liquid phase change with time for each grid setup. As expected, the finer grid shows more momentum transfer, but the difference was diminished as the grid refinement is greater. Table 4.3 compares the steady state momentum levels by setting the finest grid as a reference. The coarse grid setup showed 60 % of momentum transfer and medium grid setup showed more

than 90 % momentum transfer. Considering the computation time and convergence behaviour, the medium size grid was used for this study.

4.9.3 Wall function

To represent shear stress correctly, the boundary layer and the corresponding velocity fields must be known, but the gas side boundary layers and the turbulence behaviour around the free surface are not well known, and the experimental works on this aspect are limited.

There are several Direct Numerical Simulation (DNS) results around the free surface (Lombardi et al. 1996; Fulgosi et al. 2003). Lombardi et al. (1996) compared their counter current gas and liquid flow DNS result with the non-dimensional mean velocity profile around a solid wall from Nicuradze's log law. Their computation results show that the gas side mean velocity behaviour is almost identical to the gas around the solid wall behaviour, but the liquid side has some deviation from the solid wall behaviour (Figure 4.22).

Even though Lombardi et al. (1996) assumed a flat non-moving surface, it shows shear stress transfer from the gas to liquid can be approximated with the log-law. Log-law is well summarized in many textbooks (Schlichting 1979; White 2006; Szekely 1979) with different fitting parameters. Szekely's (1979) parameter was used in this study.

$$u^+ = \begin{cases} y^+ & ,0 \le y^+ \le 5 \\ 5\ln y^+ - 3.05 & ,5 \le y^+ \le 30 \\ 2.5\ln y^+ + 5.5 & ,30 \le y^+ \end{cases} \tag{4.45}$$

Around the free surface, the mean value of the tangential velocities can be dimensionalized with friction velocity (u_τ) and the dimensionless distance (y^+) were defined similar to the Reynolds number

$$u^+ = \frac{\overline{u}}{u_\tau} \tag{4.46}$$

$$y^+ = \frac{\rho u_\tau y}{\mu} \tag{4.47}$$

where $u_\tau = \sqrt{\tau_w/\rho}$ and $\tau_w = \mu(\partial\overline{u}_t/\partial n)$. So the apparent viscosity at the wall can be obtained with the following formula

$$\mu_t = \rho\left(\frac{\overline{u}}{u^+}\right)^2 / \left(\frac{\partial\overline{u}_t}{\partial n}\right) \tag{4.48}$$

u_τ computation requires a tangential shear stress term. The tangential shear stress was computed based on the previous iteration's μ_t value, so this procedure was updated after the velocity computation.

4.9.4 Surface Profiles and Velocity Profiles

The jet cavity depressed quickly, within 1 to 2 s after the start of blowing. The depression was more stable and did not show as much fluctuation as the experimental observations. The cavity width oscillation was due to wave generation inside of the cavity and its propagation. Figure 4.23 shows the time variation of the surface profiles for 12 cm height with 50 SLPM and 20 SLPM blowing conditions. The low flowrate (20 SLPM, Figure 4.23a) case shows wave propagation clearly. The high flowrate simulation (50 SLPM, Figure 4.23b) shows wave formation and propagation. The cavity is depressed by the impinging jet pressure and within a relatively stable cavity, shear stress from the gas initiates a wave, which grows and propagates from the cavity. Figure 4.23 shows approximately two cycle of this procedure and estimated frequency from these simulations are 5 Hz (20 SLPM) and 13 Hz (50 SLPM); they are similar to the experimentally reported frequencies (Peaslee and Robertson 1994) and within the range of the experimentally observed freqency in this study.

Figure 4.24 shows examples of the simulated surface profile with varying lance distance and flowrate. Depending on the flowrate, waves formed long extension, detached or propagated as a wave forms. The tangential gas velocity around the wave initiation was around 5 to 10 m/s, which is just above the Kelvin-Helmholtz instability criterion. Surface mean depression depth was plotted in Figure 4.25. The mean values were obtained after 10 s of simulation since the steady state time, which is explained in Section 4.9.5, is usually reached after 10 s even though the average surface shapes are stabilized much before that liquid momentum equilibrium time.

Examples of velocity fields from simulations were plotted in Figure 4.26. In Figure 4.26, 12 (a), 18 (b), 24 (c) cm lance heights were compared at the same flowrate, 50

SLPM and at the same simulation time, 10s. Since there is a large velocity difference across the phases, velocities from each phase was scaled with different factors.

In the case of Figure 4.26b and (c), the gas jet spread to the side and the shear stress initiated small waves. These waves propagated to the side wall and once they hit the wall the liquid flow was directed downward. The water flow met at the centre of the container's bottom, resurfaced under the jet cavity where they balanced with the impinging jet pressure. The liquid flow was gentle and a near symmetric shape was conserved. The wave amplitude did not grow more than 1.5 cm from crest to trough. When the initial deflection angle is low, pressure accumulation at the windward side locally accelerated the gas flow in the case of Figure 4.26c, but in other case, (b), the deflected gas flow was not affected much by the wave shapes.

For lower lance height, higher impinging gas velocity, Figure 4.26a, the cavity depressed deeper and the internal (inside of the cavity) wave formation was clear as illustrated in Figure 4.23b. The waves grew to a thin and long ligament initially directed inward or vertically and later was broken by the sideway gas pressure. Across this liquid ligament, the gas flow was separated and shear was acting in the way to increase the wave amplitude, as observed in Section 4.8.2. The liquid flow from the collapsing wave and the wave hitting the wall was eventually directed downward and circulated in the container. In this case, the liquid flow shows slight asymmetry, that is mainly caused by the imperfection of the surface reconstruction in the Volume of Fluid Method; slight imperfection in the surface reconstruction affects the shape of the surface and direction of momentum transfer.

4.9.5 Steady-State Time for Liquid Momentum Transfer

The steady state time was determined with the Sum of the absolute values of liquid momentum. Equilibrium reached around 10 to 20 s and computation was continued after reaching equilibrium for some cases. The variations of the sum of liquid momentum were plotted in Figure 4.27.

At the same lance height, the equilibrium time becomes shorter as the flowrate is increased. Especially in 20 SLPM case, long term oscillation of momentum was observed. This is discussed in Chapter 5.

4.9.6 Effect of Physical Properties

To see the effect of the physical properties on the momentum transfer through the moving free surface, some important physical properties related with the free surface shape and instability were changed and the flow behaviours were observed. The modified physical properties are density of liquid, viscosity of liquid, surface tension and gravitational constant. Each property or constant multiplied by 10 from its real value for water/air. Lance height of 12 cm and 20 SLPM and 50 SLPM case were used for this test.

Figure 4.28 shows the surface profile variation with the physical properties. Density and gravity increases prevent generation of the dimples, but surface tension and viscosity did not affect the depression depth. Increasing surface tension smoothed the surface waves more than a viscosity increase in both 20 SLPM and 50 SLPM cases.

The Momentum transfer efficiency can be compared with the sum of momentum in liquid phase. Figure 4.29 shows the variation of the sum of momentum with time. The density increase made the liquid move very slowly, so the computation takes much time and it could not reach to the steady state within 1 min; 10 times higher density resulted in 10 times higher momentum in the plot. The increase in the gravity and surface tension reduced the liquid momentum more effectively than the viscosity increase.

4.9.7 Modelling of Gas-Liquid Interactions in a BOF

The present model was applied to make some preliminary calculations regarding the interactions between an impinging jet and a liquid surface; interactions with both slag and metal surfaces were separately simulated. The results are of a preliminary nature because several important aspects, beyond the scope of this thesis, have been ignored:

- Mass transfer and heat transfer aspects of chemical reactions
- Emulsification of slag and metal droplets
- Compressible flow aspects of oxygen jets, and
- The effects of interactions between jets from multiple holes

Thus, the present model examines the development of the gas-liquid interface shape, and momentum transfer to the liquid. Two particular nozzle geometries were

evaluated. The first is from the early work of Smith (1966) because there is some data on the single-hole nozzle, and the second uses the conditions from a single hole in a 5-hole tip currently in use in Ternium Siderar, San Nicolas, Argentina (Perez 2008).

The computational domain was also simplified to a two-dimensional slice of a section of interest in a converter as shown in Figure 4.30. The physical properties used are listed in Table 4.4. The nozzle diameter and other computational conditions are listed in Table 4.5.

An oxygen jet issuing from a supersonic nozzle has lower temperature ($\sim$ -20 °C at Ma=1) than BOF environment (over 1600 °C). Solutions for the gas distributions are sought near the liquid surface where the jet has decayed to a subsonic, incompressible flow condition. The cold core gas jet entrains hot surrounding gases. To simulate this with an isothermal model, the gas jet entrainment behaviour in a BOF was modelled by the entrainment of hot and low density gas into a cold and high density gas. A schematic diagram is shown in Figure 4.31.

The entrainment behavour of different density gas was studied by Ricou and Spalding (1961). The following is the mathematical relationship for the entrainment mass variation.

$$\frac{\dot{m}_e}{\dot{m}_0} = E\frac{x}{d_0}\left(\frac{\rho_1}{\rho_0}\right)^{1/2} \tag{4.49}$$

where $E = 0.32$, $\dot{m}_e$ is the mixed gas mass flux, but its physical properties are similar to the surrounding gas when it is far away from the nozzle exit. So $\dot{m}_e$ was approximated with a Gaussian distribution of the jet velocity profile and the jet envelope was approximated with a cut off of 95 % of the velocity distribution (two times of $r_{1/2}$). The average x-direction velocity was obtained using the Gaussian assumption:

$$\overline{u}(x) = 2\pi \int_0^{2r_{1/2}} u_m e^{-0.693(r/r_{1/2})^2} dr \sim 0.34 u_m \tag{4.50}$$

Substituting this relationship to Equation (4.49) with $\dot{m}_e = \rho_1 A\overline{u}(x)$ gives the following model turbulent jet coefficient.

$$K = \frac{E}{0.34}\left(\frac{x}{d_0}\right)^2\left(\frac{\rho_0}{\rho_1}\right)^{1/2} \tag{4.51}$$

where $d/x = 2\tan(\theta_{\text{expansion}}/2)$ and the expansion angle is around 20°. For 1600°C environment, the computed turbulent jet coefficient K value is 18.24 and it was used for the simulation.

Simulations were separately conducted for steel and slag baths. Figure 4.32 shows an example of the surface profile and velocity field of TH1 (see Table 4.5 for the label) and LH1 case after reaching steady state of momentum. The larger density of steel prevents the momentum transfer process even for higher gas velocities. The surface movement was slower compared to the water case. In the case of the slag melt, the density was lower than steel case, so the surface movement was vigorous and momentum transfer was more efficient.

The depression depth of the surface and liquid velocity were lower than expected from the turbulent jet force balance, Equation (2.4)—less than half. This is due to the inexact computation of turbulent jet propagation in sonic and supersonic and hot gas environment; this model did not include compressibility and temperature change.

However the local force balance at the impinging point shows good agreement, Figure 4.33 shows the balance between the gas pressure at the impinging point and buoyancy force ($\rho g n_0$), to be consistent with local modified Froude number, Equation (5.1), the balance equation was modified as

$$Fr_{lm} = \frac{2p}{\rho g n_0} = \frac{2\left(\frac{1}{2}\rho_g u_g^2\right)}{\rho_l g n_0} \tag{4.52}$$

so 2.0 is the balanced value. See section 5.8.4 for further discussion.

Table 4.1: The list of physical properties at 1 atm and 20 °C and constants for the broken dam test problem. Data were obtained from White (2006).

Physical Properties	Values	Units
Air Density (ρ_g)	1.20	kg/m^3
Water Density (ρ_l)	998.0	kg/m^3
Air Viscosity (μ_g)	1.80×10^{-5}	Pa s
Water Viscosity (μ_l)	1.003×10^{-3}	Pa s
Surface Tension (σ)	7.28×10^{-2}	N/m
Contact angle	90	°
Acceleration of gravity (g)	9.81	m/s^2

Table 4.2: The lance height and flowrate tested in the simulation

	12 cm	18 cm	24 cm
20 SLPM	○	○	○
30 SLPM	○	○	○
40 SLPM	○	○	○
50 SLPM	○	○	○
60 SLPM	○		
70 SLPM	○	○	○
80 SLPM		○	○

Table 4.3: The grid size conditions and the comparison of the effect on the momentum transfer.

Label	Grid size around the surface	Number of grid	Ratio
Coarse	1 cm	26×45	0.597
Medium	0.5 cm	35×92	0.913
Fine	0.25 cm	70×184	1.0

Table 4.4: List of physical properties of O_2, slag and steel at 1600 °C. References are shown in the parenthesis; (O): (Oeters 1989), (SA): (VDEh 1995), (G): (Gaskell 1992), (R): (Richardson 1974).

Properties	**Steel**	**Slag**	**O_2**
ρ (kg/m^3)	7.02×10^3 (O)	3.5×10^3 (O)	0.24 (G)
μ $(Pa\,s)$	6.0×10^{-3} (O)	8.7×10^{-2} (SA)	6.53×10^{-5} (G)
σ (N/m)	1.788 (R)	0.42 (SA)	

Table 4.5: Computational conditions and the symbols for BOF size modelling. Each condition was labelled with following scheme, s(**T**)eel or s(**L**)ag, (**H**)igh or (**L**)ow velocity and nozzle diameter(**1**, 9 cm) or (**2**, 3.81 cm).

	$u_0 = 340$ **m/s**	$u_0 = 480$ **m/s**	Lance height (m)
Steel	TL1	TH1	2 m
Slag	LL1	LH1	2 m
Steel	TL2	TH2	2 m
Slag	LL2	LH2	2 m

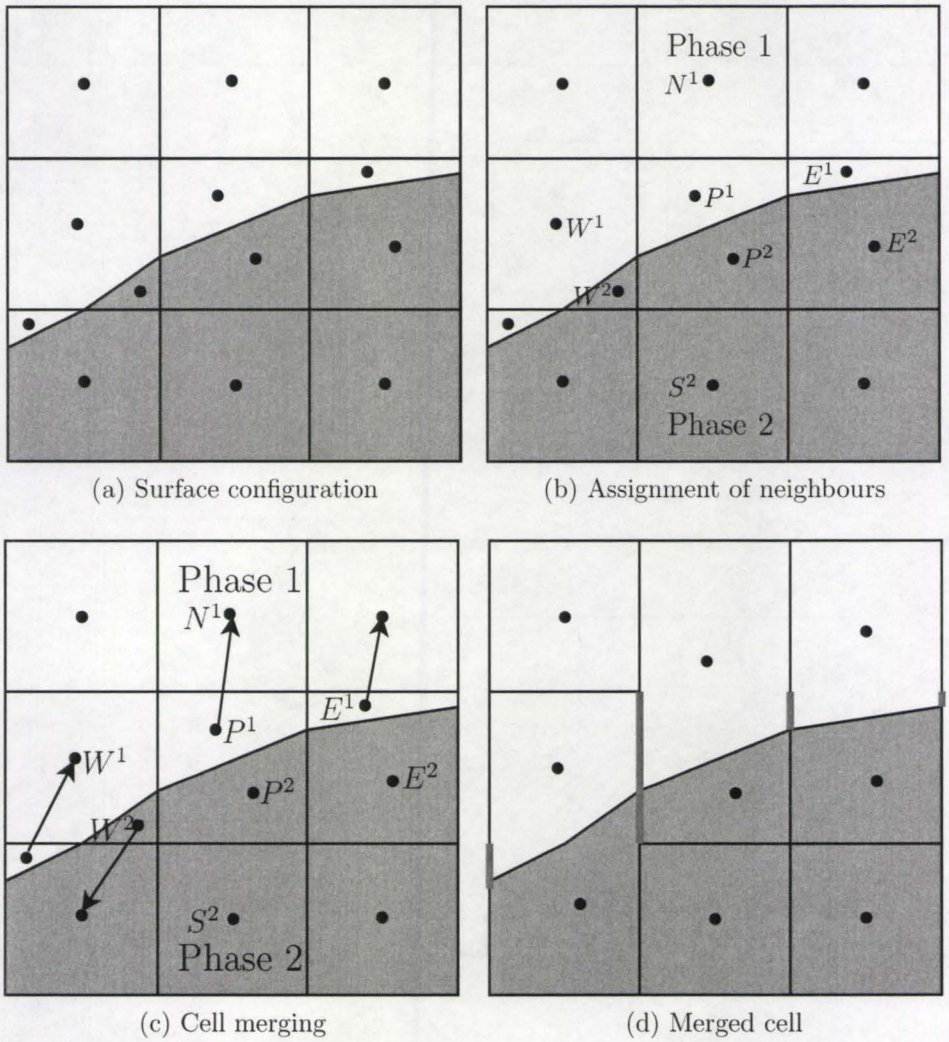

(a) Surface configuration

(b) Assignment of neighbours

(c) Cell merging

(d) Merged cell

Figure 4.1: Cartesian cut cell configuration and simple merging procedures and geometry changes

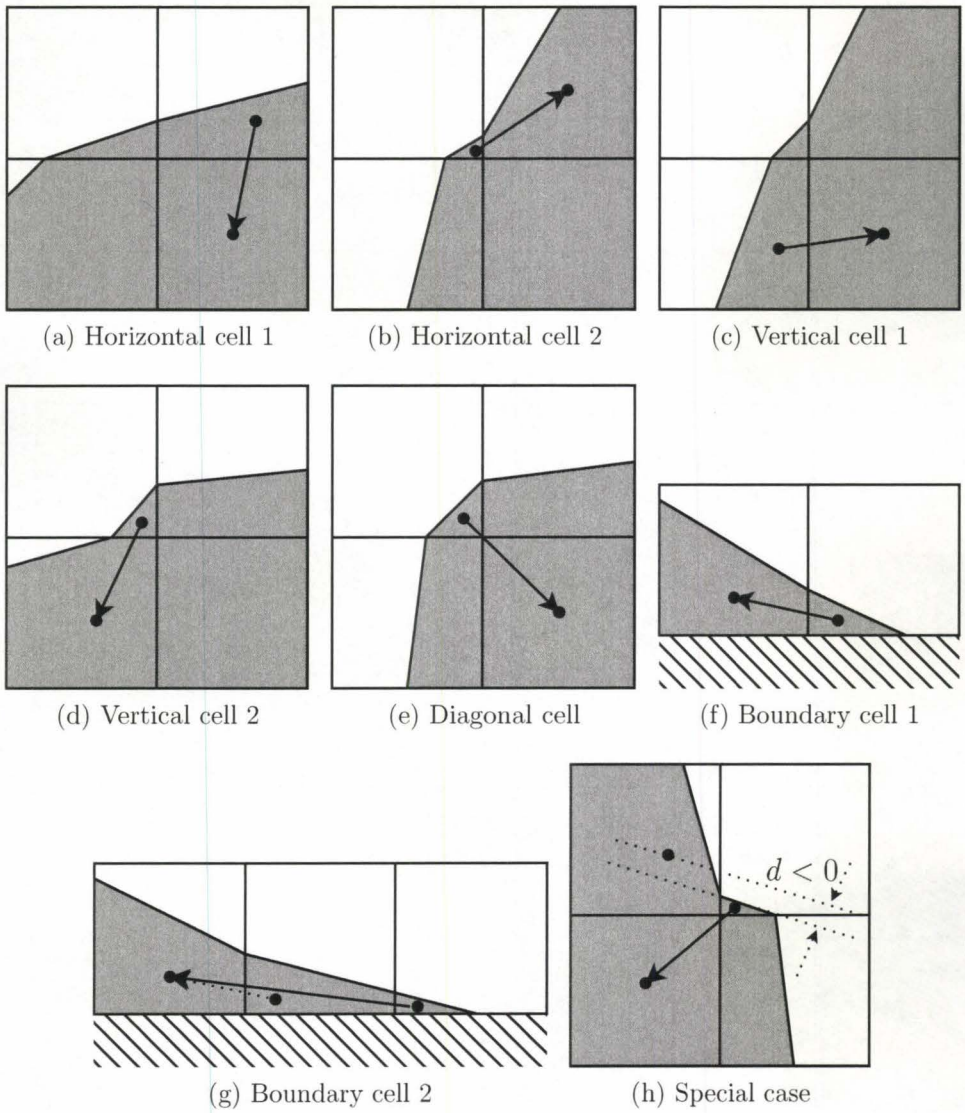

(a) Horizontal cell 1 (b) Horizontal cell 2 (c) Vertical cell 1

(d) Vertical cell 2 (e) Diagonal cell (f) Boundary cell 1

(g) Boundary cell 2 (h) Special case

Figure 4.2: Different cases for cell merging procedure, d in (h) is the distance from the surface to be merged and the sign is defined to be plus to the cell to be merged.

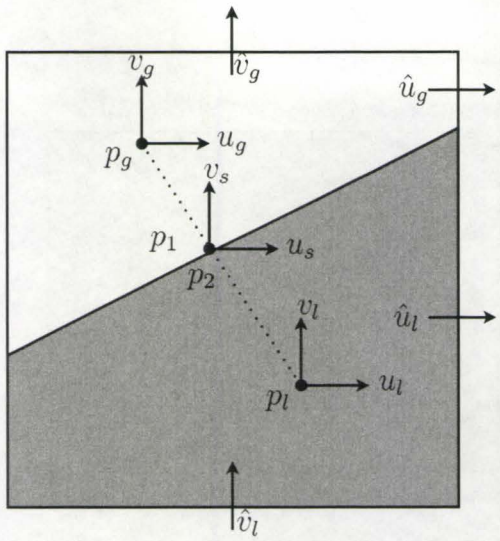

Figure 4.3: Collocated arrangement of momentum variables around the surface cells

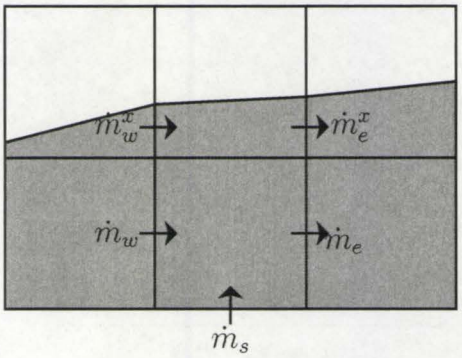

Figure 4.4: An Example of mass flux in cut cell configuration and this naming scheme can be applied to other variables

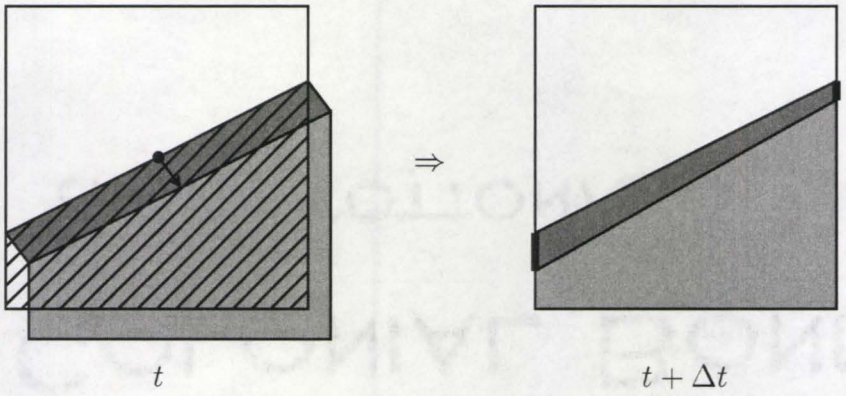

Figure 4.5: Mass Change in the surface cells. The surface normal direction contribution is largest in the mass change and the change in the wetted sides contribute to the distorted movement, but those are neglected in the computation.

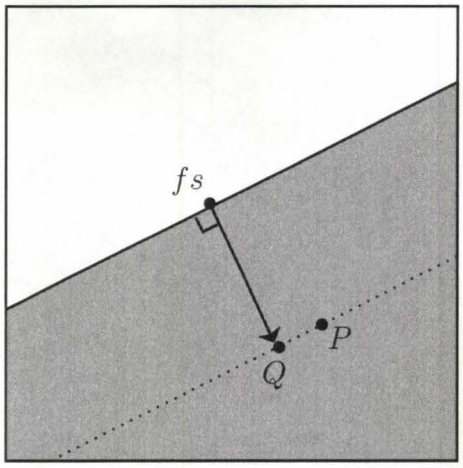

Figure 4.6: Second part of the pressure correction, due to the cell irregularity around the surface.

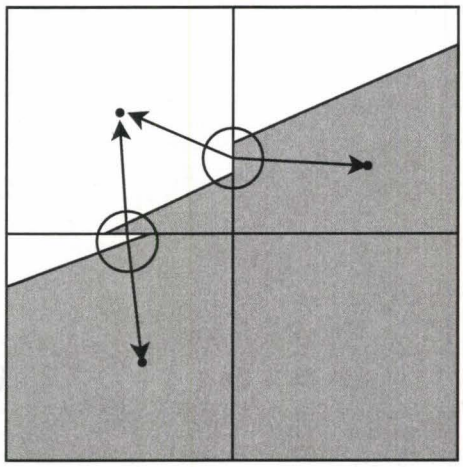

Figure 4.7: An example of a non-matching cell face of line construction. The circle shows the nonmatching face and the arrow indicates the cells to transfer this part information for each phase.

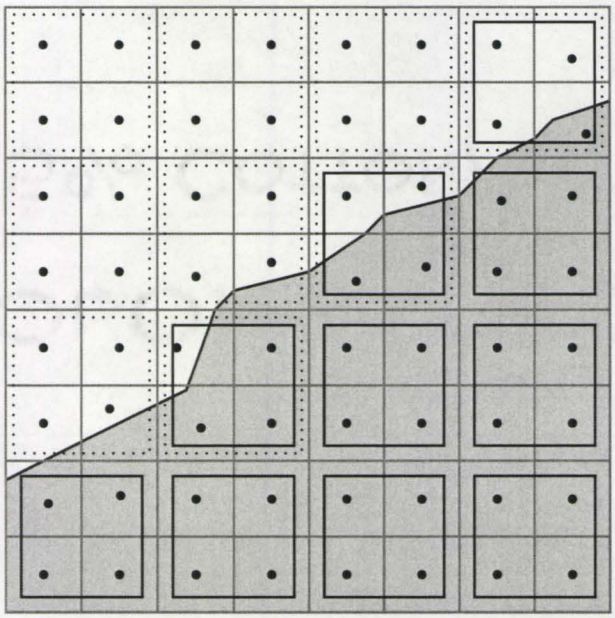

Figure 4.8: An example of the selection of coarser grid cells for each phase, the gas phase coarse grid was indicated with dotted lines (- - -) and liquid phase with solid lines(——)

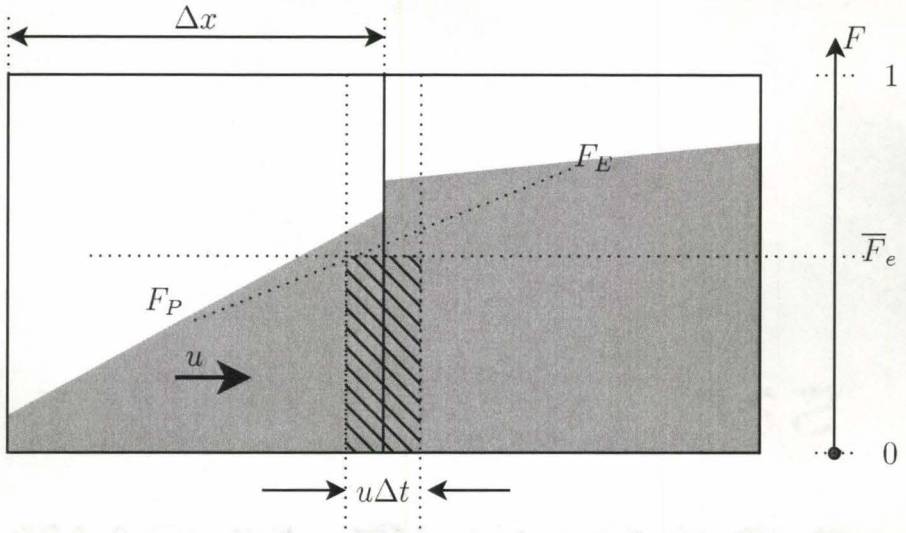

(a) Young's Advection

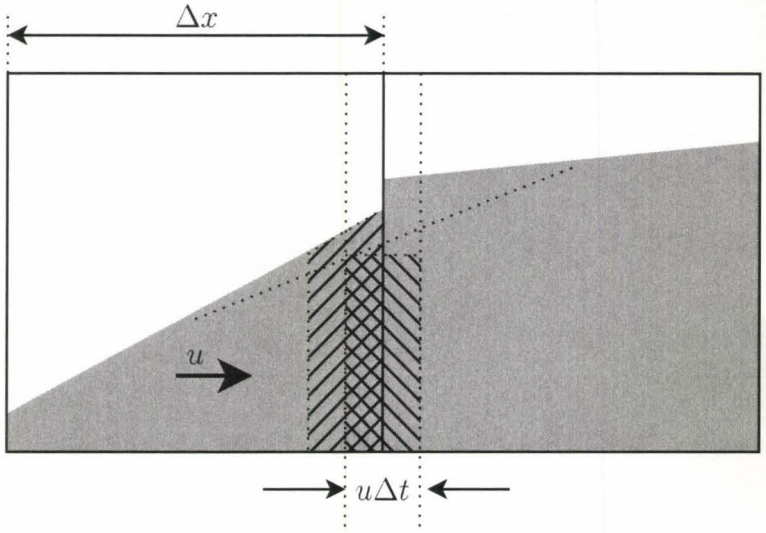

(b) Geometrical Error

Figure 4.9: Young's Method and its geometrical error, left hatched region must be advected to the right cell.

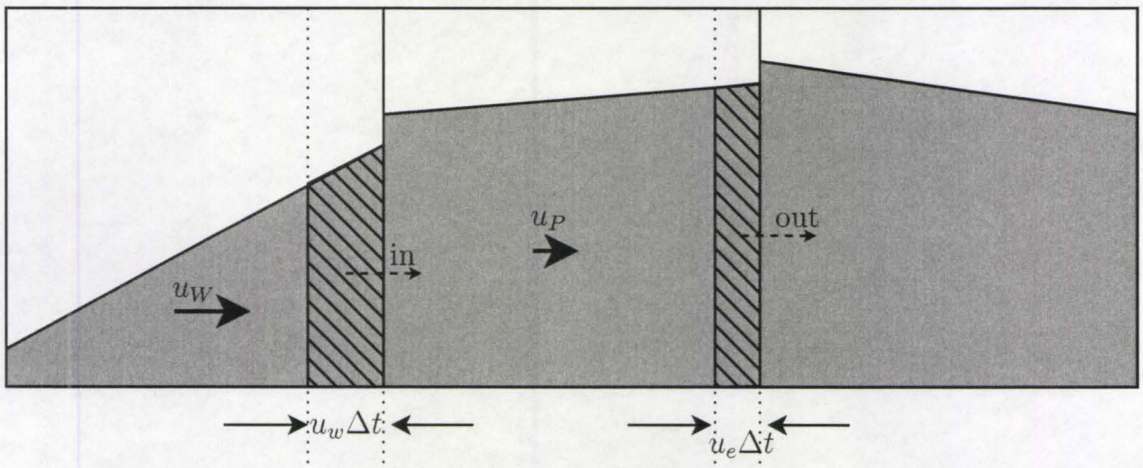

(a) Geometrical Flux

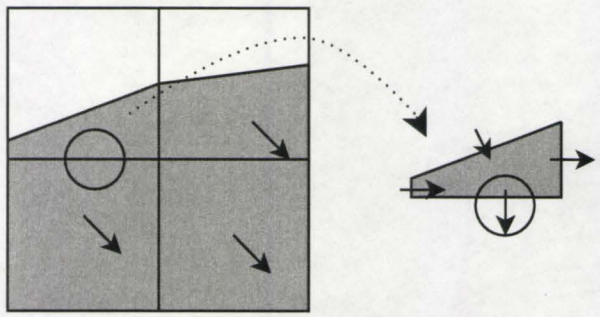

(b) Mass balancing velocity

Figure 4.10: Schematic diagram of volume flux computation and mass balancing velocity computation at the merged cell face.

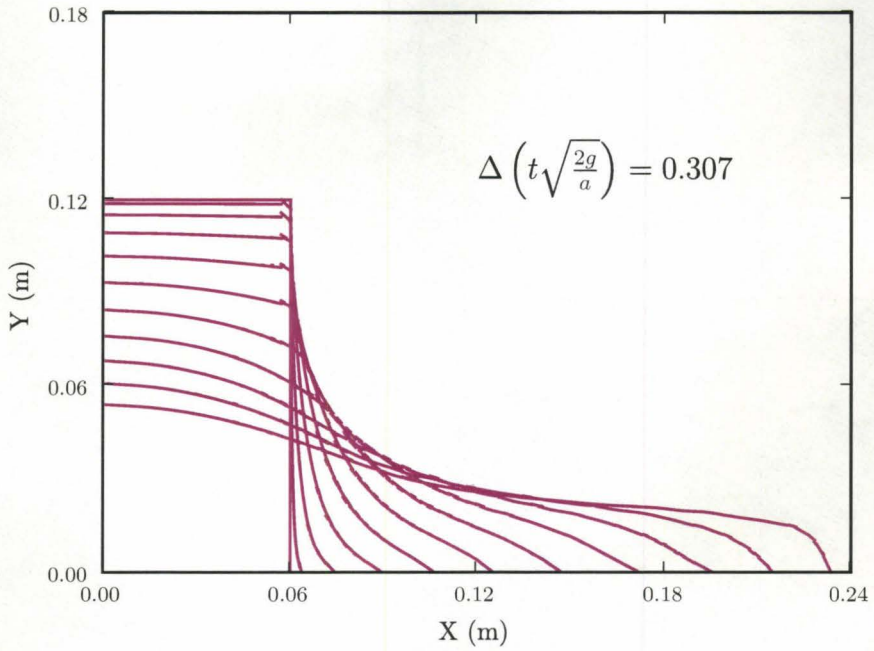

(a) $a = 6$ cm

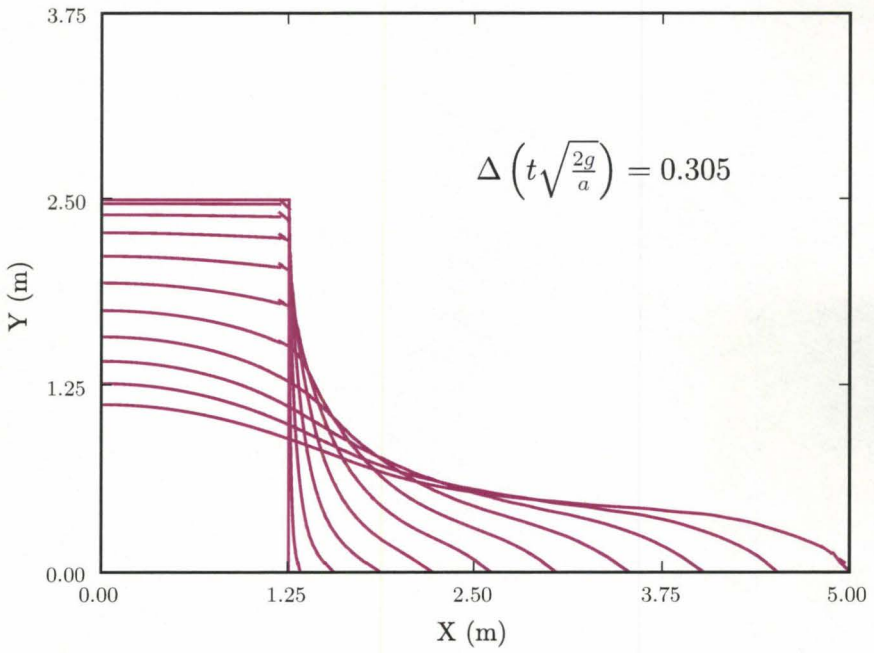

(b) $a = 1.25$ m

Figure 4.11: The free surface profile change with dimensionless time $\left(t\sqrt{\frac{2g}{a}}\right)$.

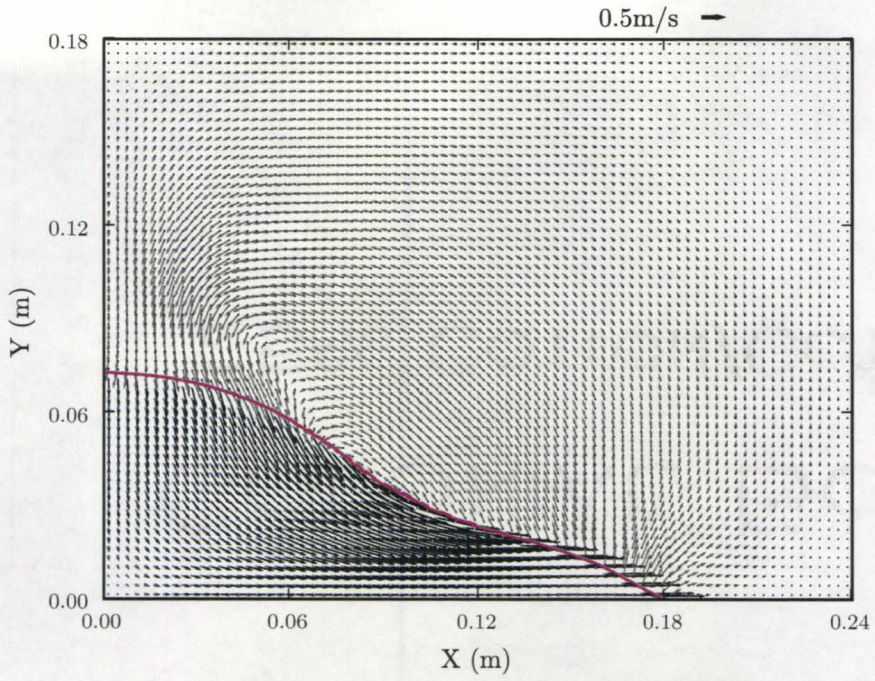

(a) $a = 6$ cm

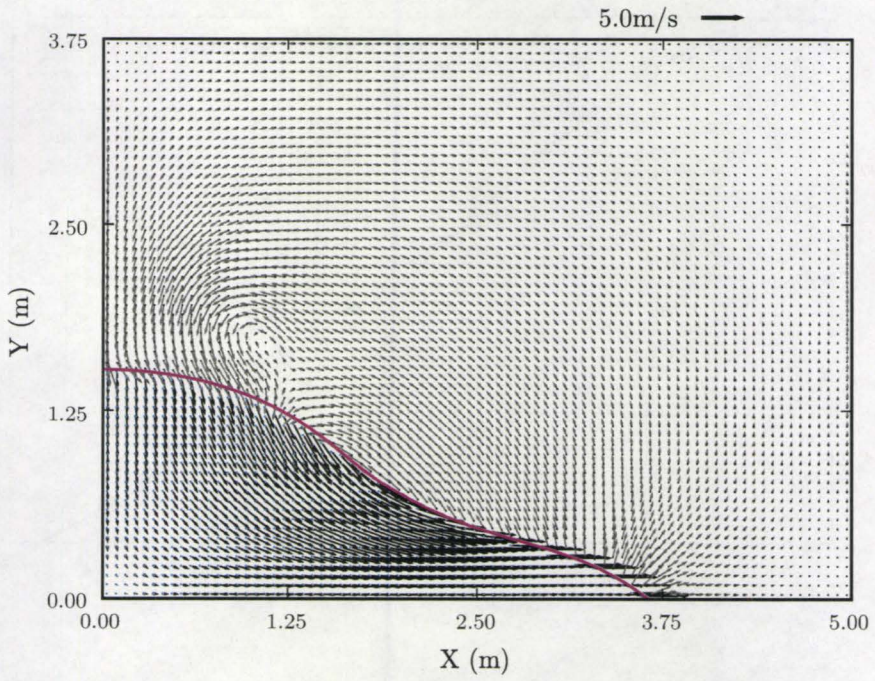

(b) $a = 1.25$ m

Figure 4.12: The velocity profile at the dimensionless time $\left(t\sqrt{\frac{2g}{a}}\right) \sim 2.22$.

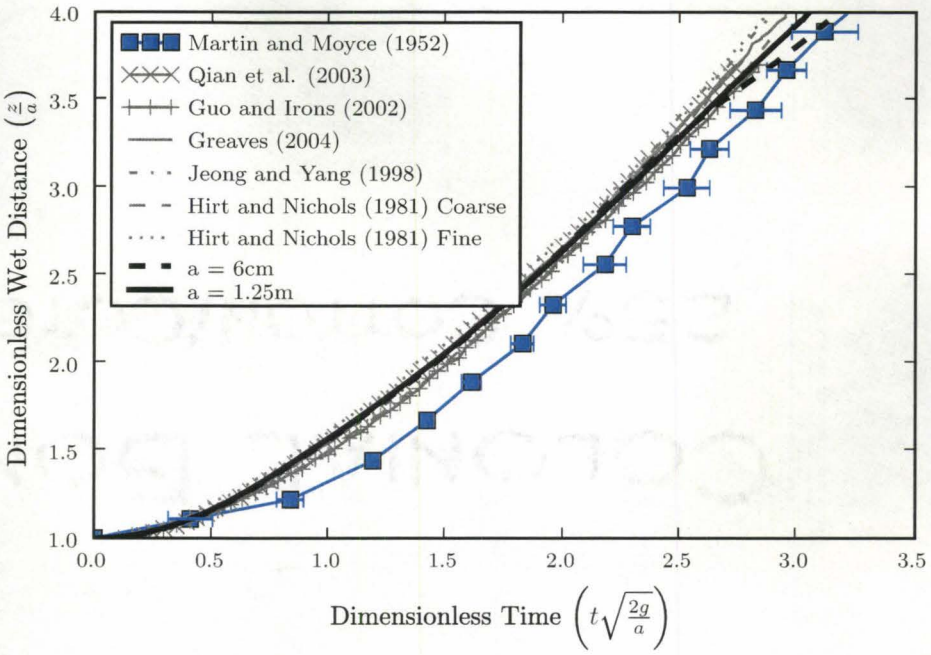

(a) Leading Edge

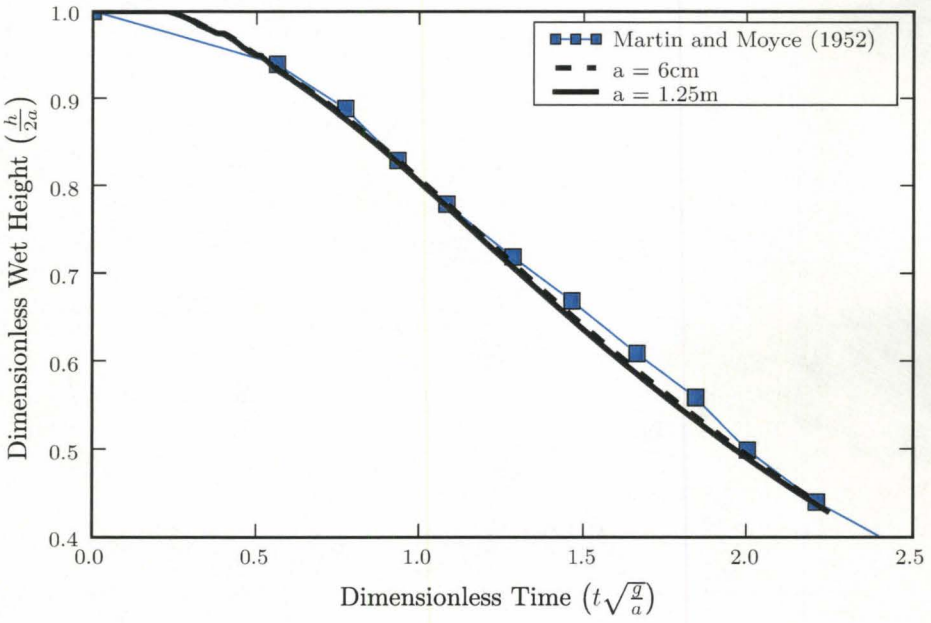

(b) Remaining Height

Figure 4.13: The comparison of dimensionless distance and time with Martin and Moyce (1952)'s experimental results and other computations. In (a) the error bar size is $\pm$ 1 standard deviation of Martin and Moyce's result.

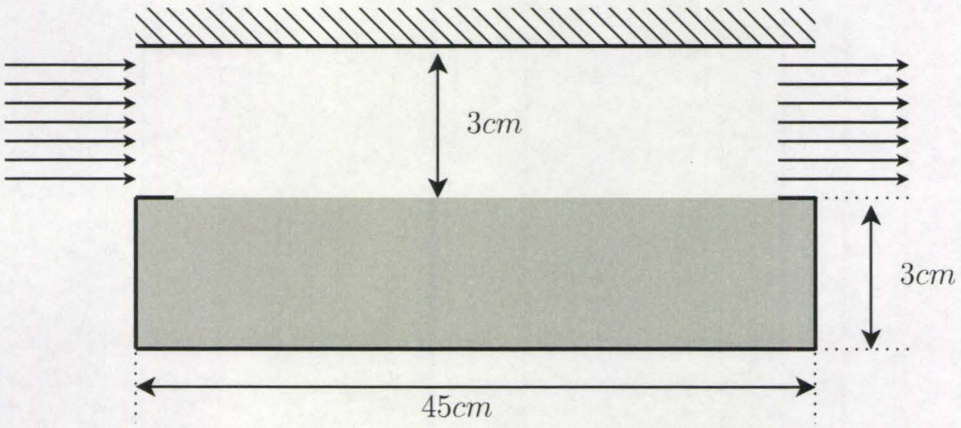

Figure 4.14: A simulation situation and the geometry of the wave generation test, Gas inlet condition was applied at the left side and pressure outlet condition was applied at the right side.

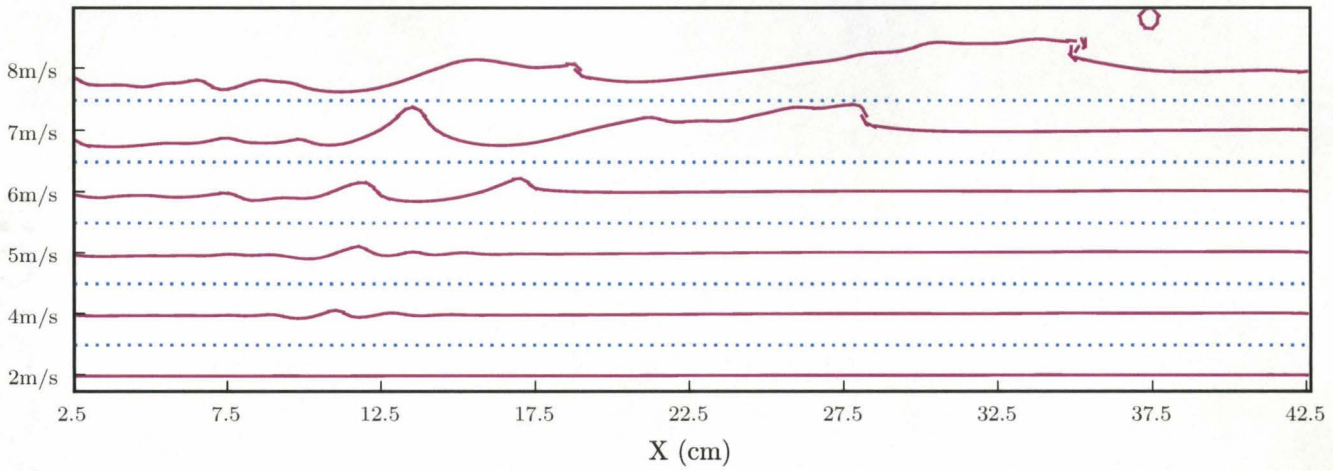

(a) $t = 0.52$s

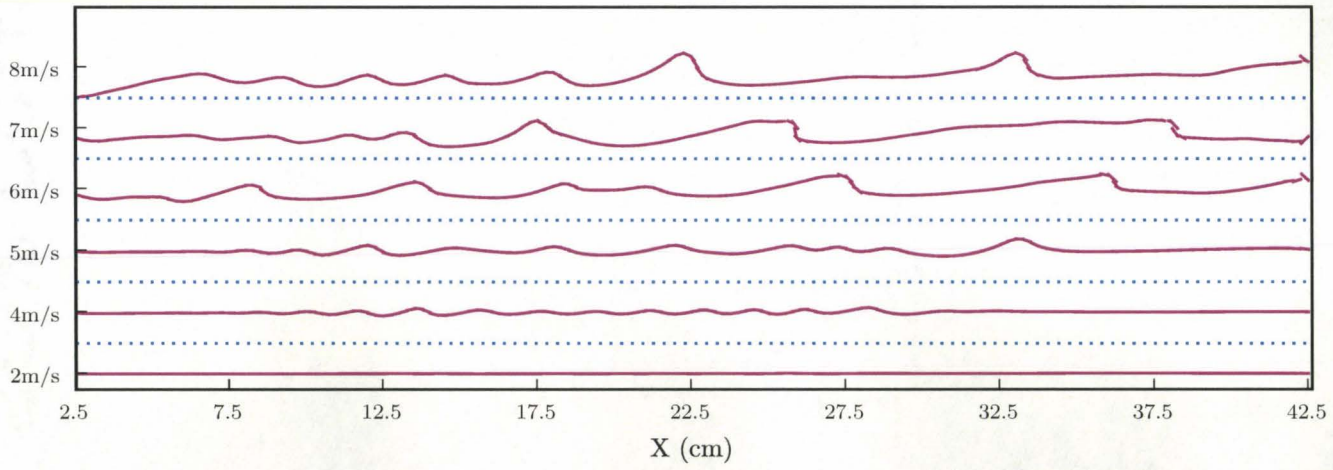

(b) $t = 1.6$s

Figure 4.15: A comparison of wave surface profiles at different time from the start of blowng wind. The x- and y-axis are scaled to the actual aspect ratio.

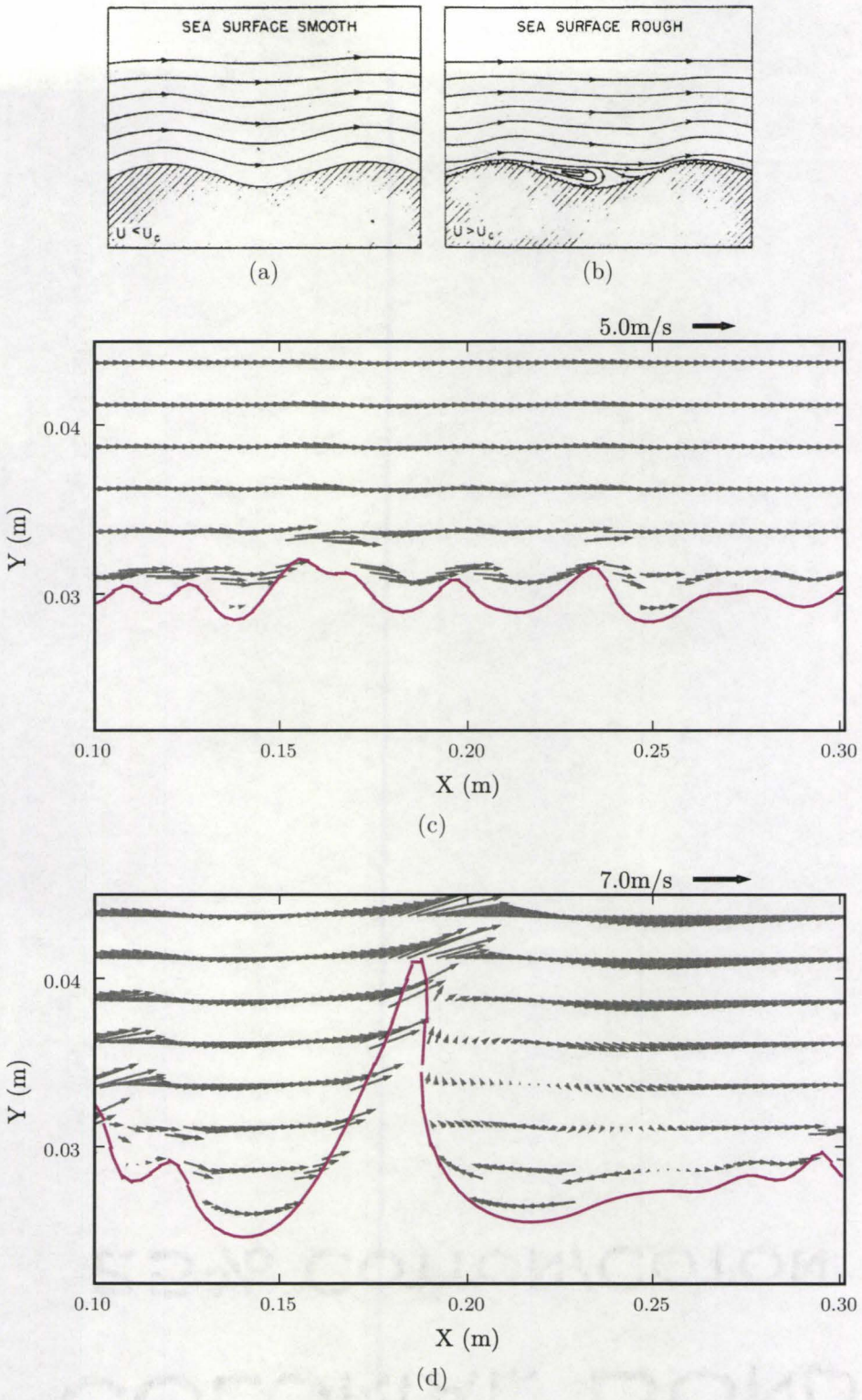

Figure 4.16: Comparison of Munk's assumption and example pictures of the current numerical test, (a) Smooth surface streamline, (b) Rough surface case, (c) Numerical test of wind speed 5 m/s case, (d) Numerical test of wind speed of 7 m/s case.

(a) 5 m/s

(b) 7 m/s

(c) 8 m/s

Figure 4.17: A comparison of wave surface profiles from the FLUENT^{TM} simulation at the simulation time 1.4 s. The surface line is the collection of the contour lines of 5 equal steps from 0 to 1 and bright to dark colour. The x- and y-axis are scaled to the actual aspect ratio.

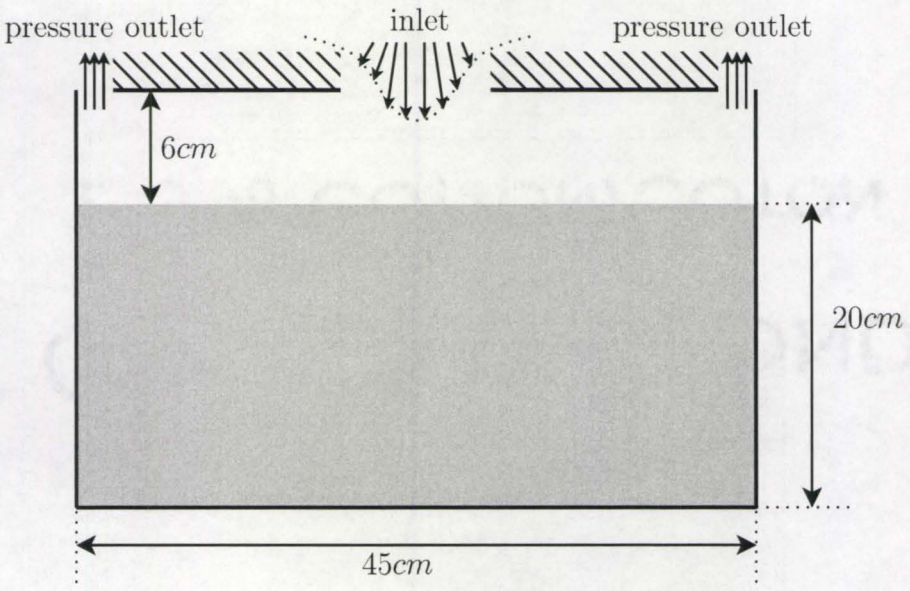

Figure 4.18: A schematic diagram of numerical grid setup.

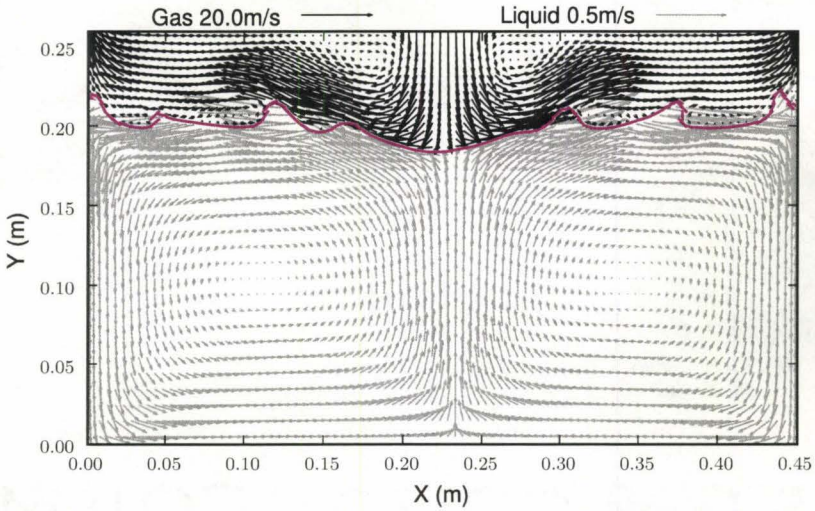

(a) 6 cm

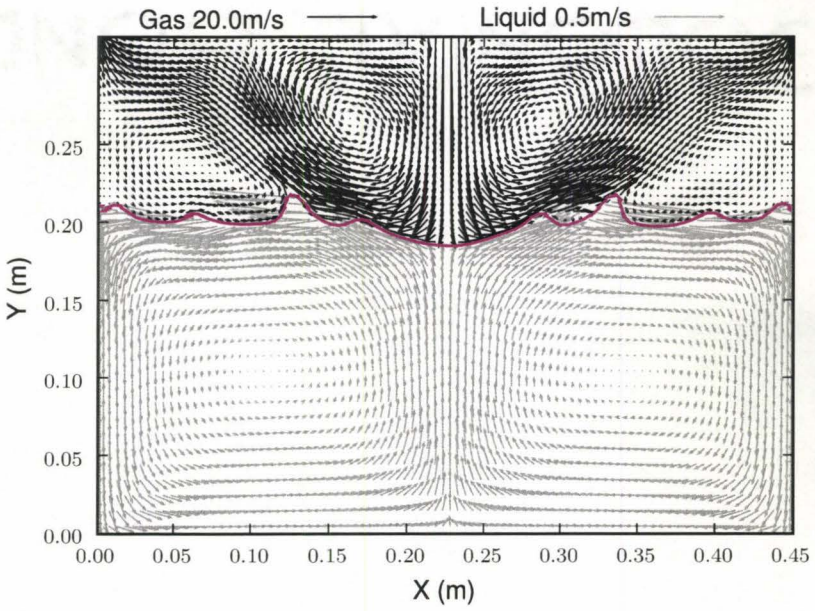

(b) 12 cm

Figure 4.19: Examples of the velocity field for two top boundary locations.

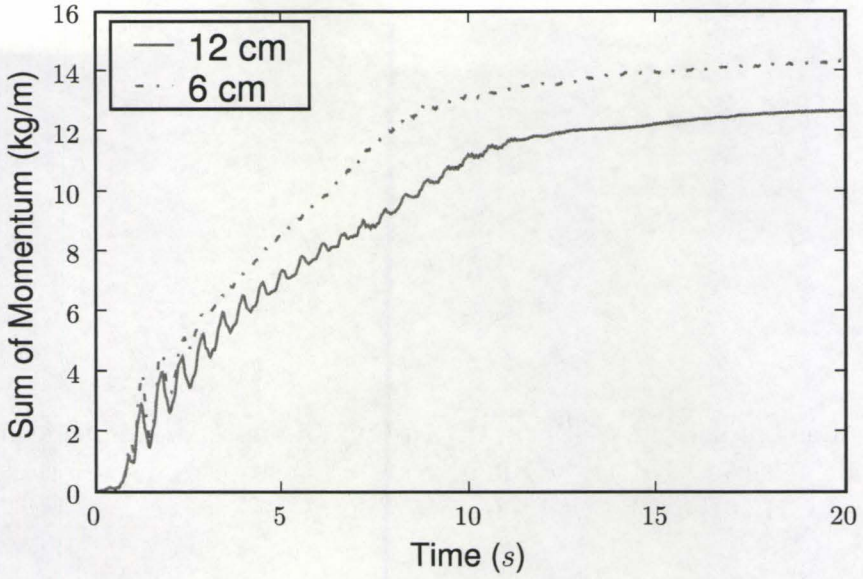

Figure 4.20: The momentum level change with time in short gas area and large gas area.

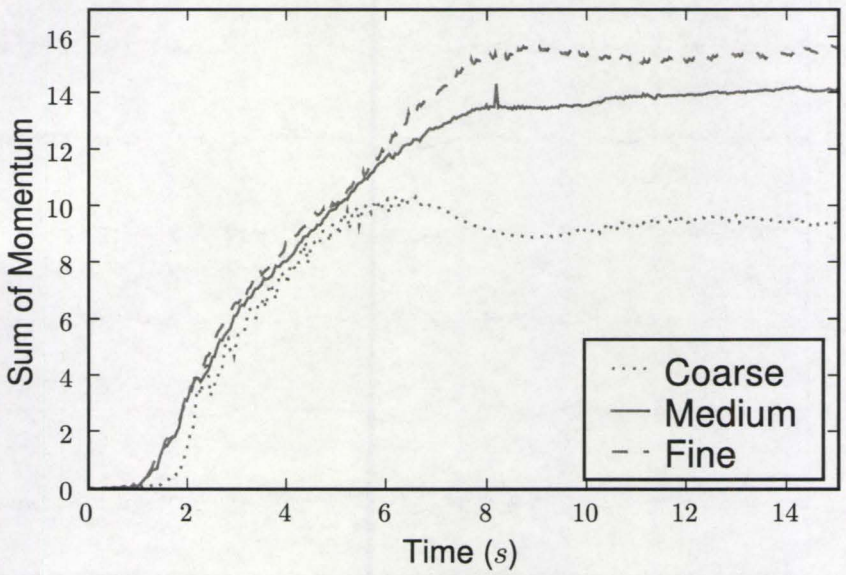

Figure 4.21: The Sum of liquid momentum over time for different grid size. For labels see Table 4.3

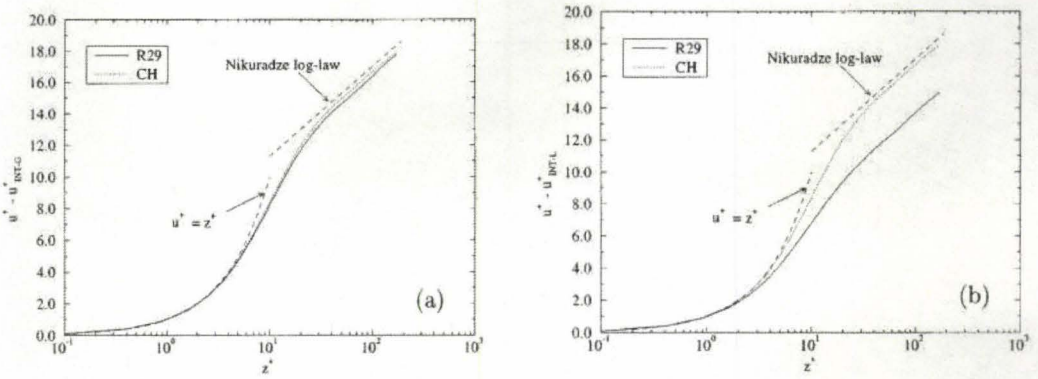

(a) Gas (b) Liquid

Figure 4.22: Lombardi et al.'s (1996) DNS result of gas and liquid mean velocity profile around the surface. **R** is the square root of density ratio, so 29 is close to an air/water case, **CH** is the solid wall reference state.

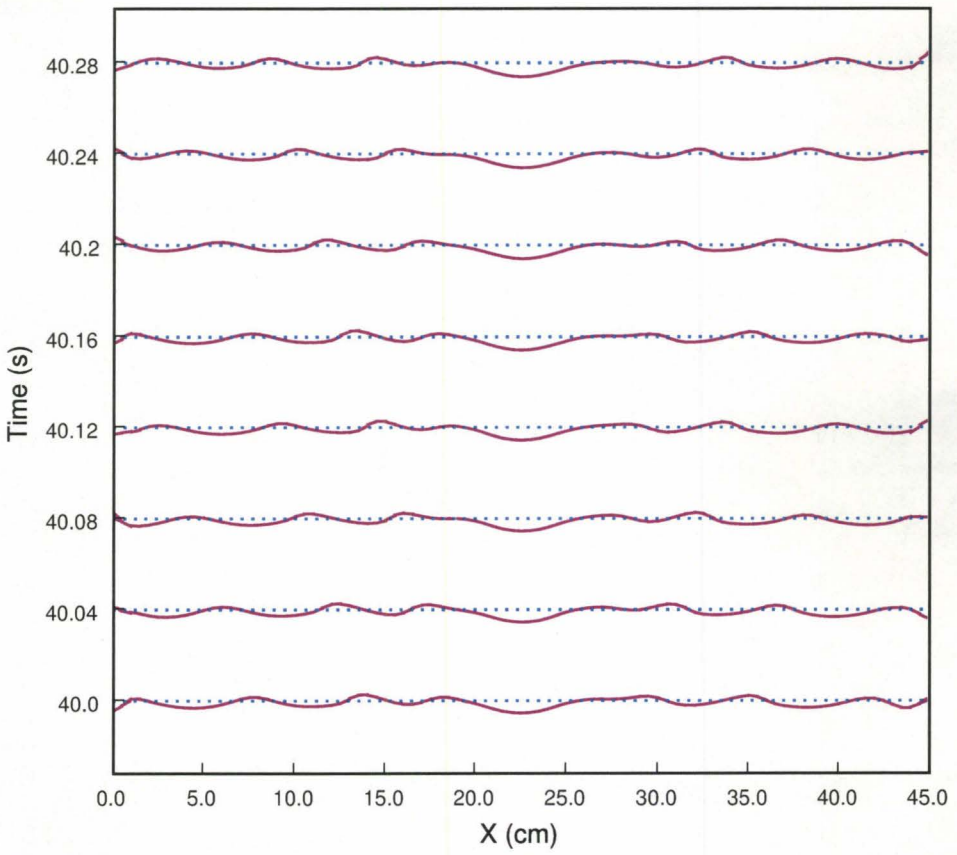

(a) 12 cm 20 SLPM

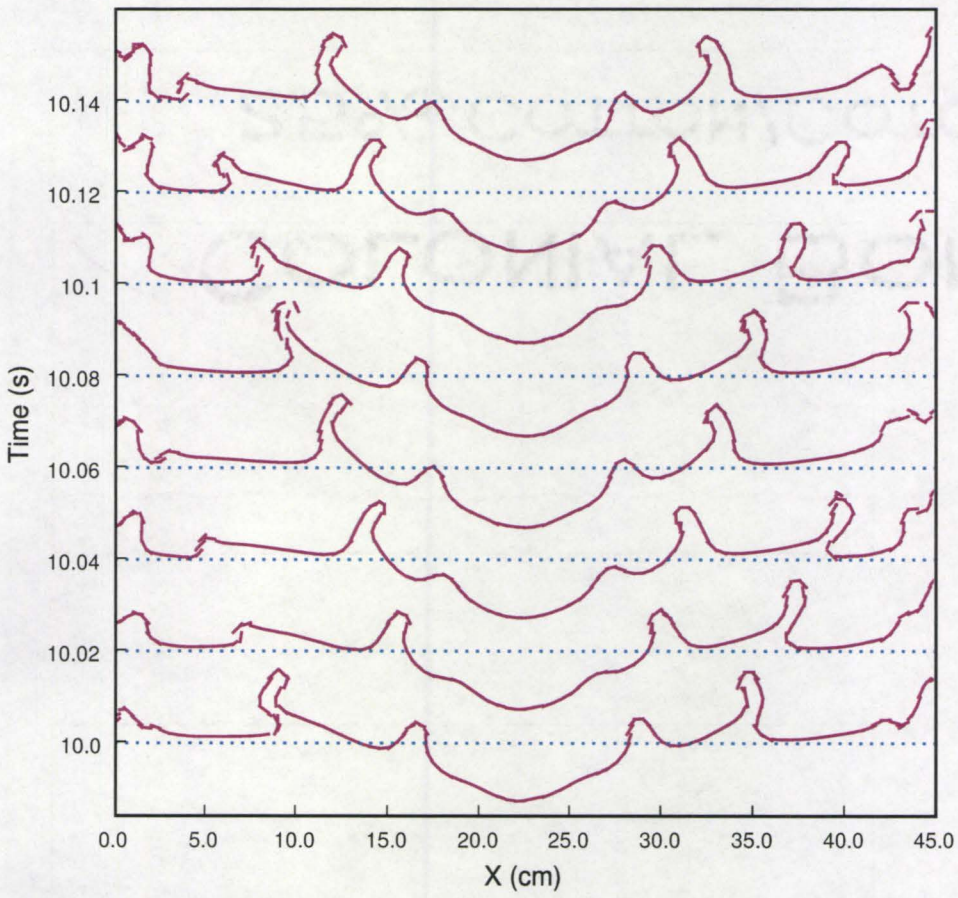

(b) 12 cm 50 SLPM

Figure 4.23: Surface profile change with time variation. (a) Δt is 0.04 s. (b) Δt is 0.02 s.

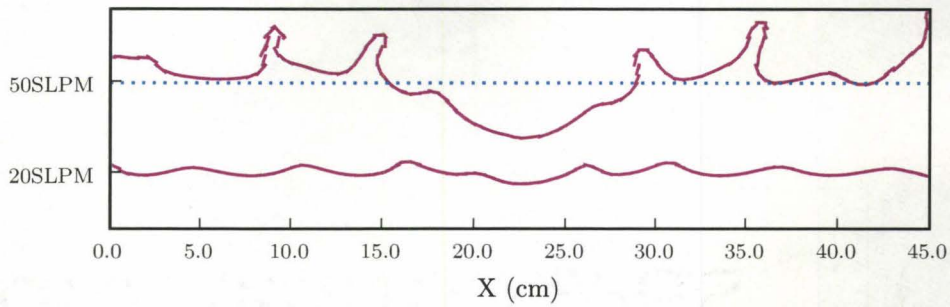

(a) 12cm

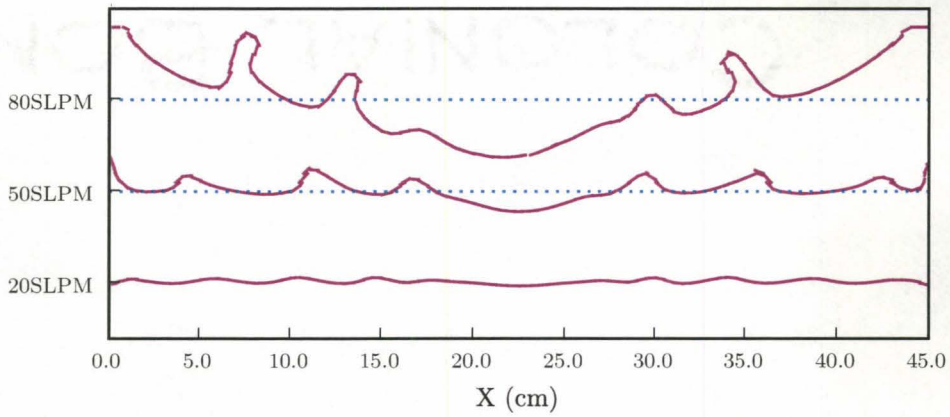

(b) 18cm

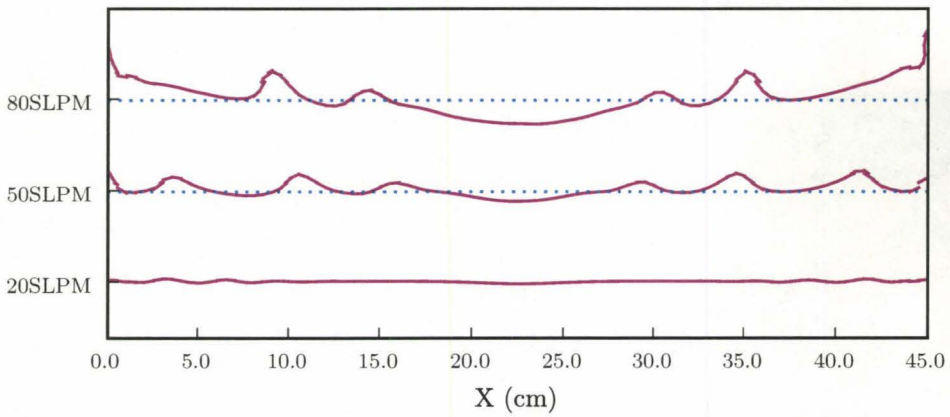

(c) 24cm

Figure 4.24: Surface profile change with changing lance height and flowrate at 10 s.

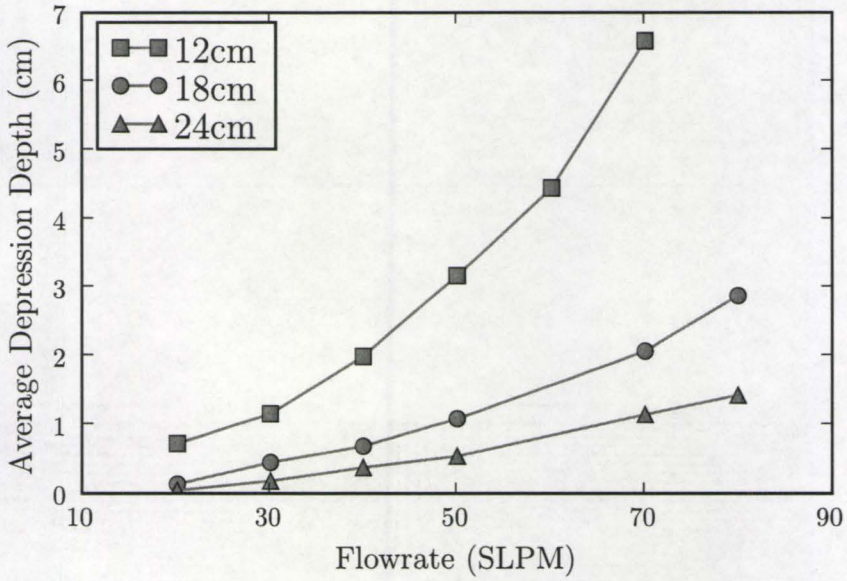

Figure 4.25: Simulated mean depth variation with changing lance height and flowrate.

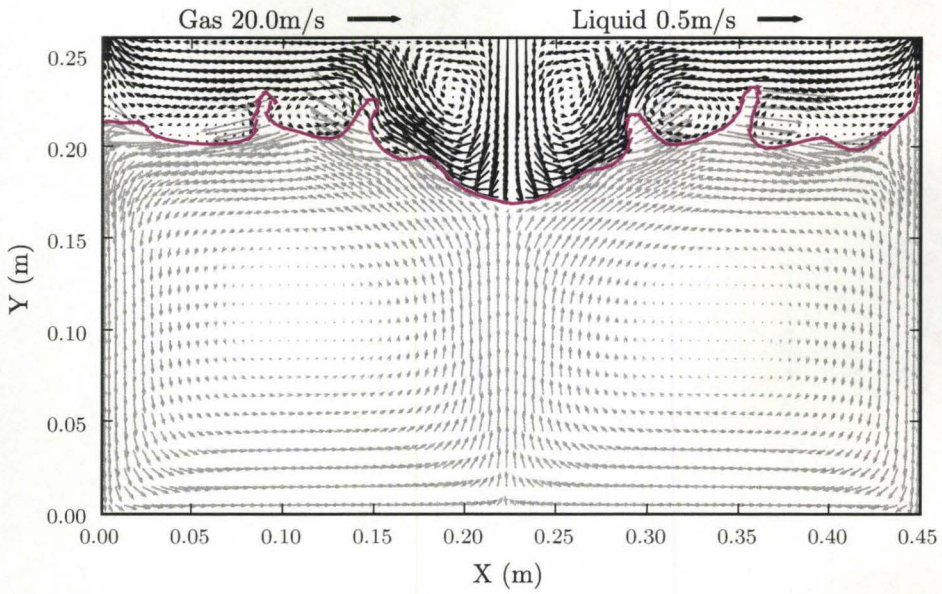

(a) 12cm 50 SLPM

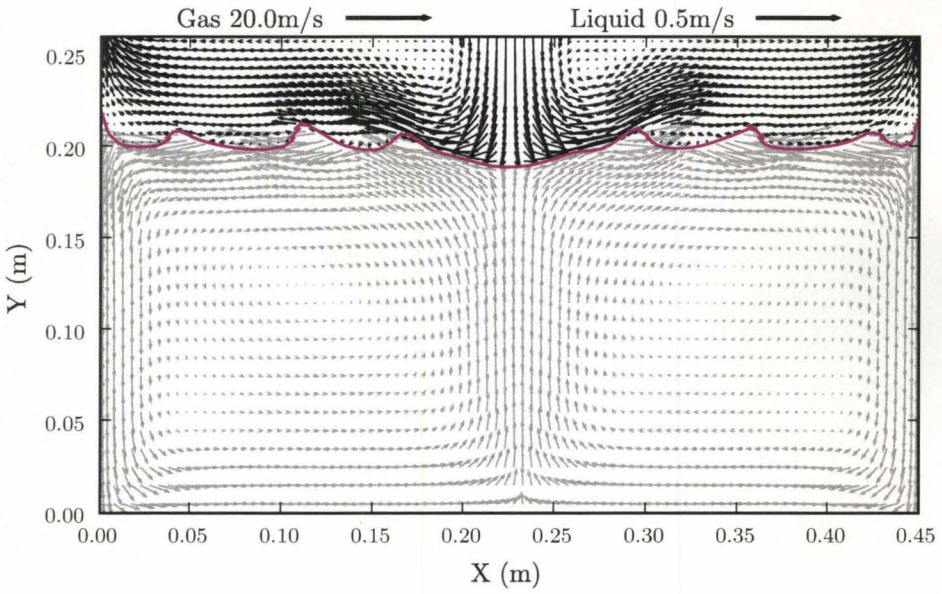

(b) 18cm 50 SLPM

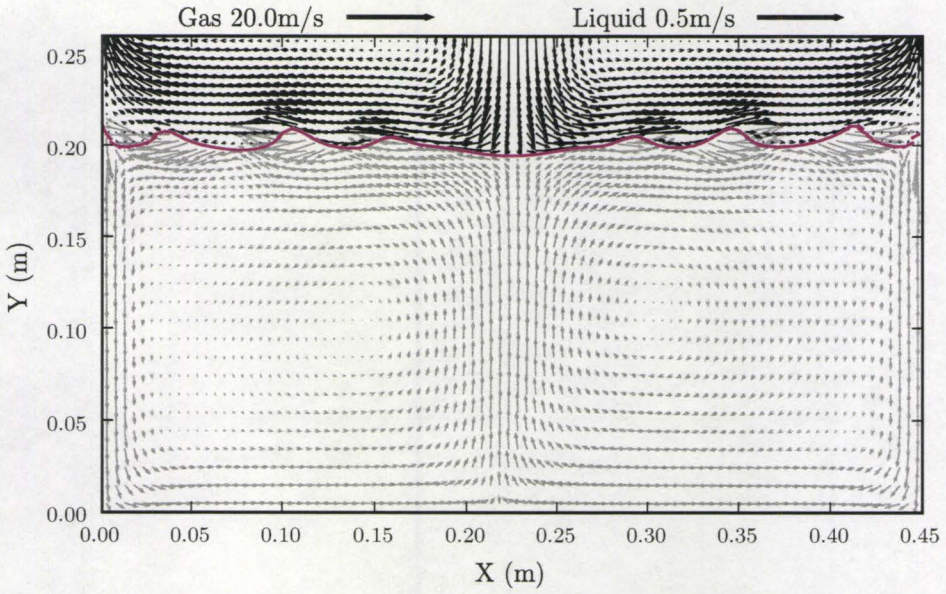

(c) 24cm 50 SLPM

Figure 4.26: Examples of velicity profile at 10 s. Gas and Liquid are scaled with different scaling factor and the scale is shown on the top of each figure.

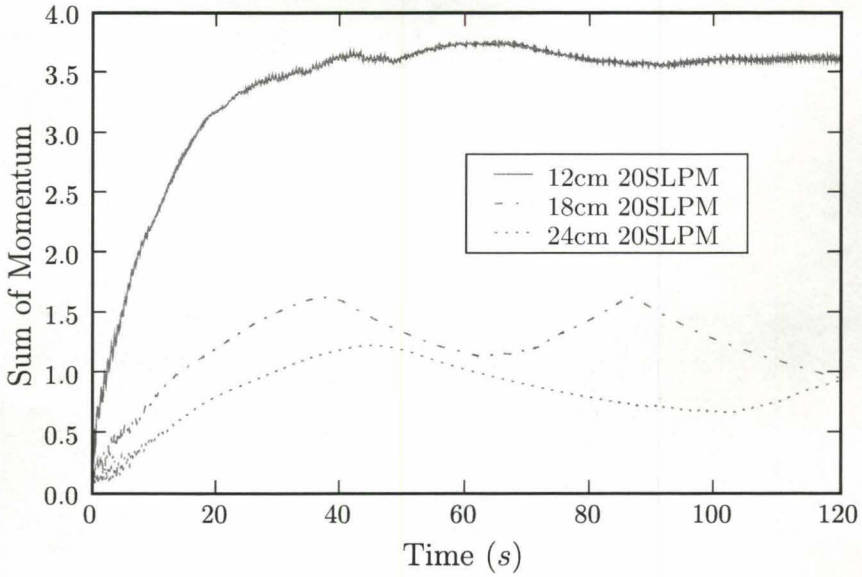

(a) 20 SLPM

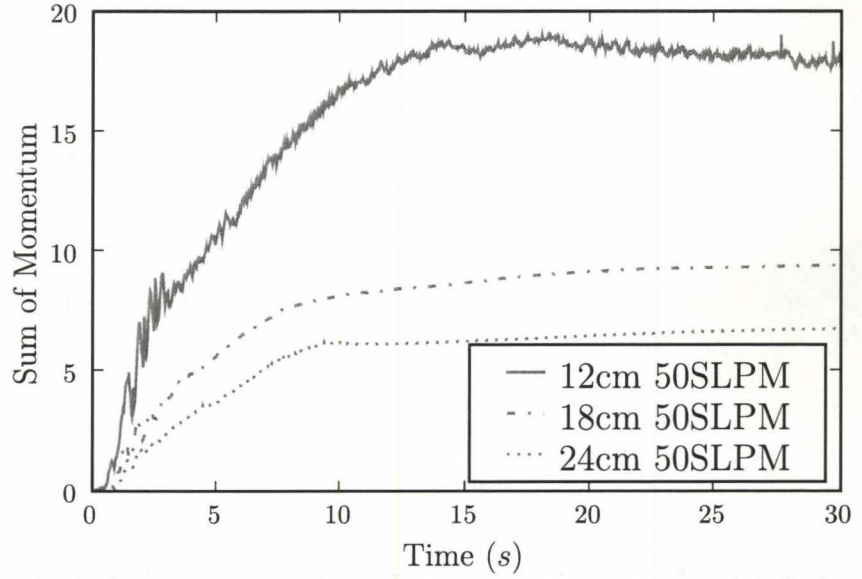

(b) 50 SLPM

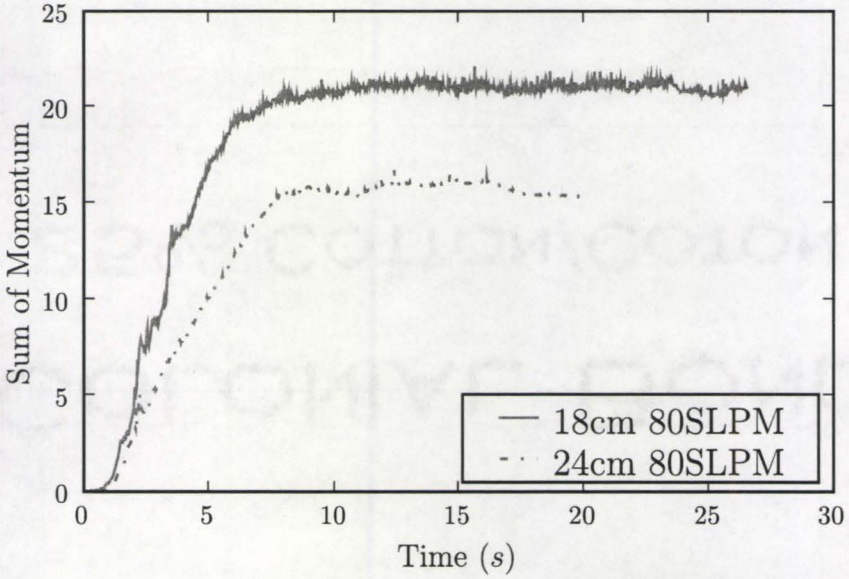

(c) 80 SLPM

Figure 4.27: Equilibrium time comparison for the same gas flowrate.

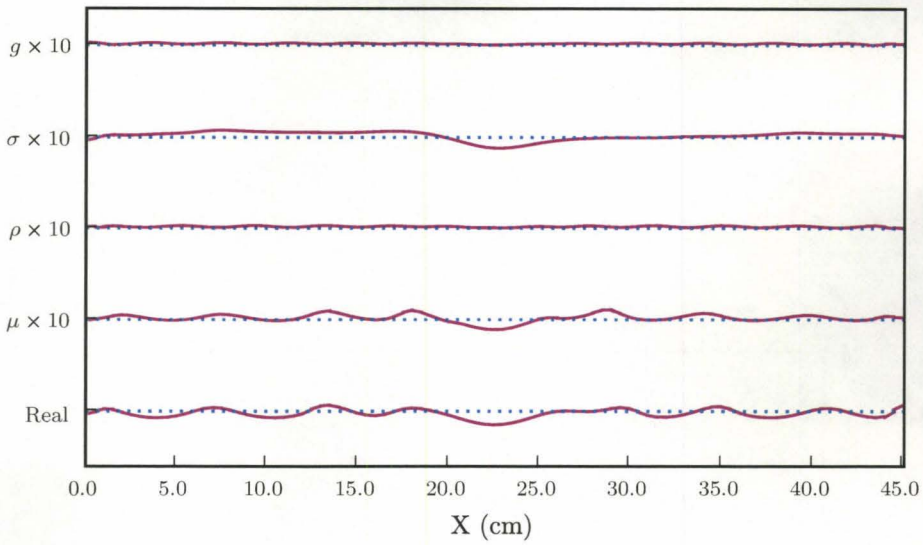

(a) 20 SLPM

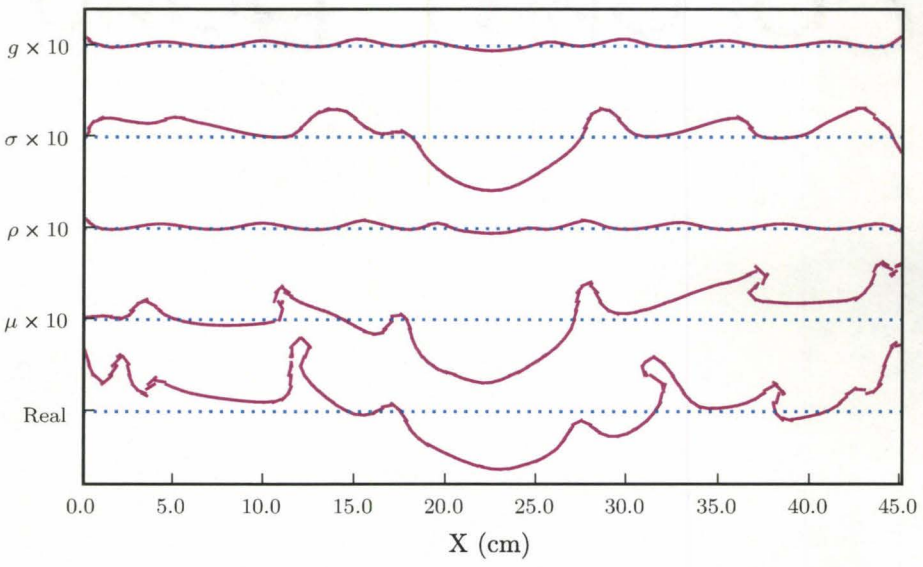

(b) 50 SLPM

Figure 4.28: Surface profile variation with the physical properties of liquid or gravity.

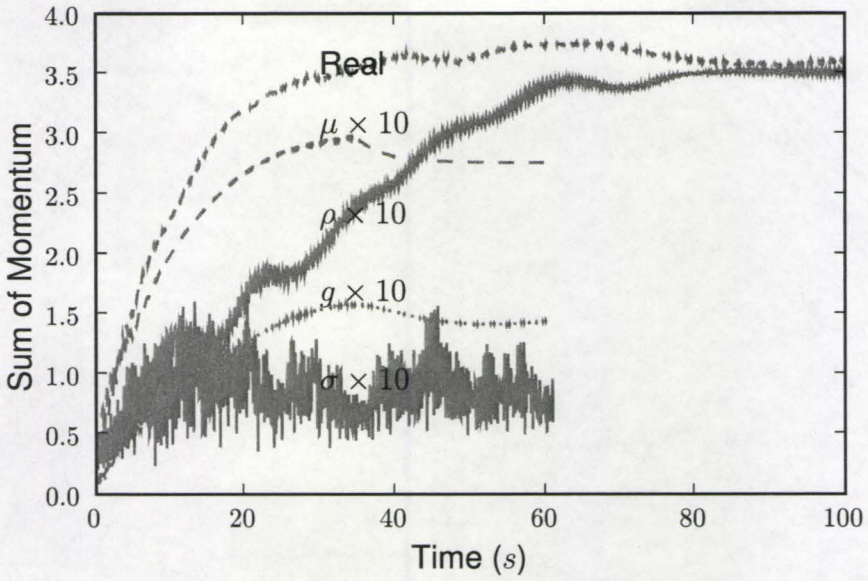

(a) 20 SLPM

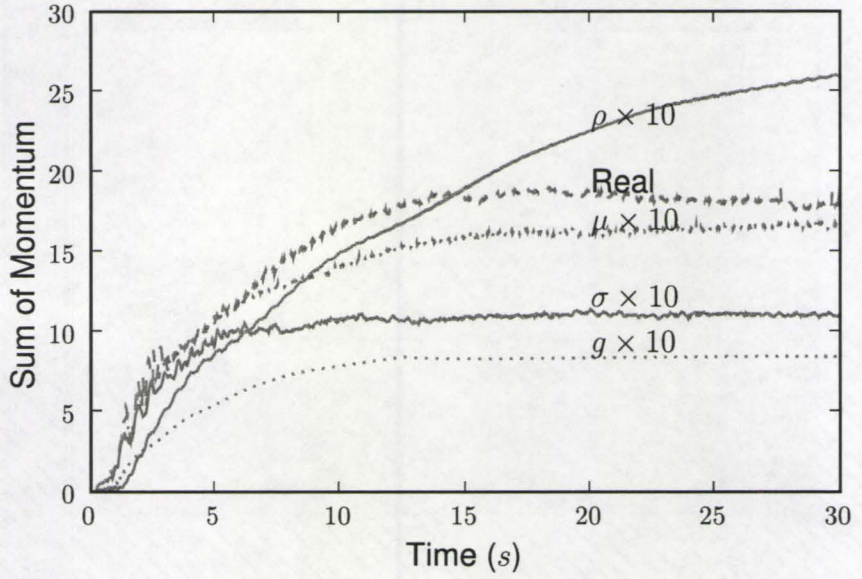

(b) 50 SLPM

Figure 4.29: The variations of sum of momentum in liquid phase with time for physical property variations.

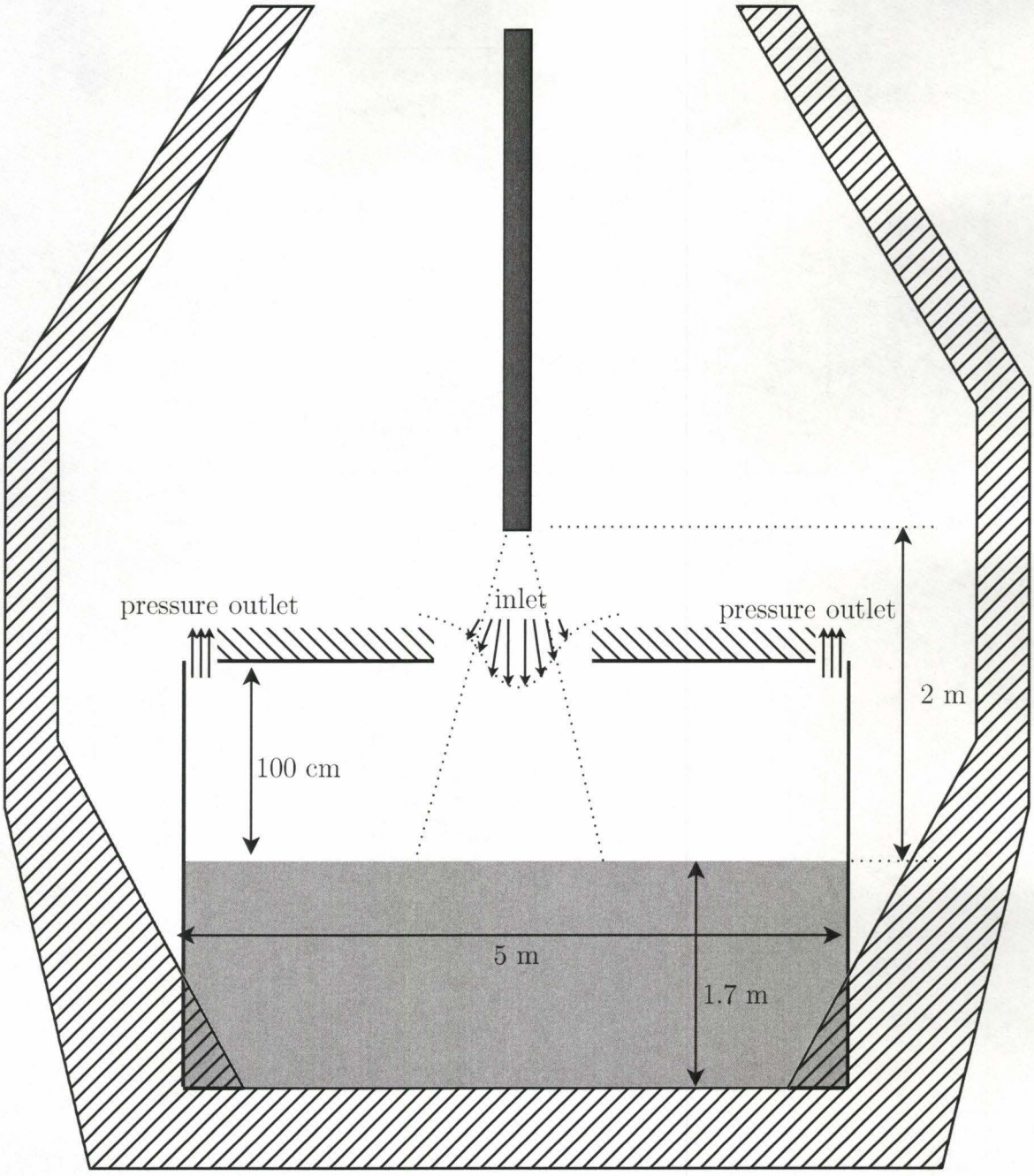

Figure 4.30: A schematic diagram of computational setup of BOF. Actual computation geometry is similar to air water case. The hatched area is the BOF dimension shown in Deo and Boom (1993).

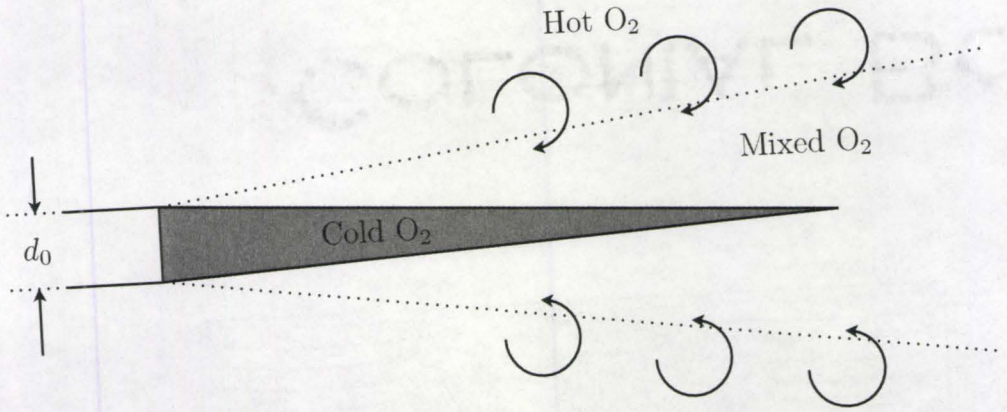

Figure 4.31: A schematic diagram of hot gas entrainment to the cold core gas in BOF situation.

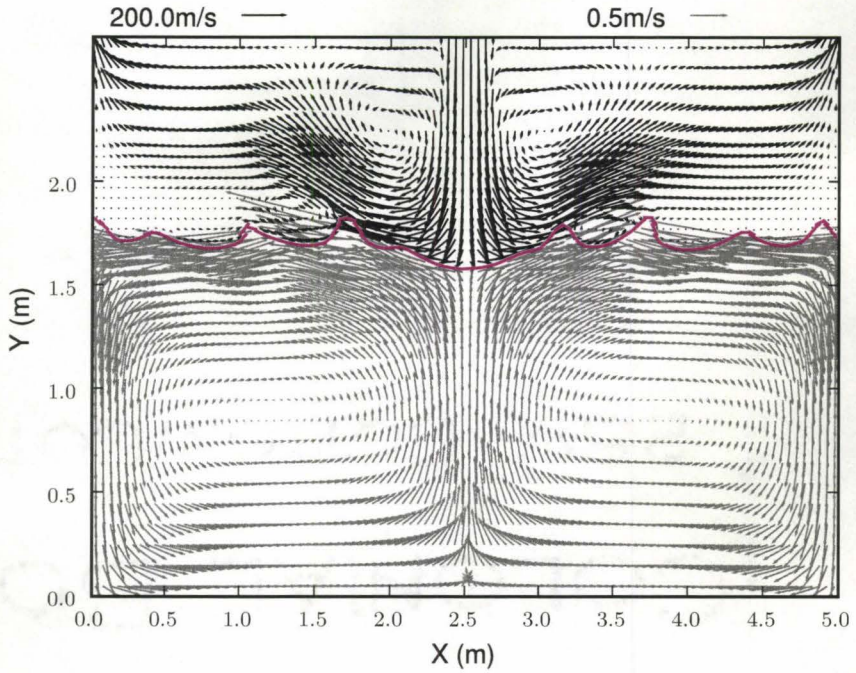

(a) TH1 case, Steel 480 m/s gas inlet velocity

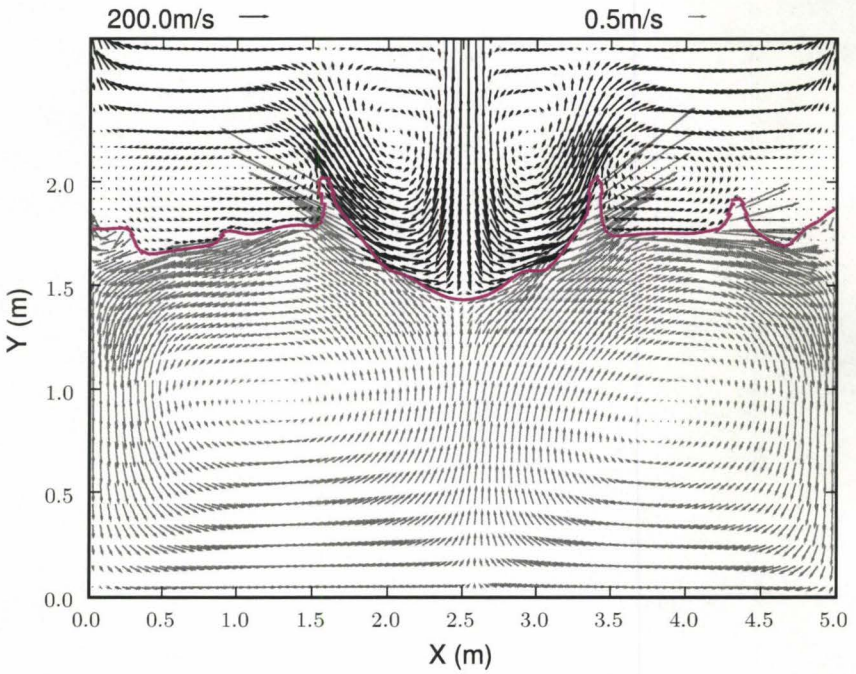

(b) LH1 case, Slag 480 m/s gas inlet velocity

Figure 4.32: Examples of surface profile and velocity fields of computation after reaching steady state, 60 s.

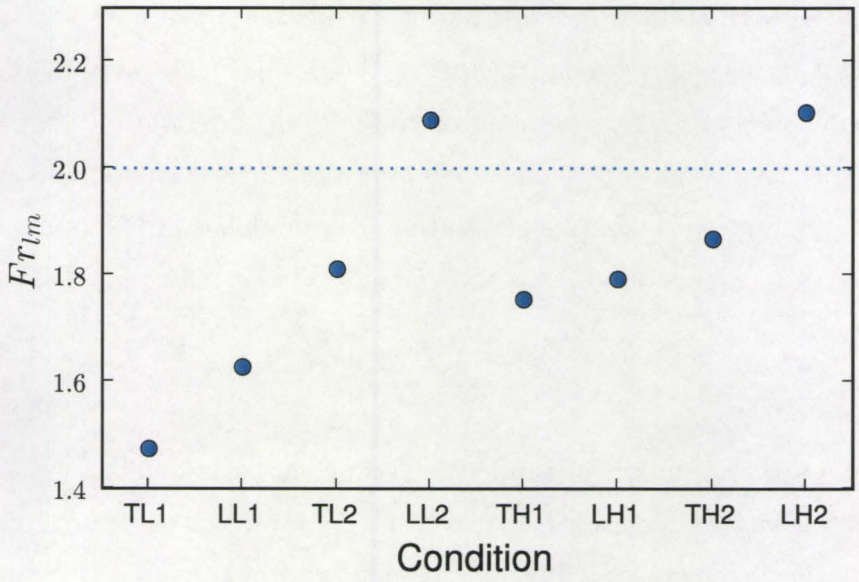

Figure 4.33: The modified local Froude number for each condition tested.

Chapter 5

Discussion

5.1 Dimensionless Number Relationships

The impact point velocity, the vertical impinging velocity at the stagnation point of the jet cavity, was obtained according to the calibration procedure (Section 3.2). As indicated by Banks and Chandrasekhara (1963) the local force balance at the stagnation point is the starting point of their theoretical derivation for the dimensionless analysis. The local force balance between the vertical kinetic energy and the potential energy (Equation (2.4)), leads to the local modified Froude number

$$\mathrm{Fr}_{\mathrm{lm}} = \frac{\rho_g u_g^2}{\rho_l g n_0} = 2.0 \tag{5.1}$$

Figure 5.1 shows the variation of the local modified Froude number with the computed impact velocity. There is some scatter of the data, but the scatter diminishes as the impact velocity increases. Beyond the penetration stage the decrease in variation is clear and that means the vertical force balance becomes more dominant in this physical system. Molloy's (1970) criteria for transitions between the three stages—Dimpling, Splashing and Penetrating, were 15 m/s for splashing and 75 m/s for penetrating for air and water. The discrepancy between Molloy and this study in Figure 5.1 comes from the difference in the computation of the impact point velocity. Molloy used the initial nozzle to undisturbed liquid surface distance, but this study used the actual distance from the nozzle exit to the depressed liquid surface point. With these criteria the Dimpling to Splashing change occurs around the impact velocity of 13 m/s, Splashing to Penetrating change occurs around 28 m/s.

Qian et al. (1996) defined a new parameter (F_q in Equation (2.7)) to determine a functional behaviour of the dimensionless number and the dimensionless distance

(Section 2.2.2). At higher flowrate and deeper penetration, F_q increases quadratically with dimensionless distance which was defined as $\frac{h+n_0}{d_0}$. The fitted equation was

$$F_q = 0.024\left(\frac{h+n_0}{d_0}\right)^2 + 0.0072\left(\frac{h+n_0}{d_0}\right) + 0.84 \tag{5.2}$$

Figure 5.2 shows the Equation (5.2) and the experimental results of this study. Qian et al.'s measurements were up to around $(n_0+h)/d_0 = 50$. The present experiments and the equation matches well up to $(n_0+h)/d_0 = 40$. However, for higher flowrates experimental results deviated from the Qian et al.'s formula. Therefore a new regression formula, which fits the data better as shown in Figure 5.2, was obtained.

$$F_q = 0.0358\left(\frac{h+n_0}{d_0}\right)^2 + 0.353\left(\frac{h+n_0}{d_0}\right) - 22.615 \qquad \text{rms} = 3.17 \tag{5.3}$$

Banks and Chandrasekhara (1963) derived a dimensionless relationship as reviewed in Section 2.2.2. Figure 5.3 shows the plot of the width to depth ratio and dimensionless momentum parameter. The slope changes according to the assumed cavity shape. Banks and Chandrasekhara's equations are compared with the present data. Present cavity width to depth ratio is closer to a parabolic shape. Contrary to Turkdogan (1966) and Cheslak et al. (1969), the cavity width was affected by the jet momentum.

5.2 Splashing and Critical Depth

As discussed in the Section 2.3.3, a Blowing number of unity corresponds to the onset of the Kelvin-Helmholtz instability to produce droplets. The ratio of the tangential velocity to the axial velocity, η has been taken as 0.447 based on solid flat plates (Subagyo et al. 2003); it has not been determined for fluid surfaces. Multiplying this value by the vertical velocity for splashing in the present work, 13 m/s, produces 5.81 m/s for the critical tangential velocity. This value is much closer to the critical velocity from the Kelvin-Helmholtz theory accounting for the viscosity of water, 5.75 m/s (Funda and Joseph 2001) than the value for inviscid ones, 6.50 m/s (Chandrasekhar 1961). Therefore, even with some discrepancy in the deflection velocity, the Blowing number can be used as the criterion for how many times the critical Kelvin-Helmholtz instability has been exceeded, as originally proposed (Subagyo et al. 2003).

The onset of splashing is difficult to determine since there is a distribution of droplet sizes. Very small droplets were generated around the waves even at very low flowrate; this was found when a paper tissue became wet when held near the interface, even though droplets could not be seen by eye. Therefore, the onset of splashing was determined when the surface starts to eject some visible drops (3 to 5 mm) around the perimeter of the cavity. The flowrate for the onset of splashing was summarized in Table 3.4. Figure 5.4 shows that splashing begins when the Blowing number is approximately 0.7 to 0.9.

At higher flowrates the jet penetrated into the liquid surface and bubbles were entrained into the water. This penetration was only observed in 6 cm lance height case above 60 SLPM flow rate. In the analysis of He and Standish (1990), a sharp increase of droplet generation rate occurred around the nominal Weber number of 40; this corresponds to Molloy's penetration regime. The Blowing number is around 4 when the impact velocity of 28 m/s (Penetration criterion). Molloy (1970) indicated that splashing is reduced in the penetrating regime. That finding was explained with the present observations in that the generated splash may not be able to escape a deep cavity, but larger wave generation by penetration and corresponding bubble entrainment around the jet cavity may contribute to the generation of splash by this different mechanism.

The critical depression depth (cavity depth at the onset of splashing) is another important parameter for the jet cavity. The previously reported critical depression depth was 1.54 cm for water (Chatterjee and Bradshaw 1972). However, this value depends on the jetting condition such as jet momentum and lance height as Figure 5.5 shows. The critical depth slightly decreases when the lance height increases. Chatterjee and Bradshaw (1972) recognized this slight decrease of critical depth, but they interpreted this depth simply as an "inherent property of the liquid." Larger cavity width gives an impinging jet more distance over which to transfer momentum to the liquid for the growth of unstable waves. According to the analysis of Kitscha and Kocamustafaogullari (1989) and Funda and Joseph (2001), the stable and unstable wave conditions can be determined from a force balance, but in the actual critical wave phenomena need time and distance to grow. So in their analysis, the maximum growth rate does not occur at the critical wavelength, but at smaller wavelengths that

have large growth rates. Therefore, this interpretation may explain the decrease of critical depression depth with an increase in the cavity width; there is more distance and time for the jet to disturb the surface.

5.3 Wavelength Variation

The splashing and the critical phenomena shows that this system has some relationship with the Kelvin-Helmholtz instability. As shown in Figure 2.7a the critical wavenumber increases as the shearing velocity difference increases. Since the velocity difference is mainly determined by the gas velocity, as the gas velocity increases a wavelength, which was stable at a lower gas velocity, moves into an unstable region. This unstable wave must disintegrate into the stable range. This wave behaviour can be observed qualitatively in Figure 5.6, as an example. The wavelength is relatively large in Figure 5.6a and as the gas flowrate increases, the wavelengths become smaller as in Figure 5.6b.

As the gas velocity increases further, some special cases arise in the penetration range. The gas penetration into the cavity surface leaves a deeper dimple inside the jet cavity and this dimple requires some time to recover to a regular shape of the cavity surface. Sometimes this deeper void part is trapped by the returning flow. Consequently, the cavity surface is grouped with several deep penetrations and these group of waves contains smaller waves which were generated from the returning trapped bubbles to the surface. This is seen in Figure 5.7 for the 6 cm height case.

These observations provide a good qualitative picture, but cannot explain the connection with Kelvin-Helmholtz instability. A simple application of the Fast Fourier Transform to the digitized cavity shapes did not show distinguishable results for the typical wavenumbers because of the overwhelming contribution of large waves to its power. Therefore, a Power Spectral Density (PSD) function, which is described in Appendix E, was computed for this analysis. As indicated by Elson and Bennet (1995) in their surface profile analysis, PSD of a single profile does not give a good estimation; an ensemble average must be used. For that purpose, 60 digitized surface profiles were used for PSD and the resulting PSD values were averaged. Figure 5.8 shows the ensemble averaged PSD variation with wavenumber ($k = 2\pi/\lambda$). The overall slope of PSD before the penetration stage show a value close to -5/3; it is similar to the slopes

observed in the time series spectra, which will be discussed in Section 5.4. At high lance height the PSD plot shows small fluctuations only at the highest flowrates, so only the 12 cm case was shown in Figure 5.8b. In the case of 6 cm height, the typical group of wavenumber increase is clear until it reaches to the penetration range (60 SLPM). The initial range of wavenumber fluctuation is comparable to the maximum growth factor range computed from the Kelvin-Helmholtz instability ($\sim 30\text{cm}^{-1}$), as seen in Figure 2.7b of Funda and Joseph (2001) and major part of wavenumber keep increasing until the flow reaches to the penetration range.

Once it reaches to the penetration range, the wavenumber changes to a lower value. This is caused by the penetration which produces larger wavelength. In this scheme the wave behaviour is more affected by the penetration, trapped voids and the returning bubbles than the shearing action of the gas. That is to say, the surface wave motion is influenced by the critical phenomena other than Kelvin-Helmholtz instability which arises from the shearing motion of stratified fluids. When upward returning gas flow cuts liquid ligaments extending inward to the cavity, the bulk fluid was accelerated upward and disintegrated into droplets, as described by Peaslee and Robertson (1994). This case is analogous to liquid drops in a fast gas stream as is considered by Joseph et al. (1999). Therefore, Rayleigh-Taylor instability must be applied rather than Kelvin-Helmholtz instability. The analysis was not performed since it requires the local acceleration which is difficult to measure in this system.

5.4 Spectral Analysis of Time Series

It is important to control oscillations in a metallurgical vessel for stability in operation. Typical oscillation frequencies have been reported (Peaslee and Robertson 1994; Lee et al. 2001), as indicated in Chapter 3; measurement from this study match with other studies (4 to 12 Hz). However, a typical dominant frequency and a systematic relationship with lance height could not be found. Uncertainty in the relationship between the frequency and the lance height appears in the literature also; Lee et al. (2001) reported a strong linear relationship between those two variables, but later Lee et al. (2003) indicated the wave motion is "indifferent to nozzle height and angle."

To determine a characteristic frequency for each impinging condition, PSD analysis was applied to the time series of surface geometrical variables measured in Chapter 3. Figure 5.9 to 5.11 show the PSD of each time series of surface variables. Characteristic frequencies could not be found with this method. However, the spectral decay behaviours (the slope of the graphs) all have a similar value of approximately $-5/3$; a reference line of $-5/3$ is plotted in each plot. Surface elevation spectra were measured by several researchers and they all show slightly different slopes in PSD. Metcalf et al. (2006) measured a surface elevation and pressure spectra around the NACA 0024 foil; their slope was -2 and $-5/3$ for surface elevation and the pressure, respectively. Zarruk (2005) measured surface elevation with PIV images with waves from a wave generator beneath the surface; the slope taken from their figures was around -3. Mitsuyasu and Honda (1982) measured water surface elevation spectra of waves generated from wind shear; the slope was around $-2 \sim -3$, but the slope was much reduced by the presence of surfactants. Lommer and Levinsen (2002) reported $-17/6$ in their vertically shaken vessel. Weak turbulence theory (Falcon et al. 2007; Zakharov et al. 1992) indicates the slope should be $-17/6$ for capillary waves and -4 for gravity waves. Dabiri (2003) indicated that the surface elevation is directly related with pressure for the low Froude number flow. They interpreted the surface elevation spectra as pressure spectra and obtained $-10/3$ and compared with this value the theoretical isotropic pressure spectra's slope $-11/3$ (George et al. 1984). So in all of these studies, the slope ranged between -2 and -4, depending on the flow situation.

In this impinging jet situation, the cavity surface motion was interpreted with force balance at the stagnation points, so the vertical direction turbulence and pressure variations are thought to be important. Around the surface the isotropic turbulence behaviour will be break down and length scale anisotropy is reported (Handler et al. 1993) and some DNS results show anisotropic behaviour of turbulence around the surface (Fulgosi et al. 2003). Brumley and Jirka (1987) observed an attenuation of vertical velocity spectra close to the free surface. Guo and Wood (2002) measured time spectra of velocity and pressure in the impinging gas jet to a flat solid plate. They observed an attenuation behaviour of the vertical velocity and pressure spectra close to the plate. Therefore, the $-5/3$ slope of time spectra in this study is thought

to be the result of the attenuation of turbulence velocity and pressure spectra close to the surface.

The time fluctuation of surface variables, depth, width and the horizontal position of cavity tip, all show the same spectral decay Figure 5.9 to 5.11, so the gas pressure fluctuation close to the cavity is thought to have an isotropic behaviour. From the previous section, the space spectra also show the same spectral decay slope. The space fluctuation represents a snapshot of the cavity wave profile and assuming the time spectra of a geometric variables are the same for every position inside of a cavity, time and space fluctuation have to show the similar behaviour in the spectral decay. This can be interpreted as analogous to Taylor's "Frozen turbulence approximation," an approximation of spatial correlation by temporal correlations (Pope 2000).

Time fluctuation and spectra of the mathematical results are not investigated since the current numerical method cannot account for the turbulent pressure fluctuation behaviours.

5.5 Wall jet experimental issues

As indicated in Chapter 3, the surface geometry measurements were done in the wall-jet setup, Figure 3.2. Preliminary full 3D cylindrical measurements were good to determine the depression depth only, but the detailed wave behaviour inside cavities was not observable; it was difficult to determine which wave came from which part of the section viewed from outside of the cylindrical vessel.

The wall jet and cylindrical jet have different behaviour (Rajaratnam and Pani 1974; Padmanabham and Gowda 1991; Law and Herlina 2002); in the wall jet there is larger spanwise expansion and a larger velocity profile parallel to the wall. Wall jet measurements from literature (Padmanabham and Gowda 1991; Law and Herlina 2002) and the calibration in this work show -1.066∼-1.16 exponent to the lance height variable in the centerline velocity correlation of the gas jet; $\frac{u_m}{u_0} \propto x^{-1.066\sim-1.16}$ the circular 3D jet case is -1, Equation (2.2). So the dimensionless relationship for liquid depression depth, Figure 3.9, shows almost identical behaviour with previously reported results (Szekely and Themelis 1971). The expansion is wider in wall jet close to wall, so wider cavity shape is expected. However, the results of Figure 5.3 are in good agreement with parabolic shape reported by Banks and Chandrasekhara

(1963). The width information shows some discrepancy between the investigators; some claim it is independent of the flowrate (Turkdogan 1966; Cheslak et al. 1969), and the sideway jet pressure is weaker than vertical jet pressure, so it is another difficulty to distinguish the cavity width information. The experiment itself is not full 3D or 2D, so the open side 3D fluid may have compensated the closed side effect, but this needs closer investigation.

5.6 Energy Transfer for a Jet Impinging on a Liquid Surface

To assess the extent of kinetic energy transfer from the gas to the liquid, a new parameter was defined.

$$\mathcal{I} = \frac{\int \rho \mathbf{u}^2 dV}{\dot{E}_{in}} \tag{5.4}$$

It is the ratio between the kinetic energy in the sum of the control volumes and the input kinetic energy flux at the inlet, which is obtained as

$$\dot{E}_{in} = 0.136 \rho_g K^3 \frac{Q^3}{\pi^2 d_0^3 h} \tag{5.5}$$

K is the turbulent jet parameter and the value is 7.81 (from Section 3.4.1), Q is the volumetric gas flowrate. It is difficult to define the energy input from the gas to liquid at the interface, since there are surface variations and the jet energy is consumed by producing turbulence during its propagation (Rajaratnam 1976). So appropriate input kinetic energy must be determined. The axial gas velocity profile has a Gaussian shape. If we take the summation of kinetic energy up to the half maximum of the velocity profile, it is more than 95% of entire kinetic energy. So the kinetic energy flux was integrated up to the half maximum of the velocity assuming Gaussian profile.

$$\dot{E}_{in} = \int_0^{2\pi} \int_0^{r_{1/2}} \frac{1}{2} \rho_g u^2 u r dr d\theta \tag{5.6}$$

$$u = u_m e^{-0.693(r/r_{1/2})^2} \tag{5.7}$$

Writing $\dot{E}_{in}$ in a different form, $\dot{E}_{in} = 8.5 \times 10^{-3} K^3 \rho_g Q d_0 u_0^2 / h$, and comparing with the energy dissipation rate, $\varepsilon = 0.04530 Q_T d_0 u_0^2 \cos^2\theta / W/h$ (Nakanishi et al. 1982), vertical jet has $\theta = 0°$ and using the incompressible definition of mass flow rate,

$\rho_g Q$, can be replaced with Normal Q_T with other coefficient which depends on the nozzle condition. Therefore, they are similar concepts except the bath weight, W. In a fixed nozzle condition, kinetic energy input, $\dot{E}_{in}$ is proportional to εW, so the current Energy transfer index, $\mathcal{I}$, is proportional to the ratio of liquid kinetic energy to overall dissipation rate.

$$\mathcal{I} \propto \frac{\int \rho u^2 dV}{\varepsilon W} \tag{5.8}$$

$\mathcal{I}$ has the dimension of time and the summation of $\mathcal{I}$ over the whole liquid domain can be interpreted as the effective time of energy transfer for the system at the same level of liquid kinetic energy. In cylindrical tank $\mathcal{I}$ should be obtained by summation of the volume elements, as shown in Figure 5.12.

Based on the measured PIV velocities, the contour image of $\mathcal{I}$ was plotted from Figure 5.13 to 5.16. The energy transfer index shows higher value at the side of the container wall as it is observed at the measured velocities which were larger at the wall. The centre of circulation could be observed clearly also.

Figure 5.17 shows the sum of the energy transfer parameter over the whole liquid domain. The energy transfer is more efficient at higher lance height within this measurement height, but the flowrate did not have much effect on it. Davenport et al. (1967) reported that the bath circulation was better in higher lance position when the kinetic energy levels are similar at the impinging position, so the current analysis support their claim. In the Deep penetration situation, the gas jet moves faster and the contact area between the gas and liquid is small and splashing and bubble formation requires extra energy consumption. In the wider cavity case, with the same initial jet exit velocity, the total amount of momentum is the same as deep penetration, but the larger contact area gives more chance of momentum transfer. This is illustrated in Figure 5.18. For even higher lance height, the decrease of the efficiency is expected because of the consumption of the kinetic energy by the production of turbulence. This is consistent by the fact that the slag splash practice has optimum lance height when the gas flow rate is fixed (Mills et al. 2005).

In the case of mathematical modelling of impinging jet, the energy transfer index variation is plotted in Figure 5.19. Similarly to the experiments, for higher flowrate the energy transfer index was higher and for lower lance height, the decrease of index at high flowrate were observed. A direct comparison is difficult because the

mathematical modelling was in 2-D rectangular Cartesian coordinate, while the water model was in a circular container.

5.7 Momentum transfer around the jet cavity

Transfer of momentum from the gas to the liquid is important for mixing of BOFs. The transfer was assessed in two ways, first by measuring the velocity in the immediate vicinity of the cavity, u. Due to fluctuations in the cavity shape and position, the PIV technique the liquid surface could not be measured. Figure 5.21 shows the area of investigation for these measurements. The second measurement was the volume-weighted average of the liquid velocity, $\overline{u}$.

These velocities will be related to the blowing conditions. Assuming that the momentum transfer inside of the cavity is dominated by a shear stress balance. the approximate momentum balance is

$$\mu_1 \frac{u_1 - u_s}{\delta_1} = \mu_2 \frac{u_s - u_2}{\delta_2} \tag{5.9}$$

where δ_1, δ_2 are boundary layer thickness for each phase, u_1, u_2 are tangential velocities around the cavity. This yields a simple linear relationship betwen the two tangential velocity.

$$u_2 = Au_1 + b \tag{5.10}$$

As in the Blowing number analysis, it will be assumed that there is a linear relationship betwwen the deflected or tangential gas velocity and the impinging gas velocity ($u_1 = \eta u_g$). Furthermore, it was shown that there is local modified Froude number similarity that relates the impinging gas velocity and depression depth ($= \rho_g u_g^2 / \rho_l g n_0 = 2$), u_1 is proportional to $\sqrt{n_0}$ and these substitutions can be made in Equation (5.9):

$$u_2 = A'\sqrt{n_0} + b \tag{5.11}$$

According to Equation (5.11), a linear relationship is expected between the characteristic liquid velocity and the square root of the depression depth.

Figure 5.22 shows the relationship between the measured velocity near the cavity (u) and the square root of depression depth. In general there is a increasing trend within the natural scatter in the data. The other observed trend is that for an equivalent penetration depth, there is more momentum transfer for higher lance

position, which seems counter-intuitive. This finding can be explained by reference to Figure 5.18 which shows high and low lance cases for the same depression depth, which implies that they have the same impinging gas velocity, u_g, but the gas flow rate will be higher for the high lance position. The high lance position produces a wider cavity which has more contact distance to transfer momentum to the liquid, and hence the greater momentum transfer. The same trends are observed for the average liquid velocities in Figure 5.23.

These arguments imply that there must be some cavity shape factor that influences the momentum transfer to the liquid. Several functional relationships were investigated, and that captured the phenomena illustrated in Figure 5.24. The angle of cavity slope was obtained as $\tan^{-1}(d_0/2n_0)$. The contact distance increases as the angle increases, and as cosine θ decreases. Figure 5.25 shows that when $u\cos\theta$ and $\overline{u}\cos\theta$ are plotted against the square root of the depression depth linear relationships are revealed. At this stage there is no theoretical justification for this relationship, but it should be noted that the depression depth varies from 0.5 cm to 9 cm, so that this relationship holds over a length scale more than one order of magnitude in these experiments. Nevertheless, further experimental and theoretical verification is neceessary. The potential application of this finding is quite important. It means that the penetration depth can be calculated from the gas velocity and in turn the interfacial liquid velocity (for the calculation of mass transfer coefficients) and the bulk liquid velocity (for the calculation of mixing phenomena).

5.8 Computation of the impinging jet

5.8.1 Surface Shape

The surface shape determined from the mathematical modelling could not resolve all the small size wave ripples because of the grid size limitations, so for the high amplitude wave and breaking situation, the surface profiles are not regular and show some poorly resolved and disconnected line segments.

Since the modelling was done in Cartesian coordinates the sideway momentum transfer level was much greater than in the experiments which used a cylindrical tank. The experiments showed much lower amplitude waves at the same flowrate

since the impinged momentum was spread in the radial direction. Therefore, the inertial effect was more pronounced in the mathematical modelling.

The jet cavity width in the mathematical modelling was much greater, 2 to 3 times, than in the cylindrical experiments. The depression depth of the cavity was similar at low flowrate, as shown in the Figure 4.25, but it deviated from the experiments when the flowrate was increased. The jet expansion and propagation has a plane jet behaviour in the Cartesian coordinate; the centreline velocity diminishes less than circular jet case, so a higher penetration was computed.

The impinging jet modelling simulates a plane jet situation. For, both the plane and circular jets, the gas jet expansion over distance is similar (Rajaratnam 1976). A Gaussian velocity profile can be assumed for both the plane and circular jets (Schlichting 1979), and the initial velocity in the circular situation can be converted to a plane jet initial velocities considering the relationship of the centreline velocity propagation Equation (2.1) and (2.2). The conversion is listed in Table 5.1 and the surface mean depression is compared in Figure 5.20. According to Banks and Chandrasekhara (1963), the average depression depth has the following relationship

$$\frac{n_0}{H} = \frac{1}{2}\left\{\left(1 + \frac{4M}{k\rho_l g L H^2}\right)^{1/2} - 1\right\} \tag{5.12}$$

where k is constant, L is the nozzle width, M is the momentum rate at the nozzle exit and H is the lance height. Figure 5.20 shows a comparison of the computed results and the results of Banks and Chandrasekhara (1963) about the relationship between the momentum group ($M/\rho_l g L H^2$) and length group (n_0/H). Generally the computation agrees well with the experimental data.

The PIV measurements show that the flow velocity is in the 10 cm/s range, except in the region close to the surface; they are masked out during the average velocity calculation because the movement of the surface gives erroneous PIV measurements. The simulation velocity varies up to close to 50 cm/s around the surface, but is generally less than 10 cm/s away from the surface region. Some differences between the experimental and modelling flow are due to the location of the liquid circulation. Comparing the PIV vector plots (Figure 3.13, 3.14 and Figure F.1 to F.4) and momentum contours computed from the measurement (Figure 5.13 to 5.16) with modelling flow vector plots (Figure 4.26), the centre of the circulation in the half plane of the

container is located at the centre for modelling case and closer to the wall for the experimental measurements. The horizontal shift from the cylindrical experimental case comes from the location of the shift of the centre of the mass. The vertical shift was due to the absence of the turbulence in the modelling case; the bottom corner develops a dead zone in the real case because of turbulence dissipation and separation.

In the case of modelling, the overall momentum level monotonically increased with increasing flowrate as shown in Figure 4.27, but contrary to the experimental findings the higher lance height showed a lower momentum transfer level at high flowrate, 80 SLPM. This may be caused by the pronounced sideways motion of the gas jet and its inertial effect is overwhelming the viscous stress transfer.

5.8.2 Momentum Transfer Mechanism

The momentum transfer from the gas to liquid is very complex so it it difficult to determine the major factors for the inter-phase momentum transfer. Surface motion and the surface roughness are important factors for the momentum transfer, but difficult to assess.

The increase of the surface corrugation provides more area to transfer the shear stress. The increased tangential stress and the friction velocity (u_τ) accelerate the wave growth; the wave growth factor is known to be proportional to the square of the friction velocity (Mitsuyasu and Honda 1982; Plant 1982). So the surface corrugation and the shear stress are interrelated.

The local pressure gradient generated by the surface corrugation is another important factor. As discussed in Section 4.8.2, Munk (1947) speculated on the flow behaviour around the wave crest over the critical velocity. On the leeside of the crest, separation of gas flow occurs and the pressure decreases, resulting in suction of the surrounding fluid. The accelerated gas from the windward impinges the next crest and the pressure increases. Figure 5.27 confirms Munk's suggestion. The pressure around the wave crest is similar the situation in Figure 4.16d. The windward side experiences higher pressure and the other side has low pressure; the wave crest part is accelerated by this higher pressure gradient and consequently, this increases the momentum transfer efficiency from the gas to liquid.

The significance of the surface shape to the momentum transfer can be shown in the next example. Figure 5.28a shows the oscillation behaviour of the momentum level in the case of 18 cm lance height 20 SLPM flow rate case mathematical modelling. The surface profile at the local maxima and minima of the momentum level shows completely different pattern(Figure 5.28b). The "A" position shows waves, but "B" position does not. The first maxima occurs when the centre plume of the liquid returns to the impinging position, increased liquid velocity stabilizes the surface shape and consequently the momentum transfer is diminished. This behaviour can be observed in other 20 SLPM cases—12 cm case shows very small amplitude oscillation, see Figure 4.27a.

5.8.3 Effect of the physical properties

High surface tension was shown to be most effective for reducing the momentum transfer in Section 4.9.6. In this study, the surface tension had a more pronounced effect than viscosity. The surface shape was not affected much by the viscosity change (Figure 4.28). The vigorous fluctuation stage of the surface wave can be determined by the Kelvin-Helmholtz instability and physical observations explained in Section 4.8.2 support this fact. So the effect of the physical properties on the Kelvin-Helmholtz critical velocities variation can be an indication of the degree of surface fluctuation. According to the viscous potential theory of Funda and Joseph (2001), the critical velocity difference can be written as,

$$V_c^2 = \frac{(1+\hat{\mu})^2}{1+\hat{\mu}^2/\hat{\rho}} \frac{2\sqrt{(\rho_l - \rho_g)g\sigma}}{\rho_g} \tag{5.13}$$

where $\hat{\mu} = \mu_g/\mu_l$, $\hat{\rho} = \rho_g/\rho_l$. Figure 5.30 shows the critical velocity change with varying physical properties by various factors. The effect of the viscosity on the critical velocity difference was almost negligible except when the viscosities of the two fluids become similar to each other—$\hat{\mu}$(air/water) = 0.018. However, the critical velocity is very sensitive to the surface tension change. An increase in the critical velocity difference has a stabilizing effect on surface fluctuations; consequently, the momentum transfer diminishes as the surface tension increases.

The effects of surface tension are complex, and a general conclusion is dangerous. When a surfactant concentration gradient exists and the Péclet number(Lu/D) is

large, the accumulation of the surface active elements generates local surface tension gradients and causes Marangoni flow. Ceniceros (2003) modelled wave flow containing surfactants. When the Pe number was large the surface tension forces were changed, and stabilized the capillary wave in front of a breaking wave.

5.8.4 BOF Simulations

As shown in Chapter 4 the gas velocity was not reproduced well in this study. The surrounding gas temperature plays an important role. The isothermal jet core length (Szekely 1979) and case with high-temperature surrounding gas shows significant differences in supersonic jet core length. Odenthal et al. (2007) indicated that "the jet core length in a hot environment increases by the factor of three."

There are limits to the computation due to ignoring the gas reaction equilibrium. In real case, the CO created by reaction at the impingement point will recirculate and become entrained in the jet and will react with O_2 and generate CO_2; this exothermic reaction and corresponding reduction of gas density around the jet envelope will extend into the jet core length.

The time change of kinetic energy transfer index was plotted in Figure 5.29. Generally the time to achieve momentum stationary state was around 30~40 s for any case, and was not affected much by the flow rate and physical property change similar to air/water case. The steel melt showed poorer kinetic energy transfer relative to slag melt. Since the density is high in both cases, higher initial velocity case showed better energy transfer and smaller nozzles were also more effective.

5.8.5 Limitations of current method

The focus for this study is a fast gas stream impinging on an initially flat liquid surface. As a result, the liquid surface is deformed vertically and horizontally. The vertical movement is mainly affected by the balance of the dynamic pressure and the opposing force (buoyancy) from the liquid, and the horizontal movement is affected by the gas jet cone envelope, surface tension and the shear stress from the deflected gas flow.

The total amount of momentum in the liquid flow will be determined by the shear stress transfer across the gas/liquid interface and by the oscillations from waves. If

the interface is in steady state, the momentum is solely determined by the shear stress transfer. However, the interfaces show oscillatory behaviour, so disturbed surfaces do not reach to a strict steady state, but a pseudo steady state in a time average sense.

In the case of extremely high flowrates over the penetration range, waves break and a sharp interface determination is required to resolve each bubble and drop; to resolve the interface requires higher computational capability. The present code is capable of generating drops and bubbles, but the number of computational nodes in the drops and bubbles was limited, so it could not resolve every motion of the liquid and gas which resided in those small area.

In the impinging jet modelling, droplets were generated for high flowrates, but they were removed from the computation by changing the cells to gas cells. Once a droplet detached from the liquid flow, it did not affect the bulk flow, but it caused some instability because of grid size limitation; the droplets have a very limited number of cells in them. Similarly, bubbles were trapped inside of the liquid. The trapped bubbles showed similar instability, so they were removed by changing the gas cells to the liquid cells. In both detaching and trapping cases, an increase or decrease of mass and momentum was inevitable. The overall mass was corrected to its original value to compensate for these effects.

Other kinds of modelling may be applied to those bubbly and splashing cases. One example is well summarized theoretically by Brocchini and coworkers (2001a, 2001b, 2002), but those theories are not implemented numerically.

5.9 Steelmaking and Surface Instability

In steelmaking situations, interfacial instabilities occurs around the following three interfaces schematically illustrated in Figure 5.31 for a BOF vessel.

- Gas/Steel
- Gas/Slag
- Slag/Steel

These instabilities influence momentum transfer to the liquid; the formation of slag-metal emulsion and splashing inside the steelmaking vessel. In the following sub-sections the instabilities at the interfaces will be examined. Table 4.4 lists physical properties of the phases for steelmaking used in these calculations.

5.9.1 Gas/Steel interface

As shown in Figure 5.31, steel is exposed only around the cavity area and the other part of the liquid steel level is covered by slag. Figure 5.32 shows the critical velocity changes with physical property change of liquid steel. The viscosity of iron-carbon alloys has been observed to decrease slightly with increasing carbon content, or was unaffected by the carbon content, depending on the investigators. However, the combined effects of carbon content and temperature are quite large; a change from 4% C at 1250°C to 0.5% C at 1600 °C changes the viscosity from 10 mPa s to 5 mPa s (Kawai and Shiraishi 1988). When oxygen or sulfur content increases, surface tension decreases up to 50% to 60% from the clean surface case; this can reduce the critical velocity more than 30 %. Therfore, the carbon-oxygen reaction and corresponding temperature change at the impact points has very complex, but favorable effect on the critical phenomena of Gas/Steel interface that it makes it easier for droplets to form and provide sites for reaction in the slag-metal emulsion.

5.9.2 Gas/Slag interface

The gas jet does not usually impact the slag surface because it is pushed to the side as shown in Figure 5.31; however, other processes with deep slag (Such as smelting/reduction) could encounter this situation.

It should also be noted that shear transfer and instability are important in the slag splashing practice used in BOFs to generate a slag splash coat to protect the refractory linings (Mills et al. 2005). A washing coating protects the bottom of the converter and splashing protects the top part of the converter. So the viscosity and surface tension have different roles in slag splashing practices. Figure 5.33 shows the critical velocity for the gas/slag case. In contrast to the gas/steel case, viscosity has virtually no effect unless the viscosity is drastically reduces, but the surface tension effect is pronounced. For the gas/slag case, the physical properties vary with composition and the range is quite wide, so the combined effects must be investigated. Figure 5.34 shows the physical property variation and critical velocity change with FeO content. Physical properties are computed with models proposed in the literature; density (VDEh 1995), viscosity (Shu and Zhang 2006), surface tension (Vadász et al. 2000). A typical composition change in BOF operation is shown in Figure 5.35. FeO content starts

high (around 27 wt%) , $X_{FeO} = 0.23$ in Figure 5.34, and stays almost constant 16 wt%, $X_{FeO} = 0.14$, during the main blowing stage. Towards the end of the blow, the FeO content rises again. The calculated critical velocity is at a maximum at X_{FeO}=0.14 and decreases as the FeO content increases, so the slag is relatively susceptible to critical phenomena at the initial and final stage of the BOF oxygen blowing. However, the critical velocity of slag itself is much higher than steel/gas or steel/slag interface (see next section).

Generally the critical phenomena are dominated by the surface tension as influenced by the FeO content, but the other properties effects are not negligible; the maximum in the critical velocity is shifted away from the maximum of surface tension at X_{FeO}=0.14.

5.9.3 Slag/Steel interfaces

Critical velocity differences are shown in Figure 5.36 and the effect of FeO is shown in Figure 5.37. For a liquid-liquid interface, the critical behaviour is affected by the change of density difference much more than gas/liquid interfaces, since small difference of density will increase the instability due to gravitational forces. An increase in slag viscosity, decreases critical velocity, but steel viscosity has the adverse effect. A larger viscous force transfer in the lighter fluid helps the instability, but the denser fluid's viscosity stabilizes the interface. Surface tension has a direct effect on interfacial stability, as clearly shown in Figure 5.37. Compared to gas/liquid interfaces; the critical velocity is one order of magnitude lower, so the slag/steel interface is more susceptible to instability.

As confirmed with physical and mathematical model by Krishnapisharody (2006), Kelvin-Helmholtz instability is the main mechanism of the droplet formation at the interface of Oil/Water system and other mechanisms proposed by Mietz et al. (1991) and Wei and Oeters (1992), which are based on the force imbalance formulation, cannot serve as the onset criteria of interfacial instability.[1] Thus, an investigation of

[1]Normal mode analysis, on which Kelvin-Helmholtz instability analysis is based, is a perturbation analysis to the flow equations, including a momentum rate balance—force balance. So the force imbalances analysis gives the necessary condition for the onset of instability, but not the sufficient condition.

the chemical effect on the slag and slag/steel interfacial properties and corresponding change of the Kelvin-Helmholtz instability criteria is important.

In the initial blow stage of BOF operation, the FeO content is high in slag, so viscosity and surface tension are low and the small density difference between the slag and high [C] steel contribute to low critical velocity; Figure 5.36 shows the decrease of critical velocity on either side for a slag density increase or steel density decrease. Therefore, this low critical velocity is beneficial for the generation of large interfacial area for the reaction and emulsion formation. This may account for the emulsion formation and corresponding fast reaction rate in BOF.

The Gas/Steel and Slag/Steel interfaces are affected by the [O] and [S] concentration. During the main blowing period, the [O] content is low and constant, but it increases at the end of blow (Deo and Boom 1993). Typical diffusion coefficient of oxygen and sulfur in iron at 1600 °C are 1.33×10^{-8} m^2/s and 4.40×10^{-9} m^2/s, respectively; the calculation is based on the data from Kawai and Shiraishi (1988). A typical length scale of wavelength of Kelvin-Helmholtz or Rayleigh-Taylor instability is $\sqrt{\sigma/\rho g}$, which is of the order of centimetres in steel and slag and the liquid velocities are at most 0.1 to 5 m/s. Therefore, a typical Péclet number would be around 10^6 for slag and steel cases. Such a Péclet number can induce an adverse effect on the surface tension by the Marangoni effect. So it is difficult to be definitive on the effect of surfactants; there is some possibility of localized surface tension gradient and flow effect, as discussed in Section 5.8.3.

Table 5.1: The conversion table for simulation condition to plane jet equivalence. Lance height was set to be the same and the nozzle exit velocity (u_0) was converted.

Lance height (cm)	Flowrate	u_0 (m/s)
12	20 SLPM	19.3
	30 SLPM	29.0
	40 SLPM	38.3
	50 SLPM	48.4
	60 SLPM	58.0
	70 SLPM	67.7
18	20 SLPM	15.8
	30 SLPM	23.9
	40 SLPM	31.6
	50 SLPM	39.5
	70 SLPM	55.2
	80 SLPM	63.2
24	20 SLPM	13.9
	30 SLPM	20.5
	40 SLPM	34.2
	50 SLPM	41.0
	70 SLPM	47.9
	80 SLPM	54.7

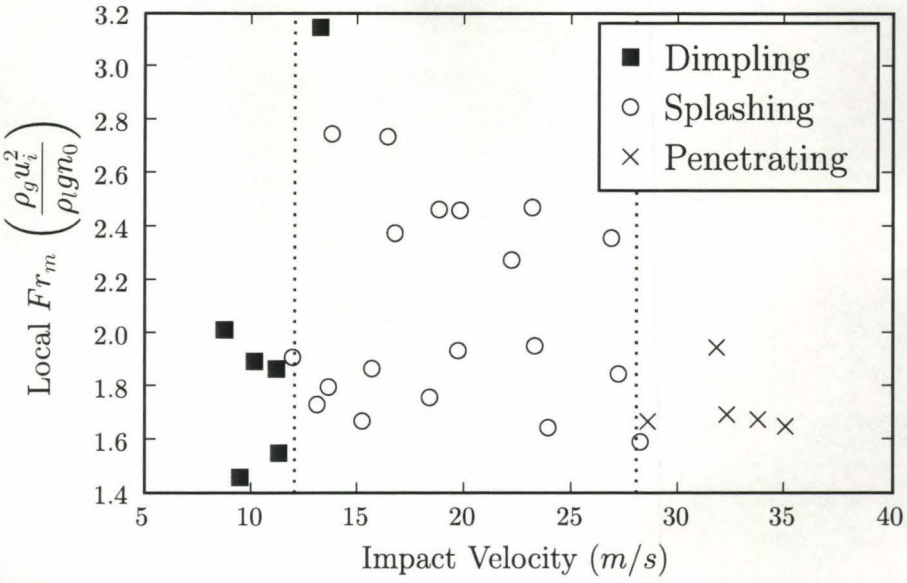

Figure 5.1: Local modified Froude number varies around 2.

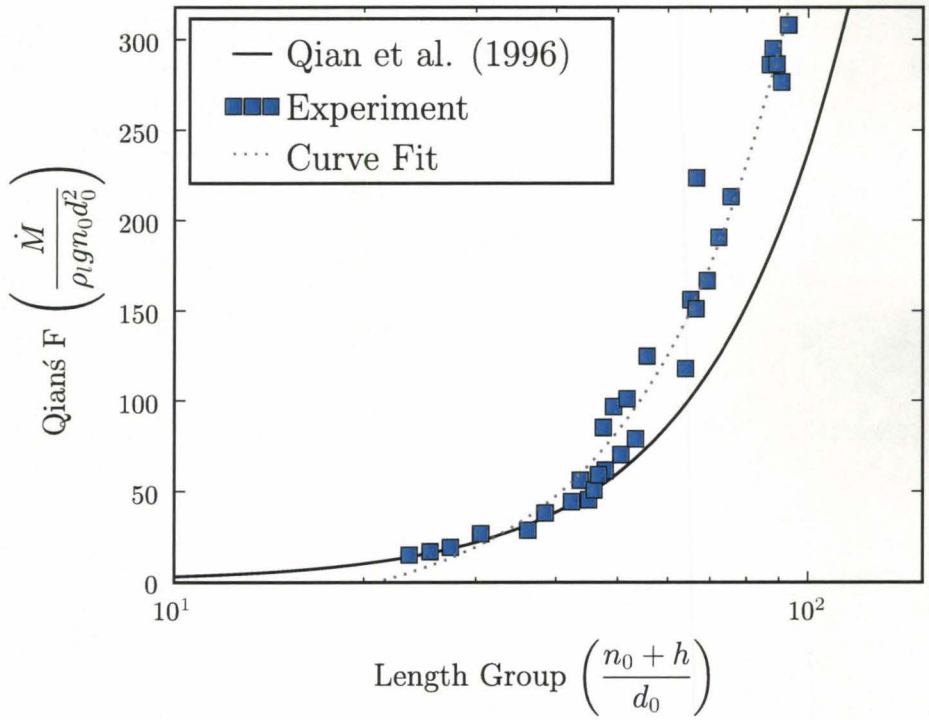

Figure 5.2: comparison with Qian et al. (1996)'s parameter F_q. The F_q shows deviation at the length group over 40.

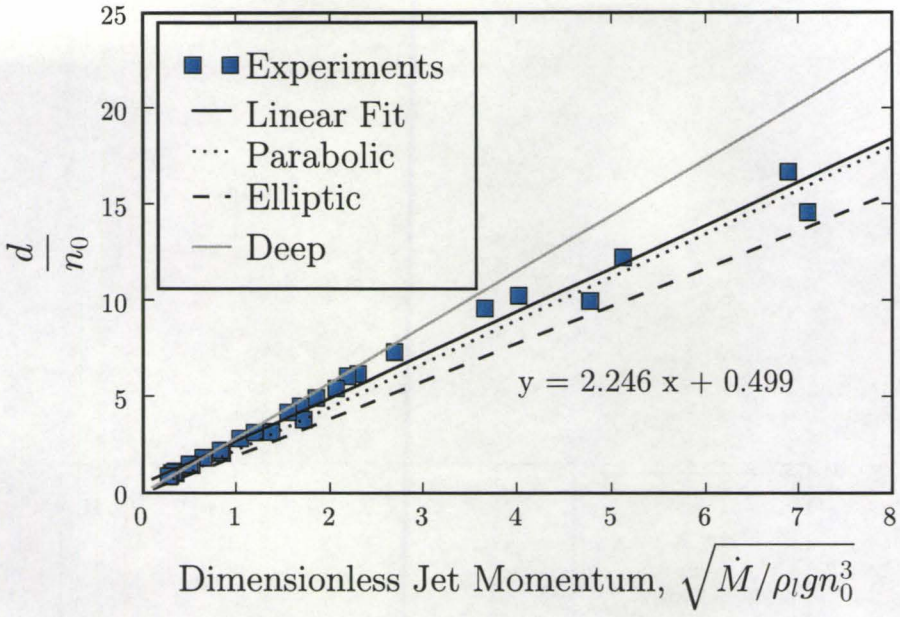

Figure 5.3: Plot of Dimensionless momentum and cavity aspect ratio. Present experiment shows the overall cavity shape is closer to the parabola.

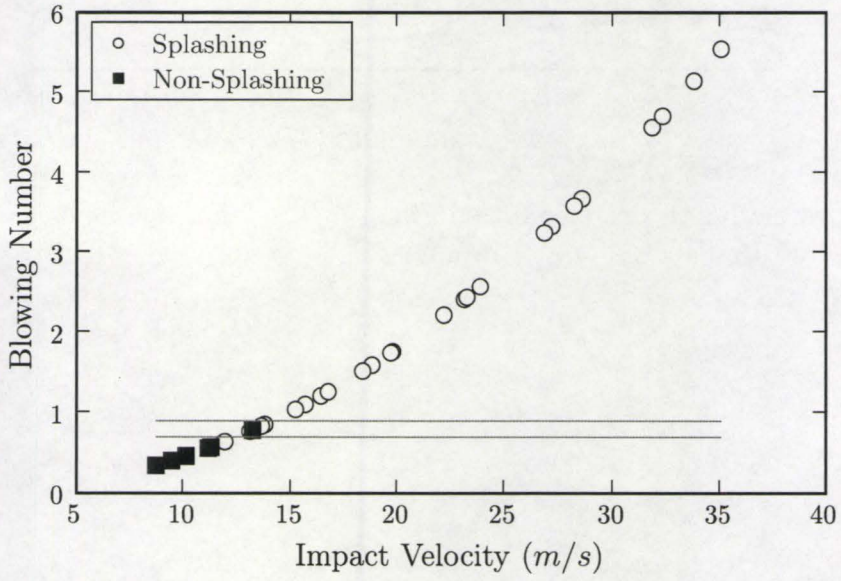

Figure 5.4: Blowing number changes quadratically with impact velocity. Splashing begins around 0.7~0.9.

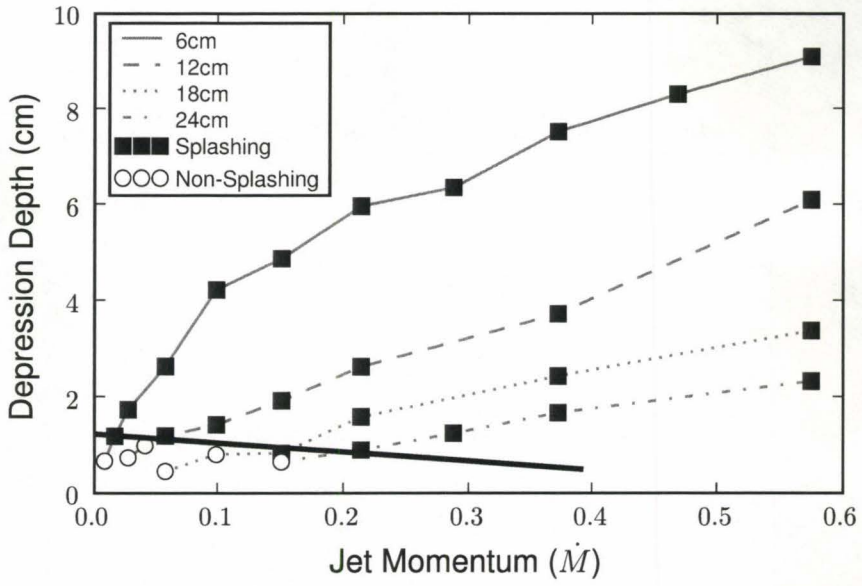

Figure 5.5: Critical depth decreases (Solid line) as the lance height increase similar to Chatterjee and Bradshaw's (1972) result.

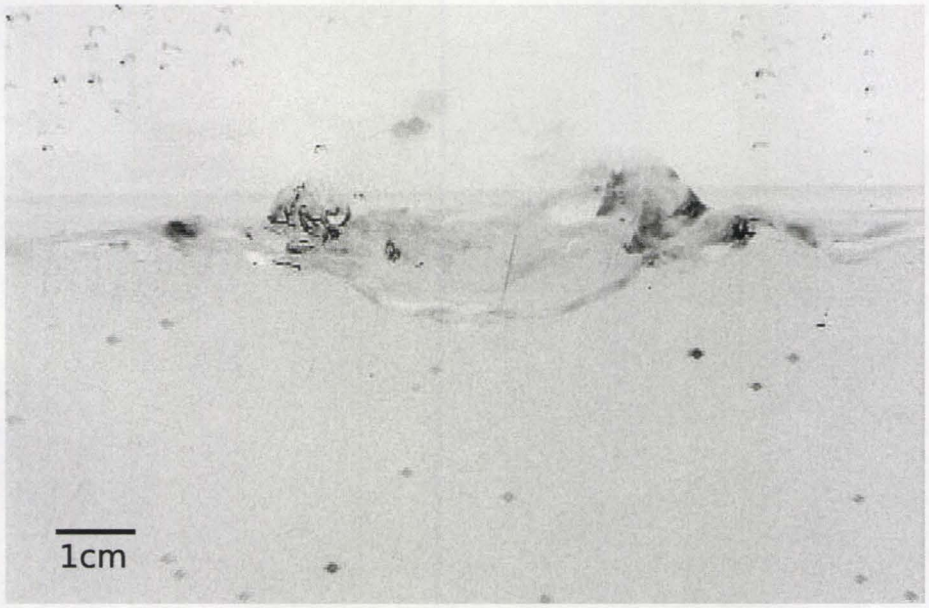

(a) low flowrate

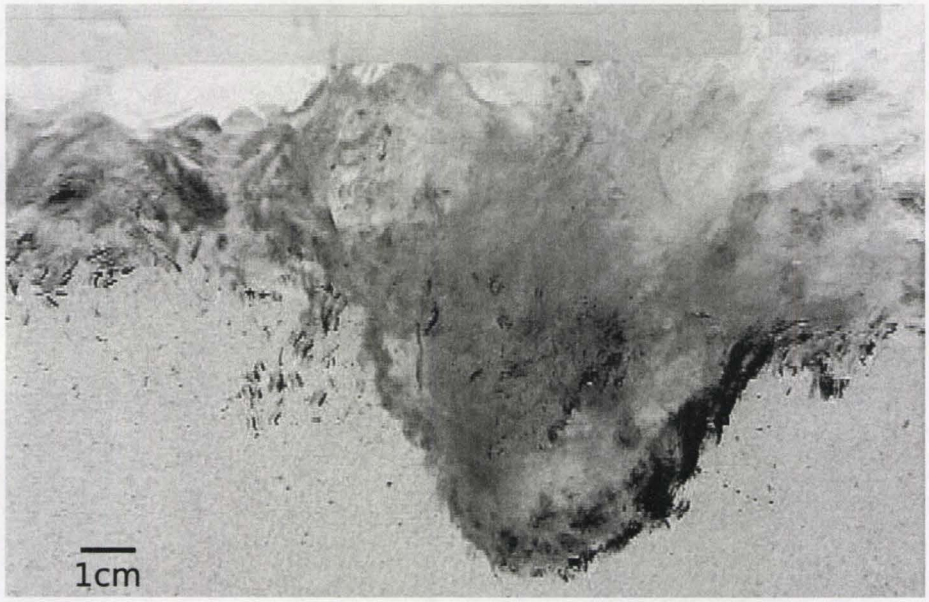

(b) high flowrate

Figure 5.6: An example of wavelength disintegration. As the flowrate increases the typical wavelength of ripples in the cavity decreases. Photographs from the 12 cm lance height, (a) 30 SLPM and (b) 100 SLPM case

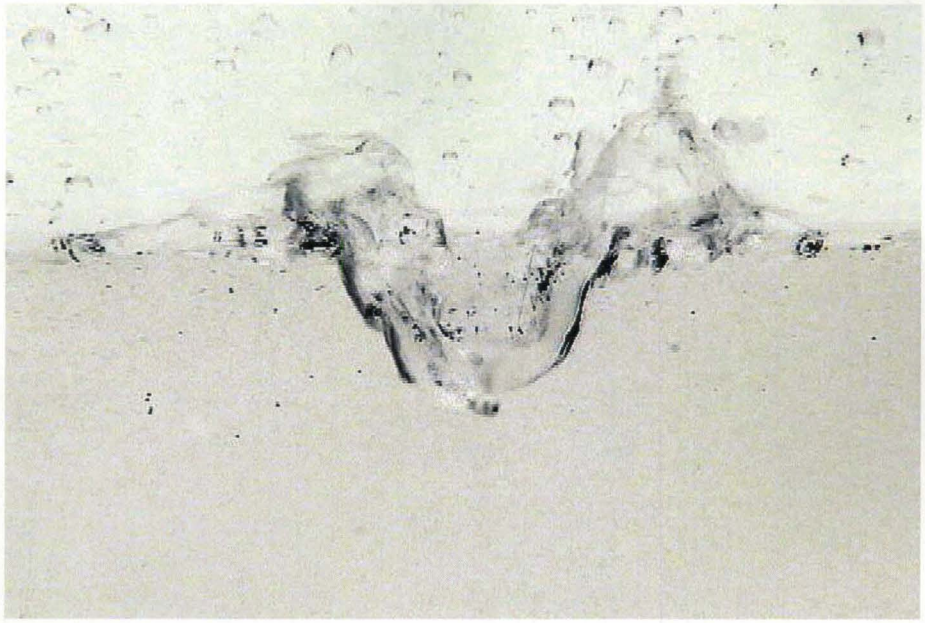

(a) Splashing

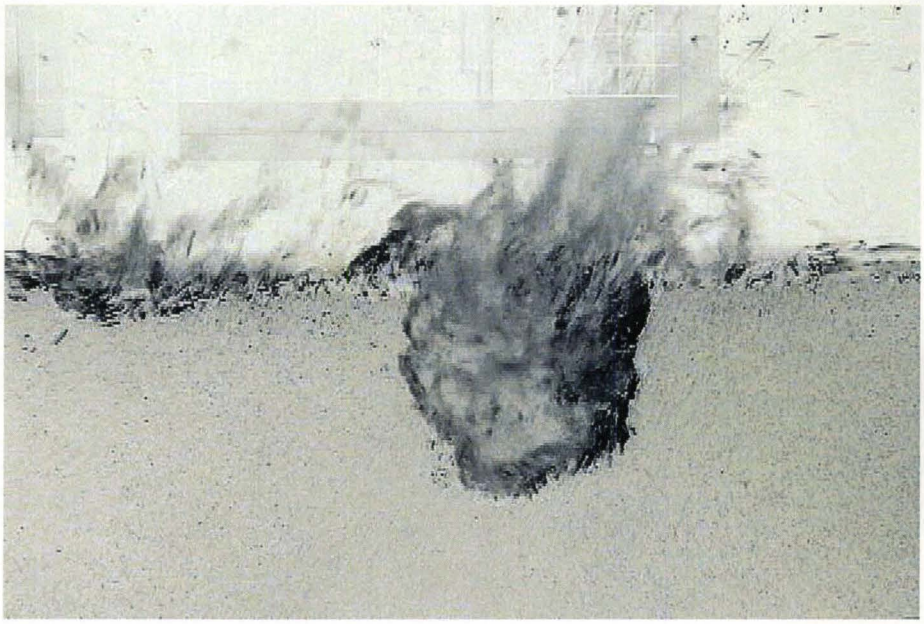

(b) Penetration

Figure 5.7: An Example of penetration wave behaviour. In penetration range, the surface was grouped with penetration dimples, and the dimple contains small ripples(b) . Pictures from the 6 cm lance height case, (a) 30 SLPM and (b) 80 SLPM .

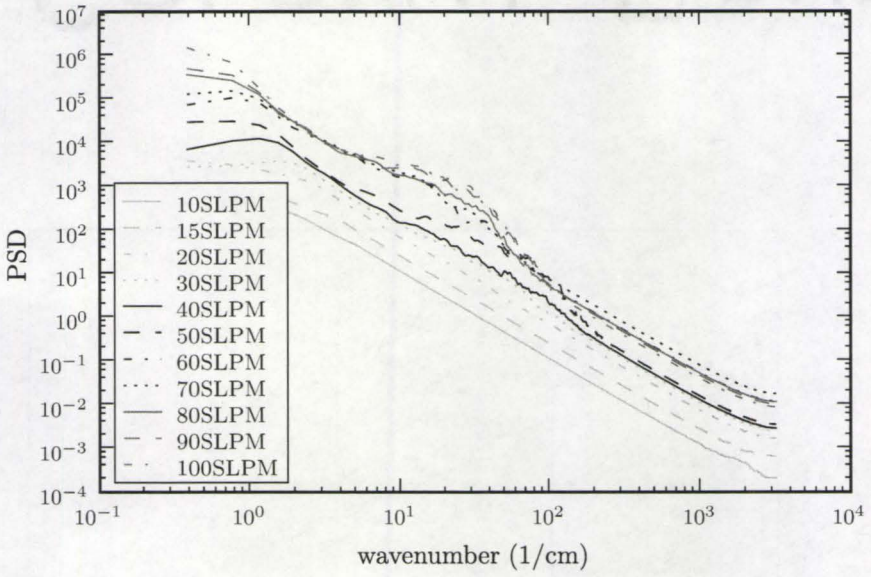

(a) 6 cm lance height

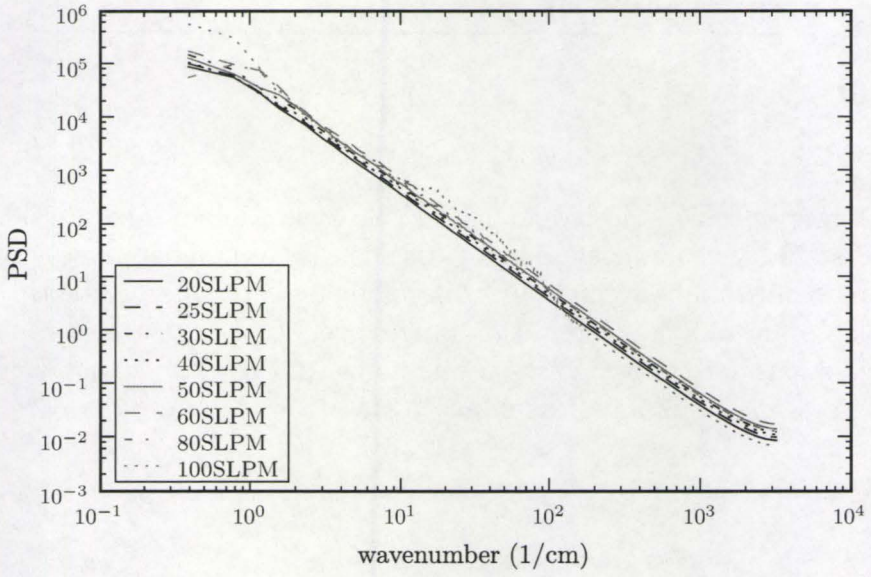

(b) 12 cm lance height

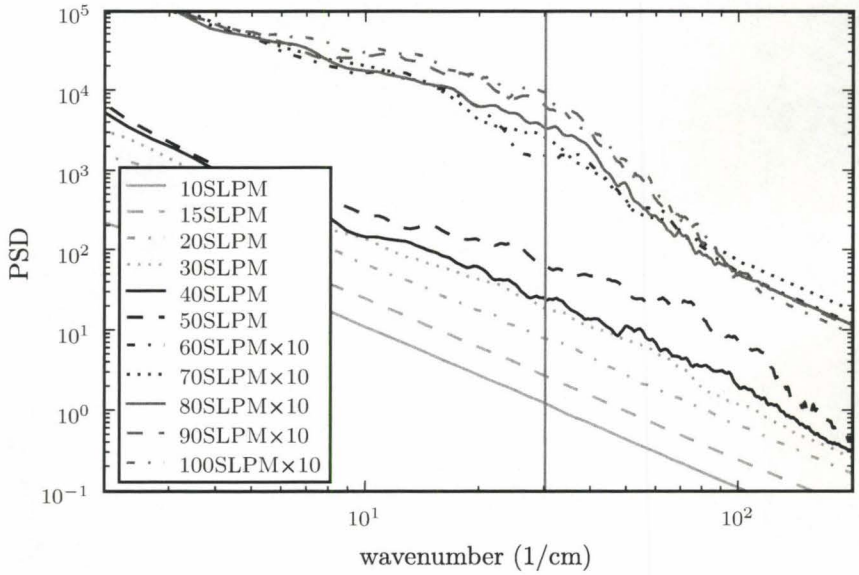

(c) 6 cm lance height magnified

Figure 5.8: Power Spectral Density change vs. the wavenumber. The splashing regime change affects the typical wavenumber variation. Wavenumber fluctuation begins around the most unstable wavenumber from Funda and Joseph's (2001) theory. (c) is a reproduction of (a) but the penetration range (over 60 SLPM) was drawn one order of magnitude higher for clarity. Vertical line indicates the most unstable wavelength at 15 m/s case from Funda and Joseph.

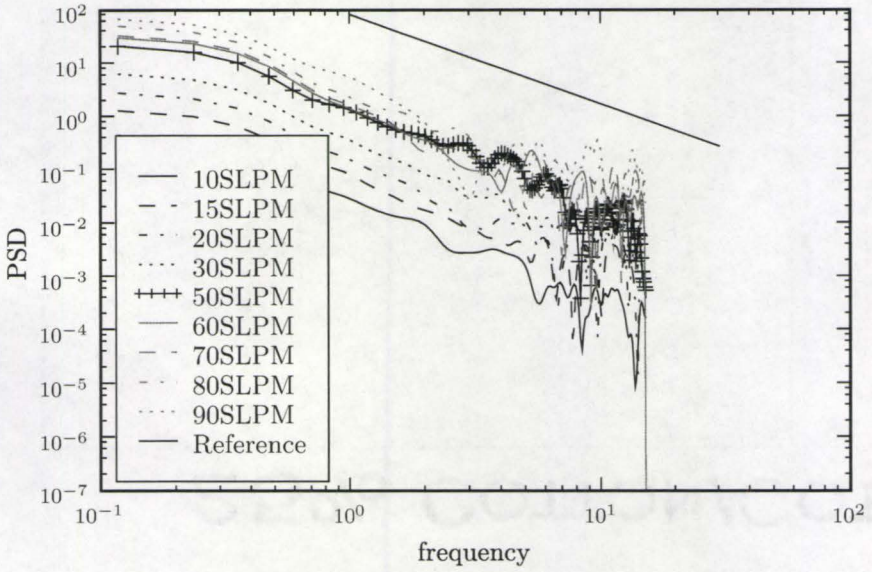
PSD
frequency
10SLPM
15SLPM
20SLPM
30SLPM
50SLPM
60SLPM
70SLPM
80SLPM
90SLPM
Reference

(a) 6 cm

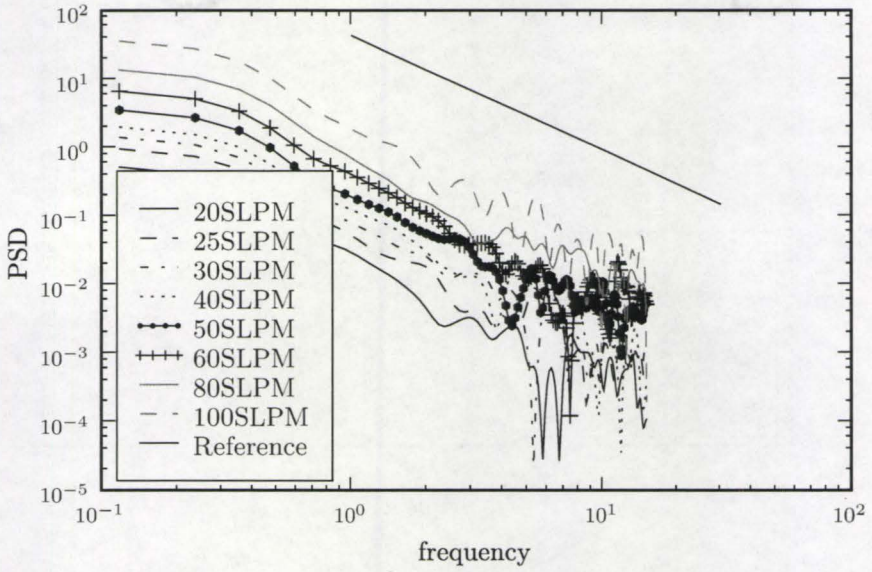
PSD
frequency
20SLPM
25SLPM
30SLPM
40SLPM
50SLPM
60SLPM
80SLPM
100SLPM
Reference

(b) 12 cm

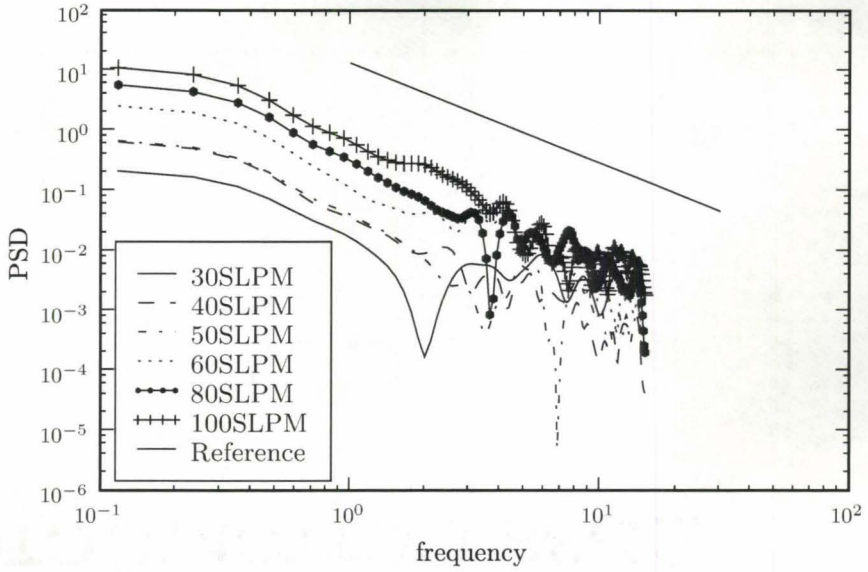

(c) 18 cm

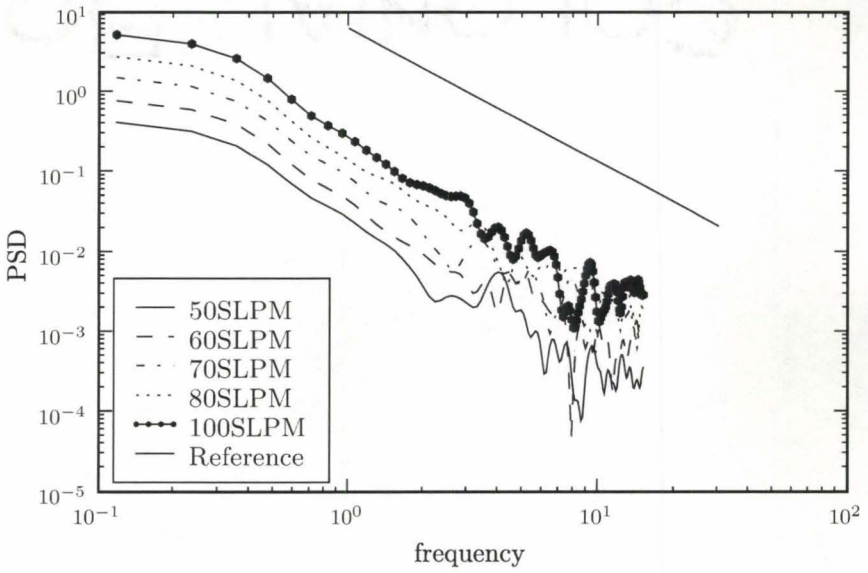

(d) 24 cm

Figure 5.9: Power Spectral Density of cavity depth time series, the slope of the reference line is $-5/3$.

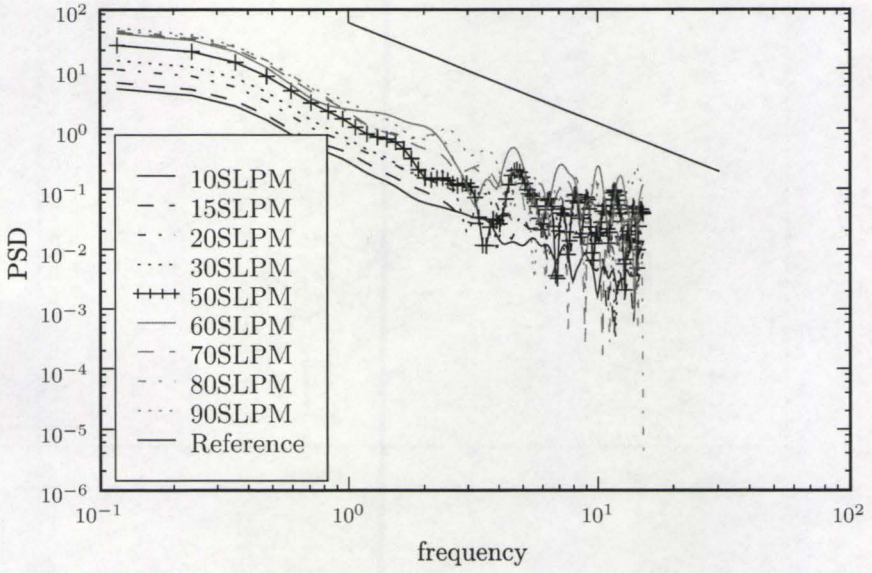
PSD
frequency
10SLPM
15SLPM
20SLPM
30SLPM
50SLPM
60SLPM
70SLPM
80SLPM
90SLPM
Reference

(a) 6 cm

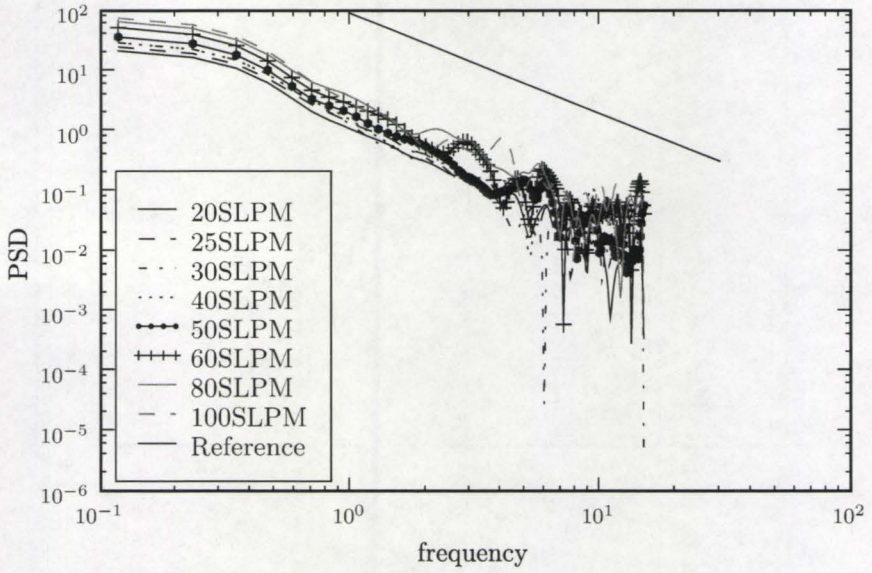
PSD
frequency
20SLPM
25SLPM
30SLPM
40SLPM
50SLPM
60SLPM
80SLPM
100SLPM
Reference

(b) 12 cm

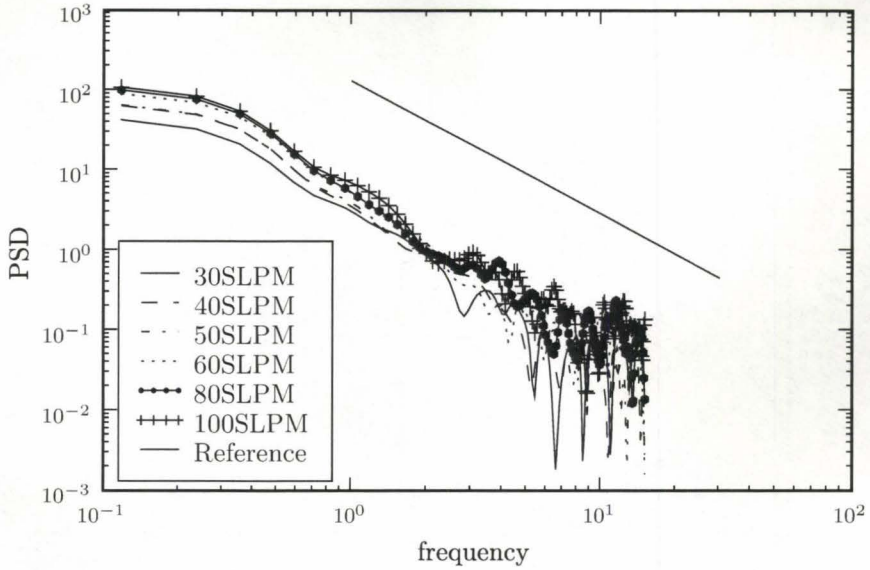

(c) 18 cm

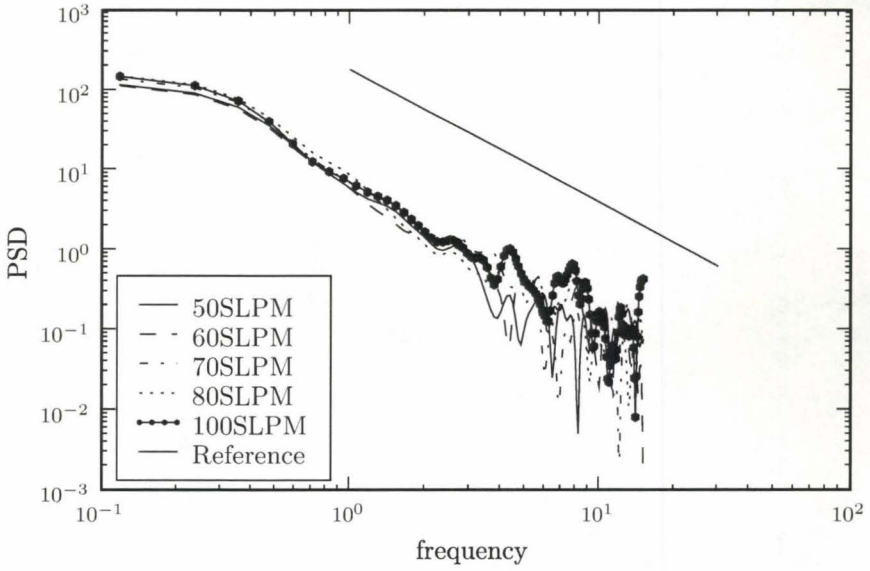

(d) 24 cm

Figure 5.10: Power Spectral Density of cavity width time series, the slope of the reference line is $-5/3$.

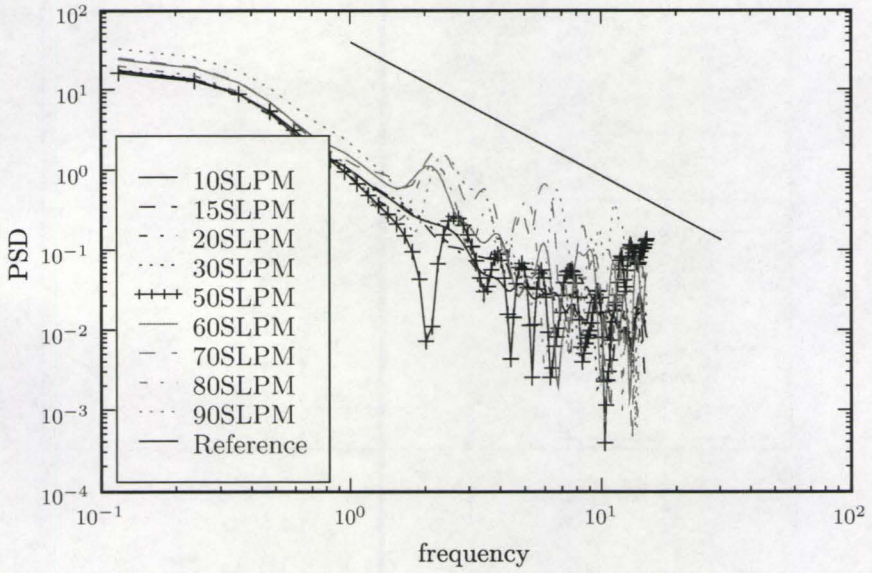
PSD
frequency
10SLPM
15SLPM
20SLPM
30SLPM
50SLPM
60SLPM
70SLPM
80SLPM
90SLPM
Reference

(a) 6 cm

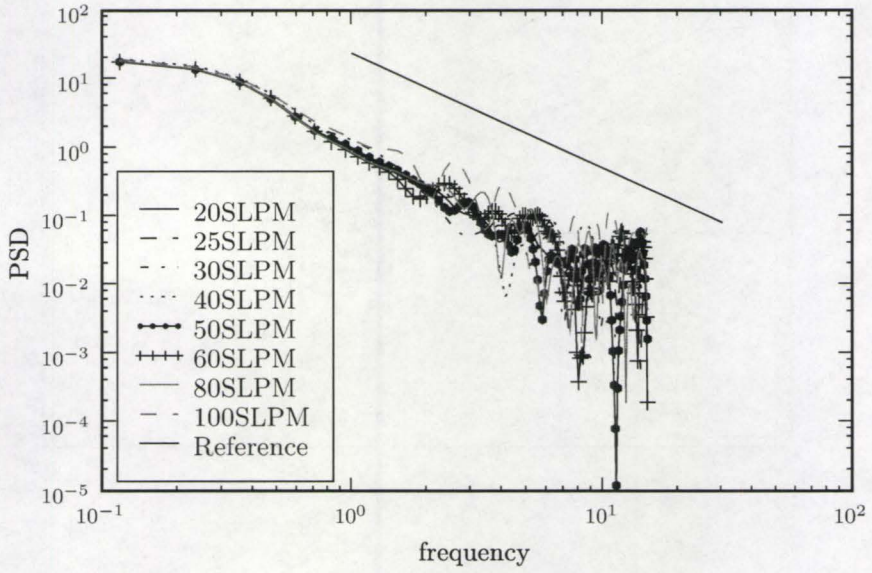
PSD
frequency
20SLPM
25SLPM
30SLPM
40SLPM
50SLPM
60SLPM
80SLPM
100SLPM
Reference

(b) 12 cm

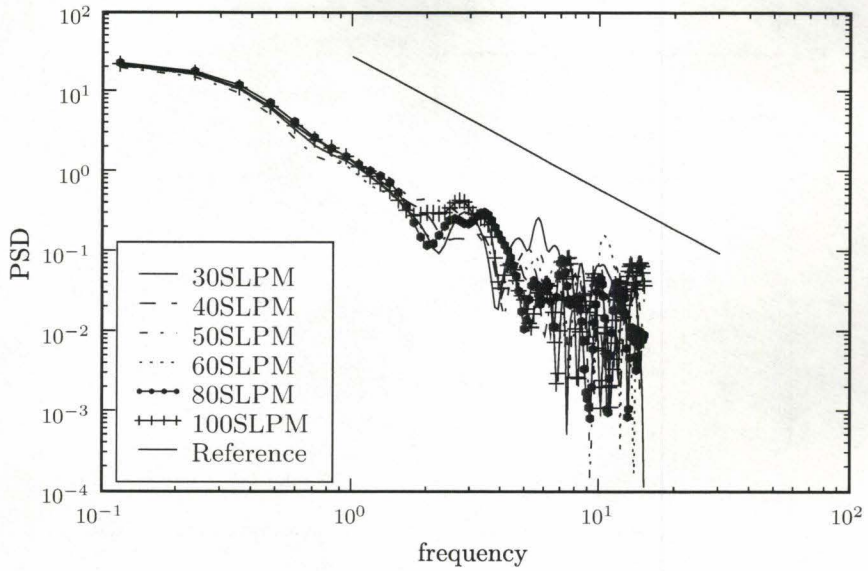

(c) 18 cm

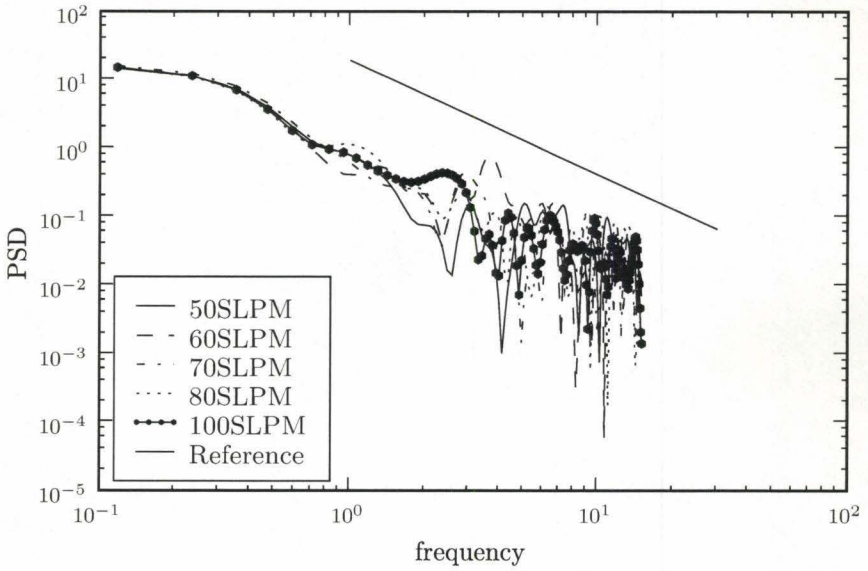

(d) 24 cm

Figure 5.11: Power Spectral Density of cavity horizontal position of stagnant point time series, the slope of the reference line is $-5/3$.

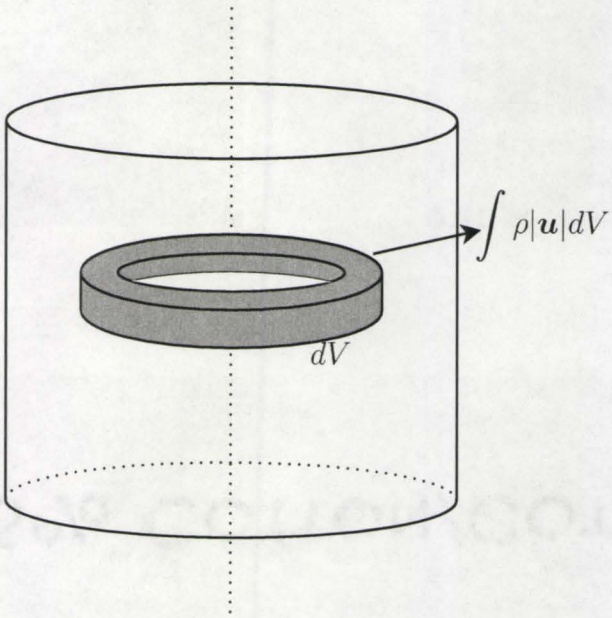

Figure 5.12: An example of circular volume to compute the integral of momentum in cylinder.

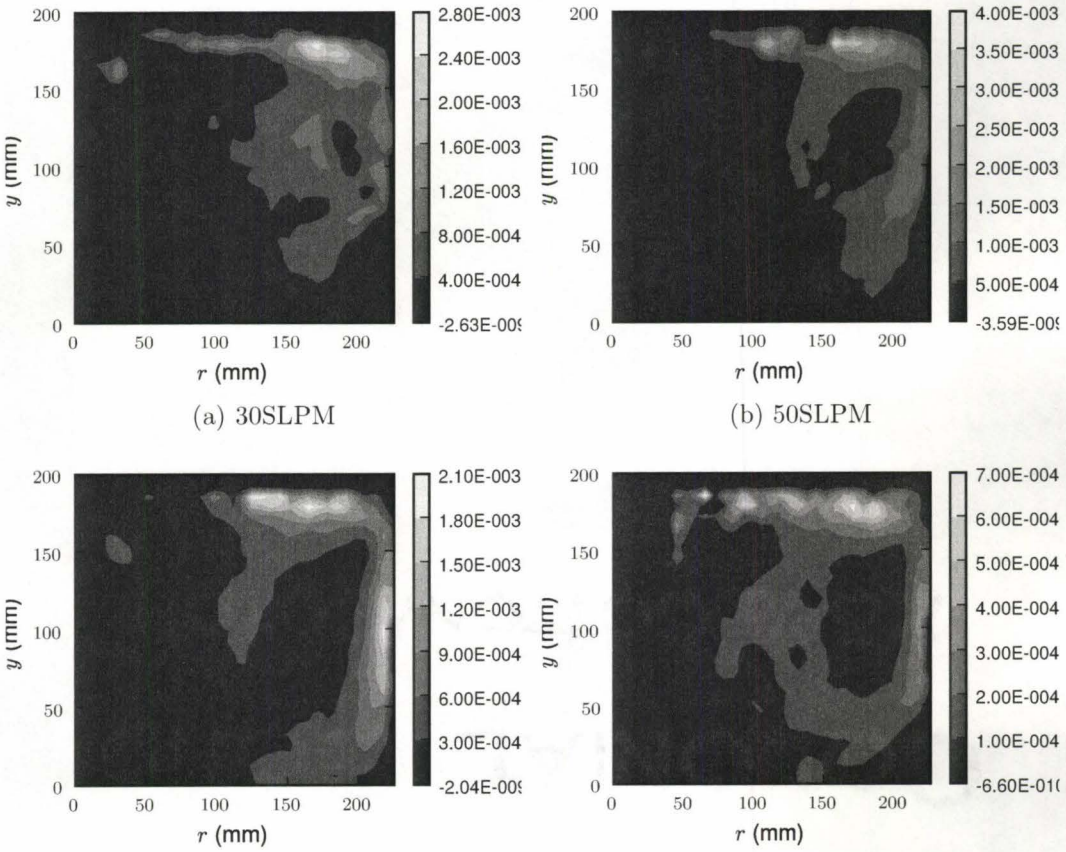

(a) 30SLPM (b) 50SLPM

(c) 70SLPM (d) 100SLPM

Figure 5.13: Selection of plots of relative energy transfer index in 6 cm height case.

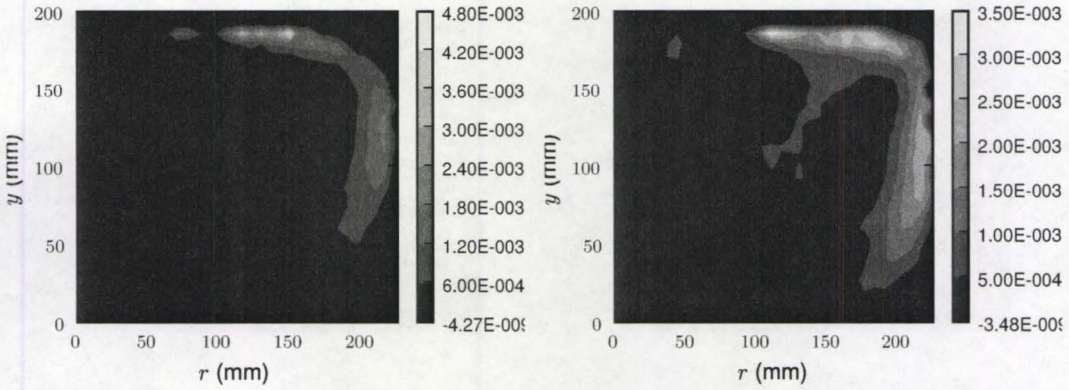

(a) 50SLPM (b) 60SLPM

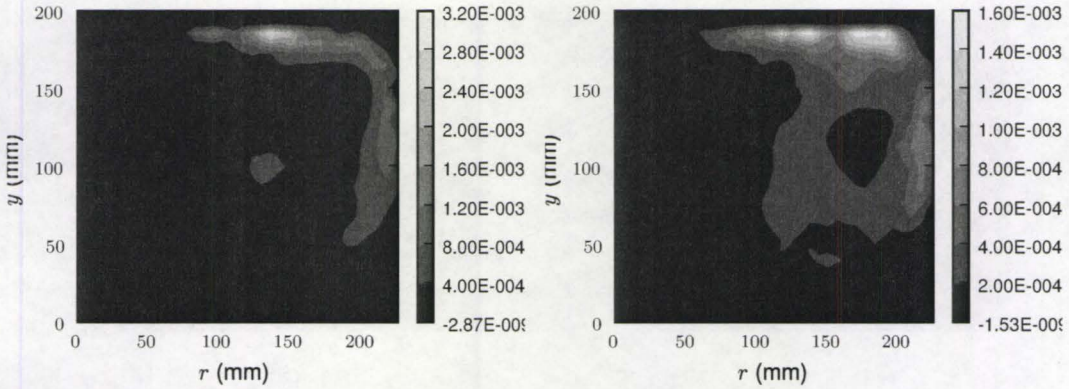

(c) 80SLPM (d) 100SLPM

Figure 5.14: Selection of plots of relative energy transfer index in 12 cm height case.

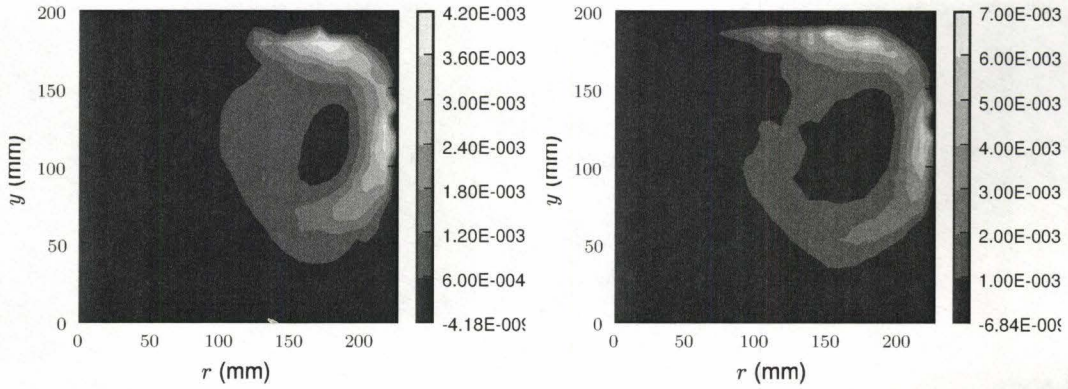

(a) 50SLPM (b) 60SLPM

(c) 80SLPM (d) 100SLPM

Figure 5.15: Selection of plots of relative energy transfer index in 18 cm height case.

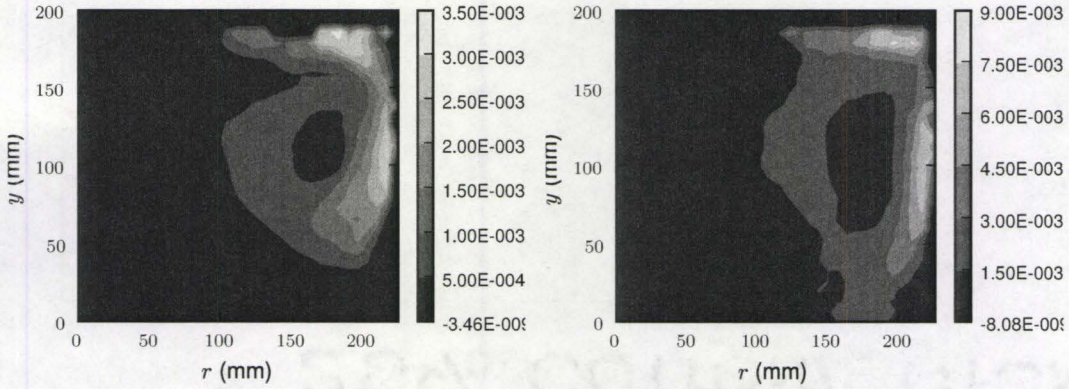

(a) 50SLPM (b) 70SLPM

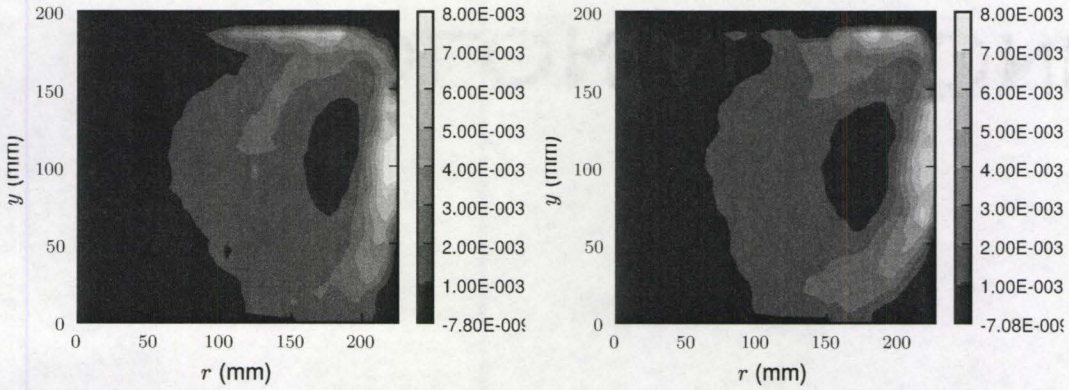

(c) 80SLPM (d) 100SLPM

Figure 5.16: Selection of plots of relative energy transfer index in 24 cm height case.

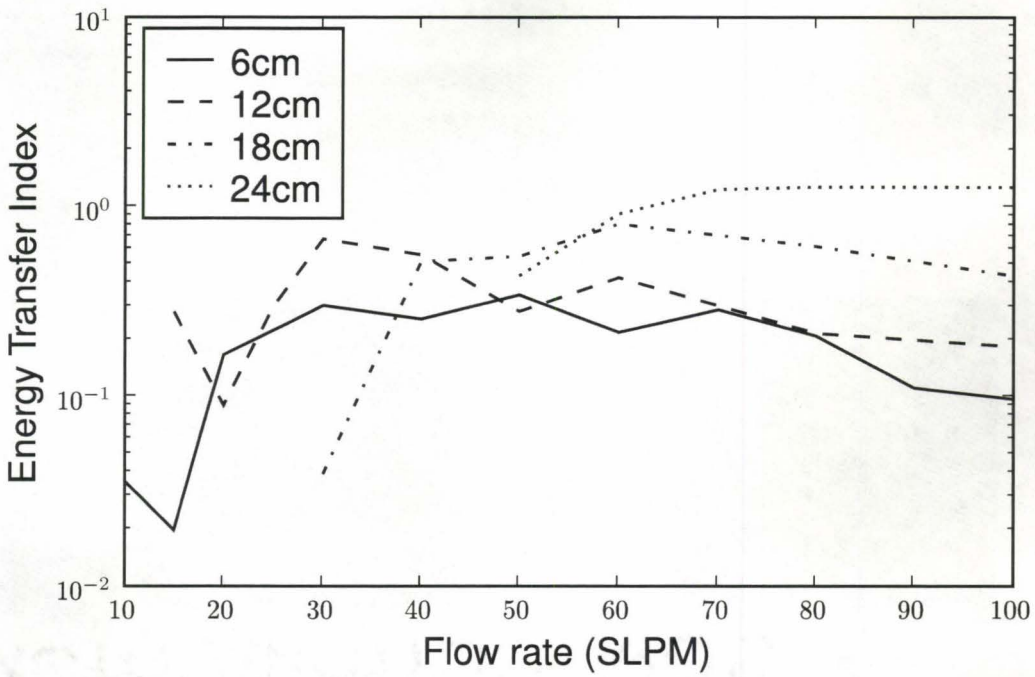

Figure 5.17: A comparison of the sum of energy transfer parameter, $\mathcal{I}$. The efficiency changes around 60 SLPM .

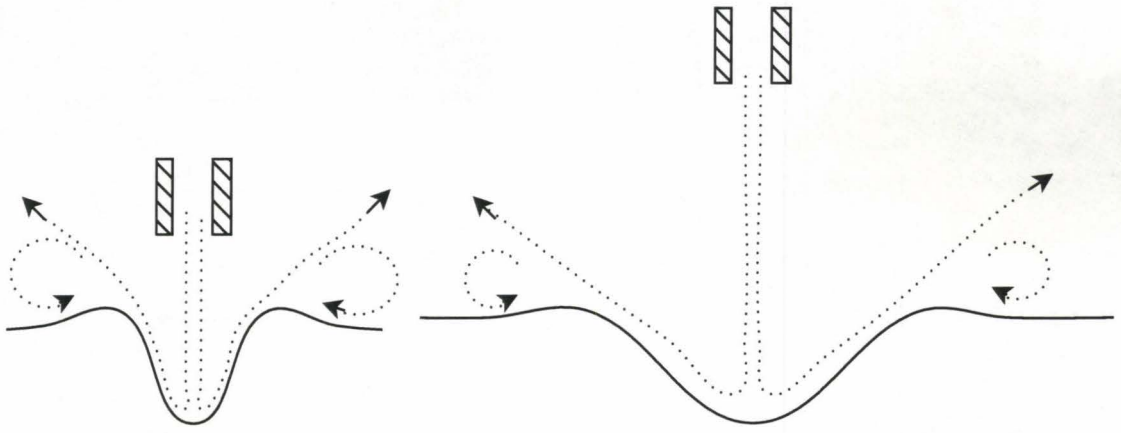

(a) Deep penetration (b) Wide depression

Figure 5.18: A Schematic diagram of momentum transfer comparison for deep penetration and wide cavity.

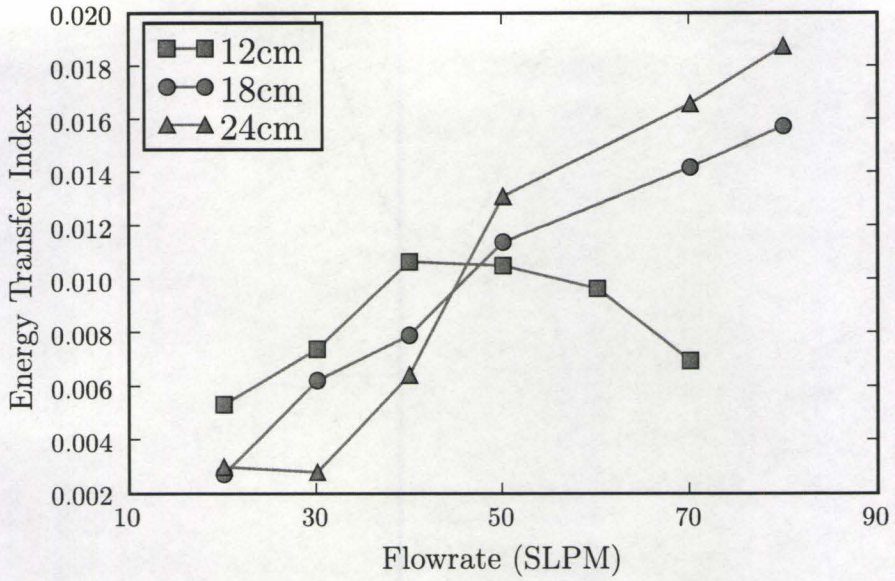

Figure 5.19: A comparison of the sum of energy transfer index, $\mathcal{I}$ in the case of impinging jet mathematical modelling.

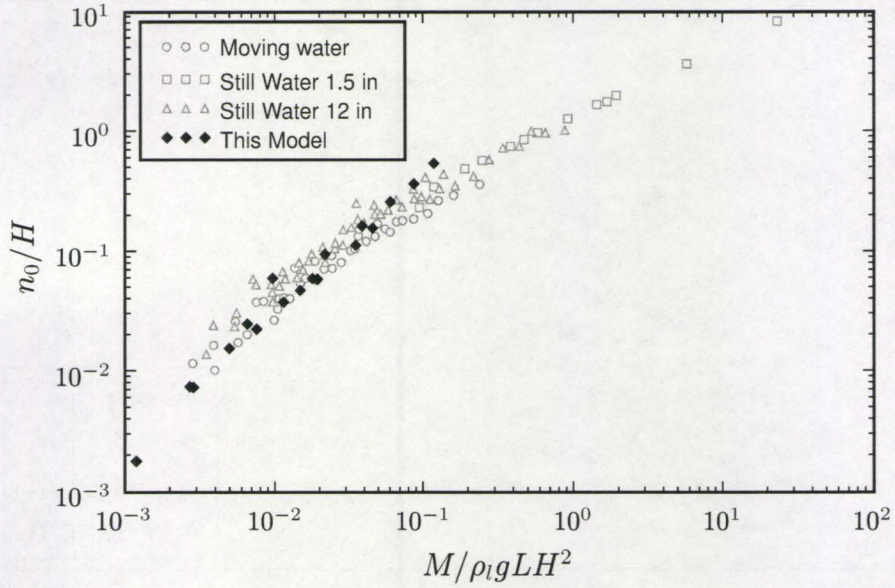

Figure 5.20: A comparison of computed and experimental dimensionless relationship for depression depth. Open symbols are from the experiments of Banks and Chandrasekhara (1963).

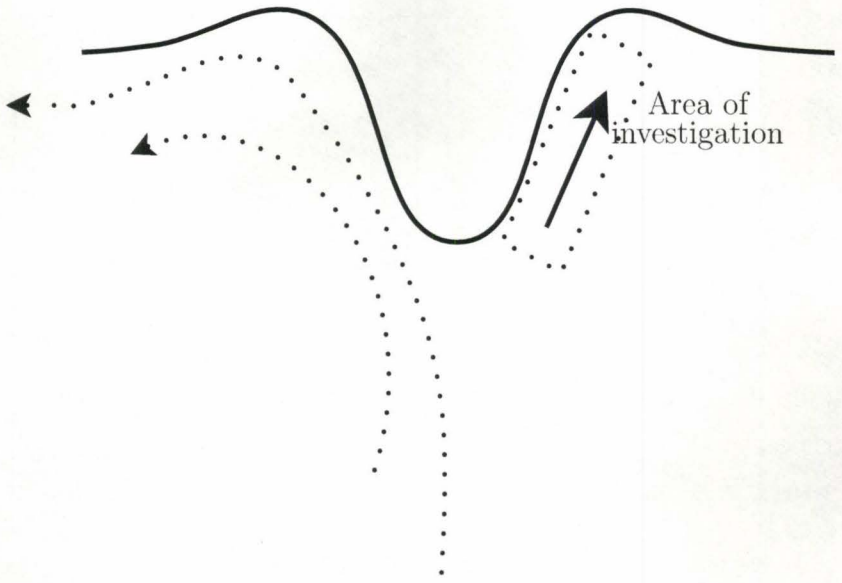

Figure 5.21: A schematic diagram of the selected area for characteristic velocity data from PIV measurement.

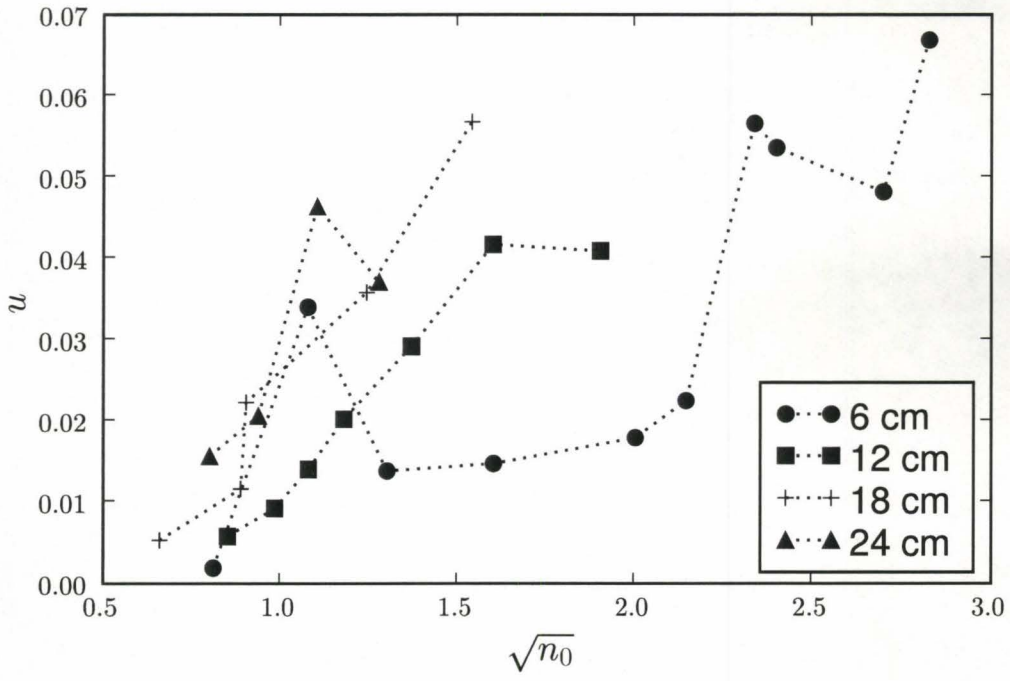

Figure 5.22: The measured characteristic velocity and length around the cavity.

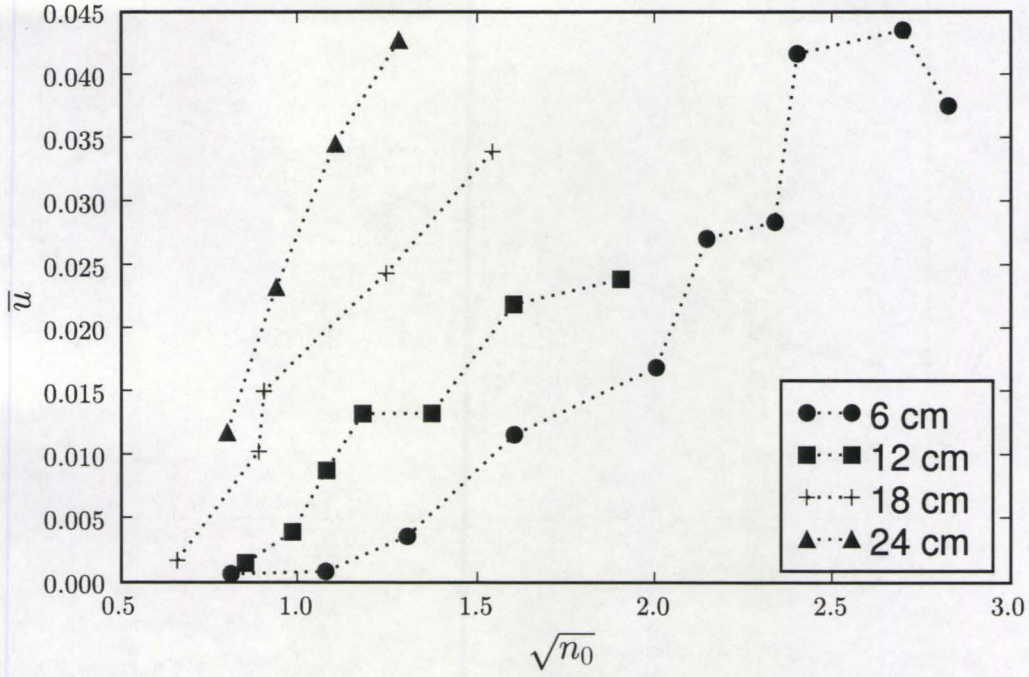

Figure 5.23: The measured volume average velocity and length

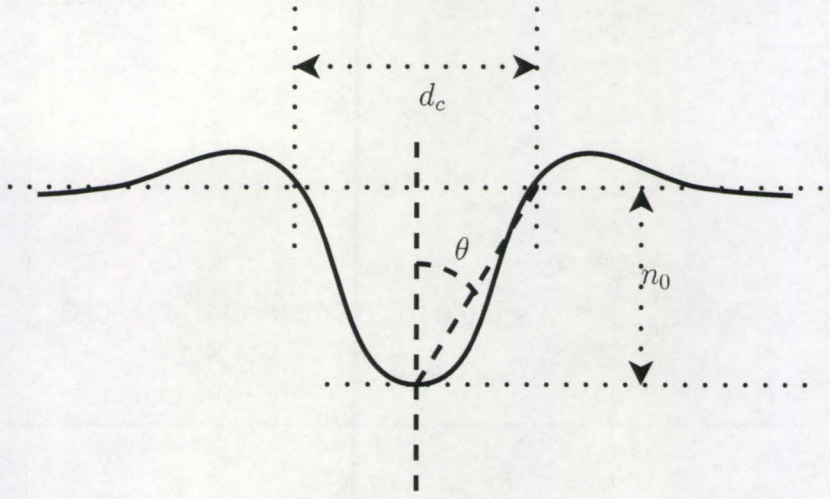

Figure 5.24: The definition of approximate angle of cavity steepness

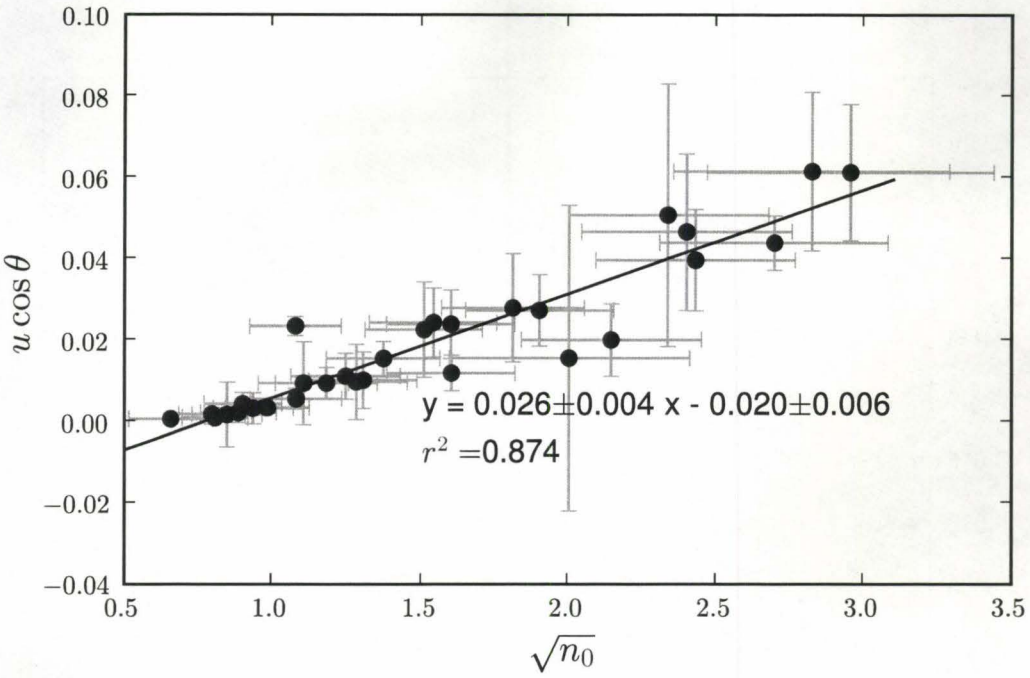

Figure 5.25: A correlation between the measured characteristic velocity with cosine shape factor and dimensionless length around the cavity.

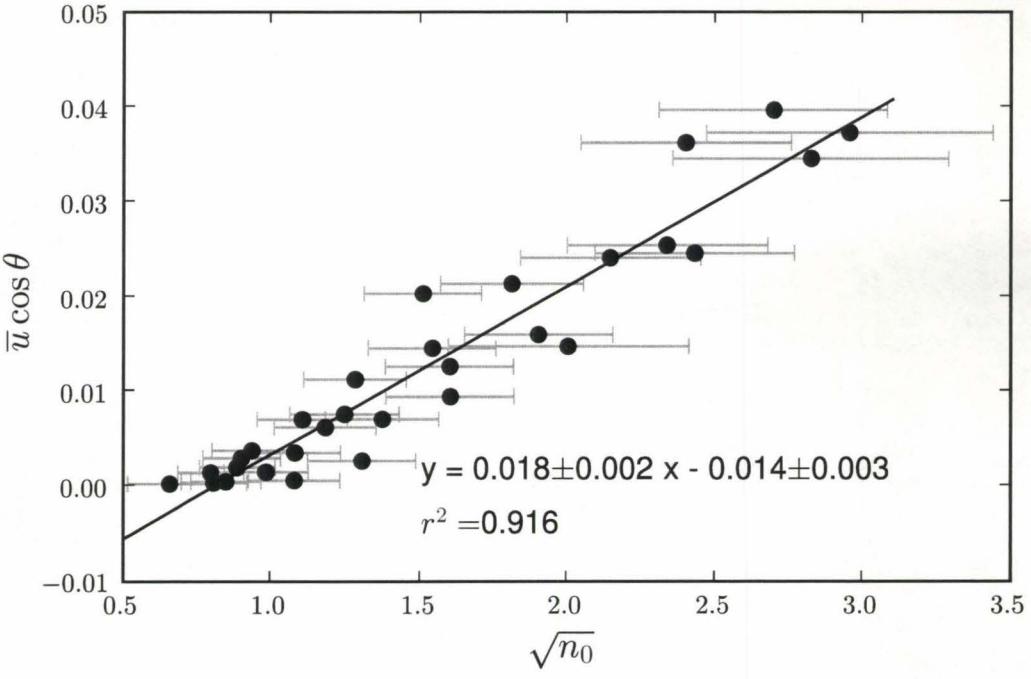

Figure 5.26: A correlation between the measured volume average characteristic velocity with cosine shape factor and dimensionless length.

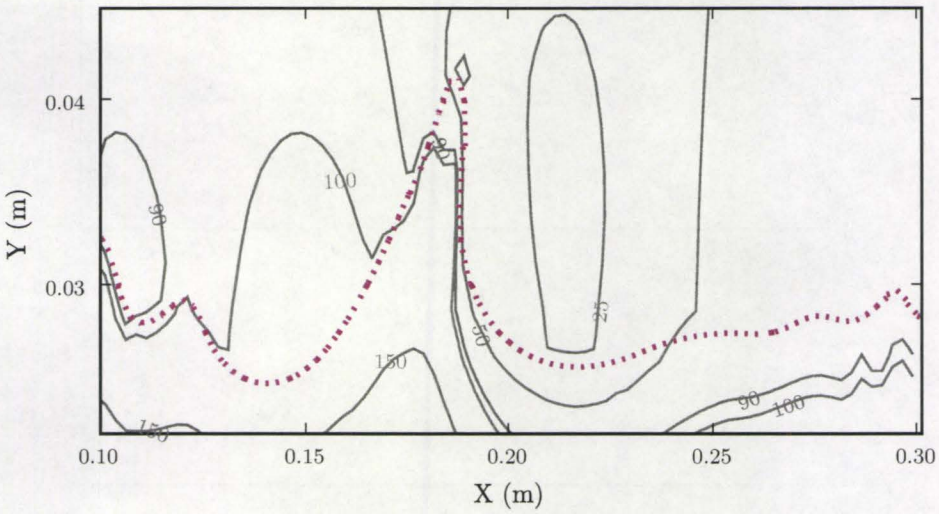

Figure 5.27: A Pressure map around the wave crest which has gas separation in the leeward side. The figure is at the same time step with the Figure 4.16d. The dotted line is the surface profile. Solid lines are pressure levels.

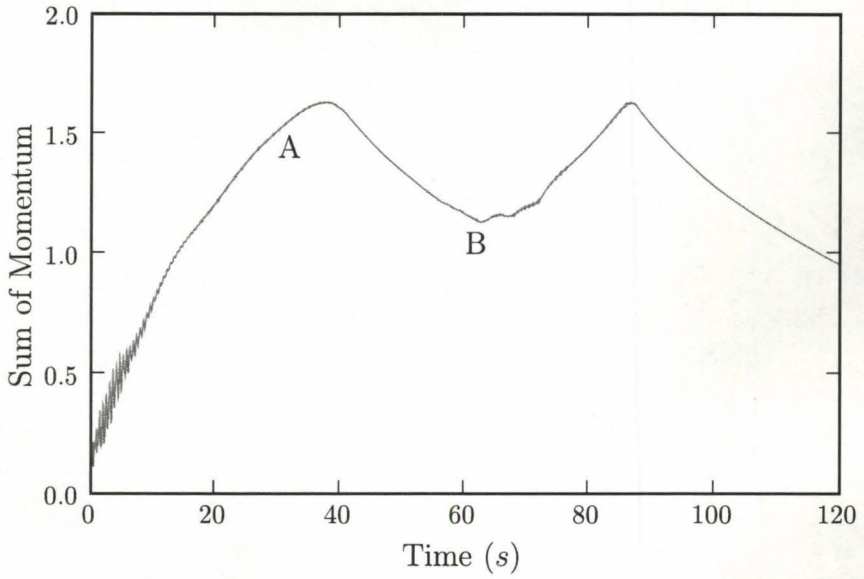

(a)

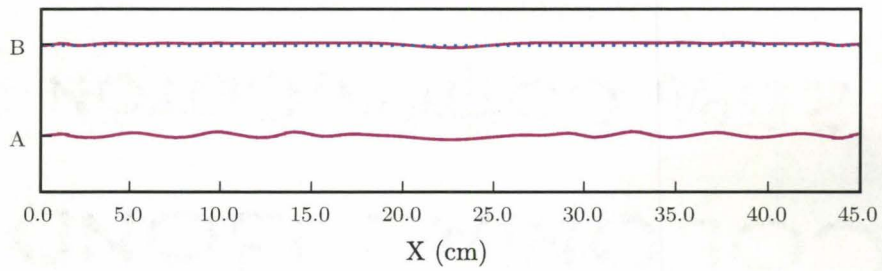

(b)

Figure 5.28: The effect of the surface shape on the momentum transfer from the gas to liquid. Presence of the surface wave increases the momentum transfer level.

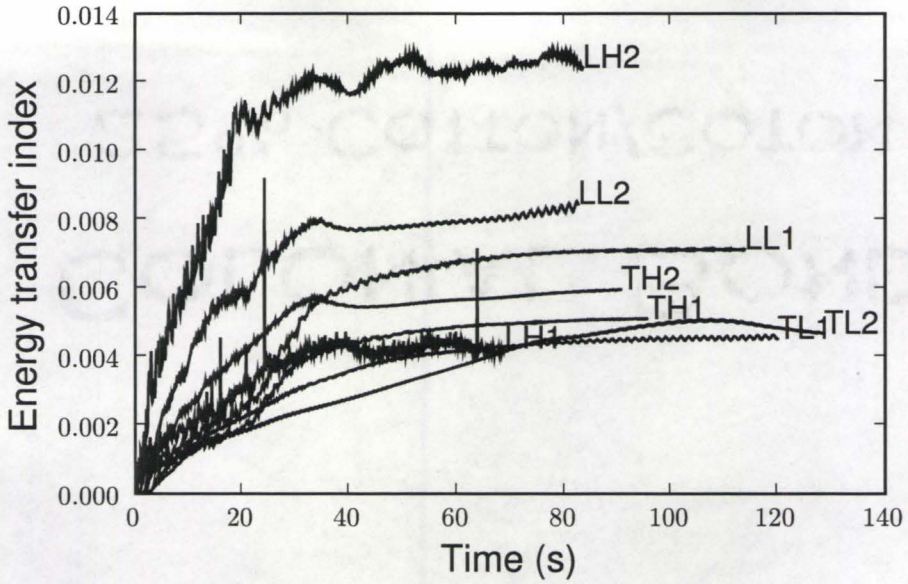

Figure 5.29: The kinetic energy transfer index for steel and slag melt cases. See Table 4.5 for Nomenclature.

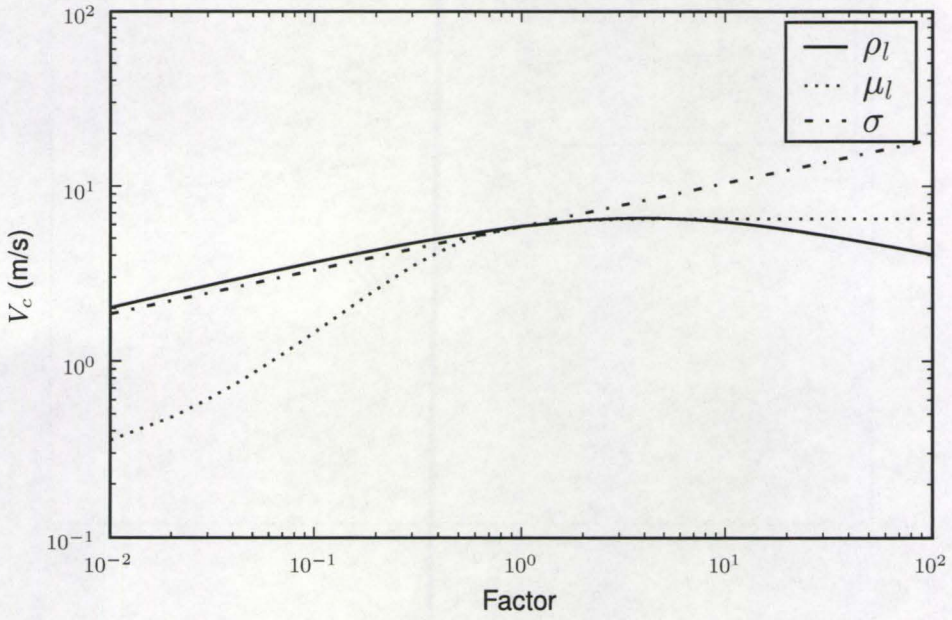

Figure 5.30: Variation of the critical velocity difference from the viscous potential theory (Funda and Joseph 2001). A factor of unity corresponds to the air water case listed in Table 4.1. The curves show the effect of changing ρ_l, μ_l, σ by factors.

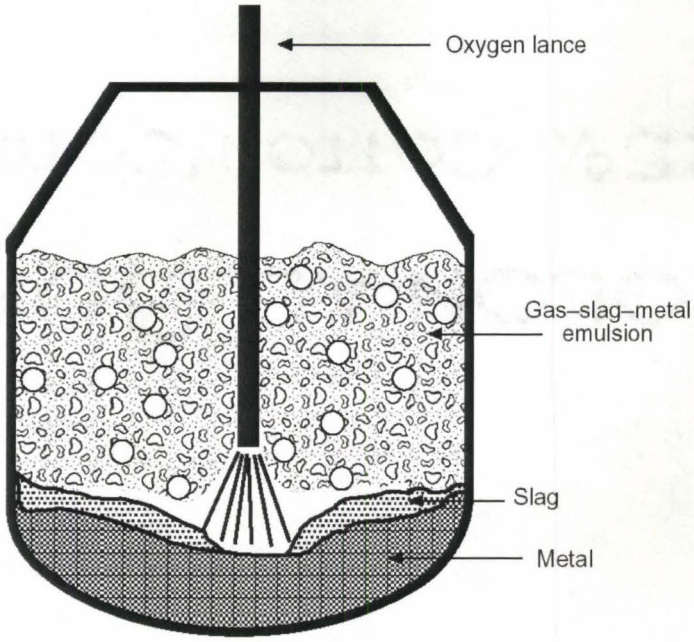

Figure 5.31: Schematic diagram of BOF steelmaking situation and interfacial boundaries (Fruehan 1998).

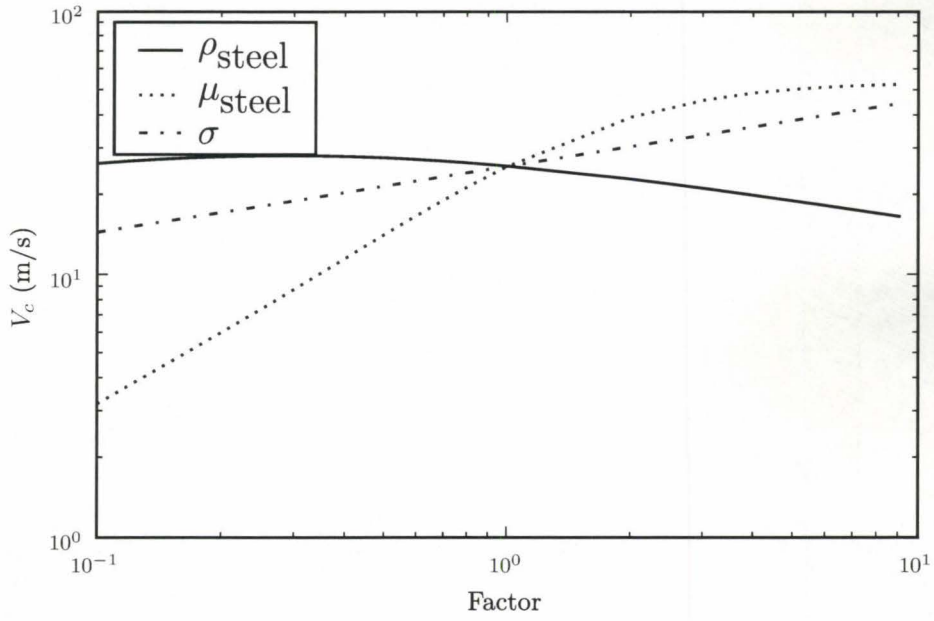

Figure 5.32: Variation of the critical velocity difference of Gas/Steel interface calculated from the viscous potential theory (Funda and Joseph 2001). A factor of unity corresponds to the O_2/Steel case listed in Table 4.4. The curves show the effect of changing ρ_{steel}, μ_{steel}, σ by factors.

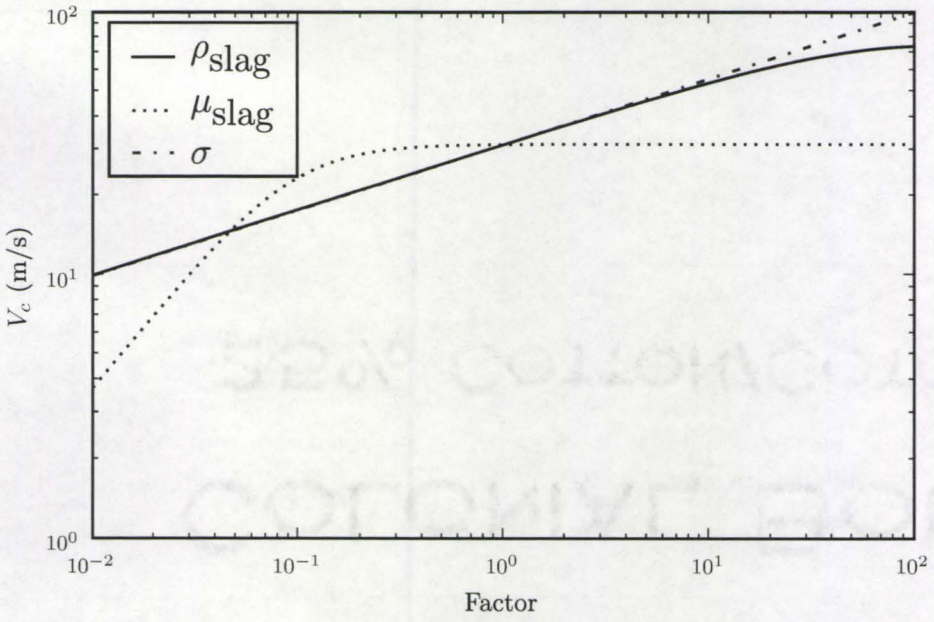

Figure 5.33: Variation of the critical velocity difference of Gas/Slag interface calculated from the viscous potential theory (Funda and Joseph 2001). A factor of unity corresponds to the O_2/Slag case listed in Table 4.4. The curves show the effect of changing ρ_{slag}, μ_{slag}, σ by factors.

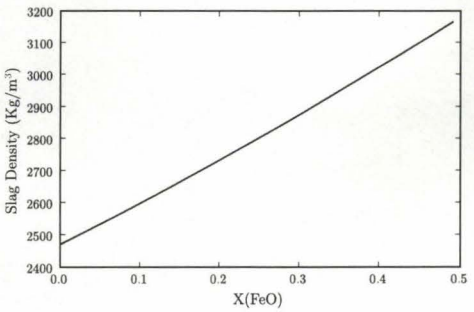

(a) Slag Density

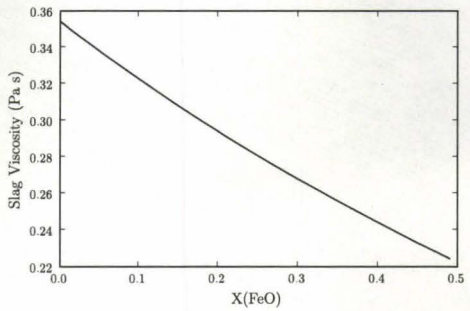

(b) Slag Viscosity

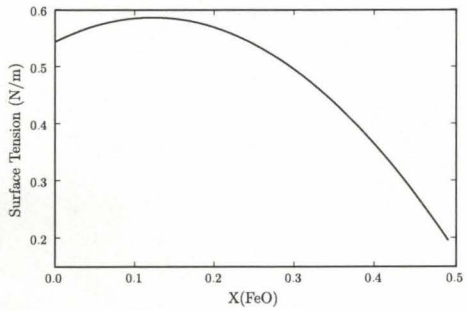

(c) Slag Surface Tension

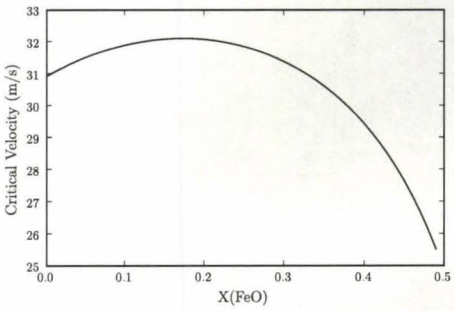

(d) Critical Velocity

Figure 5.34: Variation of slag physical properties with changing FeO content (a), (b) and (c). (d) The critical velocity for a gas/slag interface as a function of FeO content, based on the physical properties in (a), (b) and (c). X_{SiO_2} was fixed as 0.3, and the balance was a CaO.

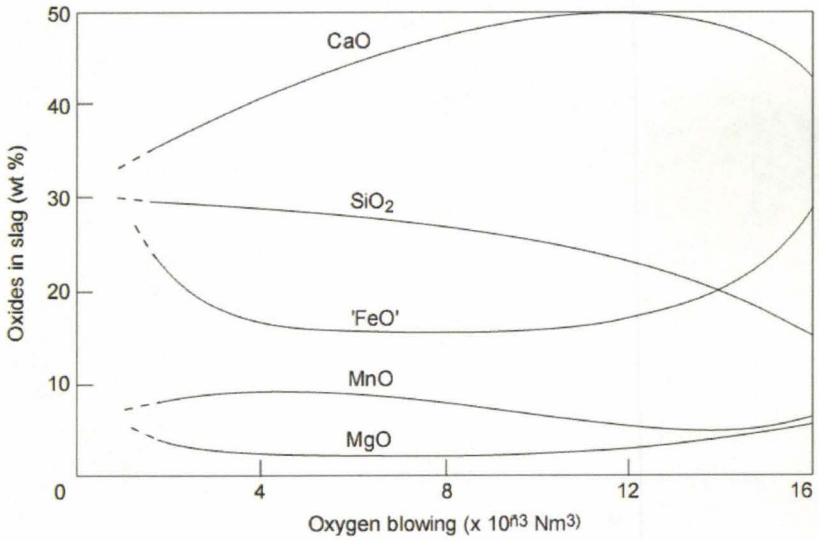

Figure 5.35: A typical slag composition change during BOF oxygen blowing operation Fig. 9.9 from Fruehan (1998).

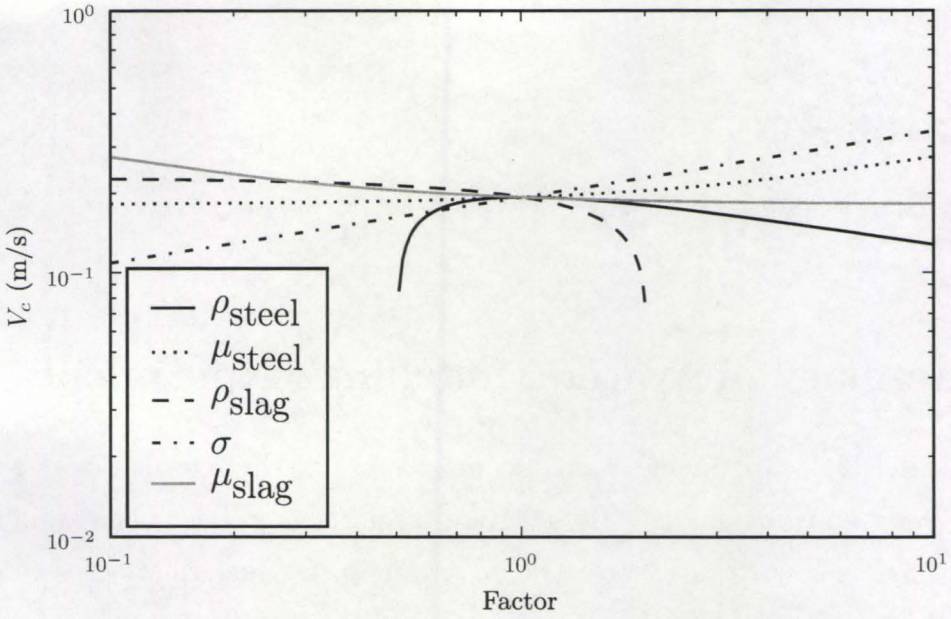

Figure 5.36: Variation of the critical velocity difference of Slag/Steel interface calculated from the viscous potential theory (Funda and Joseph 2001). A factor of unity corresponds to the Slag/Steel case listed in Table 4.4 and interfacial tension (0.4 N/m) from VDEh (1995). The curves show the effect of changing ρ_{steel}, μ_{steel},ρ_{slag}, μ_{slag}, σ by factors.

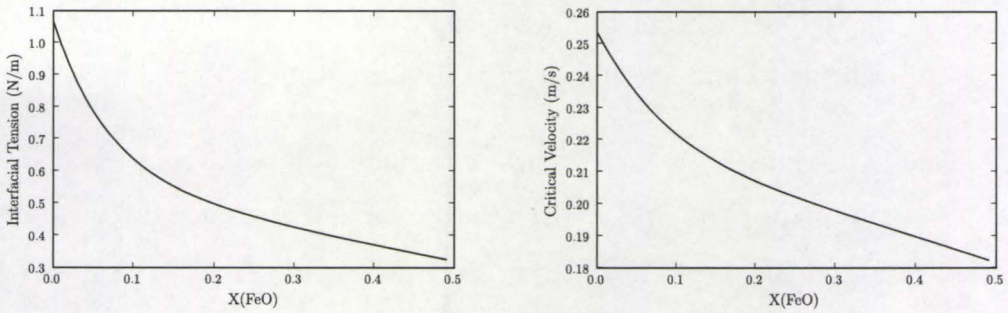

(a) Interfacial Tension

(b) Critical Velocity

Figure 5.37: Variation of Slag/Steel interfacial tension with changing FeO content and critical velocity. X_{SiO_2} was fixed as 0.3, interfacial tension data was from (VDEh 1995).

Chapter 6

Conclusions

6.1 Summary of Water Modelling Experiments

Water modelling experiments were designed to observe the deformation of a liquid surface by an impinging gas jet. Images were taken using a video camera and they were processed in a systematic way. The important surface deformation parameters: depth, width, oscillation, and their frequencies, were obtained.

Surface depression depth and the supplied gas momentum matched with other researchers' correlations and were extended to higher flowrates.

Surface instability and the onset of splashing were observed and interpreted with the Blowing number. The wave behaviours were qualitatively described through the video pictures and PSD analysis was used to extract the characteristic wavenumber range of each gas flowrate. The Fast Fourier transform technique was applied to determine the characteristic oscillation frequency. Oscillation varied within 2 to 12 Hz, but it was difficult to find specific characteristic frequencies.

PSD analysis of time series of the surface variables shows a connection to the attenuation of turbulence gas pressure fluctuation and the surface deformation by gas impingement.

Bath velocities were measured with the PIV technique. An energy transfer index was defined and the momentum and injection flowrate were compared. Characteristic velocities close to the jet cavity area were extracted from PIV data. The local characteristic velocity and the local length scale showed the Froude number similarity with an appropriate shape factor related with the cavity shape.

6.2 Summary of Mathematical Modelling

The major challenge in this work was to apply the full stress boundary condition to the impinging jet problem. A mathematical modelling using a Cartesian Cut Cell method with the surface construction by volume fraction was developed.

The surface was constructed with line segments. The orientation and curvature were improved with a least squares method. The constructed line segments separated the computation domain for each phase and each momentum and mass equation was solved. For the stability of the computation, small cells are merged to the neighbour cells. The surface boundary was modelled as a pressure boundary. The pressure was extrapolated from the gas phase and the pressure satisfying the normal stress condition was applied to the liquid domain. The tangential stress condition was treated separately. The computation was accelerated with the Multigrid method. False correction across the phase boundary was prevented by separating multigrid nodes.

The computational code was validated with the Broken Dam problem. The results were compared with those of others. Wave and instability generation were tested and compared with calculations using FLUENT^{TM}, the code better reproduced physically observed critical velocities.

Gas impingement on a liquid surface was modelled in Cartesian coordinate with similar geometrical dimensions of the experiments. Surface shape variations, time to reach steady state and momentum level were compared over a range of flowrates and physical properties. The simulation was extended to larger size container with steel and slag as liquids at the elevated temperature. The jet velocity was not well simulated because the temperature and reaction effects were omitted. However, the local force balance was well reproduced. Momentum transfer mechanisms were proposed with computational evidence and the effect of the surface tension and viscosity on the instability were discussed for air/water and steelmaking situations.

6.3 Findings from Experiments

1. Surface depression depth and jet momentum follows the dimensionless relationship

$$\frac{n_0}{h}\left(1+\frac{n_0}{h}\right)^2 = 60.941\frac{2\dot{M}}{\pi\rho_l g h} + 0.009 \qquad (6.1)$$

and the slope($K^2 = 60.941$) shows reasonable match with turbulent gas jet coefficients reported and measured by jet velocity.

2. Molloy's classification was re-interpreted with the impact velocity at the dimpled surface depth, which gives better agreement for the onset of droplet formation from the Kelvin-Helmholtz instability.
3. Qian's dimensionless relationship was extended to higher flowrate and a new relationship was obtained.

$$F_q = 0.0358\left(\frac{h+n_0}{d_0}\right)^2 + 0.353\left(\frac{h+n_0}{d_0}\right) - 22.615 \qquad \text{rms} = 3.17 \qquad (6.2)$$

4. The derivation of Blowing number was investigated and the problem of its assumption on the deflection velocity close to the cavity area was discussed. However, the practical usage and the interpretation as a criteria of the onset of splashing was valid and it is also confirmed experimentally.
5. PSD of time series of the surface variable shows the slope of $-5/3$, which is much smaller than the general surface wave theories. It seems to be related with the attenuation of the pressure fluctuation at the impinging point.
6. PIV was used to measure the bath circulation velocity. Momentum was not effectively coupled to the liquid beyond the penetration range. The momentum level was high close to the surface at the top and side, but was dissipated at the bottom.

6.4 Findings from Mathematical Modelling

1. A new computational method was developed to apply the full stress boundary condition by combining the VOF method and the Cartesian Cut Cell technique.
2. The Broken Dam test at two different sizes of grid showed almost the same dimensionless result. The surging front matches well with other papers' results, but there was some discrepancy between the computation and the measurement of Martin and Moyce.
3. The remaining height of liquid in the Broken Dam test matched well with Martin and Moyce's result.
4. Surface wave formation and instability was modelled. The wave instability started above 6 m/s gas velocity and droplets were generated at 8 m/s. The

instability behaviour and gas velocity range matched well with physically observed range. This test was compared with FLUENT^{TM}calculation using conventional VOF method, Cartesian Cut Cell version of VOF method (this study) showed more momentum transfer and wave insatbility closer to real situation than FLUENT^{TM}simulation.

5. Impinging gas jet simulation in Cartesian coordinate showed similar surface depth to experiment, but the width of the jet cavity was considerably wider than the experiments.
6. Liquid momentum level was increased as the gas flowrate increased and jetting distance decreased.
7. Simple considerations regarding the gas entrainment assumption for the gas jet propagation was not reproduced in the high temperature reacting situation. However, it was able to reproduce the local force balance and kinetic energy transfer trends.
8. The physical properties affect the surface shape, instability and momentum transfer efficiency. Increased liquid density and gravity reduced surface depression and instability. Increased surface tension did not change the depression depth, but created a reduction of instability which decreased momentum transfer efficiency. Viscosity had little effect on the surface shapes.

6.5 Conclusions

The following findings are considered to be novel.

1. Critical depth of water varies around 1.2 cm and it decreases with increasing jetting distance due to the increased chance to grow wave instability.
2. Wave behaviour was analyzed with the PSD technique and observation of images and PSD both show a sudden change in the wavenumber in the penetration range.
3. Energy transfer index shows the increase of efficiency with increase of lance height within the range of current experiments. This is due to the activated or contact area difference between the low and high lance height cases as proposed by the instability.

4. Velocities tangential to the jet cavity surface from PIV data showed good linear relationship between the cosine of velocity and the sqaure root of the depression depth. This suggests a Froude number similarity with cavity shape function. However, this requires further experimental and theoretical evidence.
5. Momentum transfer mechanisms were proposed. Besides the increased tangential shear stress, the local pressure gradient contributed to the acceleration of liquid in the wave crest.
6. A surface tension increase decreased momentum transfer efficiency by reducing instability.
7. In a steelmaking situation, the critical velocity for Kelvin-Helmholtz instability is lowest for the slag-metal interface, compared to the gas-slag and gas-steel interface. Furthermore it is directly reduced as the surface tension. Higher FeO content in slag phase reduces the surface tension and promotes instability.

Bibliography

Anderson, A. R. & Johns, F. R. 1955, Jan, Jet Propulsion, 13–15,25.

Apsley, D. & Hu, W. 2003, International Journal for Numerical Methods in Fluids, 42, 465–491.

Ashgriz, N., Barbat, T., & Wang, G. 2004, International Journal for Numerical Methods in Fluids, 44, 1–32.

Ashgriz, N. & Poo, J. Y. 1991, Journal of Computational Physics, 93, 449–468.

Banks, R. B. & Chandrasekhara, D. V. 1963, Journal of Fluid Mechanics, 15, 13–34.

Benson, D. J. 2002, Appl. Mech. Rev., 55, 151–165.

Biausser, B., Guignard, S., Marcer, R., & Fraunié, P. 2004, International Journal for Numerical Methods in Fluids, 45, 581–604.

Blackbill, J., Kothe, D., & Zemach, C. 1992, Journal of Computational Physics, 100, 335–354.

Brocchini, M. 2002, Physics of Fluids *14*(6), 1834–1840.

Brocchini, M. & Peregrine, D. H. 2001a, Journal of Fluid Mechanics, 449, 225–254.

Brocchini, M. & Peregrine, D. H. 2001b, Journal of Fluid Mechanics, 449, 255–290.

Brumley, B. H. & Jirka, G. H. 1987, Journal of Fluid Mechanics, 183, 235–263.

Caboussat, A. 2005, Archives of Computational Methods in Engineering *12*(2), 165–224.

Ceniceros, H. D. 2003, Physics of Fluid, 15, 245–256.

Chandrasekhar, S. 1961. *Hydrodynamic and Hydromagnetic Stability.* New York: Dover Publication INC.

Chang, Y. C., Hou, T. Y., Merriman, B., & Osher, S. 1996, Journal of Computational Physics, 124, 449–464.

Chatterjee, A. & Bradshaw, A. V. 1972, Mar, Journal of the iron and steel institutue, 179–187.

Chatterjee, A., Lindfors, N.-O., & Wester, J. A. 1976, Ironmaking and Steelmaking (1), 21–32.

Chen, C.-W. & Hwang, W.-S. 1995, ISIJ international *35*(4), 393–401.

Chen, S., Johnson, D. B., & Raad, P. E. 1995, Journal of Computational Physics, 116, 262–276.

Chen, X. 2003, International Journal for Numerical Methods in Fluids, 42, 929–952.

Cheslak, F. R., Nicholls, J. A., & Sichel, M. 1969, Journal of Fluid Mechanics, 36, 55–62.

Choi, S. K. 1999, Numerical Heat Transfer, Part A, 36, 545–550.

Clarke, D. K., Salas, M. D., & Hassan, H. A. 1986, AIAA Journal *24*(3), 353–358.

Coirier, W. J. & Powell, K. G. 1995, Journal of Computational Physics, 117, 121–131.

Cummins, S. J., Francois, M. M., & Kothe, D. B. 2005, Computers and Structures, 83, 425–434.

Dabiri, D. 2003, Journal of Fluid Mechanics, 480, 217–232.

Date, A. W. 2003, International Journal of Heat and Mass Transfer, 46, 4885–4898.

Davenport, W. G., Wakelin, D. H., & Bradshaw, A. V. 1967. Interation of both bubbles and gas jets with liquids. In A. W. D. Hills (Ed.), *Heat and Mass Transfer in Process Metallurgy*, pp. 207–245. London: The Institution of Mining and Metallurgy.

Demirdžić, I., Lilek, Ž., & Perić, M. 1993, International Journal for Numerical Methods in Fluids, 16, 1029–1050.

Demirdžić, I. & Perić, M. 1988, International Journal for Numerical Methods in Fluids, 8, 1037–1050.

Deo, B. & Boom, R. 1993. *Fundamentals of Steelmaking Metallurgy*. Prentice Hall International.

Egelja, A., Schafer, M., & Durst, F. 1998, IJCFD, 10, 213–234.

Elson, J. M. & Bennet, J. M. 1995, Applied Optics *34*(1), 201–208.

Enright, D., Fedkiw, R., Ferziger, J., & Mitchell, I. 2002, Journal of Computational Physics, 183, 83–116.

Ersson, M., Tilliander, A., & Pär, J. 2006, In *Sohn International Symposium Advanced processing of metals and materials*, Volume 2, pp. 271–281.

Evestedt, M. & Medvedev, A. 2004, In *AISTech 2004 Proceedings*, Volume 1.

Falcon, É., Laroche, C., & Fauve, S. 2007, Physical Review Letter, 98, 094503.

Fedkiw, R. & Liu, X.-D. 2002. The ghost fluid method for viscous flows. In M. Hafez and J.-J. Chattot (Eds.), *Innovative Methods for Numerical Solutions of Partial Differential Equations*. New Jersey: World Scientific Publishing.

Fedkiw, R. P. & Osher, S. J. 2002. *Level Set Methods and Dynamic Implicit Surfaces*. Springer.

Ferziger, J. H. & Perić, M. 2002a. *Computational Methods for Fluid Dynamics* (third, rev. edition ed.). Springer-Verlag.

Ferziger, J. H. & Perić, M. 2002b. *Computational Methods for Fluid Dynamics* (third, rev. edition ed.)., Chapter 12, pp. 381–403. Springer-Verlag.

Fluent Inc. 2006. *Fluent User's Guide*.

Forrester, S. E. & Evans, G. M. 1996, In *Third CFX International Users Conference*.

Fruehan, R. J. (Ed.) 1998. *Steelmaking and Refining Volume* (11^{th} ed.). The Making, Shaping and Treating of Steel. The ASME Steel Foundation.

Fulgosi, M., Lakehal, D., Banerjee, S., & De Angelis, V. 2003, Journal of Fluid Mechanics, 482, 319–345.

Funda, T. & Joseph, D. D. 2001, Journal of Fluid Mechanics, 445, 263–283.

Gaskell, D. R. 1992. *An Introduction to Transport Phenomena in Materials Engineering*. Macmillan Publishing Company.

George, W. K., Beuther, P. D., & Arndt, R. E. 1984, Journal of Fluid Mechanics, 148, 155–191.

Gharib, M. & Daribi, D. 2000. *Flow Visualization*, Chapter 6, pp. 123–147. World Scientific Publishing Company.

Ginzburg, I. & Wittum, G. 2001, Journal of Computational Physics, 166, 302–335.

Gloth, O., Hänel, D., Tran, L., & Vilsmeier, R. 2003, Computers and Fluids, 32, 547–570.

Golub, G. H. & Van Loan, C. 1996. *Matrix Computations* (3rd ed.)., Chapter 10, pp. 508–554. Johns Hopkins Univ. Press.

Greaves, D. 2004, International Journal for Numerical Methods in Fluids, 44, 1093–1117.

Gueyffier, D., Li, J., Nadim, A., Scardovelli, R., & Zaleski, S. 1999, Journal of Computational Physics, 152, 423–456.

Guignard, S., Marcer, R., Rey, V., Kharif, C., & Fraunié, P. 2001, Eur. J. Mech. B-Fluids, 20, 57–74.

Guo, D. & Irons, G. A. 2002, Jun, Metallurgical and Materials Transactions B, 33B, 377–383.

Guo, Y. & Wood, D. H. 2002, Experimental Thermal and Fluid Science, 25, 605–614.

Handler, R. A., Swean Jr., T. F., Leighton, R. I., & Swearingen, J. D. 1993, AIAA journal *31*(11), 1998–2007.

Harlow, F. & Welch, J. 1965, Phys. Fluid, 8, 2182.

Harvie, D. J. E. & Fletcher, D. F. 2001, International Journal for Numerical Methods in Fluids, 35, 151–172.

He, Q. & Standish, N. 1990, ISIJ international *30*(4), 305–309.

Hirt, C. W. & Nichols, B. D. 1981, Journal of Computational Physics, 39, 201–225.

Jeong, J. H. & Yang, D. Y. 1998, International Journal for Numerical Methods in Fluids, 26, 1127–1154.

Jones, E., Oliphant, T., Peterson, P., et al. 2001, SciPy: Open source scientific tools for Python.

Joseph, D. D., Belanger, J., & Beavers, G. S. 1999, International Journal of Multiphase Flow, 25, 1263–1303.

Kang, M., Fedkiw, R. P., & Liu, X.-D. 2000, Journal of Scientific Computing, 15, 323–360.

Kawai, Y. & Shiraishi, Y. (Eds.) 1988. *Handbook of Physico-chemical Properties at High Temperatures*. The Iron and Steel Institute of Japan.

Kean, R. D. & Adriantems, R. J. 1990, Meas. Sci. Technol., 1, 1202–1215.

Kitscha, J. & Kocamustafaogullari, G. 1989, International Journal of Multiphase Flow *15*(4), 573–588.

Koria, S. C. & Lange, K. W. 1987, Steel Research *58*(9), 421–426.

Krishnapisharody, K. 2006. *Model Studies of Fluid Mechnic Interactions Between Steel and Slag In Gas-Stirred Ladles*. Ph. D. thesis, McMaster University.

Lamb, H. 1993. *Hydrodynamics*. Cambridge University Press.

Landau, L. D. & Lifshitz, E. M. 1987. *Fluid Mechanics* (2nd ed.). Pergamon Press.

LaVision 2004. *DaVis FlowMaster Manual*.

Law, A. W.-K. & Herlina 2002, Feb, Journal of Hydraulic Engineering *128*(2), 161–174.

Lee, M., Whitney, V., & Molloy, N. 2001, Scandinavian Jounal of Metallurgy, 30, 330–336.

Lee, M. S., O'Rourke, S. L., & Molloy, N. A. 2003, Scandinavian Journal of Metallurgy, 32, 281–288.

Levesque, R. J. & Shyue, K.-M. 1996, Journal of Computational Physics, 123, 354–368.

Li, R. & Harris, R. L. 1995, In *Pyrometallurgy 95 Conference Proceedings*, London, pp. 107–124. IMM.

Liovic, P., Liow, J.-L., & Rudman, M. 2001, ISIJ international *41*(3), 225–233.

Liovic, P., Rudman, M., & Liow, J.-L. 2002, Applied Mathematical Modelling, 26, 113–140.

Liu, X.-D., Fedkiw, R. P., & Kang, M. 2000, Journal of Computational Physics, 160, 151–178.

Lombardi, P., De Angelis, V., & Banerjee, S. 1996, Phys. Fluids, 8, 1643–1665.

Lommer, M. & Levinsen, M. T. 2002, Journal of Fluorescence, 12, 45–50.

Lu, W. Z., Zhang, W. S., Cui, C. Z., & Leung, A. Y. T. 2004, Computational Mechanics, 33, 215–224.

Majumdar, S. 1988, Numerical Heat Transfer, 13, 125–132.

Maleewong, M., Asavanant, J., & Grimshaw, R. 2004, Advances in Fluid Mechanics, 40, 219–.

Martin, J. C. & Moyce, W. J. 1952, Philosophical Transactions of the Royal Society of London .SeriesA, Mathematical and Physical Sciences *244*(882), 312–324.

Martorano, M. A., Fortes, M. A., & Padilha, A. F. 2006, Modeling and Simulation in Materials Science and Engineering, 14, 83–98.

Meier, M., Yadigaroglu, G., & Smith, B. L. 2002, Eur. J. Mech. B/Fluids, 21, 61–73.

Melling, A. 1997, Meas. Sci. Techno., 8, 1406–1416.

Metcalf, B., Longo, J., Ghosh, & S. Stern, F. 2006, Journal of Fluid and Structures, 22, 77–98.

Meyer, H. W., Porter, W. F., Smith, G. C., & Szekely, J. 1968, Jul, Journal of Metals, 35–42.

Mietz, J., Schneider, S., & Oeters, F. 1991, Steel Research, 62, 10–15.

Mills, K. C., Su, Y., Fox, A. B., Li, Z., Thackray, R. P., & Tsai, H. T. 2005, ISIJ international *45*(5), 619–633.

Mitsuyasu, H. & Honda, T. 1982, Journal of Fluid Mechanics, 123, 425–442.

Molloy, N. A. 1970, Oct, Journal of The Iron and Steel Institute, 943–950.

Munk, W. H. 1947, Journal of Marine Research, 6, 203–218.

Muzaferija, S. & Perić, M. 1997, Numerical Heat Transfer, Part B, 32, 369–384.

Nakanishi, K., Saito, K., Nozaki, T., Kato, Y., ichiro Suzuki, K., & Emi, T. 1982, Steelmaking Conference?, 65, 101–108.

Nguyen, A. & Evans, G. 2003, December, In *The 3rd International Conference on CFD in the Minerals and Process Industries*, pp. 71–76.

Nichols, B. D. & Hirt, C. W. 1971, Journal of Computational Physics, 8, 434–448.

Nichols, D. V., Hirt, C. W., & Hotchkiss, R. S. 1980. SOLA-VOF: A solution algorithm for transient fluid flow with multiple free boundary. Technical report, Los Alamos Scientific Laboratory.

Nordquist, A., Kumbhat, N., Jonsson, L., & Jönsson, P. 2006, Steel reserach int. *77*(2), 82–90.

Odenthal, H.-J., Emling, W. H., Kempken, J., & Schlüter, J. 2007, May, In *AIST Proceedings*.

Oeters, F. 1989. *Metallurgy of Steelmaking*. Verlag Stahleisen GmbH, Düsseldorf.

Olivares, O., Elias, A., Sánchez, R., Díaz-Cruz, M., & Morales, R. D. 2002, Feb, Steel Research *73*(2), 44–51.

Olmstead, W. E. & Raynor, S. 1964, Journal of fluid mechanics, 19, 561–576.

Osher, S. & Sethian, J. A. 1988, Journal of Computational Physics, 79, 12–49.

Otnes, R. K. & Enochson, L. 1972. *Digital Time Series Analysis*. John Wiley and Sons.

Padmanabham, G. & Gowda, B. H. L. 1991, Transactions of the ASME Journal of Fluids Engineering, 113, 620–628.

Patankar, S. V. 1980. *Numerical Heat Transfer and Fluid Flow*. Hemisphere Publishing Corporation.

Peaslee, K. D. 1993, Electric Furnace Conference Proceedings, 403–411.

Peaslee, K. D. & Robertson, D. G. C. 1994, Steelmaking Conference proceedings, 77, 713–722.

Peaslee, K. D. & Robertson, D. G. C. 1995, Steelmaking Conference proceedings, 689–696.

Perez, J. 2008. personal communication.

Perot, B. & Nallapati, R. 2003, Journal of Computational Physics, 184, 192–214.

Phillips, O. M. 1957, Journal of Fluid Mechanics, 2, 417–445.

Plant, W. J. 1982, Journal of Geophysical Research, 87, 1961–1967.

Pope, S. B. 2000. *Turbulent Flows*. Cambridge University Press.

Prasad, A. K. 2000, july, current science *79*(1), 51–60.

Press, W. H., Teukolsky, S. A., Vetterling, W. T., & Flannery, B. P. 1992. *Numerical Recipes in Fortran : The Art of Scientific Computing* (2nd ed.). Cambridge Univeristy Press.

Price, D. J. 1974. L.D. steelmaking: Significance of the emulsion in carbon removal. In M. J. Jones (Ed.), *Process Engineering of Pyrometallurgy*, pp. 8–15. London: The institution of Mining and Metallurgy.

Priestley, M. B. 1981. *Spectral Analysis and Time Series, volume 1: univariate series*, Volume 1 of *Probability and Mathematical Statistics*. Academic Press.

Puckett, E. G., Almgren, A. S., Bell, J. B., Marcus, D. L., & Rider, W. J. 1997, Journal of Computational Physics, 130, 269–282.

Qian, F., Farouk, B., & Mutharasan, R. 1995, In *EPD Congress*.

Qian, F., Farouk, B., Mutharasan, R., & Machen, N. 1999, Journal of Heat Transfer, 121, 333–340.

Qian, F., Mutharasan, R., & Farouk, B. 1996, Metallurgical and Materials Transactions B, 27B, 911–920.

Qian, L., Causon, D. M., Ingram, D. M., & Mingham, C. G. 2003, Journal of Hydraulic Engineering, 129, 688–696.

Rajaratnam, N. 1976. *Turbulent Jets*. Elsevier Scientific Publishing Company.

Rajaratnam, N. & Pani, B. S. 1974, Jan, ASCE Journal of The Hydraulics Division *100*(HY1), 69–83.

Renka, R. J. 1988a, ACM Transactions on Mathematical Software *14*(2), 139–148.

Renka, R. J. 1988b, ACM Transactions on Mathematical Software *14*(2), 149–150.

Renka, R. J. 1999, ACM Transactions on Mathematical Software *25*(1), 78–94.

Rhie, C. M. & Chow, W. L. 1983, Nov, AIAA Journal *21*(11), 1525–1532.

Richardson, F. D. 1974. *Physical Chemistry of Metls in Metallurgy.* Academic Press.

Ricou, F. P. & Spalding, D. B. 1961, Jounal of Fluid Mechanics, 11, 21–32.

Rider, W. J. & Kothe, D. B. 1998, Journal of Computational Physics, 141, 112–152.

Rosler, R. S. & Stewart, G. H. 1968, Journal of Fluid Mechanics, 31, 163–174.

Rudman, M. 1997, International Journal for Numerical Methods in Fluids, 24, 671–691.

Scadovelli, R. & Zaleski, S. 1999, Annual Review of Fluid Mechanics, 31, 567–603.

Schlichting, H. 1979. *Boundary Layer Theory* (7th ed.). McGraw-Hill Book Company.

Sforza, P. M., Steiger, M. H., & Trentacoste, N. 1966, May, AIAA Journal *4*(5), 800–806.

Shen, L. & Yue, D. K. P. 2001, Journal of Fluid Mechanics, 440, 75–116.

Shen, L., Zhang, X., Yue, D. K. P., & Triantafyllou, G. S. 1999, J. Fluid Mech., 386, 167–212.

Shi, J., Thomas, T. G., & Williams, J. J. R. 2000, Journal of hydraulic research *38*(6), 465–474.

Shu, Q. & Zhang, J. 2006, ISIJ International *46*(11), 1548–1553.

Shyy, W., Udaykumar, S., Rao, M. M., & Smith, R. W. 1996. *Computational Fluid Dynamics with Moving Boundaries*, Chapter 6, pp. 195–248. Washington, DC: Hemisphere.

Smith, G. C. 1966, July, Journal of Metals, 846–851.

Smolianski, A. 2001. *Numerical Modeling of Two-Fluid Interfacial Flows.* Ph. D. thesis, University of JYVÄSKYLÄ.

Son, G. 2003, Numerical Heat Transfer, Part B, 43, 549–565.

Son, G. & Hur, N. 2002, Numerical Heat Transfer, Part B, 42, 523–542.

Spivak, B., Vanden-Boeck, J.-M., & Miloh, T. 2002, European Journal of Mechanics B/Fluids, 21, 207–224.

Standish, N. & He, Q. 1989, ISIJ international *29*(6), 455–461.

Subagyo, Brooks, G., Coley, K., & Irons, G. A. 2003, ISIJ international *43*(7), 983–989.

Sussman, M., Fatemi, E., Smereka, P., & Osher, S. 1998, Computers and Fluids *27*(5–6), 663–680.

Sussman, M. & Puckett, E. G. 2000, Journal of Computational Physics, 162, 301–337.

Sussman, M., Smereka, P., & Osher, S. 1994, Journal of Computational Physics, 114, 146–159.

Szekely, J. 1979. *Fluid Flow Phenomena in Metals Processing.* Acadamic Press.

Szekely, J. & Themelis, N. J. 1971. *Rate Phenomena in Process Metallurgy.* John Wiley and Sons.

Tago, Y. & Higuchi, Y. 2003, ISIJ international *43*(2), 209–215.

Tai, C.-F. & Shyy, W. 2005, Numerical Heat Transfer, Part B, 48, 405–424.

Teixeira, M. A. C. & Belcher, S. E. 2006, Dynamics of Atmospheres and Oceans, 41, 1–27.

Thé, J. L., Raithby, G. D., & Stubley, G. D. 1994, Numerical Heat Transfer, Part B, 26, 367–380.

Theodorakakos, A. & Bergeles, G. 2004, International Journal for Numerical Methods in Fluids, 45, 421–439.

Trentacoste, N. & Sforza, P. 1967, May, AIAA Journal *5*(5), 885–891.

Tryggvason, G., Bunner, B., Esmaeeli, A., Juric, D., Al-Rawahi, N., Tauber, W., Han, J., Nas, S., & Jan, Y.-J. 2001, Journal of Computational Physics, 169, 708–759.

Turkdogan, E. T. 1966, Chemical Engineering Science, 21, 1133–1144.

Ubbink, O. & Issa, R. I. 1999, Journal of Computational Physics, 153, 26–50.

Udaykumar, H. S., Kan, H.-C., Shyy, W., & Tran-Son-Tay, R. 1997, Journal of Computational Physics, 137, 366–405.

Udaykumar, H. S., Mittal, R., Rampunggoon, P., & Khanna, A. 2001, Journal of Computational Physics, 174, 345–380.

Udaykumar, H. S., Mittal, R., & Shyy, W. 1999, Journal of Computational Physics, 153, 535–574.

Udaykumar, H. S., Shyy, W., & Rao, M. M. 1996, International Journal for Numerical Methods in Fluids, 22, 691–712.

Unverdi, S. O. & Tryggvasson, G. 1992, Journal of Computational Physics, 100, 25–37.

Urquhart, R. C. & Davenport, W. G. 1973, Canadian Metallurgical Quarterly *12*(4), 507–516.

Vadász, P., Havlík, M., & Daněk, V. 2000, Canadian Metallurgical Quarterly *39*(2), 143–152.

Vanden-Broeck, J.-M. 2002, J. Fluid Mech., 193–201.

VDEh (Ed.) 1995. *SLAG ATLAS* (2 ed.). Verlag Stahleisen GmbH, Düsseldorf.

Versteeg, H. K. & Malalasekera, W. 1995. *An Introduction to Computational Fluid dynamics*. Prentice Hall.

Wang, J. P., Borthwick, A. L., & Taylor, R. 2004, International Journal for Numerical Methods in Fluids, 45, 485–508.

Wei, T. & Oeters, F. 1992, Steel Research, 63, 60–68.

White, F. M. 2006. *Fluid Mechanics*. McGraw-Hill.

Wygnanski, I. & Fiedler, H. 1969, J. Fluid Mech., 38, 577–612.

Yang, G., Causon, D. M., Ingram, D. M., Saunders, R., & Battern, P. 1997, February, The Aeronautical Journal, 47–56.

Ye, T., Mittal, R., Udaykumar, H. S., & Shyy, W. 1999a, Journal of Computational Physics, 156, 209–240.

Ye, T., Mittal, R., Udaykumar, H. S., & Shyy, W. 1999b, AIAA paper, 99-3312.

Young, D. L. 1982. Time-dependent multi-material flow with large fluid distortion. In K. W. Morton and M. J. Baines (Eds.), *Numerical Methods for Fluid Dynamics*, pp. 273–285. New York: Academic Press.

Zakharov, V. E., Falkovich, G., & Lvov, V. S. 1992. *Kolmogorov Spectra of Turbulence I.* Springer-Verlag.

Zarruk, G. A. 2005, Meas. Sci. Technol., 16, 1970–1975.

Zwart, P., Raithby, G. D., & Raw, M. 1999, Journal of Computational Physics, 154, 497–519.

Appendix A

Addition to Discretization

$$\begin{aligned}\int_A \boldsymbol{n}\cdot\mu\nabla\boldsymbol{u}dA \Rightarrow &+\mu_e A_e \left.\frac{\partial v}{\partial x}\right|_e + \mu_e^x A_e^x \left.\frac{\partial v}{\partial x}\right|_e^x \\ &-\mu_w A_w \left.\frac{\partial v}{\partial x}\right|_w - \mu_w^x A_w^x \left.\frac{\partial v}{\partial x}\right|_w^x \\ &+\mu_n A_n \left.\frac{\partial v}{\partial y}\right|_n + \mu_n^x A_n^x \left.\frac{\partial v}{\partial y}\right|_n^x \\ &-\mu_s A_s \left.\frac{\partial v}{\partial y}\right|_s - \mu_s^x A_s^x \left.\frac{\partial v}{\partial y}\right|_s^x\end{aligned} \tag{A.1}$$

$$\begin{aligned}\int_A \boldsymbol{n}\cdot\mu\left(\nabla\boldsymbol{u}\right)^T dA \Rightarrow &+\mu_e A_e \left.\frac{\partial u}{\partial y}\right|_e + \mu_e^x A_e^x \left.\frac{\partial u}{\partial y}\right|_e^x \\ &-\mu_w A_w \left.\frac{\partial u}{\partial y}\right|_w - \mu_w^x A_w^x \left.\frac{\partial u}{\partial y}\right|_w^x \\ &+\mu_n A_n \left.\frac{\partial v}{\partial y}\right|_n + \mu_n^x A_n^x \left.\frac{\partial v}{\partial y}\right|_n^x \\ &-\mu_s A_s \left.\frac{\partial v}{\partial y}\right|_s - \mu_s^x A_s^x \left.\frac{\partial v}{\partial y}\right|_s^x\end{aligned} \tag{A.2}$$

Appendix B

Surface Geometries

B.1 Surface Normal and Curvature

The surface normal vector is defined in Equation (2.22). Equation (2.22) is the normalized form and actually the numerical way to find the surface normal is the calculation of ∇F. With any kind of variable, the directional change $dF/\,dr$ can be divided into coordinate components. So ∇F can be expressed in the following way,

$$\nabla F = \frac{F_{i',j'} - F_{i,j}}{|\boldsymbol{r}_{i',j'} - \boldsymbol{r}_{i,j}|} \frac{\boldsymbol{r}_{i',j'} - \boldsymbol{r}_{i,j}}{|\boldsymbol{r}_{i',j'} - \boldsymbol{r}_{i,j}|} \tag{B.1}$$

The convolved Volume method is uses the summation of Equation (B.1) and the un-normalized normal vector($\hat{\boldsymbol{n}}$) can be computed with the following equation

$$\hat{\boldsymbol{n}} = \sum_{i',j' \neq i,j} \frac{F_{i',j'} - F_{i,j}}{|\boldsymbol{r}_{i',j'} - \boldsymbol{r}_{i,j}|} \frac{\boldsymbol{r}_{i',j'} - \boldsymbol{r}_{i,j}}{|\boldsymbol{r}_{i',j'} - \boldsymbol{r}_{i,j}|} \tag{B.2}$$

Based on Equation (B.2), approximate normal vector is determined and the LVIRA scheme (Martorano et al. 2006) was applied to obtain better representation of the surface normal vector. This scheme starts from an assumed surface construction line and this line is rotated and a line construction, which minimizes the error between the actual volume fraction and the volume fraction obtained with this line construction. This is illustrated in Figure B.1a. A golden section algorithm was used to find the best fit.

The curvature was obtained with polynomial fitting of surface points with local coordinates of normal and tangential axis as illustrated in Figure B.1b. The number of surface points can be adjusted and up to second neighbor cells are considered to find the surface points. The curvature was determined with a general formula

$$\kappa = \frac{y''}{(1 + y'^2)^{3/2}} \tag{B.3}$$

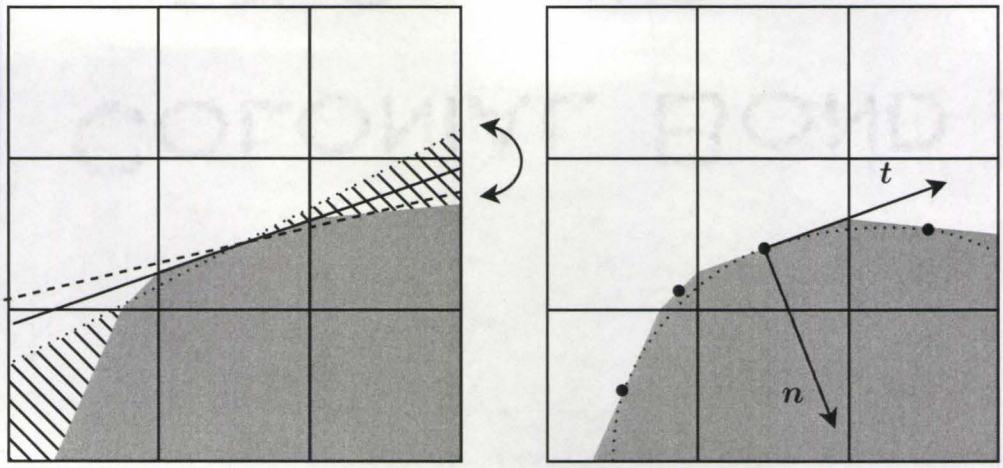

(a) Normal vector (b) Curvature

Figure B.1: The LVIRA scheme to find normal vector and curvature

B.2 A distance function

The procedure for surface construction and extraction of the geometric information is very tedious and time consuming, because of many different cases of surface orientation. (Son and Hur 2002) devised a smart and efficient way to obtain the geometrical information in PLIC construction with only one variable. Once the distance(s) from the cell origin to the surface line is known, the sidewet fraction and other geometric informations are easily determined.

Starting from a simple geometrical balance, from the Figure B.2a, the computation cell rectangle of $dx \times dy$ and the cross section of the extension of surface construction line and each axis can construct a rectangle of $dx_0 \times dy_0$. the balance equation can be written as

$$2Fdxdy = dx_0dy_0 - \frac{dy_0}{dx_0} < dx_0 - dx >^2 - \frac{dx_0}{dx} < dy_0 - dy >^2 \qquad \text{(B.4)}$$

,where $< a >= max(0, a)$.

With the definition of $s = |n_x|dx_0 = |n_y|dy_0$, and some new variables, $dx_1 = |n_x|dx$ and $dy_1 = |n_y|dy_0$, Equation (B.4) can be simplified to volume fraction and void fraction part.

$$2Fdx_1dy_1 = s^2 - < s - dx_1 >^2 - < s - dy_1 >^2 \qquad \text{(B.5)}$$

$$2(1-F)dx_1dy_1 = (s_m - s)^2 - < s_m - s - dx_1 >^2 - < s_m - s - dy_1 >^2 \qquad \text{(B.6)}$$

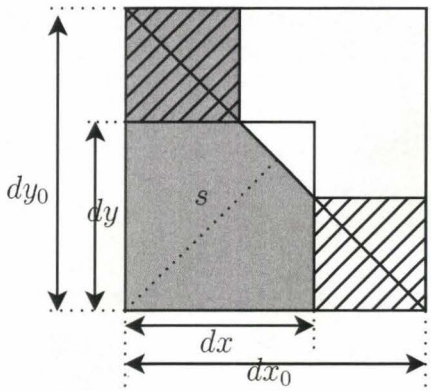

(a) s function

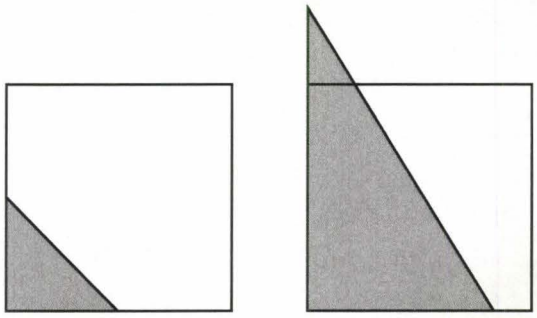

(b) two cases

Figure B.2: s function construction of the surface

where s_m is the distance when the surface construction is located at the other vertex from the cell origin.

Setting $F_c = min(F, 1-F)$, $s_c = min(s, s_m - s)$, $dx_c = max(dx_1, dy_1)$ and $dy_c = min(dx_1, dy_1)$ yields simpler relationship for volume and void case,

$$2F_c dx_c dy_c = s_c^2 - < s_c - dy_c >^2 \tag{B.7}$$

where, in this case, there will be only two cases of surface construction as shown in Figure B.2b and s_c can be determined by

$$s_c = \begin{cases} \sqrt{2F_c dx_c dy_c} & , s_c < dy_c \\ F_c dx_c + 0.5 dy_c & , s_c \geqq dy_c \end{cases} \tag{B.8}$$

Appendix C

Surface Profile Analysis Procedure

The digitization was separated to give two sets of data, inside of the cavity and outside of the cavity. The outside wave digitization was used for the average level of the surface; the cross section of this level and the inside digitization determines the width variable. The width at the top lip was determined with the local maxima in the left and right side of inside cavity digitization. The depth was determined from the undisturbed surface which was determined from reference calm surface. The cavity minimum positions were determined with the minimum position inside of cavity.

The cavity digitization was not evenly distributed and to obtain a more accurate cross section position, a cubic-spline interpolation was used. The spline interpolation results are evenly digitized; it is used for the Fourier Transform analysis.

The actual analysis program was written in the programming language PYTHON and SciPy scientific library (Jones et al. 2001) was used for Fast Fourier transform and power spectra.

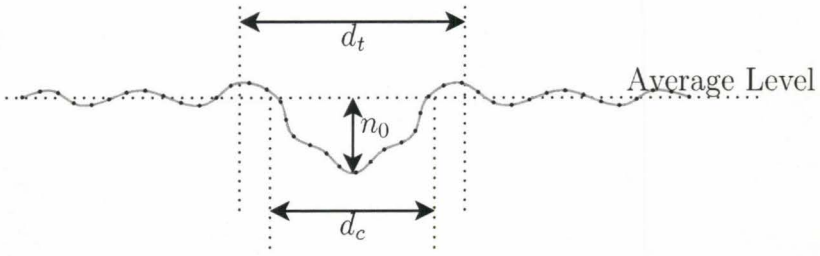

Figure C.1: Schematic diagram of analysis of digitized data

Appendix D

Analytic solution of free jet

The formula of Götler's type of solution is presented page 42 in (Rajaratnam 1976).

$$\frac{u}{u_m} = \frac{1}{(1+0.125\xi^2)^2} \tag{D.1}$$

$$\sigma\frac{v}{u_m} = \frac{\xi - 0.125\xi^3}{2(1+0.125\xi^2)^2} \tag{D.2}$$

where $\xi = \sigma y/x$. The centerline velocity u_m was determined with

$$\frac{u}{u_0} = \frac{\sigma}{3.22}\frac{d_0}{x} \tag{D.3}$$

and the suggested value for σ was 18.5, which is fitted to the experimental result of Reichardt[1]

[1]Rajaratnam (1976) indicates the original reference from Schlichting (1979), Reichardt. H. : Gesetzmässigkeiten der freien Turbulenz. VDI-Forschungsheft 414 (1942) 2nd Ed. 1951

Appendix E

Power Spectral Density

When there is a time variation or space variation of a variable, $X(t)$, the Power Spectral Density (PSD) can be expressed with the Fourier transform of $X(t)$

$$\mathrm{PSD}(f) = \lim_{T\to\infty} \frac{1}{2T} \left[\int_{-T}^{T} X(t) e^{-i2\pi f t}\, dt \right]^2 \tag{E.1}$$

This is equvalent to the Fourier transform of an autocorrelation of $X(t)$

$$\mathrm{PSD}(f) = \int_{-\infty}^{\infty} \lim_{T\to\infty} \frac{1}{2T} \left[\int_{-T}^{T} X(t) X(t+\tau)\, dt \right] e^{-i2\pi f \tau}\, d\tau \tag{E.2}$$

According to Priestley (1981) the PSD can be interpreted as "contribution to the total power of $X(t)$ by components with frequencies between f and $f + df$." This PSD is widely used for time series analysis, wave analysis and mathematically equivalent to the Energy density spectra of spectral analysis in turbulence.

The numerical implemetations are well described in Otnes and Enochson (1972) and Press et al. (1992). A numerical library matplotlib[2] was used for PSD calculation; the Hanning windowing option was used to reduce numerical leakage which is well described in Otnes and Enochson.

Figure E.1 shows an example of PSD representation of a test function which is composed of several small sine waves in a big wave. Frequency information can be obtained with this PSD application.

[2] `http://matplotlib.sourceforge.net/`

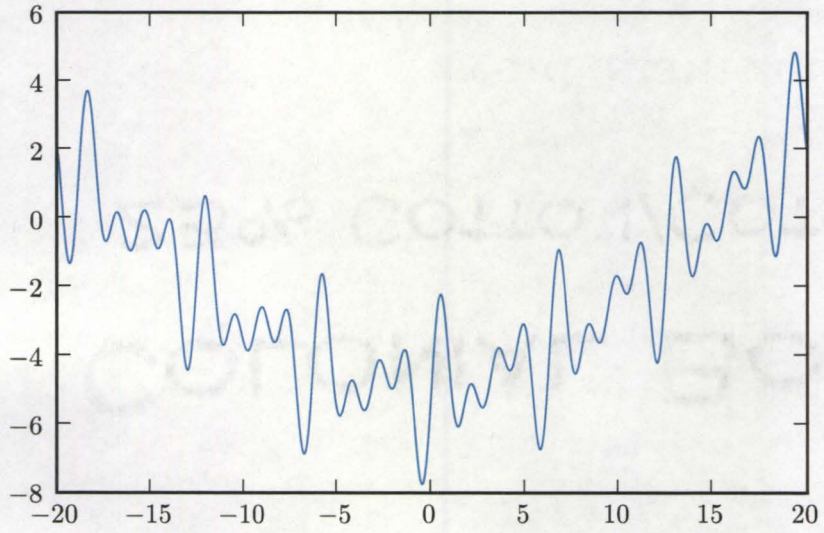

(a) test wave

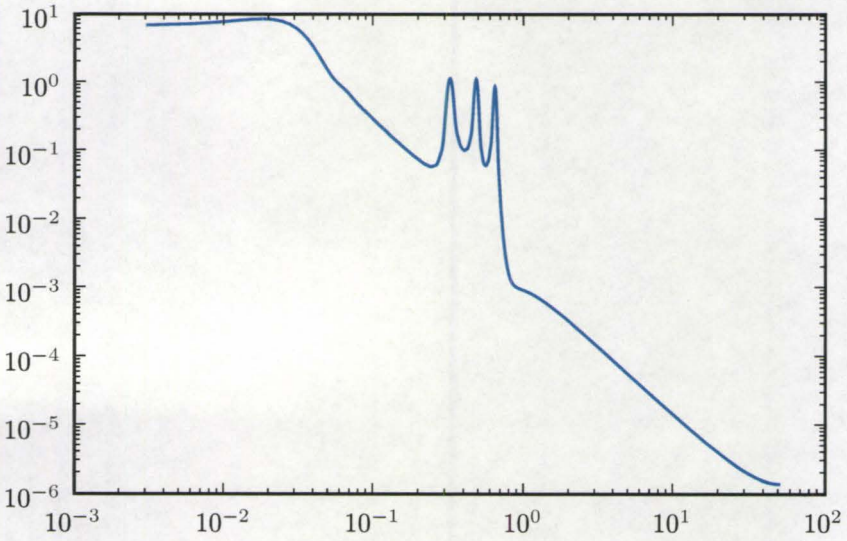

(b) PSD

Figure E.1: An example of PSD application of a test wave, (a) $y = \sin(2x) + \sin(3x) + \sin(4x) + 5\sin(0.1x - 1.5)$. (b) PSD of (a) showing dominant frequencies at $2/2\pi = 0.32$, $3/2\pi = 0.48$, $4/2\pi = 0.64$ and the broadening at $0.1/2\pi = 0.016$ due to the base sinuous wave.

Appendix F

PIV measurement plots

The PIV measured vectors were plotted here with the background of PIV image which is taken at that measurement. Some insignificant vectors, low flowrate cases are not plotted because the vectors are not properly visible. The plots are labeled from Figure F.1 to Figure F.4.

The Fast Fourier Transform of time series of cavity dimension results are plotted from Figure 3.10 to Figure F.13.

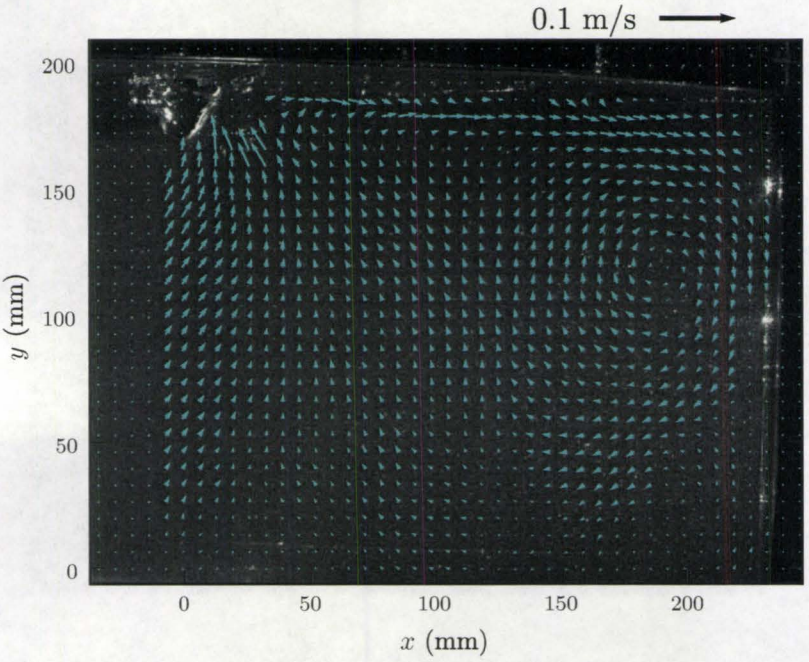

(a) 30 SLPM

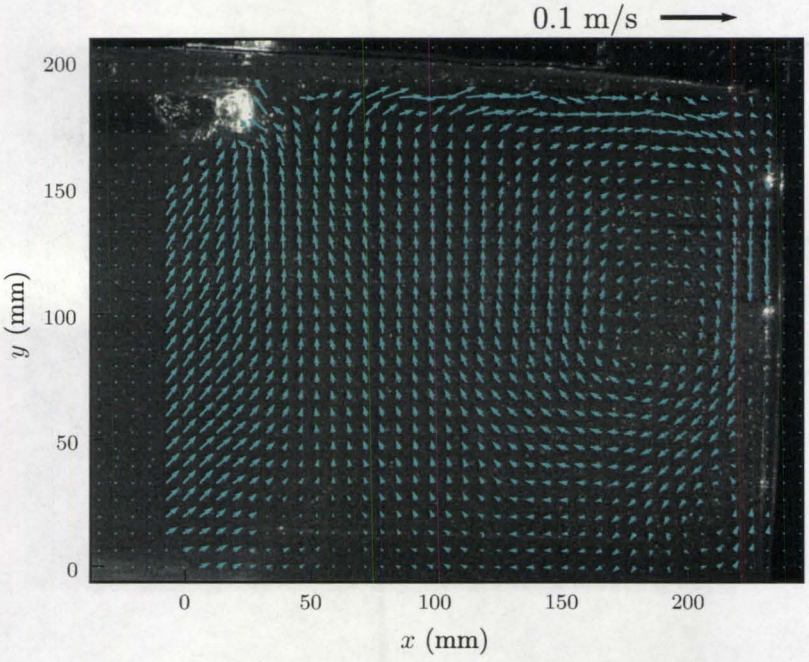

(b) 40 SLPM

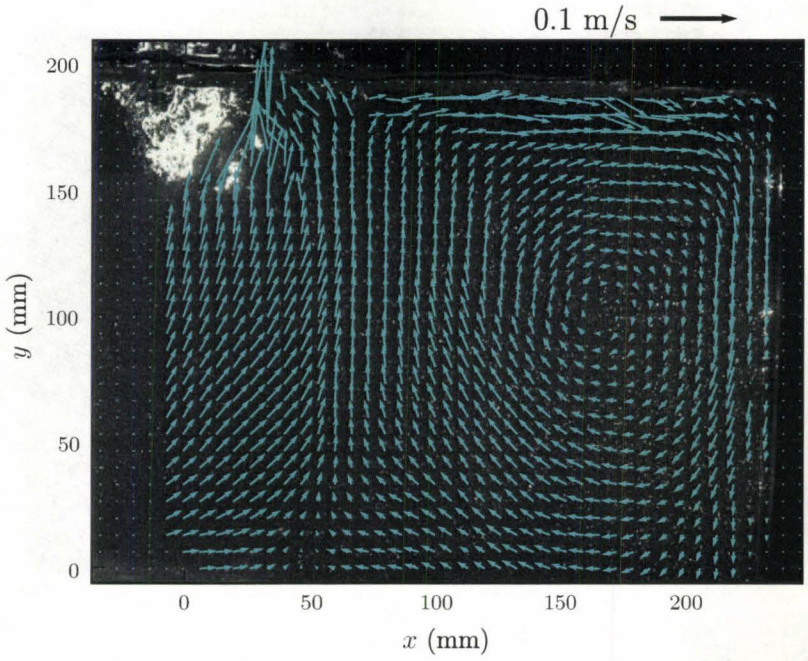

(c) 60 SLPM

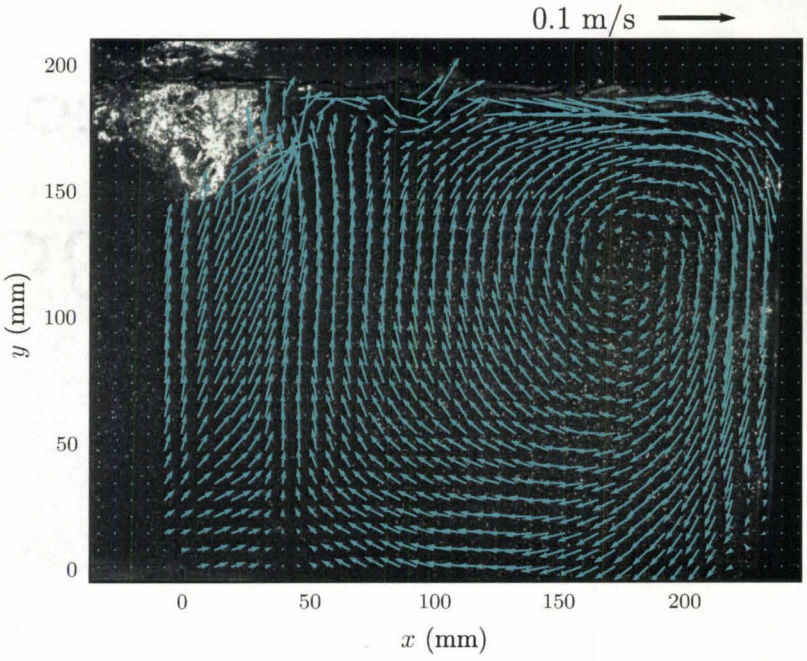

(d) 70 SLPM

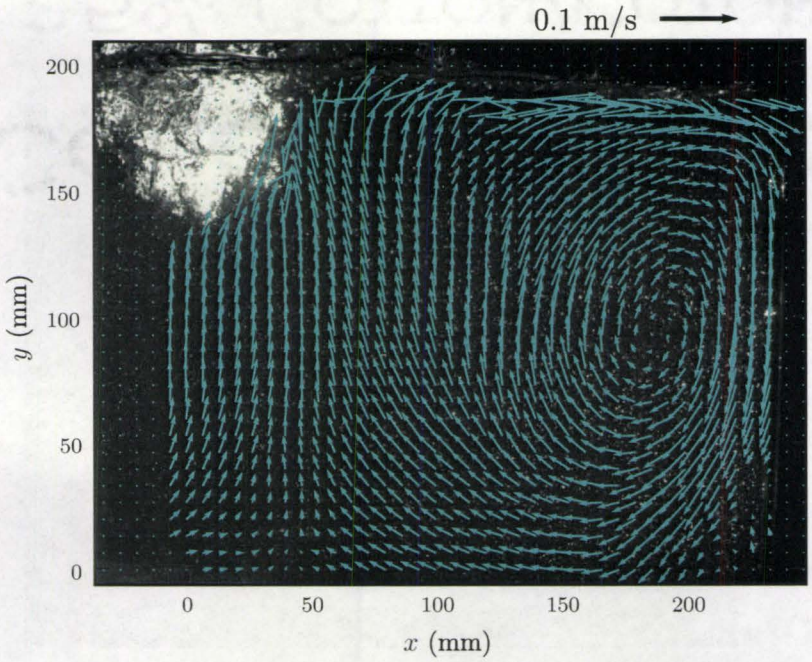

(e) 80 SLPM

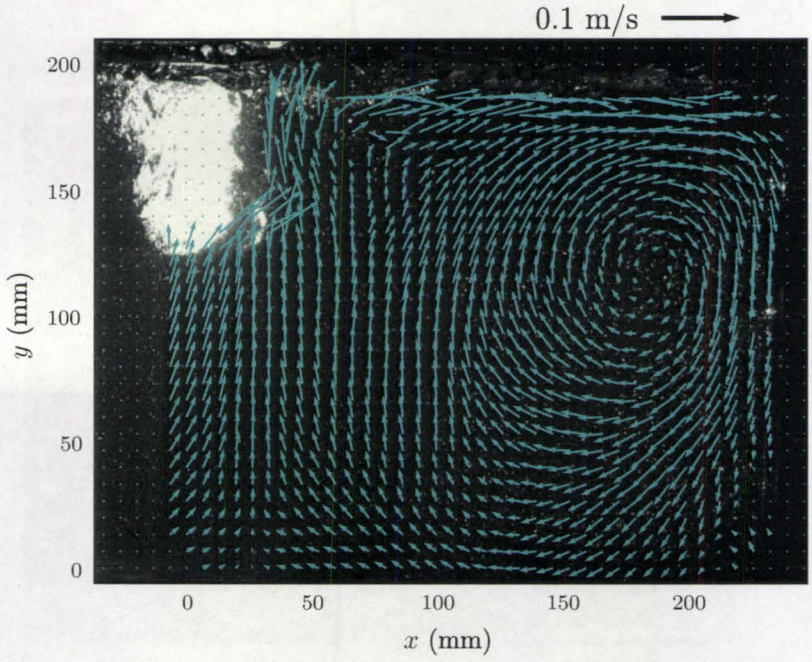

(f) 90 SLPM

Figure F.1: PIV measurement of liquid velocities, cases for the 6cm lance height from the calm surface level

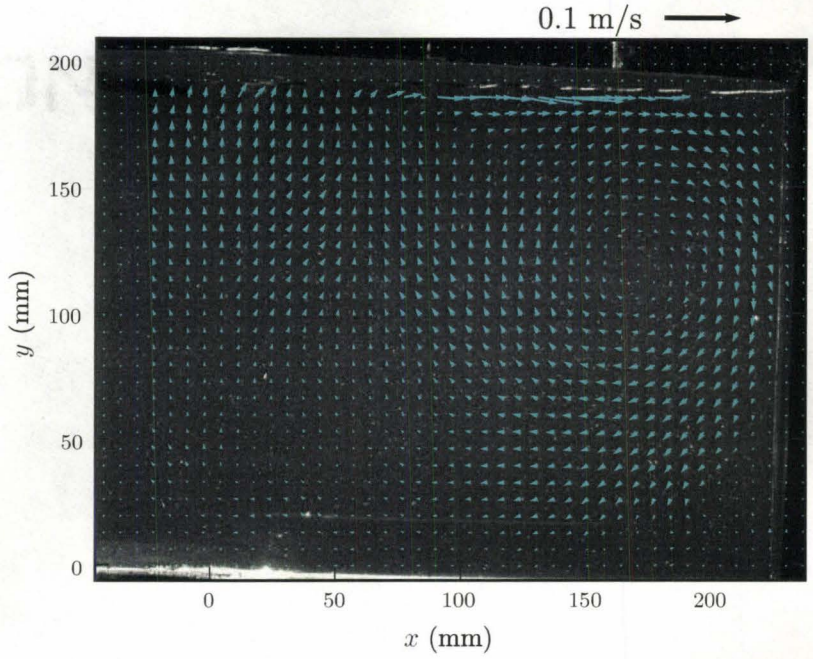

(a) 30 SLPM

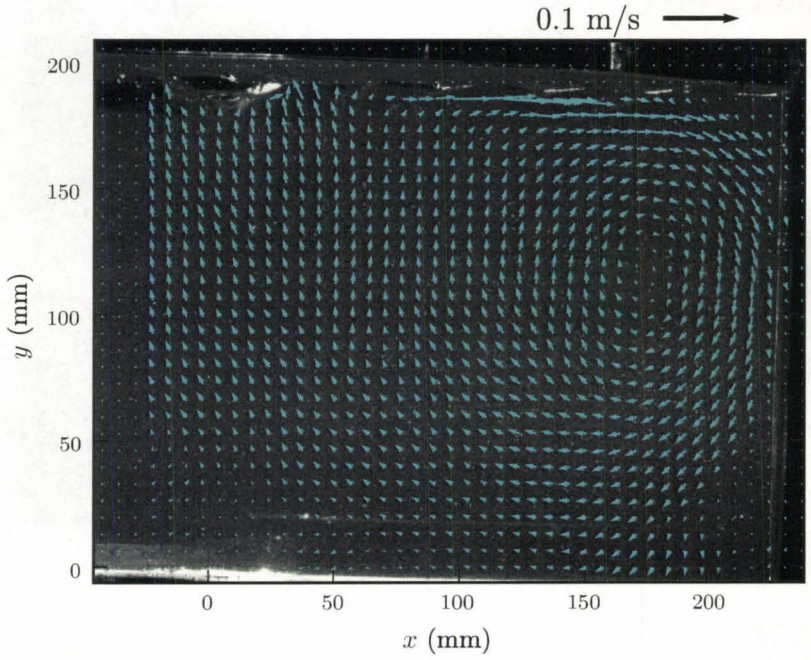

(b) 40 SLPM

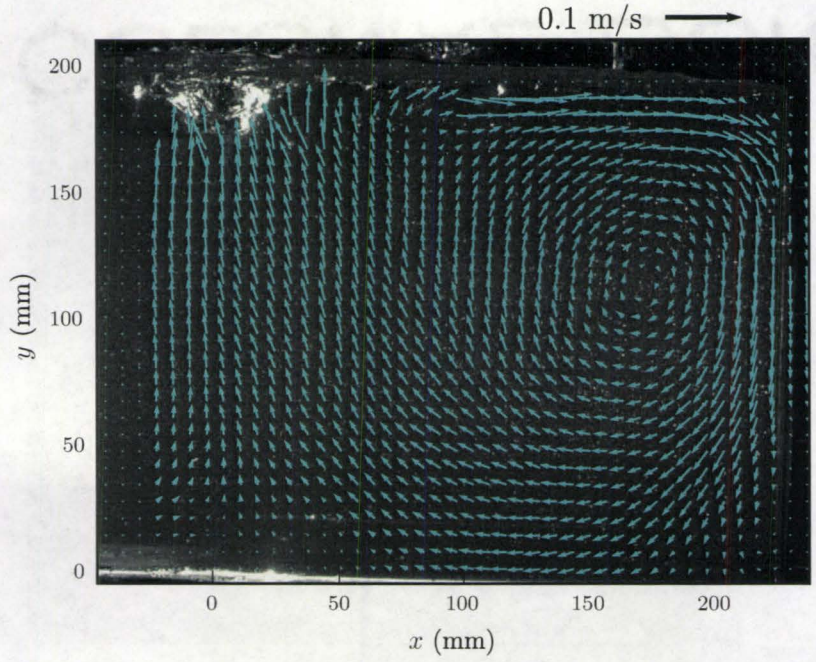

(c) 60 SLPM

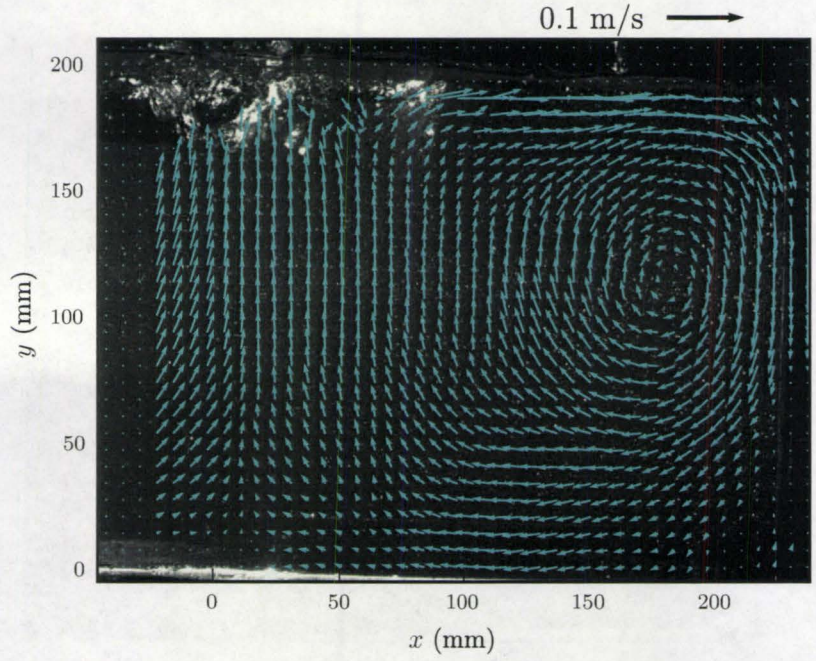

(d) 80 SLPM

Figure F.2: PIV measurement of liquid velocities, cases for the 12cm lance height from the calm surface level

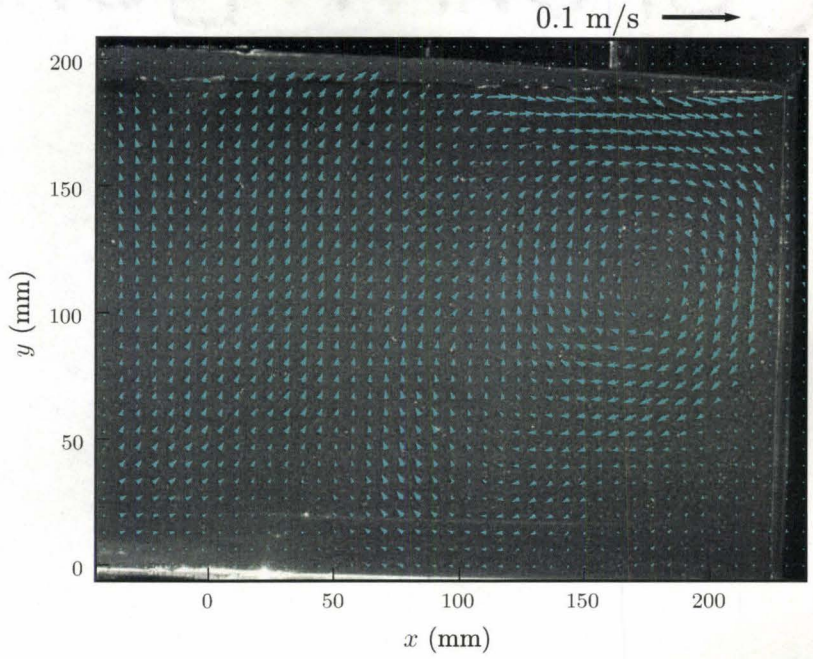

(a) 40 SLPM

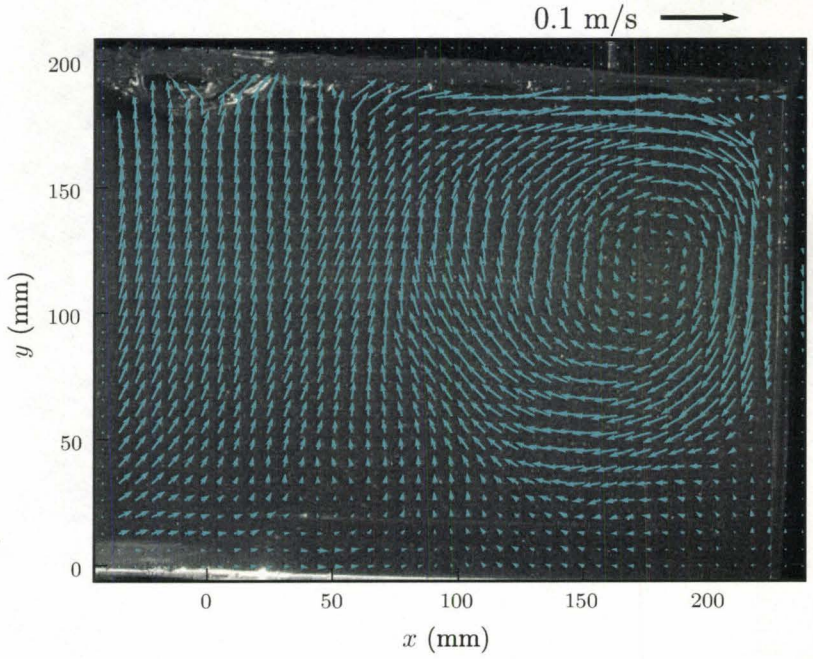

(b) 60 SLPM

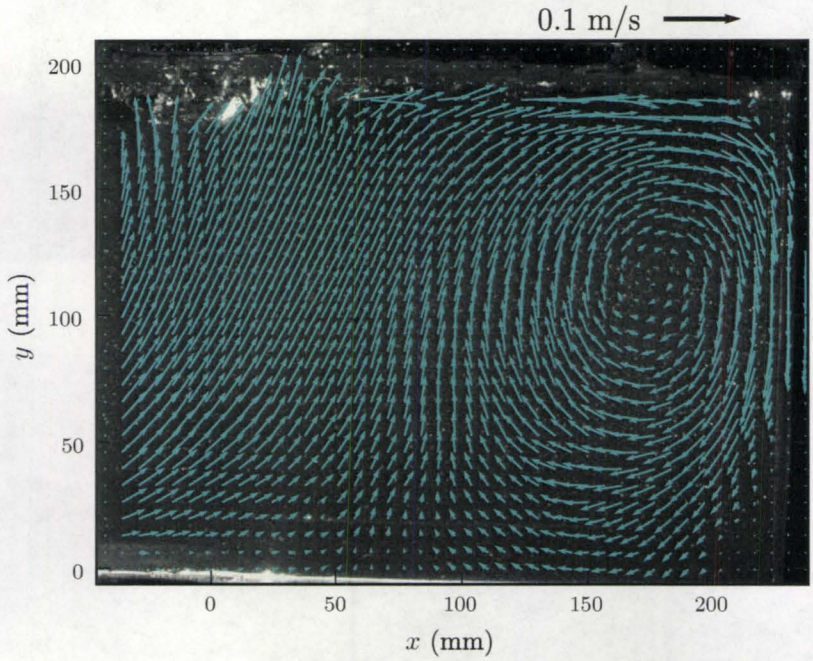

(c) 80 SLPM

Figure F.3: PIV measurement of liquid velocities, cases for the 18cm lance height from the calm surface level

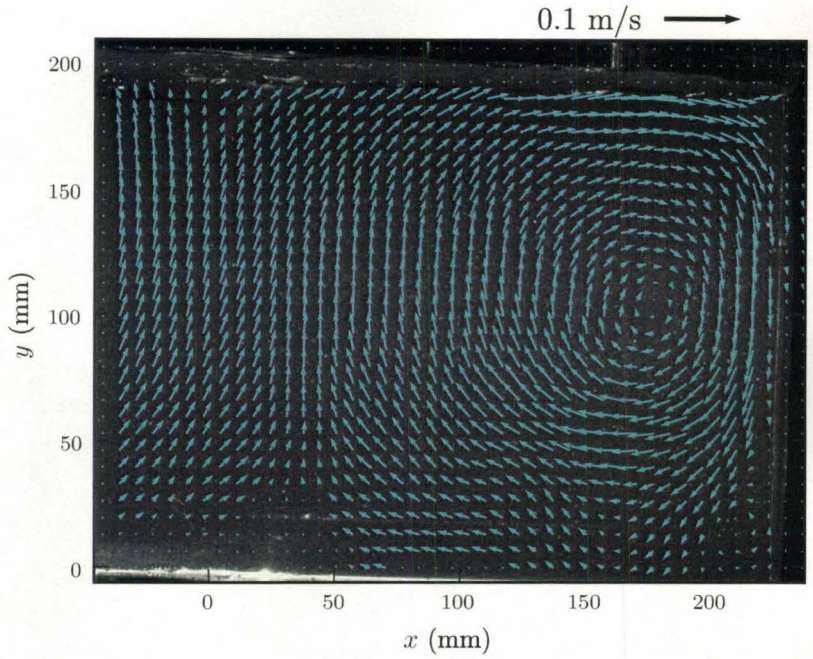

(a) 60 SLPM

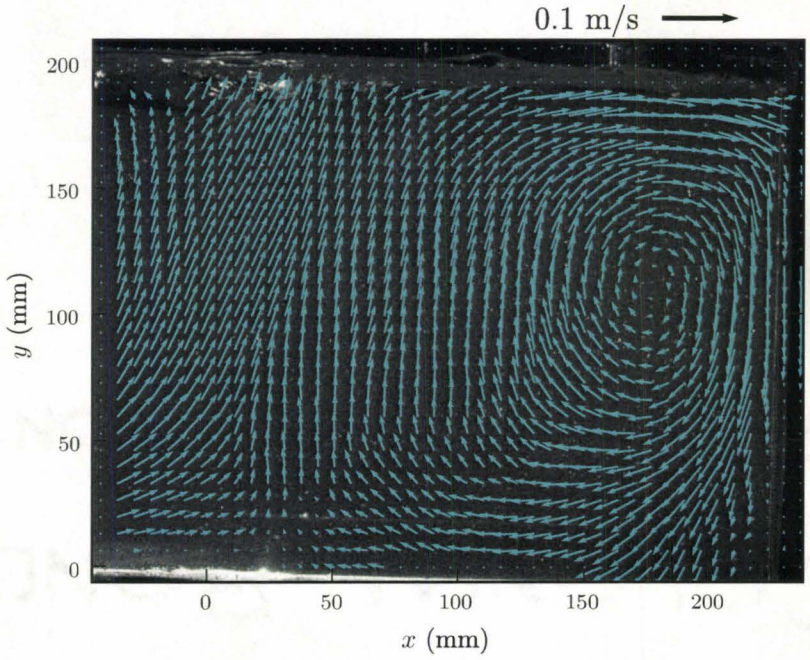

(b) 70 SLPM

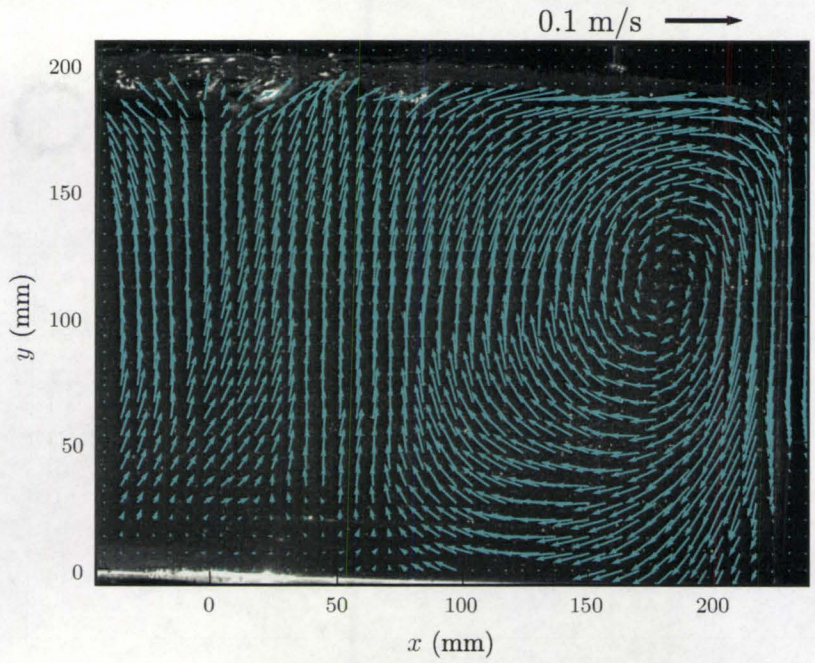

(c) 80 SLPM

Figure F.4: PIV measurement of liquid velocities, cases for the 24cm lance height from the calm surface level

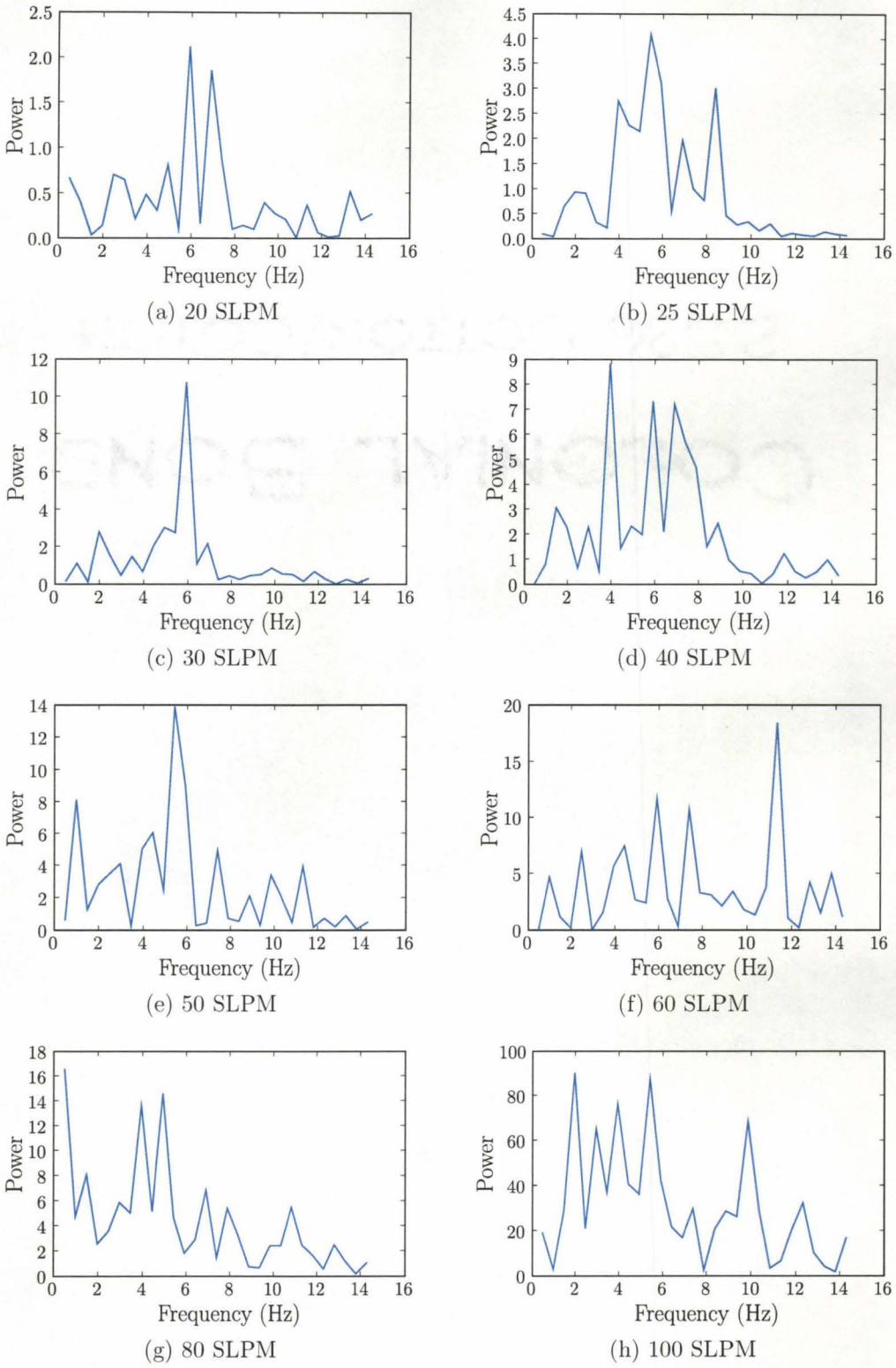

(a) 20 SLPM (b) 25 SLPM

(c) 30 SLPM (d) 40 SLPM

(e) 50 SLPM (f) 60 SLPM

(g) 80 SLPM (h) 100 SLPM

Figure F.5: Fast Fourier transform of time series of cavity depth change when the lance height is 12cm.

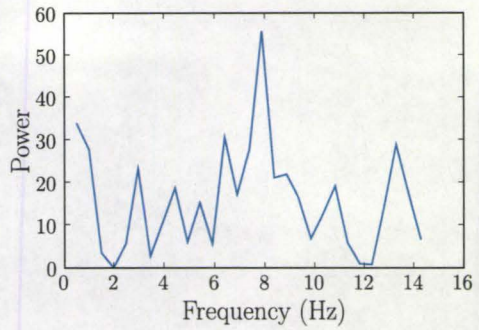

(a) 20 SLPM

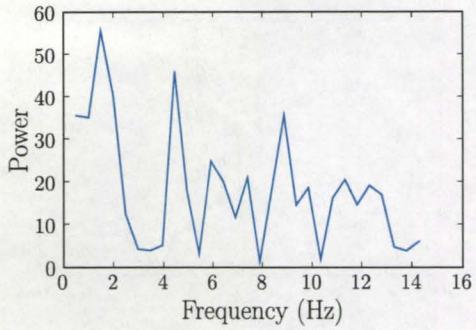

(b) 25 SLPM

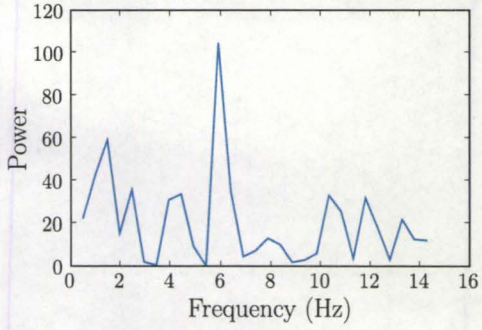

(c) 30 SLPM

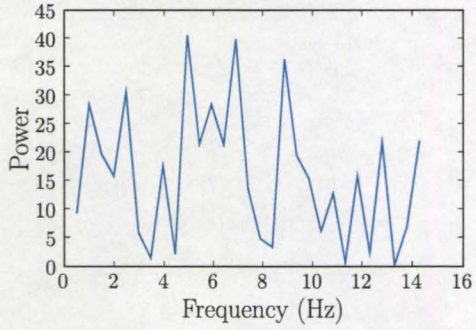

(d) 40 SLPM

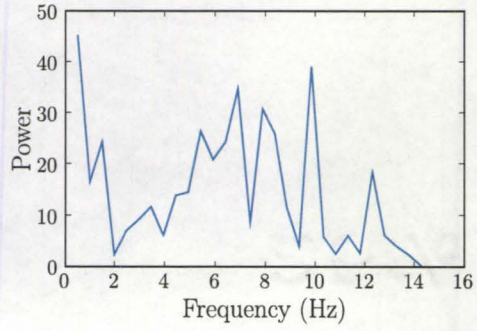

(e) 50 SLPM

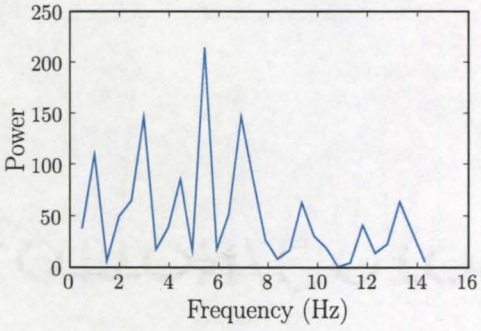

(f) 60 SLPM

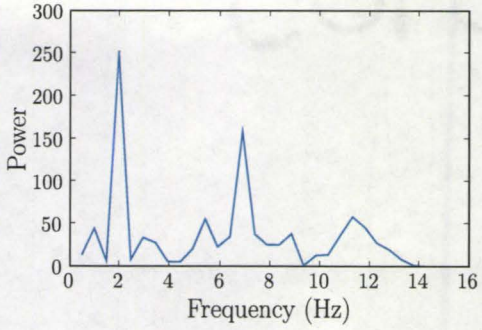

(g) 80 SLPM

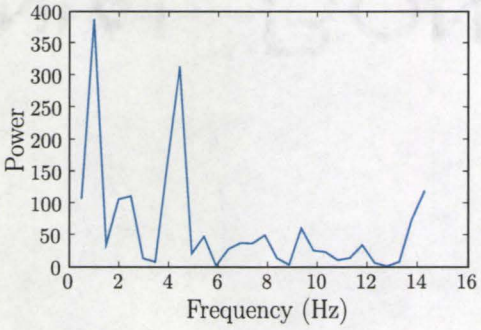

(h) 100 SLPM

Figure F.6: Fast Fourier transform of time series of cavity width change when the lance height is 12cm.

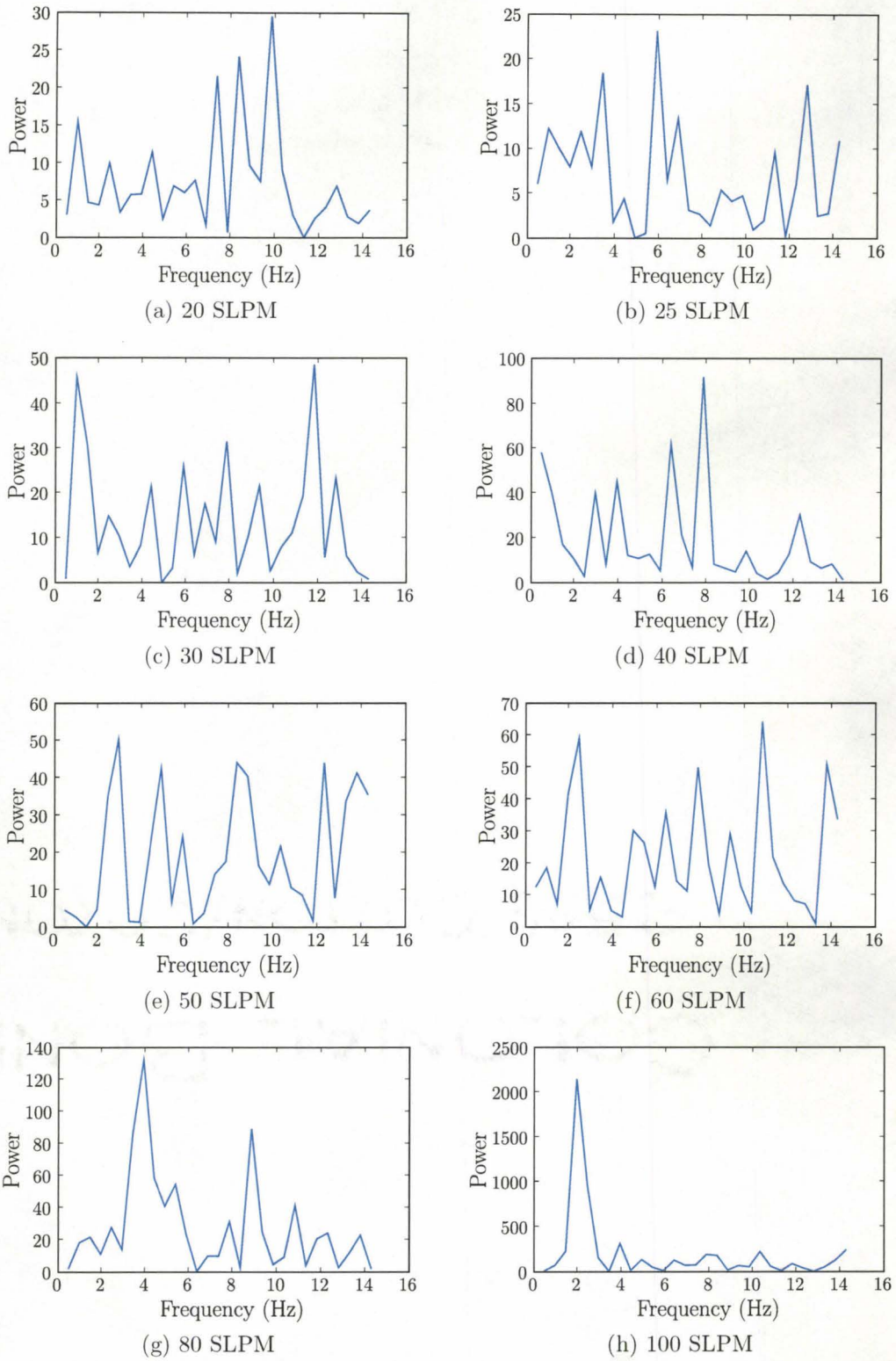

(a) 20 SLPM (b) 25 SLPM

(c) 30 SLPM (d) 40 SLPM

(e) 50 SLPM (f) 60 SLPM

(g) 80 SLPM (h) 100 SLPM

Figure F.7: Fast Fourier transform of time series of horizontal position of the cavity depth change when the lance height is 12cm.

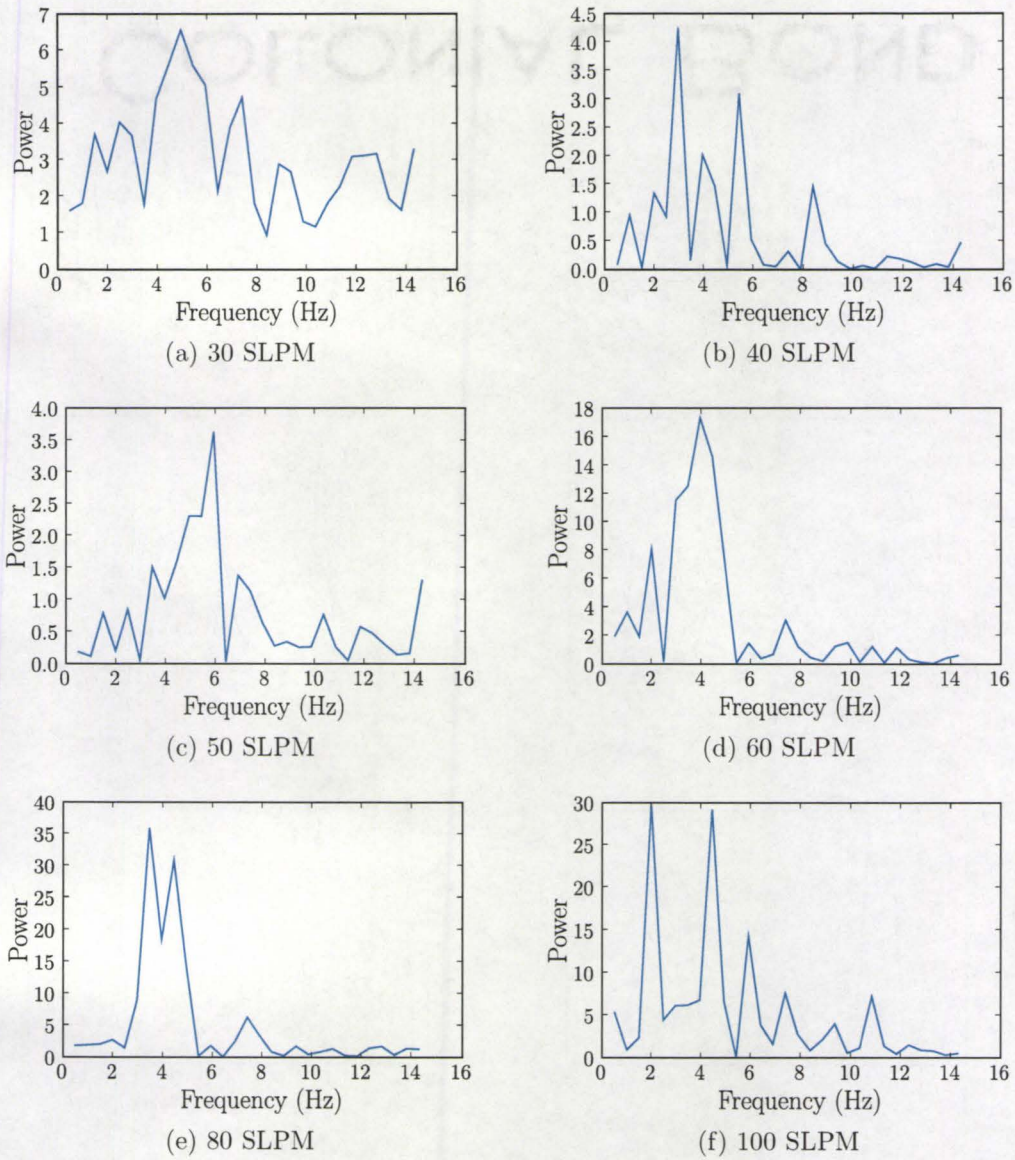

(a) 30 SLPM (b) 40 SLPM

(c) 50 SLPM (d) 60 SLPM

(e) 80 SLPM (f) 100 SLPM

Figure F.8: Fast Fourier transform of time series of cavity depth change when the lance height is 18cm.

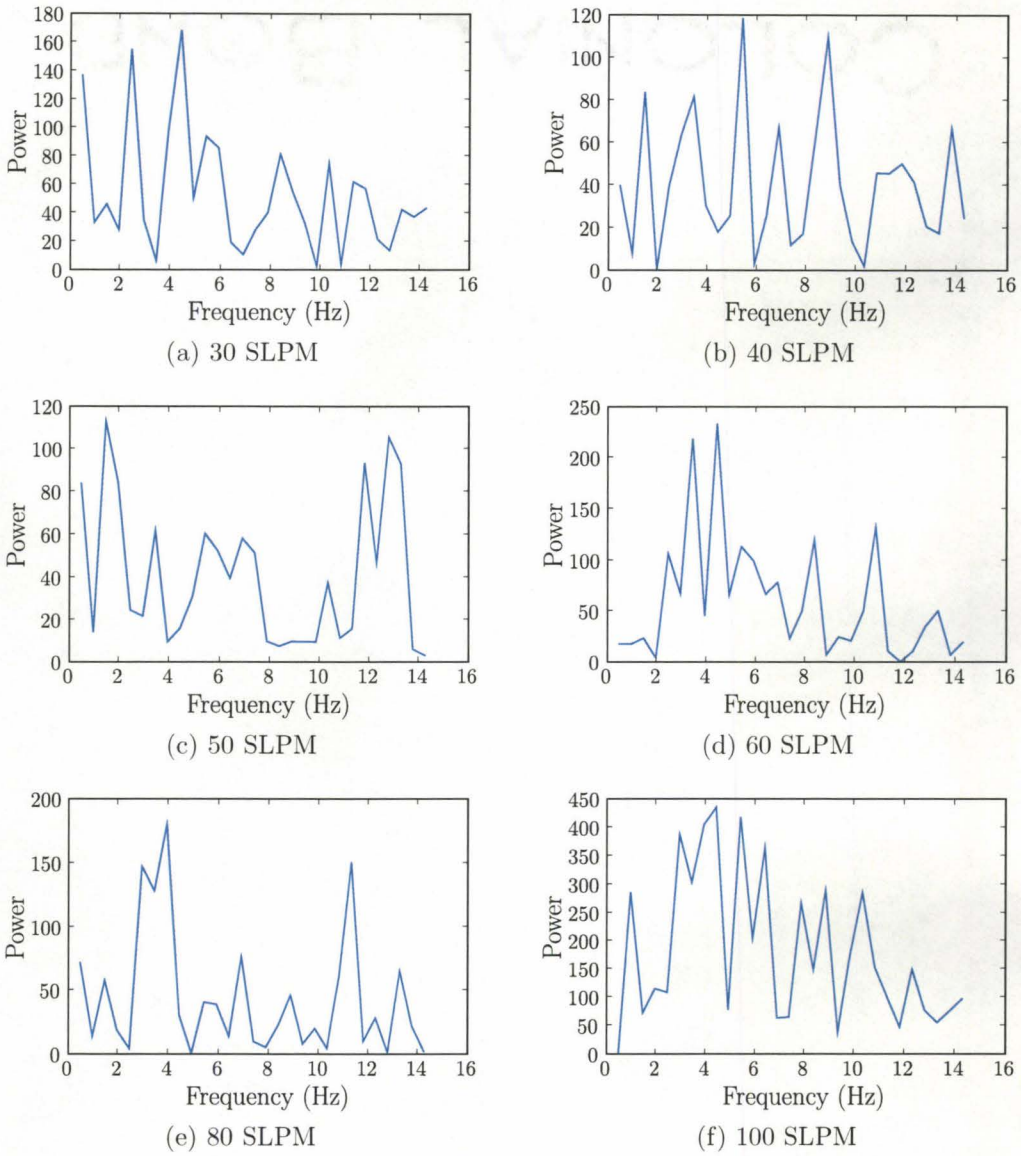

(a) 30 SLPM (b) 40 SLPM

(c) 50 SLPM (d) 60 SLPM

(e) 80 SLPM (f) 100 SLPM

Figure F.9: Fast Fourier transform of time series of cavity width change when the lance height is 18cm.

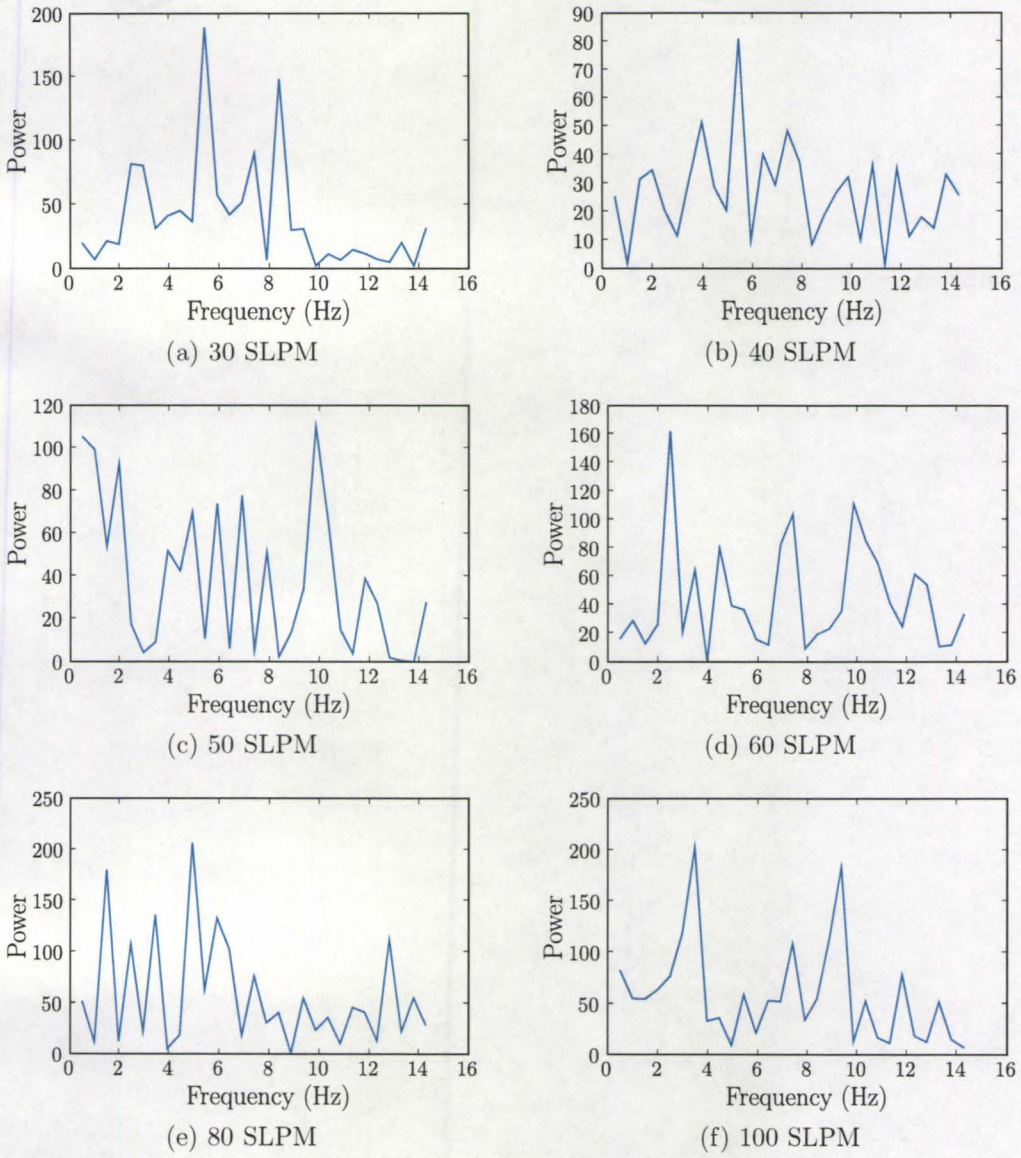

(a) 30 SLPM (b) 40 SLPM

(c) 50 SLPM (d) 60 SLPM

(e) 80 SLPM (f) 100 SLPM

Figure F.10: Fast Fourier transform of time series of horizontal position of the cavity depth change when the lance height is 18cm.

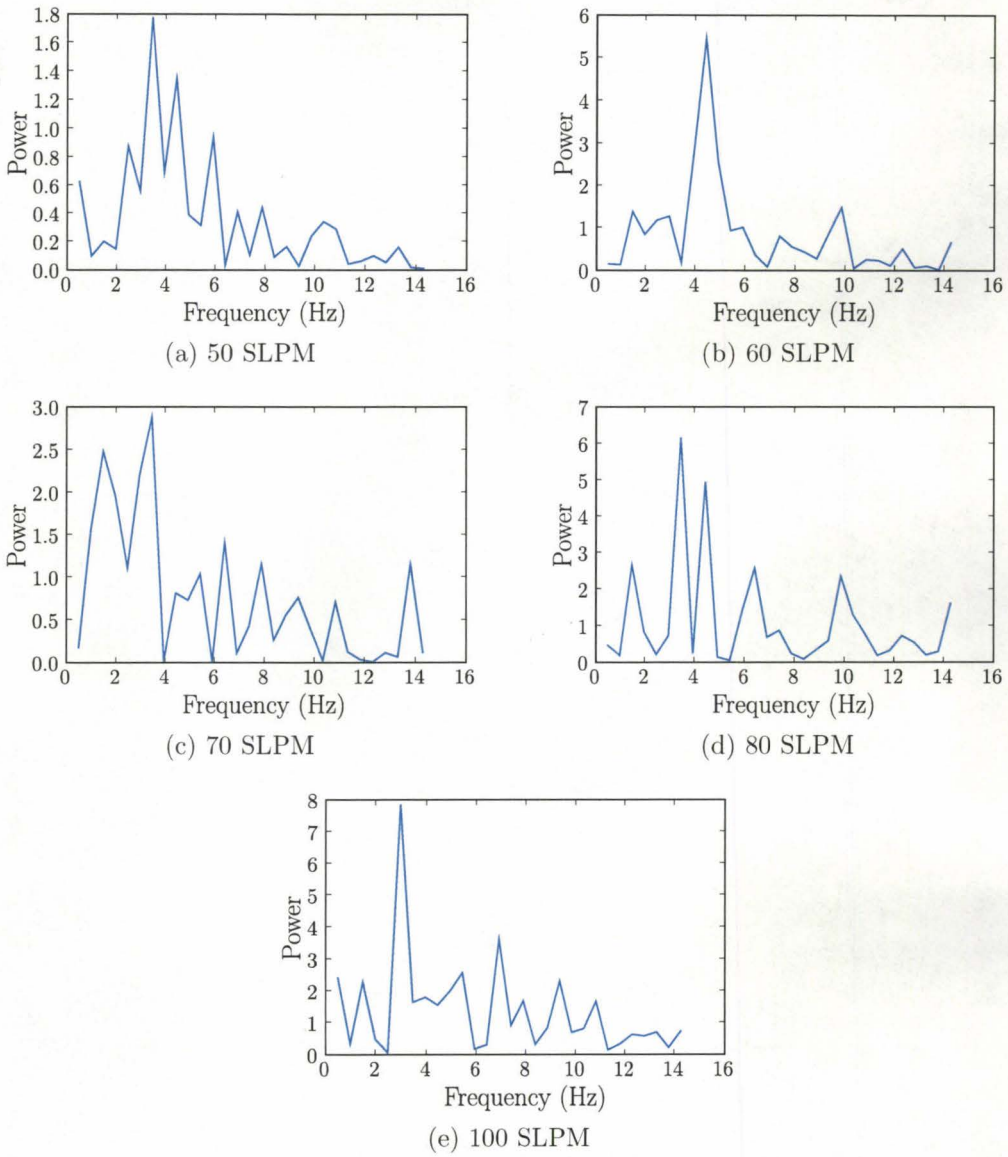

(a) 50 SLPM

(b) 60 SLPM

(c) 70 SLPM

(d) 80 SLPM

(e) 100 SLPM

Figure F.11: Fast Fourier transform of time series of cavity depth change when the lance height is 24cm.

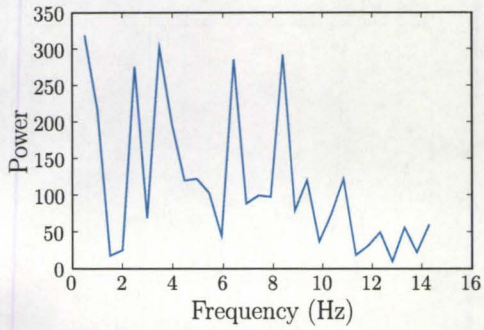

(a) 50 SLPM

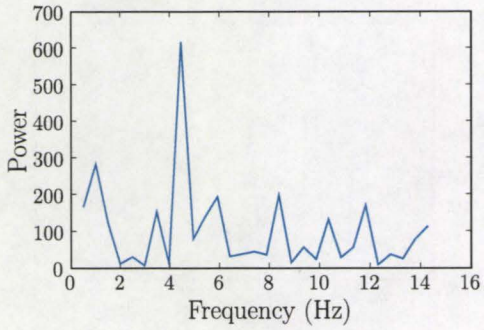

(b) 60 SLPM

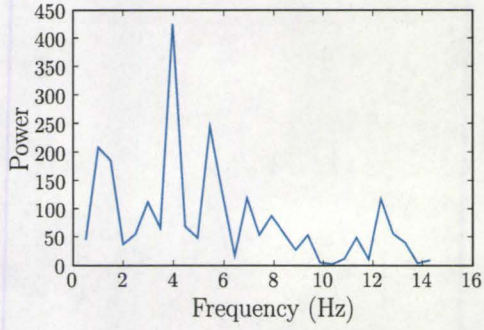

(c) 70 SLPM

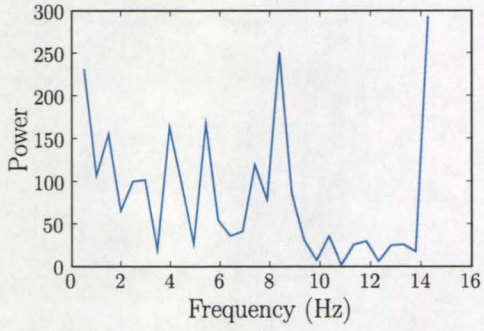

(d) 80 SLPM

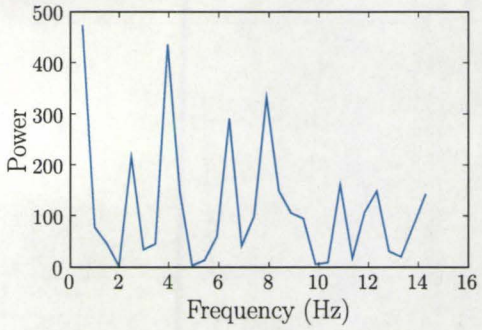

(e) 100 SLPM

Figure F.12: Fast Fourier transform of time series of cavity width change when the lance height is 24cm.

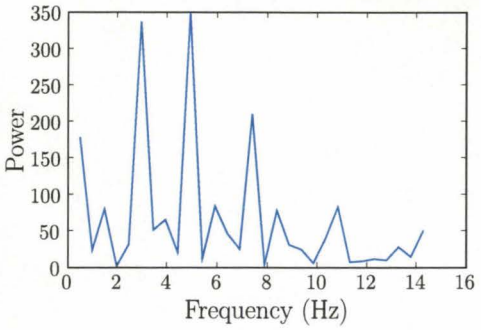

(a) 50 SLPM

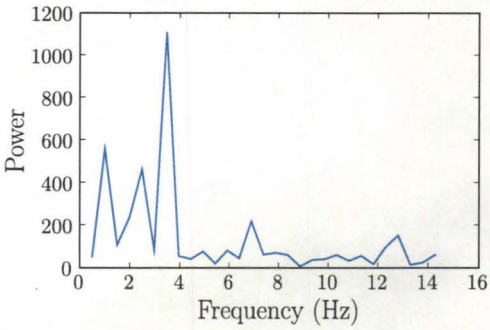

(b) 60 SLPM

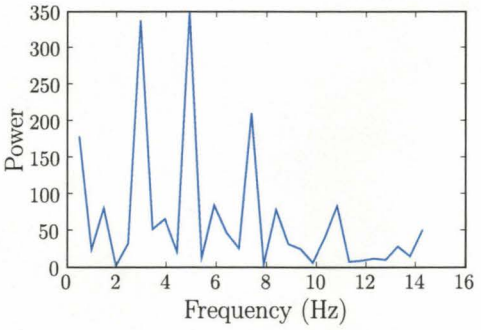

(c) 70 SLPM

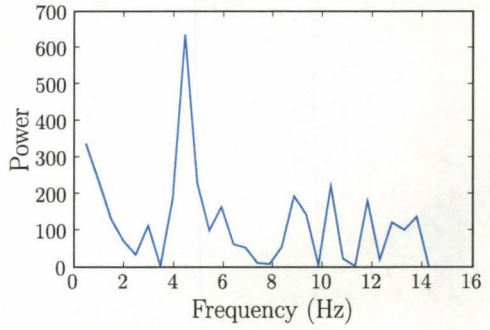

(d) 80 SLPM

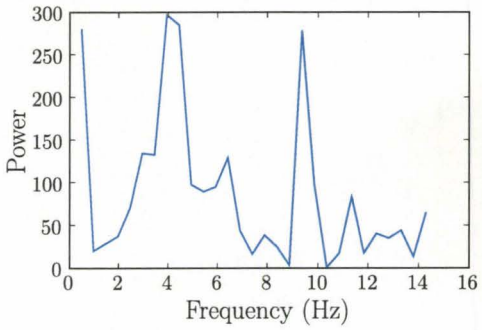

(e) 100 SLPM

Figure F.13: Fast Fourier transform of time series of horizontal position of the cavity depth change when the lance height is 24cm.